Investigation into Factors affecting Precision Positioning Instruments with a view to Standardisation of Specifications.

Thomas Wemyss

Department of Engineering Technology

Waterford Institute of Technology.

Submitted for the degree of Ph.D.

December 2011

Research Supervisors: Mr. Joseph Phelan

Declaration

I, the author, hereby declare that this submission is my own work, except where indicated by special reference in the text and that, to the best of my knowledge and belief, it contains no material previously submitted for the award of any other degree.

Signature of Author: ………………………………….

Tom Wemyss

Date: ………………

To Nora

Acknowledgements

Abstract

This thesis investigates the requirements in their totality of precision positioning instruments with a view to suggesting standardised specification guidelines. Although concerns over inadequate vendor specifications were voiced as early as 2003, no national or international standards have yet been published that address this issue.

To facilitate this investigation, a comprehensive design was undertaken of a three axis nanopositoning instrument. A state-of-the-art design was realised, based on an extensive review of the literature, while also incorporating particular novel features and procedures.

Mechanically, the instrument designed in this work consists of a support frame that is kinematically mounted onto a base plate. A piezo driven monolithic flexure stage/force-frame and a metrology frame are both mounted isostatically onto this support frame. The movements of the stage are measured by a parallel metrology arrangement of three capacitance sensors that are calibrated in place by three Michelson interferometers. Use of commercially-available adjustable optical mounts provides adequate flexibility for set-up and experimentation. Specified set-up procedures, in combination with a specifically designed orientation jig ensure that all capacitance sensors and interferometers are properly aligned and that the measurement and movement axes coincide in accordance with the Abbe principle. A set of LabView programs, are used to control and monitor the stage position to calculate the coordinates of locations, to allow scanning over curved surfaces and tracking along curved paths, to calibrate the capacitance sensors, to compensate for positioning bias, arising from measured environmental disturbances and to correct for measurement non-linearity through fourth order error mapping.

An iterative design process was employed, using an effective approach of parallel prototyping, calculation, Finite Element Analysis (FEA) and MathLab modelling. Propagation mechanisms of uncertainties associated with all identified error sources were studied, leading to the establishment of an uncertainty budget and an estimate of instrument positioning tolerance. An efficient and effective experimental regime was proposed, reflecting the numerous known factors and unknown interactions between factors that may be significant. This provided a means to validate the design, theory, and analysis and also to gain insight into the necessary experimental rigor,

Although the instrument was not assembles or tested, the instrument comprehensive design and analysis provided an effective vehicle for attaining insight into the relative significance of multiple factors that affect the performance of precision instruments in general. Consequently, it was possible to suggest appropriate standardising guidelines for the specification of precision positioning instruments.

Contents

Table of Figures

7

9

16

Table of Tables

17

Chapter 1

1 Introductory Chapter

Taniguchi [1] introduced the concept of nanotechnology in 1974 as "*concrete target accuracy for fabrication processes*". Since then technological progress towards greater accuracies has allowed nanotechnology to become a key enabling technology in such diverse high-tech fields as semiconductor fabrication, precision machining, the shaping of precise optical lenses and surface characterising nanometrology. A growing variety of nanopositioning devices has also been developed, each claiming the capability of repeatedly producing motion in increments as small as 1 nm or below [2]. The American National Institute of Standards and Technology NIST [3], for example, has developed a precise surface measuring instrument named 'the Molecular Measuring Machine' that has a scanning range of 50 mm × 50 mm and is capable of distinguishing between surface molecules. Examples of commercially available devices, including their capabilities, along with a list of instruments that have been developed by academic research groups, are reviewed by Hansen et al. [5].

For all these instruments nano-level precision positioning success requires the combined application of diverse technologies. Instrumentation typically consists of tool/part mountable stages, high resolution actuators, precise friction free mechanical guidance mechanisms, closed loop disturbance compensated and error mapped proportional integral (PI) control; all in conjunction with a high resolution position measurement system traceable to international standards of length.

The most commercially significant application of nanopositioning is in the manufacture of semiconductor chips. These are fabricated by sequentially etching mask defined patterns into silicon wafers. Hence the ever-increasing chip feature density is critically dependant on the sequential mask/wafer two-dimensional alignment resolutions. According to NIST, chip feature placement tolerances of 5 nm are currently facilitated [6].

Ultra precision machining on the other hand necessitates extremely accurate three-dimensional location positioning control of tools relative to work pieces and vice-versa. Miniaturized machine parts and macro-components incorporating, features such as ultra precise smooth surfaces, micro-holes, micro grooves etc., "currently require the achievement of dimensional tolerances of the order of 10 nm and surface roughness

of 1 nm" [7] and involve machining processes that include precision drilling, turning, milling and grinding.

Nanopositioning and contouring capabilities are also a prerequisite to several metrological techniques that have emerged as suitable for imaging surfaces at the nanometre scale such as scanning probe microscopes (SPMs) or scatterometry ("used extensively in the semiconductor industry to measure grating periods and structured surfaces" [8]). SPMs have, up to now, generally been 2.5 dimensional techniques, scanning over 2 dimensional surfaces while measuring along axes normal to those surfaces. A need for true three-dimensional (3D) measurement techniques, that can access sidewalls, undercuts, bores, etc., is now also emerging, particularly in the semiconductor industry and for the development of micro electrical mechanical systems (MEMS) where critical dimensions of high aspect ratio structures need to be measured [8].

Without capable measurement techniques and instrumentation, the process control necessary for industrial manufacture of components would not be possible [9]. Since a "general rule of thumb indicates that the measurement uncertainty should be 1/10 of the specified tolerance", absolute dimensions in the micrometre or even nanometre level, pose significant metrological difficulties [9]. To meet these challenges, new tools, in terms of instrumentation, calibration artefacts, specification standards and procedures, all incorporating traceability, are being developed by national measurement institutes (NMIs) (e.g. the U.K. National Physical Laboratory (NPL), the U.S. NIST, the German Physikalisch-Technische Bundesanstalt (PTB), the French Laboratoire National de Métrologie et d'Essaise (LNE)) and are a major focus of attention of the international organizations in the field (e.g. the European Society for Precision Engineering and Nanotechnology (euspen)). Much research effort on the part of academic research groups and NMIs is also aimed at improving the resolution, increasing the lateral scanning ranges (commonly less than 500 nm) and speeds of SPMs in order to facilitate measurements to be made of large areas of structures, wafers and optics. To this end, various strategies are being considered, e.g. the use of intelligent probing control systems, the application of a variety of sampling strategies, combining SPMs with other instrumentation for overview and 'coarse' scanning, etc. [7].

1.1   Specification concerns

One could be led to believe from many manufacturers' instrument descriptions that nanopositioning is a mature and well established technology. However, Chetwynd et al. [10] report that some very significant concerns related to this were expressed at a meeting of the 'Nanometre Metrology Network' held in London in 2003. The aim of the meeting was to identify the most recent 'Trends in nanometre metrology' and was attended by academics, industrialists and representatives from NPL. Related as chief among the concerns was that

 "instrument makers discouraged proper use of their products by the varied and often favourably interpreted way in which specifications were quoted".

An unnamed instrument manufacturer was reported as stating that "this was driven by commercial and not scientific demands" and that "any company that specifies its systems in a conservative, traceable manner risked them appearing inferior to those of less fastidious rivals, losing sales since most customers do not appreciate the subtle differences".

Mc Carthy [9] indicates that vendors simply accommodate customers' preference for accuracy to be summarized in single "easily digestible small numbers". He questions whether there is "a complete lack of awareness of the meaning and limitations of high accuracy systems or an overly aggressive marketing of 'small numbers' for competitive advantage". Murashov et al. [11] report that there also exists a lack of knowledge on the part of instrument users regarding the necessity for measurement traceability and often neglect calibration.

Chetwynd et al. [10] suggest that, in order to enable customers to compare rival systems sensibly:

- all manufacturers should be forced to clearly justify their claimed specifications in their literature;

- standard specifications need to be accompanied by a statement of uncertainty; and

- a European set of guidelines on best practice for specifications would be useful.

This view is reflected as recently as 2010 in the 'UK Nanotechnologies Strategy' [12]. The document acknowledges the relevance of standardisation in the context of these emerging technologies as "an important step towards the commercialisation of research and fostering of innovation; they establish a common framework and understanding, providing the bridge between research and industry".

1.2   Standardization efforts

Johnstone [13] describes standards as self consistent documents that describe generally accepted ways of doing things, which are developed by experts in consultation with stakeholders. Large numbers of national and international standards, guides and recommendations are published each year to address issues in many areas of human endeavour. The International Standards Organization (ISO) [14], for example, claims to publish more than 1000 standards per annum.

Activities of governments, standards institutes, academia and industry indicate an appreciation for the necessity of nanotechnology focused standards. Such standards would ensure:

- quality, reliability and compatibility of nanotechnology based products;

- enhanced trade and market development for such products by providing confidence to the market;

- knowledge transfer through clearer communication;

- guidance on best practice;

- improved management;

- supported innovation and commercialisation;

- a basis for procurement; and

- support for appropriate legislation/regulation. [13][14]

In light of this, various working groups and committees have been set up to address this need, e.g. the Nanotechnology Standards Panel (ANSI), the Committee E56 on Nanotechnology (ASTM), the British Standards Committee on Nanotechnologies (NTI/1) (BSI), the European Committee for Standardisation (CEN/TC352) (CEN), the

ISO Technical Committee on Nanotechnologies (TC229) and the National Technical Committee on Nanotechnology Standardization 279 (Standardisation Administration of China - SAC). Berger [15] presents a chronology of the formation of these groups and the publication of standards in the period 2004 to 2008 that is attributed to the chairman of the NTI/1 and the ISO TC229 committees, Dr. Peter Hatto.   A comprehensive list of ASME, ASTM, BSI, IEEE, NIST published international standards related to nanotechnology, as well as those that are currently under development, is given in the Good Nanoguide web-site [16], while Dupeng [17] and the Organization for Economic Cooperation and Development (OECD) [18] provide a comprehensive list of Chinese standards. Furthermore, ISO TC229 [14] provides an up to date list of ISO nanotechnology standards. It is apparent from reviewing these lists that the standardization process is still in its infancy. It is clear that no standards yet address the identified concerns particular to specification of instruments dependant on nanopositioning technology, i.e. the characterisation of these systems, including tolerancing, measurement traceability, calibration, modelling of uncertainties, control, error compensation, etc. The 2011 report of the ObservatoryNano project (a 7th Framework Programme) [19] blames this lack of progress on the increasing number of nanotechnology applications, gaps in knowledge, slow progress in research, differing viewpoints of regulatory agencies and the proprietary nature of relevant information. Furthermore the ObservatoryNano report asserts that regulation in the field of nanotechnology is currently substantially based on existing provisions with only some changes to address nanotechnology specific issues.

Numerous international standards currently exist that are essential to world-wide manufacturing of macro-scale products. The ISO Technical Product Specification (TPS) standards, for example, is a collection of 242 standards that are claimed to facilitate global manufacturing and trade by providing a basis for communication of requirements, legislation, specification and verification. It is prudent to consider the possibility of utilising such existing standards or variants thereof in the specification of nanopositioning devices, as this approach may expeditiously lead to effective and comprehensive standardisation. Osanna et al. [20] propose that it is feasible to adapt the ISO Geometric Product Specification and Verification standards (GPS) (a sub-set of TPS) for use in the field of nanotechnology. GPS is a suite of 118 individual standards that have been collected in line with a master plan, under the responsibility

of the technical committee TC213 [21] that address macro- and micro-geometry specification (including tolerancing); surface properties, and verification principles; dimensional measuring equipment and calibration; measurement uncertainty; and drawing layout and symbols.

Hansen et al. [4] suggests the use of GPS would be the most straightforward approach for tolerancing in micro- and nanometrology, but identifies several problems in this regard.

Conformance assessment, in the case of macroscopic production, is closely related to metrology [22]; assessment involves standardised measurement definitions, unambiguous descriptions of appropriate measurements methods, traceability to SI measurement units, standardised measuring instruments and laboratory capabilities [22]. Uncertainty traceability is commonly achieved by transfer standards, realised as artefacts such as scales, gauge blocks, optical flats, etc. Similarly, nanometrology is a prerequisite to standardising conformance assessment of nanosystems. It is recognized by Hansen et al. [4] that standards for transfer of traceability and calibration are needed since "the standards available today are still merely miniaturisation of macro-scale standards". They also identify the existence of a metrology gap in terms of new measuring principles, instrumentation, tolerancing rules, procedures and calibrations. Furthermore, Hansen et al. [4] identify a need to develop models for estimating uncertainty for new types of measuring principles and instrumentation in order to facilitate an internationally common basis for evaluating and comparing new technologies.

Two existing ISO/IEC standards, written by the ISO committee on conformity (CASCO), are of particularly interest because their purpose is stated to be the provision of assurance to customers with regard to the conformity of products to specified performance requirements. ISO/IEC 17050-1:2010 specifies the requirements of suppliers' declarations of conformity, while ISO/IEC 17050-1:2004 specifies the supporting documentation to substantiate a supplier's declaration of conformity. It is suggested that these standards promote new product development by facilitating self-certification, instead of certification by external bodies. Furthermore, the generic nature of these standards, not being applicable to particular products or product types, suggests that perhaps they could be used in relation to nanopositioning devices.

1.3   The research question

The preceding sections illustrate that concerns exist regarding how highly accurate positioning stages are specified/marketed and that despite structured international standardisation effort, these concerns have so far not been addressed through the development of new nanopositioning targeted standards, while the viability of existing standards in this regard requires further consideration. It is therefore proposed that this thesis should address the following question.

What are the documentation requirements of a comprehensive generic specification for instruments capable of positioning and contouring at nanometre scale accuracy?

1.4   Structure

As a vehicle for identifying and gaining insight into the requirements of a highly accurate positioning instrument, a three axis contouring stage, capable of nanometre positioning accuracy is designed and characterized for this thesis. Through the design process, the tolerance determining uncertainties associated with the mechanical, measurement and control aspects of the instrument are quantified while the environmental, set-up and procedural requirements are established.

A review of the related literature is given in Chapter 2. This review is substantially targeted at ensuring that the instrument design is based on best practice. The chapter also examines the design process itself, including the effectiveness of FEA and model validation through prototyping. General design principles are adopted from this review concerning metrology alignments, stage size and symmetry, as are techniques ensuring that the biases resulting from identifiable error sources are properly avoided or minimised.   The chapter also forms the basis for specific design decisions that underpin the mechanical system (the material choice, actuation, guidance mechanisms, coupling of structures, component mounting arrangements); the metrology system (the choice of reference and process measurement sensors, set up procedures for ensuring alignment and orthogonality); and the control system (choice of controller, error mapping). Additionally, a standardised approach for the expression of uncertainties, identified in this chapter, is used to characterise the instrument through the establishment of an error budget, and to ultimately identify the specification requirements of such instruments in general.

Chapter 3 describes the design of the instrument mechanical structures. The design strategy, principles and early design decisions, including material choice are described. Comparison between FEA, theoretical predictions and the measured results from a prototyped single axis stage is used to validate the subsequent use of FEA and theoretical methods. The meticulous design, analysis and development of the mechanical structural components of the 3D nanopositioning instrument is then described.

Both the process and the reference metrology arrangements and their associated error sources are described in Chapter 4.

Chapter 5 describes the instrument command and control system. The functionality of various inter-dependant programs, developed in Labview and Mathcad software for this thesis, is explained. These programs are used to automatically calibrate the process sensors with respect to the reference sensors; linearise the process sensor through error mapping; compensate for environmentally induced bias; translate Cartesian coordinates to instrument coordinates for commanding the stage and vice versa when monitoring its position; and formulate the command sequences for driving the 3D stage over defined paths. The chapter also examines the axial dynamic characteristics of the designed stage. Transfer functions are derived for both open loop and closed loop proportional integral (PI) control with a notch filter. Standard second order analysis of the system is applied, allowing the axial response characteristics to be balanced across all axes and provisional controller parameters to be established.

The propagation of the measurement system component uncertainties (Type B) into uncertainties of displacement positioning is investigated in Chapter 6. These are ultimately quantified for the designed instrument and tabulated in accordance with NIST guidelines [23] to form an error budget.

Chapter 7 addresses the instrument set-up, environmental requirements and the design of experiments capable of validating the design work and theory described in previous chapters. Although the chapter is concerned primarily with the future development of this project, the chapter also accommodates the investigation into the influence of each of these factors on instrument specification. Included is a step-wise set of set-up procedures and descriptions of specially designed jacks, jigs and decoupling plates aimed at ensuring proper alignment. Environmental data obtained by monitoring the

existing room and enclosure is presented and an improved arrangement is proposed in light of the predicted effects on accuracy of environmental variation. A screening fractional multi-factorial design is advanced as the most efficient and effective experimental approach in the context of the numerous known factors and interactions between factors that may significantly affect the instrument performance. Additionally, a subsequent full factorial set of experiments is proposed to examine the effects of factors arising from dynamic contouring.

A thesis summary and conclusions are finally presented in Chapter 8. Observations and findings arising from the design process, as presented in the previous chapters, are ultimately used as the basis for suggesting appropriate specification requirements of precision positioning instruments. The use of the design as a vehicle of investigation is therefore justified and the subject of this research is successfully addressed. Presented also is a specification of the designed instrument, as an example of a documentation set that is based on these proposals.

The desired outcome of this thesis is a set of proposals for standardising the specification of nanopositioning devices in general, which are based on insightful knowledge acquired through the design and analysis of one such instrument. To fully capitalise in terms of possible insights, attainable from the development of this instrument, major structural components have been manufactured; a complete set of control software has been written; a suitable environment realised; a rational set of assembly procedures (including tooling) has been planned (see Section 7.2.); and a complete experimental regime has been designed (see Section 7.4). However, the assembly and testing has not been undertaken within this thesis, as it would not contribute significantly to understanding the documentation requirements of such instruments. Also, it should be appreciated that completion would not be a simple undertaking; it would constitute a separate post-graduate level project, involving difficult and time consuming alignments; requiring additional funding for instrumentation and tooling. Furthermore, for this particular instrument, it is not the physical build or testing, but the correctness of the design based uncertainty budget that ultimately determines confidence about positioning accuracy.

Chapter 2

2   Literature Review

2.1   Introduction

Nanopositioning, the capability of repeatedly producing motion in increments smaller than 100 nm, is now a key enabling technology in high-tech fields such as scanning microscopy and microlithography [2].   It should be kept in mind throughout this chapter that the main purpose of designing a nanopositioning instrument for this thesis is to investigate factors relevant to the standardisation of specifications for precision positioning instruments in general.   Consequently, even though the instrument will not be physically assembled, this chapter aims to identify the state of the art in design of precision positioning instruments and principles on which to base a successful design of such an instrument while simultaneously identifying key factors that should be incorporated in specifications of such devices in general.

Instruments attributed with nano or near nano scale resolution have already been developed by researchers. Wei Gao et al. [24], for example, present a nanomachining instrument developed for conducting nanoscratching, nanoindentation and nanocutting experiments (with maximum depth of cut of 4 μm with a 0.1 nm resolution). Atherton et al. [25] describe the design of an ultra precision XY positioning/scanning stage with sub-nanometre resolution and long term stability.   Ruijl [26] provides an extensive description of an ultra precision CMM design, indicating sources of error and listing their contribution to the instrument's volumetric measuring uncertainty.

Commercially, a variety of very highly specified positioning instruments are also available from numerous suppliers:

- PI [27] for example sells a XYZ NanoCube with a 350 µm x 350 µm x 250 µm travel range and a 1 nm resolution.   This also boasts an integrated parallel metrology system.

- Queensgate Instruments [28] supply a range of multi-axis devices that can position with sub-nanometre accuracy.   As described by Ying Xu et al. [28], the system comprises of "nanomechanisms" including single axis, XY and tilting stages, which are then combined to provide three, four or six degrees of freedom.

- SIOS have developed a nanopositioning and nanomeasuring machine called the NNM-1. This has a measurement range of 25 mm × 25 mm ×25 mm and claims a resolution of 0.01 nm.

The necessity for positioning and contouring accuracy has arisen from a desire to realise various application goals. As early as 1995 Taniguchi [1] indicated the need for processing systems capable of manufacturing products to nanometre accuracies and sub-nanometre resolution. Chih-Liang Chu et al [29] indicate that the development of various probe-type measuring techniques (scanning probe microscopes) relies heavily on the development of high precision positioning stages. They also state that there is currently a requirement for a range of devices capable of performing at 10-100 nm scale such as IC stepper machines, precision machining devices, optical fibre alignment systems, high density information storage, nano coordinate measurement, etc. Yeh et al. [30] state that devices with ultra precision tracking capability are essential to scanning probe microscopy.

2.2 Nanopositioning devices

A precision positioning system in general require nano-drives, nano-guides, and nano-ruler sub-systems according to Yeh et al. [30] and must include the function of calibration and traceability of measurement results. Furthermore, closed-loop feedback control is necessary to reduce non-linearity, hysteresis, and measurement noise arising from environmental fluctuations.

Fig. 1 illustrates the complexity of a precision positioning system. All of these sub-systems and techniques must be carefully considered if a successful design of such an instrument is to be achieved.

The main elements of a nanopositioning device are the:

Mechanical system: This consists of a:

- Stage: This is the platform for supporting a work-piece or tool.

- Guidance system: Its purpose is to guide stage movement along desired paths, while minimising all parasitic movement.

- Force frame: The reaction forces necessary to balance the actuators displacement force exist on this frame.

- Metrology frame: This supports the components of the metrology system.

- Support frame: This supports the stage, the guidance system, the force frame and the metrology frame.

Environmental Control

Mechanical Structures

Mounting

Guides

Force frames

Stage

Support Frame

Mechanical Vibration

Control systems

Piezo actuation

Command Signal

Command errors

Error Mapping

LabView algorithm

PID control

Accuracy Repeatability Reproduceability

Feedback

Humidity

Displacements

Resonance frequencies

Metrology frame

Component mounts

Parasitic displacements

Measurement errors

Capacitance sensors

Electrical noise

Interferometer calibration

Thermal Variation

Set up and alignment

Metrology

Fig. 1 Elements of a precision positioning system.

Metrology system: This consists of:

- Position measuring system which measures displacements of the stage as it moves through a commanded path.

- Calibration system which is used to calibrate the position measurement system. It must also provide traceability to international measurement standards.

Control system: This consists of:

- Actuators, adequately responsive and resolute so that curved paths may be accurately tracked.

- A closed loop controller, capable of instantaneous correction of positioning biases.

- Software programs that provide an interface allowing the desired displacement paths to be defined, sensors to be calibrated and predictable positioning errors to be compensated.

The environment: This consists of:

- Anything or anybody in the vicinity of the instrument that may affect its performance. It includes all influences on temperature, pressure, humidity, electrical noise and mechanical vibrations.

2.3 Positioning error sources and uncertainties

All aspects of a positioning system, including design analysis, mechanical structures, metrology arrangements, control systems and set up methodologies as well as system characterisation are dominated by the existence of errors. To effectively specify a precision positioning instrument and to establish confidence in its capability, all possible sources of error must be identified and their effects and interactions understood so that their associated uncertainties can be quantified. In order to design such an instrument, much effort has to be targeted at minimising, avoiding, compensating for or eradicating all such errors and their sources.

2.3.1 Common terms defined

To address the subject of positioning errors, an unambiguous understanding of what is meant by terms such as error, repeatability, reproducibility, precision, accuracy, trueness and uncertainty is a prerequisite. For the purpose of this thesis, the interpretation of these terms is based on ISO5725 [31], since it is this standard that is referenced extensively in the International Vocabulary of Metrology (VIM) [33].

The value of a measurement can only be an approximation of the true value and uncertainty may exist even when there is no error. Therefore, the result is complete only when accompanied by a quantitative statement of uncertainty [33]. The U.S. National Institute of Standards and Technology (NIST) published a set of guidelines (TN1297) [33] for evaluating and expressing uncertainty of measurement results. This

is based on the ISO Guide to the expression of Uncertainty in Measurement GUM [23]. Throughout this thesis, uncertainty will be expressed in accordance with GUM.

Fig. 2 Constituent parameters of accuracy [25].
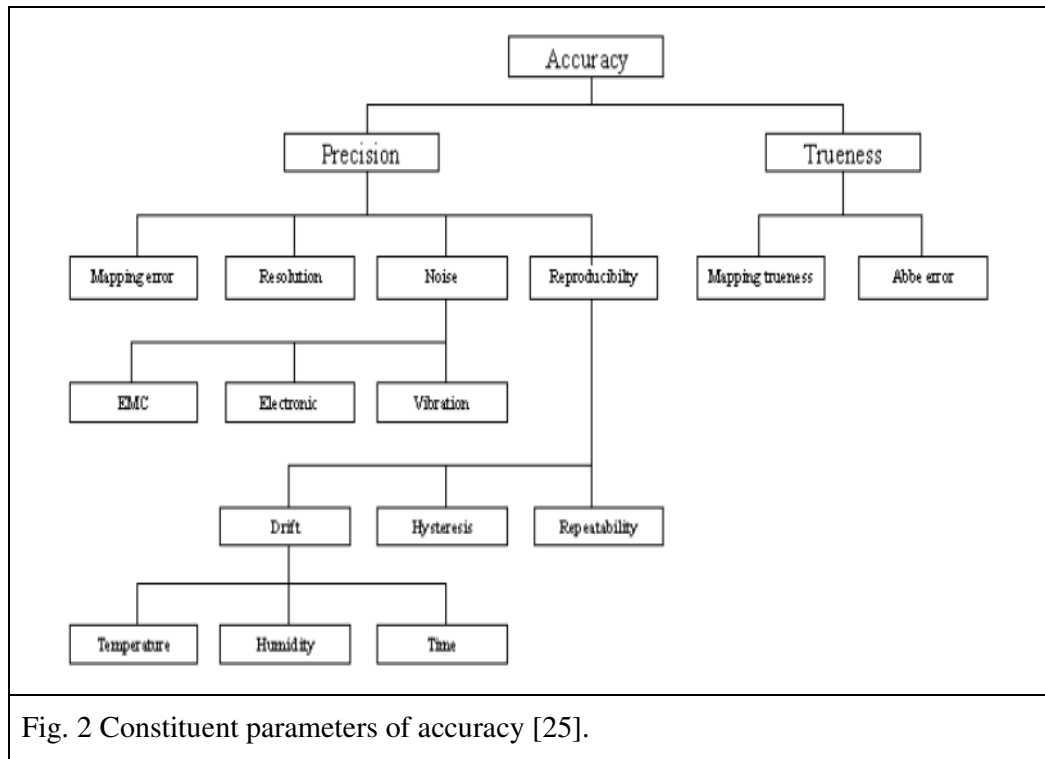
The factors which may affect the accuracy of a nanopositioning stage (Fig. 2) are identified by Xu et al. [25] and are presented in Fig. 2. Fig. 2 clearly indicates areas to which attention must be paid if accuracy is to be achieved.

2.4 Identification of errors

Some error sources are associated in particular with the physical movement and positioning of the stage while other error sources are associated with the measurement of this movement. It must also be recognised that unintended actual physical movement may also cause errors in measurement, e.g. pitch, roll or yaw may cause cosine and/or Abbe errors, which will be described in Section 2.4.3.4. This section looks at error sources that are regarded as being significant by most researchers.

2.4.1 Thermal Variability

Ruijl [26] indicates that thermal effects are the largest source of apparent non-repeatability of machine position accuracy and lists a variety of ways by which temperature variability affects a positioning system:

- Expansions of mechanical structures, i.e. stage, force frames, guides, mounts, etc. may cause unwanted stage displacements.

- Unequal relative expansion of components, when combined with linking constraints, can cause stresses to be induced within the instrument structures, which in turn may result in asymmetrical distortions.

- Unpredictable thermal gradients may also cause stress and warping of overly constrained structures causing stage response to be unpredictable.

- Metrology frame and/or components may expand or warp, causing undetected relative displacements within metrology loops.

- Thermal expansion of interferometer refractive optical media can give rise to relative changes in beam geometric paths and phase shifts in optical paths, which can be misinterpreted as stage displacements.

- Interferometer laser wavelength varies with temperature.

- The electric constant (ε_0) varies with temperature affecting capacitance measurements.

- Noise in conductors may be introduced and may affect the noise factors calculated for sensors.

The spreading of heat by radiation, convection and conduction results in a temperature distribution (time and space dependant) in and around instruments and Ruijl [26] further indicates a variety of thermal sources including the instrument environment, coolants, processes, the instrument itself, people, computers, etc. It is suggested that it is necessary to consider the contribution of the work piece, the frame and the measurement system when analysing the total thermal positioning or measuring error.
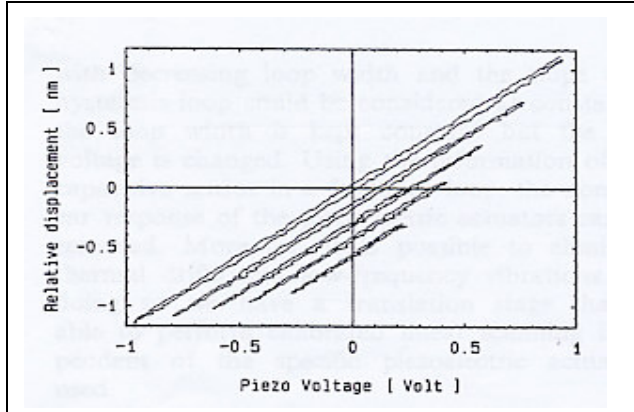
Fig. 3 Hysteretic single axis stage displacements repeated at 80 sec intervals illustrate the positioning drift due to thermal drift as presented by Holman et al. [34]

The effect of thermal drift is illustrated in the work of Holman et al. [34]. Having carried out a series of experiments on a single axis piezo driven translation stage using capacitance position sensing. They present a graph (Fig. 3) showing hysteresis curves generated approximately 80 sec. apart. The clearly illustrated downward displacement of the curves is assigned by Holman to thermal drift and has been estimated to be 0.12 nm(min)$^{-1}$.

Unfortunately a detailed description of the environmental control used or a record of the temperature variability during the tests is not provided.

2.4.1.1 Minimising thermal error

A variety of techniques are presented by numerous researchers aimed at reducing the affects of thermal variability on positioning accuracy.

Ruijl [26], for example, lists the following series of measures:

- Liquid flow over the machine to control heat flow.

- Thermal insulation to minimize heat flow.

- A simple enclosure without active temperature control can be effective method for instruments with small internal heat generation.

- Transparent coatings are available to reduce infra-red heat radiation (Coolshield [35]).

- A highly thermal conductive aluminium sheet surrounding the instrument metrology frame at a distance of approximately 5 mm can be used to create a homogeneous temperature distribution. The method is called thermal shielding and its effectiveness is illustrated in Fig. 4, where the temperature distribution

along the cross-section of an aluminium frame, with and without aluminium shielding, is shown, when subject to a heat source q.

Fig. 4 Comparison between a thermally unshielded and shielded frame subjected to a heat source q presented by Ruijl [320].
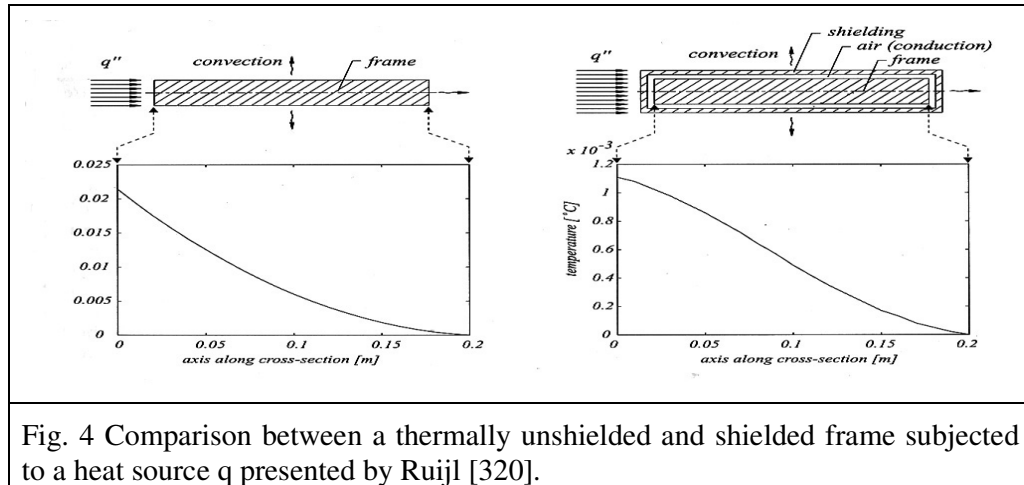
- Optimisation of the machine design to obtain small sensitivity to thermal disturbances.

- Compensation for errors via software.

Yeh et al. [30] reports the very practical use of a 5 cm thick polyfoam box, pasted with aluminium foils on the inner and outer sides, to cover their entire scanning probe microscopy positioning system. Its purpose is to shield most acoustic noise and thermal fluctuation. Their experiments are performed also in a very stable environment where the variations of room temperature and humidity are controlled to within 0.05 K and 2 %, respectively.

Smith et al. [36] are of the view that performance only depends on the stability of the metrology loop and suggest various possible mechanical compensation strategies for minimising the influence of thermal expansion on the loop:

- Use materials with low thermal expansion, e.g. Invar.

- Construct all components from the same material.

It is suggested that if components within a measuring loop are made from the same material, then the thermal expansion related changes around that loop will compensate.

- Use materials with carefully chosen expansion coefficient ratios to make up for lost expansion occurring at air gaps.

38

- If a measuring loop structure must carry a heat source, it is a good idea to place the source at an axis of symmetry. Then equal conduction paths and thermal capacities should lead to equal thermal gradients.

- With proper mounting arrangements (isostatic or kinematic), thermal expansions of attached structures can be substantially decoupled so that very little stress is transmitted between components, thus avoiding distortions [37]. Additionally, isostatic and kinematic methods allow relative displacements of metrology components/ locations, resulting from expansion, to be controlled [36], predicted and compensated.

2.4.1.2 Thermally induced errors in the metrology system

Interferometers are commonly used as external reference measurement systems [29], [26], [25], [37], but a variety of interferometer specific errors are possible.

Expansion of mirror substrates

The expansion of interferometer mirror substrates would lead to variations in the relative optical path lengths. Mirror manufacturers such as Melles Griot Inc. [38] and Linos Photonics Gmbh. [39] supply their standard mirrors with ranges of substrates, all of which have relatively low coefficients of thermal expansion (Zerodur, Low Expansion Borosilicate Glass (LEBG), Synthetic Fused Silica, etc.). Commonly-used Zerodur has a coefficient of thermal expansion (CTE) of $0 \pm 0.15 \times 10^{-6}$ K^{-1} at room temperature i.e. a 6 mm thick mirror would expand 0.9 nm along its thickness axis for a rise of 1 K.

Ruijl [26] reports that some CMM manufacturers claim that by using a measuring system with a very low thermal sensitivity, fluctuations in temperature can be ignored. Ruijl is of the view that only a limited improvement can be obtained in this manner since some sections of the metrology loop will invariably not be made of Zerodur.

Thermal expansion of interferometer optical components

According to McCarthy [9] thermal expansion of interferometer refractive components such as the beam splitters or retro-reflectors can result in large measurement error if the optical paths of the measurement and reference beams differ significantly through

these media. It is claimed that for a two-pass Michelson interferometer, a very significant error, in the order of 0.5 μm K^{-1}, is typical.

Of course, if the temperature is kept constant or if it is arranged so that the optical paths for both beams are identical through each media, then this problem would not arise. Ensuring that the reference and measuring beams travel through identical thickness of media must be seen as a critical design criterion.

 The affect on the wavelength of a He-Ne laser

He-Ne laser light, which has a 633 nm wavelength in vacuum, is commonly used in interferometers used for displacement measurement. Any uncertainty in the laser wavelength would translate into positioning uncertainty. The calculated effects of environmental changes on the wavelength are shown in Table 1.

	Normal Temperature & Pressure (NTP)	1 K Rise in Temp	1 kPa rise in Pressure	1 % rise in Humidity
λ (Vacuum) (nm)	633	633	633	633
Air Temperature (K)	293.15	293.15	293.15	293.15
Atmospheric Pressure (kPa)	101.325	101.325	102.325	101.325
Air Humidity (Relative Humidity %)	50	50	50	51
CO_2 content (micromoles/mole)	450	450	450	450
Refractive Index of Air	1.000271375	1.00027042	1.000274056	1.000271364
λ (Air) (nm)	632.828268	632.82887	632.82657	632.828273
Relative change in λ (ppm)	1	0.951	2.68	0.0076

Table 1 Effect of environmental factors on the wavelength of HeNe laser light.

All calculations in Table 1 were made using the NIST 'Engineering Metrology Toolbox' [3], which is a web-based tool for calculating the index of refraction of air and the wavelength of light in air as a function of various input parameters, using the Ciddor equation [40].

It can be deduced from Table 1 that the effects on the laser wavelength (λ) are very small (<<0.001 nm), but for accurate measurement of long stage travel distances, this could still be problematic where the displacement is represented by a large number of wavelengths [41].

Expansion of capacitance plates

According to L.K. Baxter [42] thermal expansion is a limiting factor to the precision of capacitive sensors. The choice of construction material is critical in this respect. An aluminium (CTE = 23.4×10^{-6} K^{-1}) sensor with plate area of 16.6 mm^2 would be expected to increase its capacity by 0.005 % K^{-1} due solely to increased plate area. In addition, the gap between the plates may be reduced by as much as 46.8 nm per mm plate thickness K (dependant on how the plates are fixed to their base). This error may also be increased due to the expansion of the mount material itself.

The effects on the dielectric constant

The following affects on the dielectric constant (ε_0), due to variability in temperature, pressure and humidity, are presented by Baxter [42]. The effects on measurement are calculated based on these values and a 4.5 mm diameter circular plate capacitor operating at a gap size of 8 μm.

	Effect on ε_r	Effect on measurement
Temperature	5 ppm K^{-1}	0.085 nm K^{-1}
Relative Humidity	1.4 ppm $(\%RH)^{-1}$	0.02 nm$(\%RH)^{-1}$
Pressure	100 ppm $(atm.)^{-1}$	1.5 nm $(atm.)^{-1}$
Table 2 Environmental effects on the dielectric constant.		

The effects can be regarded as negligible for the expected small environmental variation. Baxter suggests that a three plate capacitor with two capacitances and ratiometric measurement is less sensitive to thermal expansion.

2.4.2   Metrology set-up errors

If adequate care is not taken at set-up, non-linearity and scale factor errors can be introduced into measurement. Here, the affects of misalignment of interferometer components, the misalignment of capacitance plates, and the non-orthogonality of measurement axes are examined.

2.4.2.1   Interferometer set-up errors

<u>Tilting of interferometer mirrors</u>

If the moving mirror is not perpendicular to the interferometer measuring beam, errors arise. Ruijl [26] presents a schematic diagram of the measuring beam path resulting from moving mirror tilt along with analysis leading to an expression for calculating errors.

Fig. 5 Beam path through a plane mirror laser interferometer when a tilted measuring mirror is translated as presented by Ruijl [26].
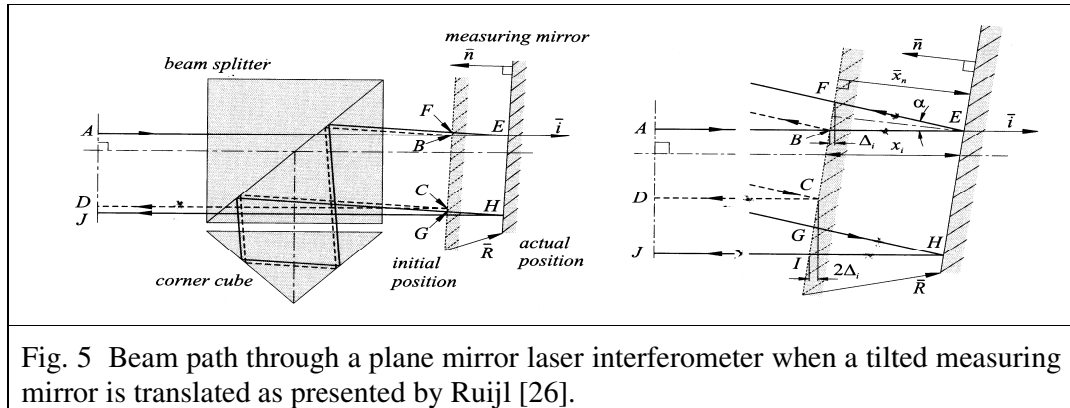
If the moving mirror is tilted, the measuring beam follows a varying path through the optics as the stage moves [26]. For the purpose of identifying errors arising from mirror tilt, it is also assumed that as the stage moves, the mounted mirror translates along a path normal to its surface (no cosine error as described in Section 2.4.3.4).

 According to Ruijl [26], as the mirror translates, the length of the measuring beam changes by

$$\Delta L = 4x_i + 2\Delta_i$$

Equ. 1

x_i = actual stage movement, Δ_i = small additional measured distance.

Alignment and orthogonality of measurement axes

Since the mirror table on his precision CMM "has to fulfil long term stability", Ruijl [26] has devised an error separation technique for regular calibration of the mirror flatness and measuring axis out-of-squareness. This is based on what is claimed to be a commonly used reversal method.

Fig. 6 Polygon orientations to establish the angle α between mirrors [26].
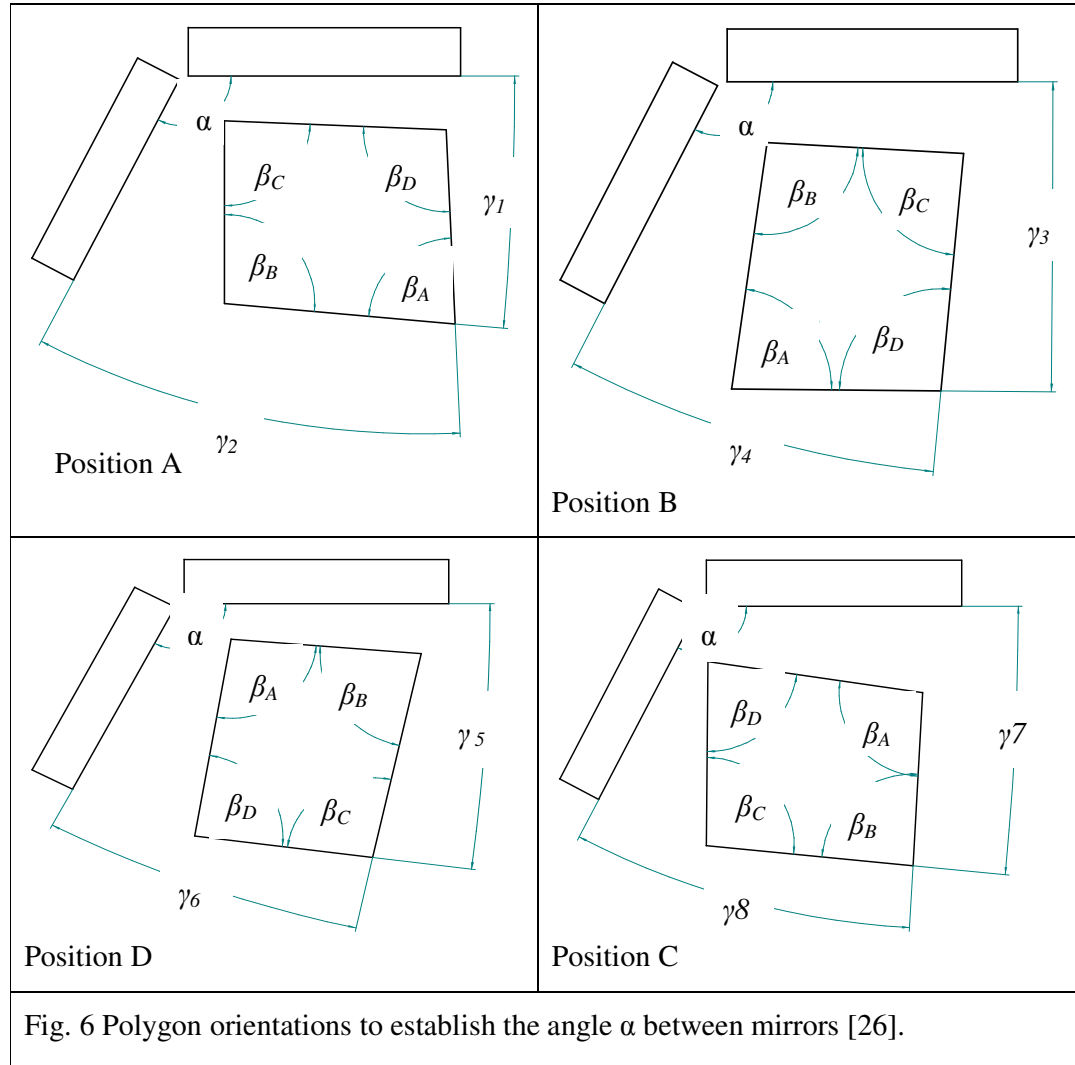
Position A $\beta_A + \gamma_1 + \gamma_2 = \alpha$ *Position B* $\beta_D + \gamma_3 + \gamma_4 = \alpha$

Position C $\beta_C + \gamma_5 + \gamma_6 = \alpha$ *Position D* $\beta_B + \gamma_7 + \gamma_8 = \alpha$

also $\beta_A + \beta_A + \beta_A + \beta_A = 2\pi$

43

$$\frac{2\pi + \gamma_1 + \gamma_2 + \gamma_3 + \gamma_4 + \gamma_5 + \gamma_6 + \gamma_7 + \gamma_8}{4} = \alpha$$

Equ. 2

The method for ensuring measuring axis orthogonality involves using a target polygon with four faces orientated in four different positions (see Fig. 6). The angles between the mirrors and the polygon faces are measured for each position. The unknown angle errors of the polygon can be separated from the desired value of the angle being measured using Equ. 2

Capacitance Sensor set up errors

Because of particular attributes such as size, resolution, linearity, etc., capacitance sensors are ideal for use as in-process displacement sensors on precision positioning instruments. Some errors, though, can arise when using capacitance sensors. These errors are discussed below.

Plate non-parallelism

According to Baxter [42], plate tilt is a source of non-linearity which corrupts the performance of simple parallel plate sensors. Tilt can be caused by errors in mounting or by parasitic movements of the stage on which the target plates are mounted. These unwanted movements vary with the magnitude of stage displacement, thus resulting in a varying angle of tilt with stage movement. This can add additional complexity to subsequent error mapping. Hicks et al. [37] report that a 5 mRad tilt gives rise to 0.6 % measurement non-linearity when using a 6 mm radius sensor with nominal gap size of 0.1 mm to measure over a range of -50 μm to +50 μm.

Holman et al. [34] propose the following equation to determine the capacitance of a two plate capacitive sensor (rectangular) with tilt about two orthogonal axes (X and Y).

$$C = \frac{\varepsilon_0 \varepsilon_r ab}{d_0} \left\{ 1 + \frac{a^2 \sin^2 \theta_x + b^2 \sin^2 \theta_y}{12 d_0^2} + \frac{a^2 b^2 \sin^2 \theta_x \sin^2 \theta_y}{24 d_0^4} + \frac{a^4 \sin^4 \theta_x + b^4 \sin^4 \theta_y}{80 d_0^4} \right\}$$

Equ.3

44

C is the capacitance (Farads); ε_0 is the permeability of free space (electric flux density in vacuum electric field strength =8.85419 pFm^{-1}), ε_r is the relative permeability in medium (approximately 1.006 for air), d_0 is the gap width between plates (m), *a* and *b* are the plate dimensions (m), while θx and θy are the angles of rotation about the X and Y axes respectively.

The Holman et al. [34] paper asserts that the tilting angles are often small and can usually be neglected. To reduce the sensitivity of capacitance sensors to tilt, Baxter [42] suggests adding a third electrode which effectively results in two capacitors. To reduce the effect of parasitic movement on a capacitive, Holman et al. [34] propose the use of four capacitors in a bridge arrangement. Although an expensive approach, this has the additional advantages of increased effective capacitance and reduced influence of changes in the dielectric.

2.4.3 Parasitic stage displacements

2.4.3.1 Pitch, Roll & Yaw
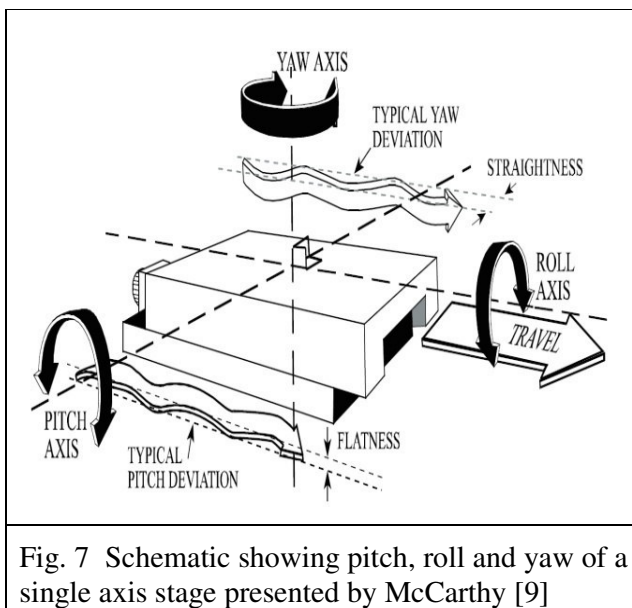
Fig. 7 Schematic showing pitch, roll and yaw of a single axis stage presented by McCarthy [9]

As can be seen in Fig. 7, roll is rotation about the axis of movement, pitch is rotation about an axis normal to the direction of this movement and yaw is rotation about the axis which is normal to both the aforementioned axes.

The effect on the positioning measurement of an XY stage commanded to follow a circular path is shown in Fig. 8 below.

45

	Y	Y_p	Y_y	Y_pY_y
X	(1) $r^2[\cos^2\theta+\sin^2\theta]$	(2) $r^2[\cos^2\theta+\sin^2\theta\cos^2\theta_p]$	(3) $r^2[\cos^2\theta+\sin^2\theta\cos^2\theta_y]$	(4) $r^2[\cos^2\theta+\sin^2\theta\cos^2\theta_p - \cos^2\theta_y]$
X_p	(5) $r^2[\cos^2\theta\cos^2\theta_p+\sin^2\theta]$	(6) $r^2[\cos^2\theta\cos^2\theta_p+\sin^2\theta\cos^2\theta_p]$	(7) $r^2[\cos^2\theta\cos^2\theta_p+\sin^2\theta\cos^2\theta_y]$	(8) $r^2[\cos^2\theta\cos^2\theta_p+\sin^2\theta\cos^2\theta_p\cos^2\theta_y]$
X_y	(9) $r^2[\cos^2\theta\cos^2\theta_y+\sin^2\theta]$	(10) $r^2[\cos^2\theta\cos^2\theta_y+\sin^2\theta\cos^2\theta_p]$	(11) $r^2[\cos^2\theta\cos^2\theta_y+\sin^2\theta\cos^2\theta_y]$	(12) $r^2[\cos^2\theta\cos^2\theta_y+\sin^2\theta\cos^2\theta_p\cos^2\theta_y]$
X_pX_y	(13) $r^2[\cos^2\theta\cos^2\theta_p\cos^2\theta_y+\sin^2\theta]$	(14) $r^2[\cos^2\theta\cos^2\theta_p\cos^2\theta_y+\sin^2\theta\cos^2\theta_p]$	(15) $r^2[\cos^2\theta\cos^2\theta_p\cos^2\theta_y+\sin^2\theta\cos^2\theta_y]$	(16) $r^2[\cos^2\theta\cos^2\theta_p\cos^2\theta_y+\sin^2\theta\cos^2\theta_p\cos^2\theta_y]$
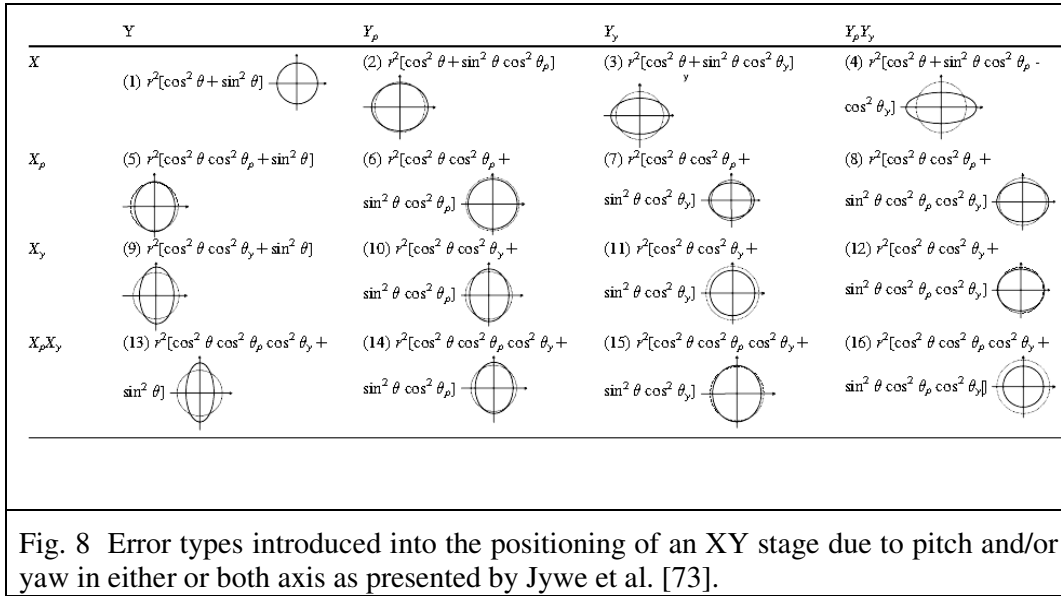
Fig. 8 Error types introduced into the positioning of an XY stage due to pitch and/or yaw in either or both axis as presented by Jywe et al. [73].

Pitch, roll and yaw displacements can arise from internal forces, possibly due to misalignment of the actuator and displacement axes and/or due to asymmetrical guidance arising from manufacturing limitations (dimensional tolerances).

It is possible to quantify these parasitic displacements by mounting a plane mirror on the stage and using an autocollimator, while moving the stage over its entire range along each axis in turn. Atherton [37] suggests that since parasitic displacements are normally measurable and repeatable, they can be reduced by optimising the mechanical design and through the use of compensating techniques (error mapping).

2.4.3.2   Crosstalk

Crosstalk is a term used to describe unwanted motion in one axis resulting from desired motion in another axis (including pitch, roll and yaw). Yeh et al. [30] state that misalignments of the interferometer system and machining error generates crosstalk

An X axis interferometer can be used to measure any Y-axis movement as the stage is scanned over it's entire X axis range. If the X axis is perfectly orthogonal to the laser beam, no Y axis movement is detected. This test can also be repeated for the Y axis.

Yeh et al. [30] report that a correlation matrix in the feedback control algorithm is an effective method to compensate the crosstalk, but is ineffective in compensating for the non-orthogonality of the metrology coordinate frame.

2.4.3.3   Hysteresis

Open loop piezo actuators, commonly used to drive positioning stages, exhibit hysteresis due to crystalline polarisation and molecular effects. Janocha et al. [43] describe a hysteretic system as one where the output signals relies not only on the immediate value of the input signal but also on the order of its past amplitudes. This implies that the absolute position of a piezo driven stage depends on both the command signal and on the dynamic history of the piezo actuator [34]. According to Xu et al. [28] this positioning error can be in the order of 10% - 15%, though repeatability can still be in the order of 1 %. Fig. 9 illustrates the typical characteristic behavior of a piezoelectric actuator system.

Fig. 9   Electromechanical transfer characteristic of a piezoelectric transducer as an actuator: a. electrical excitation x versus t., normalized to the maximum amplitude;

b. mechanical reaction y versus t, normalized to the maximum amplitude;

c. mechanical reaction y versus the electrical excitation x. (from Janocha et al.)
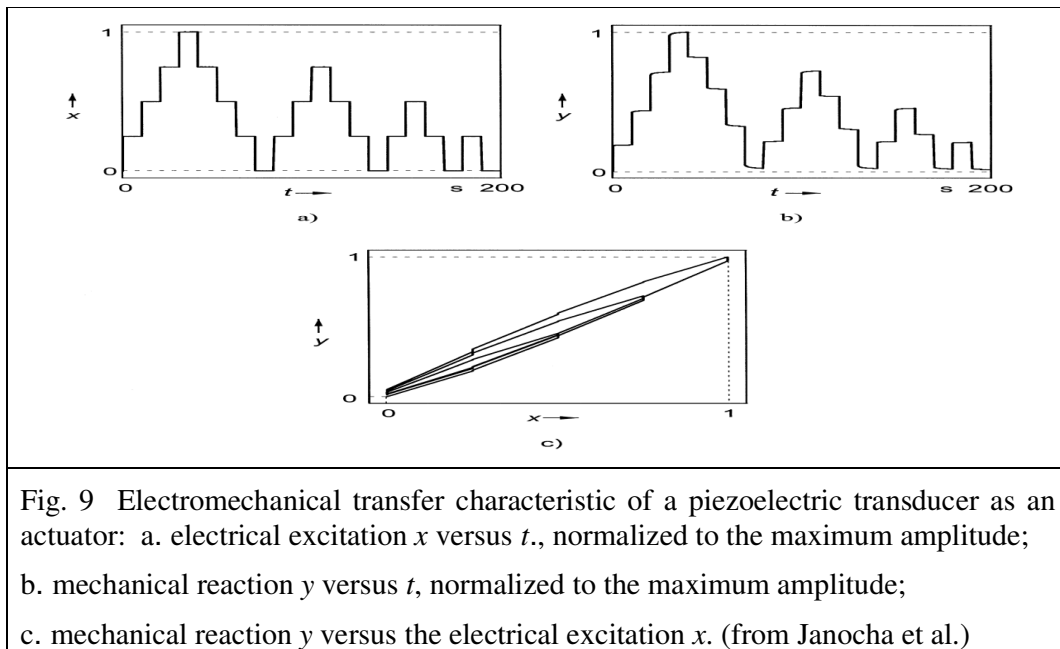
A comprehensive and in-depth description of the science behind the hysteresis associated with piezoelectric materials is given by Mayergoyz et al. [44], but a detailed understanding of the underlying mechanisms is not necessary for the purposes of this thesis. What is necessary, though, is an appreciation the effect of undesired hysteresis in high-precision sensor and actuator applications [44].

Several approaches to minimising hysteresis are presented by several researchers. One method is to construct an active feedback system for controlling the driving-field input signal to reduce hysteresis of the output signal [44]. This approach is adopted by many

piezo actuator manufacturers. Physik Instrumente (PI) GmbH & Co. [27], for example, claims that hysteresis can be virtually eliminated by using closed loop feed back control.

2.4.3.4 Cosine and Abbe error

Castro [41] describes cosine error as an error between the measured distance and the actual distance travelled arising from misalignment of the measurement axis with respect to the mechanical axis of motion. This situation is illustrated in Fig. 10   and Fig. 11.

Fig. 10 Misalignment of measurement and movement axis causing cosine error.	Fig. 11 Cosine error. (Hicks [37])
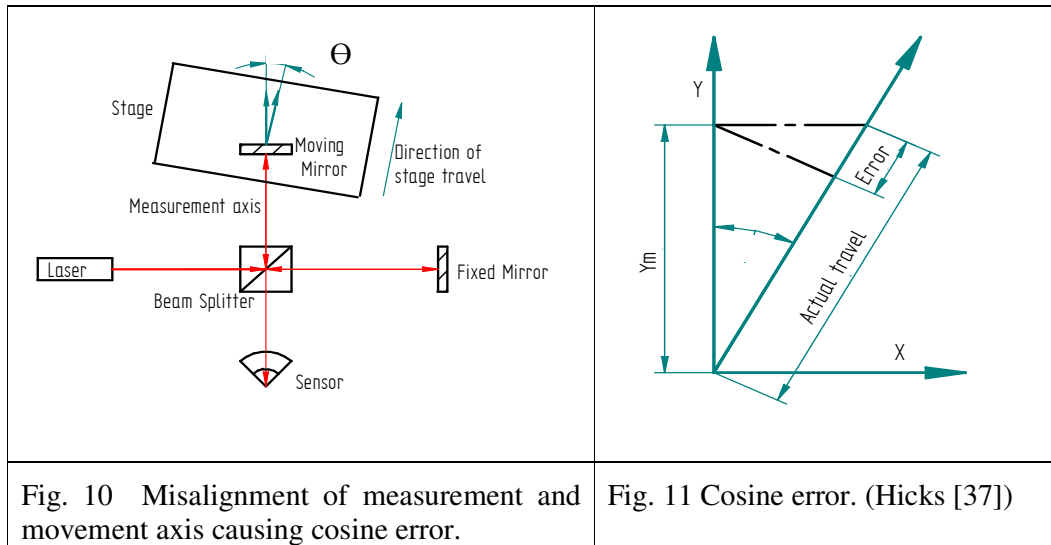
As the stage moves, the point of interest is displaced a greater distance than is measured. This additional distance is the cosine error and can be calculated using Equ. 4.

$$cosine\ error = \left(\frac{1 - \cos\theta}{\cos\theta}\right) Y_m$$

<div align="right">Equ. 4</div>

It can be determined, using this expression that a misalignment as large as 1 deg gives rise to a cosine error < 2.5 nm for a stage displacement of 15 μm.

Abbe error is more serious than cosine error. This is the name given to an error resulting from parasitic angular displacement (such as pitch, roll or yaw) combined

with an offset between a point of interest and the axis of the measurement sensors. The following diagram (Fig. 12) serves to illustrate this [37].

$$AbbeError = \Delta \sin \alpha$$

Fig. 12 Diagrams illustrating the mechanism, by which Abbe Error is introduced, based on an interpretation of diagrams presented by Hicks et al. [37].
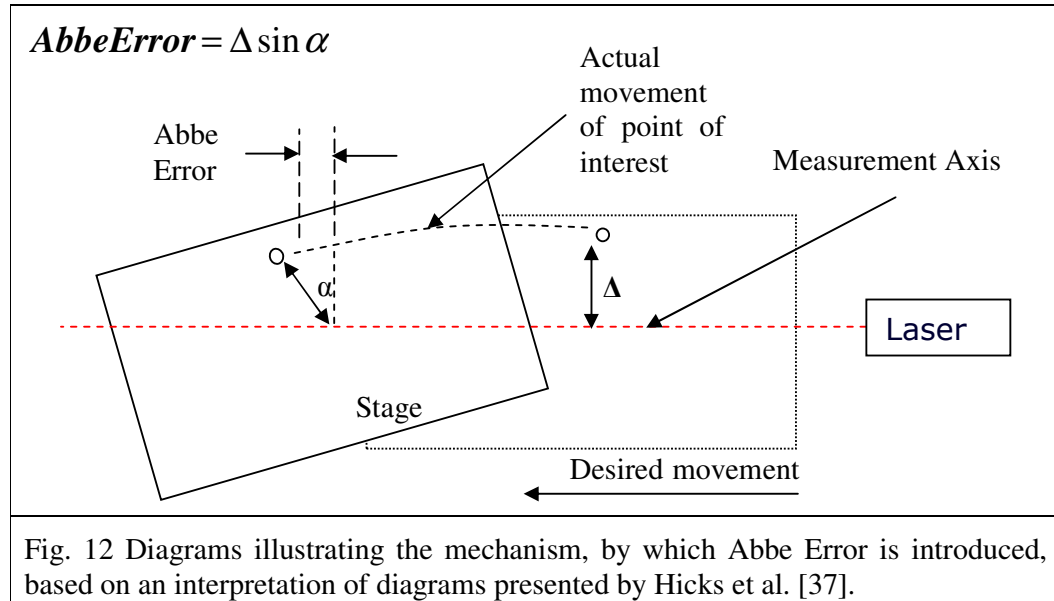
Point o is a distance Δ (Abbe offset) from the measurement axis. As the stage moves along its X axis, it also rotates about its Z axis through a small angle α (yaw).

The point o travels a greater distance over a curved path than is measured by the interferometer. Res [45] describes Abbe error as the product of the perpendicular distance from the scale to the measuring point times the sine of the pitch angle error. Kramar et al. [46] describes how the interferometers measure in a plane that is 10 mm above the sample level in the NIST molecular measuring machine and because of this arrangement, any tilt of the stages causes an Abbé error equal to the sine of the tilt angle times this height offset.

$$\text{Abbe Error} = \Delta . \sin (\alpha)$$

Equ. 5

According to Xu et al. [25], Abbe errors have to be considered carefully when mounting specimens on nanomechanisms. As an example they state that a tilt of just 1 μRad (0.0000573^0) with an offset of 1 mm gives a 1 nm positioning error.

Compensation is only possible if rotation angles are known over the entire travel range along each stage movement axis. This is unlikely to be the case, so reduction of the

error is probably a more practical approach. To this end, the Abbe principle, first published by Abbe in 1890, proposes that the measurement scale should be in line with the distance to be measured. Revisiting the Abbe principle in 1979, Bryan [47] proposes that the Abbe principle should be restated as

"The displacement measurement system should be in line with the functional point whose displacement is to be measured. If this is not possible, either the slide-ways that transfer the displacement must be free of angular motion or angular motion data must be used to calculate the consequences of the offset".

2.4.4   Noise

2.4.4.1   Quantisation noise

Quantisation noise is described by Hicks et al. [37] as the uncertainty arising from the fact that there are a finite number of digital bits used to encode an analogue signal.

2.4.4.2   Electrical and electronic and noise

Measurement sensor resolution is limited by noise [48]. Even when there is no gap change between the plates of a capacitor displacement sensor, there is a small fluctuation in the output from the sensor electronics. Many manufacturers specify their capacitance sensors using voltage spectral density or noise factor (the square root of the power spectral density which is the same at all frequencies i.e. white noise)

$$N = (kTR)^{1/2} \left(\frac{V}{\sqrt{Hz}} \right)$$

Equ. 6

where k is Boltzmans constant (1.38×10^{-23} JK^{-1}), T is the temperature (K), R is the resistance (Ω).

Baxter [42] recommends the use of high sensor excitation frequencies. As excitation frequency increases, the effect of external and circuit-generated noise decreases.

2.5   Mechanical structures

This section is concerned with the design of the physical structures which constitute a precision positioning instrument. Before discussing each element of a positioning

system, it is necessary to investigate the materials that could be utilised in its construction.

2.5.1 Material selection

The requirements of the nanopositioning instrument naturally influence the choice of material, so initially it is important to recognise the desired characteristics of the proposed instrument. These characteristics provide a context for investigating relevant material issues and are defined as follows:

Guides must be adequately stiff so as to minimise parasitic movement [28]

Stiffness of the guides is promoted by the material having a high value of Young's modulus for a given guide geometry, but the conflicting need for maximum stiffness and maximum stroke length retention must be balanced [9].

Adequate stroke lengths and pre-loads should be achievable without permanent deformation.

The material yield stress must be considerably greater than the maximum stress occurring at full stoke with pre-load applied [50]. The maximum stress can be calculated for differing stage geometry/material/stroke length combinations based on the methodology described by Elmustafa et al. [51] and Woronko [50].

Metrology loops must be environmentally robust

Supports and structures should have high resonance frequencies so as to keep the magnitude of the response to external cyclic disturbances small [52].

Hicks et al [37] give the following expression for calculating stage resonance

$$f_0 = \frac{1}{2\pi} \sqrt{\frac{k_x}{m_{load} + m_{stage}}}$$

<div align="right">Equ. 7</div>

where k_x is the stage stiffness, f_0 is the resonance frequency, m_{load} is the mass of the load, m_{stage} is the mass of the stage.

From Equ. 7, it can be deduced that light stages combined with stiff guidance flexures have high resonant frequencies. Ruijl [26] recommends that, for light and stiff

construction, the material specific stiffness, E/ρ (E = Young's modulus, ρ = density) should be as large as possible.

<u>Thermal gradients, characterised by uneven thermal distributions and hot spots, can cause un-nulled expansions, unpredictable stress and distortions of the stage, force frame, supports and metrology frame [36] [48].</u>

Thermal expansion of itself is not regarded by some researchers as being particularly problematic for the mechanical assemblies. Smith et al [36], for example, outline geometric design techniques by which thermal expansions can be physically nulled (Section 2.4.1.1), while both Hicks [37] and Koevoets [48] propose that if the temperature is known and expansivity predicted, then compensation is effective.

On the other hand, a mismatch of thermal expansion may lead to metrology errors and/or unpredictable (hence not correctable) distortions. Ruijl [26] sees a close expansivity match between components as more important than low thermal expansivity in some instances. It is suggested that the same material should be used where possible for the stage, supporting frame and metrology frame.

The mismatch between the stage material and that of the piezo actuator is also identified by Xu et al. [28] as a possible source of error. If the position is measured using a sensor mounted close to the point of interest on the stage, then the differential expansions are of little relevance from the point of view of measurement error. Relative dimensional changes of the frame and piezos may, though, result in loose piezo location if adequate preload is not applied.

Koevoets et al. [48] propose an error compensation method for dealing with thermo-mechanical deformations arising from transient thermal gradients. The deformations are regarded as offsets which can be compensated for, having been predicted using real time temperature information and FEM informed knowledge of thermo-mechanical coupling.

Fig. 13 Expansion conductivity chart [53].

Avoidance/minimisation of gradients is critical to successful positioning. To minimise thermal gradients, the material property quotient α/λ (α = thermal expansion coefficient, λ = thermal conductivity) should be as small as possible [26] i.e. the material should have low thermal expansion and high thermal conductivity. Charts of these ratios, sourced from Slocum [53] show Super Invar (Cr Ni alloy) and aluminium alloy to be possible candidates based on this criterion (Fig. 13).

Another related important relationship is thermal diffusivity [26], described by the quotient $\lambda/\rho C_p$ (C_p = specific heat and ρ = density). The magnitude of this relationship determines how quickly uniform temperature distribution is attained in

response to a transient heat distortion or, in other words, how quickly thermal gradients are dissipated.

<u>Contouring demands a rapid positioning/repositioning capability of the stage.</u>

For a fast response, a high resonant frequency is required i.e. a light stage (low density material) with stiff (high value of Young's modulus) guiding flexures.

<u>The ability to maintain a position over a prolonged period of time may be necessary for some stage applications</u>

Two time dependant material properties are of interest: creep and temporal stability. Because the stage must be preloaded, the flexure and piezo materials may creep. Again, this should not be a problem as it can be corrected if closed loop control is used and the measuring sensor is located at the point of interest on the stage.

Temporal stability, as explained by Hicks [37], refers to a materials dimensional change with time without external force being applied to the sample. This is a long term effect and data is available only for a few low thermal expansive materials. Invar for example has a temporal stability of $0.1 \times 10^{-6} \text{ day}^{-1}$.

<u>Cost</u>

The material cost is a significant issue in practice and high performance materials are expensive. For machining operations to be affordable, material chosen should allow the system to be manufactured easily, utilising standard machining processes, while special heat treatment should not be necessary.

Having discussed the required properties of the materials suitable for the development of a nanopositioning instrument, it is now necessary to discuss the individual parts that make up the system.

2.5.2   Guidance systems

A guidance system, as the name suggests, guides the translation stage along a desired path. Guidance must allow nearly unrestricted displacement along the path while resisting all off-path movement. Furthermore, for accurate and repeatable positioning, movements must be frictionless and free of hysteresis and back-lash. Although a variety of positioning guide systems are available such as linear, roller bearing, hydrostatic and aerostatic slides (Taniguchi [1] and Chen et al. [53]); piezo actuation

and flexure guidance is becoming common for guiding positioning instruments. Flexures rely on the elastic deformation of a component to provide the desired degrees of freedom [55]. Taniguchi [1] reports that such hinge systems are capable of guiding the relative movement of elements at nanometer accuracy since friction and backlash is removed. Cuttino et al. [55] also indicate that flexures are wear free and highly repeatable. Flexures are ideal for achieving pure axial motion, while implementing constraining off-axis motion according to Xu et al. [28].

Taniguchi [1] sees the main drawback to the use of flexures as being their relatively short range of movement, while Moon et al. [56] explain that the range of motion of a flexure joint is limited by the permissible stresses and strains in the material. The problem of limited stroke length can be overcome, according to Xu et al. [28], through the use of flexure lever design. Imbalance in flexures, due to manufacturing errors, can result in coupling between axes [53].

Many of the flexure joints developed over the last fifty years are of two varieties [56], leaf springs or notched type flexures both of which are referred to as primitives (Fig. 14).

(a) planar notch joint   **(b) spherical notch joint**   **(c) leaf-springs**

Fig. 14 Primitive flexure types presented by Moon et al. [56]
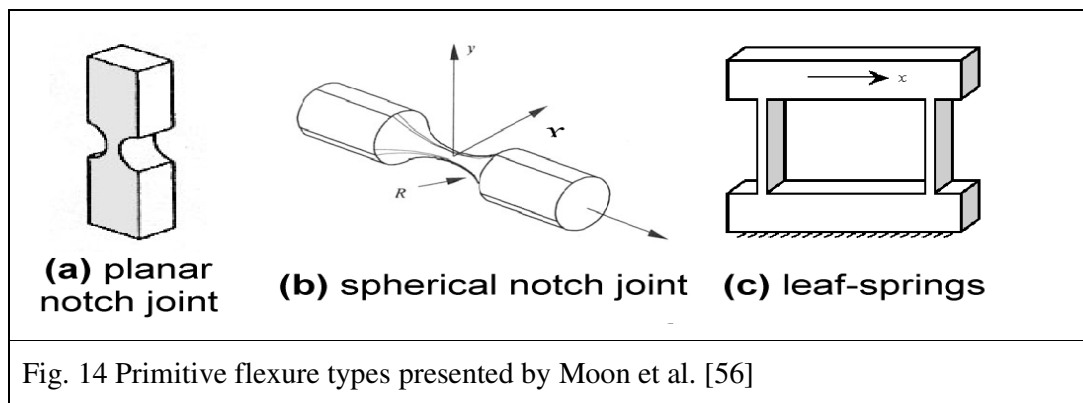
These primitives are commonly used in assemblies as revolute joints, universal joints or parallel four bar translation joints, which deliver a larger range of straight-line motion. Although flexures have been used successfully over the years, new and novel designs are still being developed [55] [57] [56].

2.5.3 Flexure design

Having decided on flexures as the mechanism for guidance, a logical, effective approach to dimensioning the hinges is essential.

A methodology for the design of flexure-hinge guided motion nanopositioners is presented by Elmustafa et al. [51]. Their approach involves the application of linear elastic beam theory to find the appropriate flexure dimensions of a cantilever beam type hinge (Fig. 15) for a desired deflection and material choice.

Fig. 15 Flexure arrangement used with a single axis stage presented by Elmustafa et al. [51]	Fig. 16 Single bracketed flexure drawn by Elmustafa et al. [51]
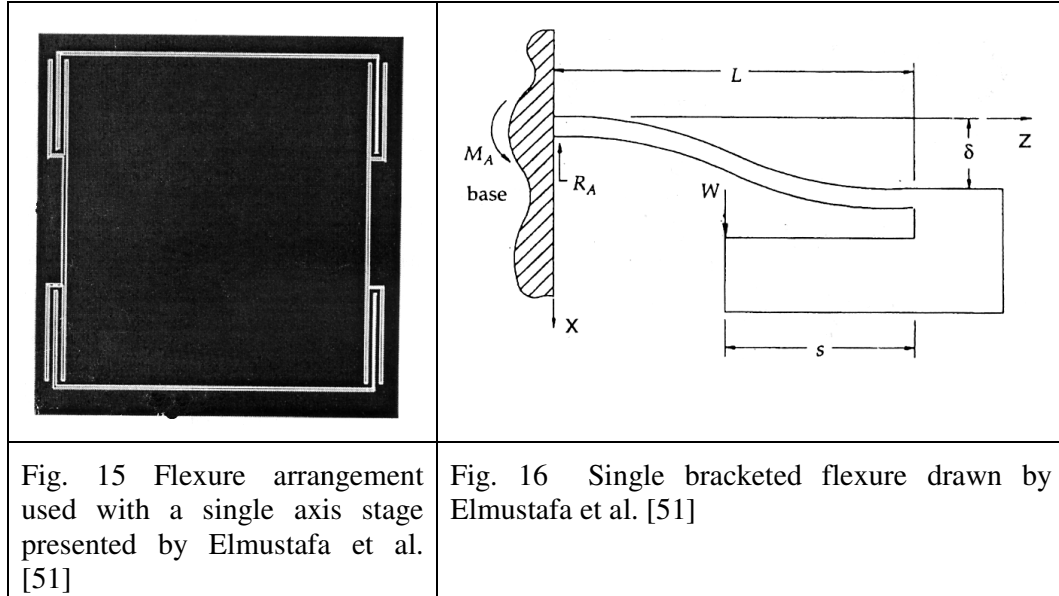
A set of useful equations is given by Elmustafa et al. [51] for deflection, flexure stiffness and allowable bending stress.

Deflection of a single bracketed flexure, as shown in Fig. 16, is given by;

$$\delta = \frac{WL^3}{12EI}$$

<div align="right">Equ. 8</div>

W is the load, *L* is the flexure length, *E* is Young's modulus and *I* is the moment of area

Equ. 8 is used to derive the following expressions for the stiffness of a single bracketed flexure, λ, and the maximum allowable tensile stress, σ_{max}, of flexures in the stage guidance arrangement shown in Fig. 15.

$$\lambda = \frac{12EI}{L^2} \quad and \quad \sigma_{max} = \frac{3Ed\delta_{max}}{L^2} \quad where \quad d = width$$
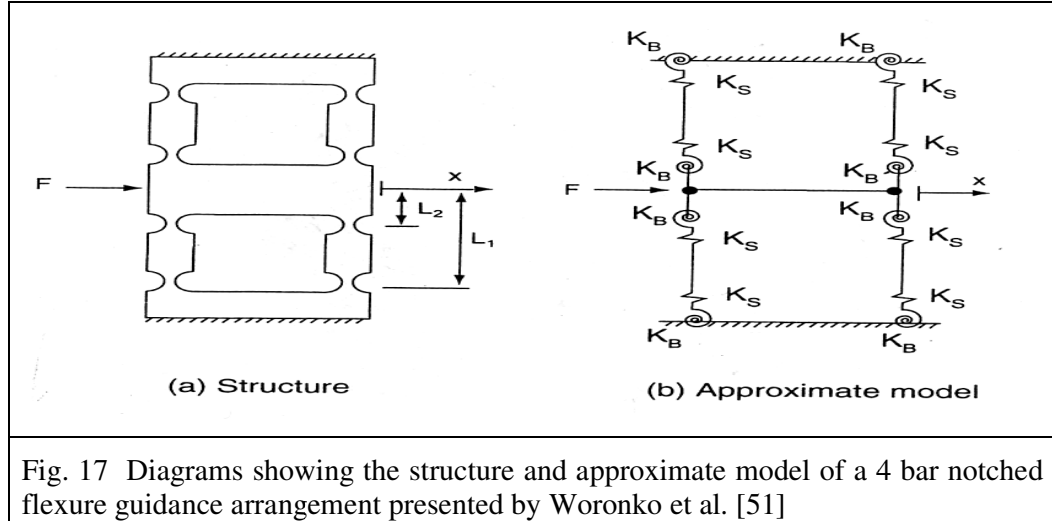
Fig. 17 Diagrams showing the structure and approximate model of a 4 bar notched flexure guidance arrangement presented by Woronko et al. [51]

Woronko et al. [51] also describe their design strategy for a cantilever circular notch hinge stage (Fig. 17) which was previously described by Paros et al., balancing the conflicting need for maximum stiffness and maximum stroke length retention.

Having decided on overall stroke length and guiding unit stiffness, an analytical model of the flexures is developed to calculate the 'equivalent linear stiffness' of the flexures based on expressions for bending stiffness and axial stiffness.

$$K_x = \frac{8K_B}{L_1 - L_2} + 4K_S\left(1 - \frac{L_1 - L_2}{\sqrt{x^2 + (L_1 - L_2)^2}}\right) \quad where \quad K_B = \frac{2Ebt^{\frac{5}{2}}}{9\pi\sqrt{r}} \quad and \quad K_S = \frac{Eb}{\pi\sqrt{\frac{r}{t}}}$$

Equ. 10

K_x is the linear stiffness, K_B is the bending stiffness, K_S is the axial stiffness, t is the hinge thickness, r is the hinge radius and b is the hinge width.

Equ. 10 allows choice of suitable stage flexure dimensions. Woronko [51] also presents an expression for calculating the dynamic load due to resonance.

$$F_d = 4\pi^2 f^2 m_{eff}\frac{\Delta L}{2}$$

Equ. 11

where f is the oscillating frequency (Hz), $\varDelta L$ is the nominal stroke length (m), m_{eff} is the effective mass (kg).

The dynamic force must be less than the piezo stack pre-load so that the actuator always remains in contact with the stage. Knowing the necessary pre-load, piezo stack stiffness and flexure unit stiffness, allows the space requirements for accommodating the actuator to be determined.

2.5.4   Actuator and force frame issues

Three dynamic effects are indicated by Rankers [52] when an actuator is used to push a sage:

Actuator flexibility

A driven system does not behave as one rigid body due to compliance between the actuator and the load. If not accounted for at the design stage, unexpected shorter stroke lengths and modal resonance may result. Choosing a stiff actuator, careful positioning of the displacement sensor and pre-loading the actuator are necessary.

Guiding system flexibility

If the driving force is not applied at the centre of gravity, while the device has to rely on the guiding system to suppress motion in an undesired direction, translational and rotational resonance may arise. Rankers [52] suggests that, as a rule for good design, the actuator driving force be directed in such a way that it may produce the desired motion in the absence of the guiding system.

Limited mass and stiffness of the stationary parts

This refers to the effect on the system performance of reaction forces on its stationary part (the force fame). This is negligible if the stationary part is infinitely stiff, but will exhibit a resonance otherwise when excited by the reaction forces. After the stage has reached its commanded location motion the frame motion may not have ended and the actuator has to follow the motion of the frame and thus introduces a positioning error.

2.5.5 Mounting

An important design element is the physical arrangement by which the components of the instrument are linked. In this section the method by which the metrology frame and stage is mounted on the supporting frame is considered in particular.

Fig. 18 Precision instrument suspension illustrated by Rankers et al. [52].

$$f_1 = \frac{1}{2\Pi}\sqrt{\frac{m_1+m_2}{k_{20}}} \qquad f_2 = \frac{1}{2\Pi}\sqrt{\frac{m_1}{k_{12}}} \quad m_2 \gg m_1$$

Fig. 19 Curve showing typical sensitivity to external vibrations given by Rankers et al. [52]. (f_1=3 Hz with 5 %relative damping and f_2 =100 Hz with little relative damping)
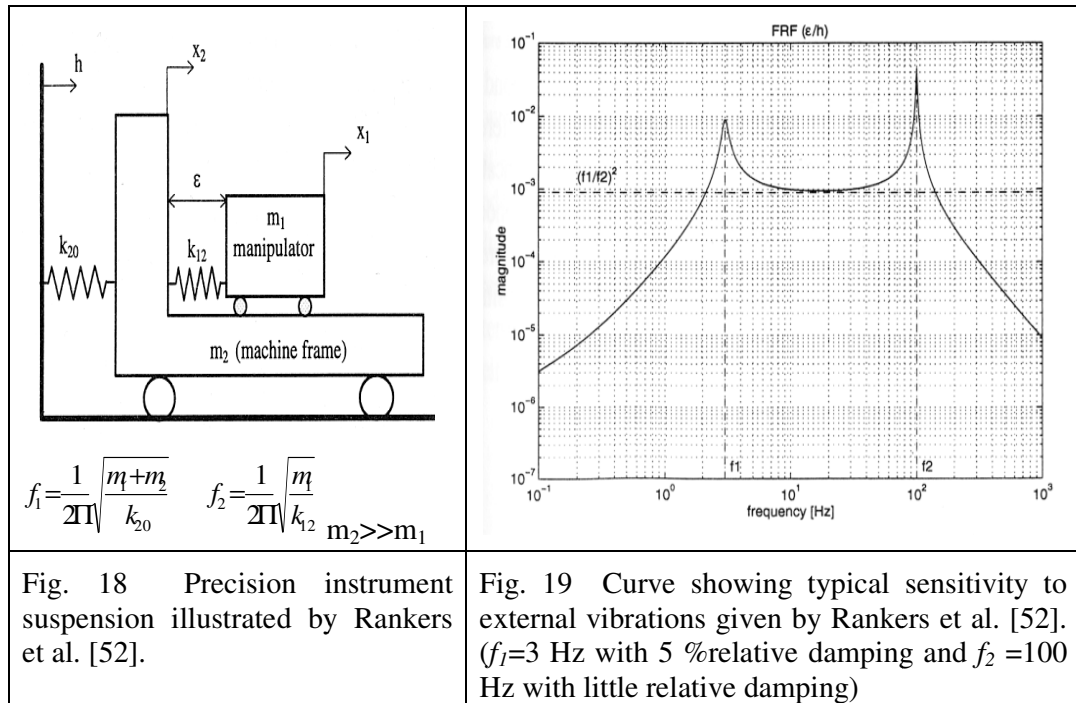
Inadequately stiff mounting can lead to low instrument natural frequencies resulting in increased sensitivity to external vibrations. This sensitivity is described by the transfer function ε/h (internal error/external vibrations) [52]. An outline of a precision instruments mounting/suspension system (Fig. 18) is given by Rankers [52] in which a manipulator is mounted onto a machine frame which in turn is supported by a soft suspension. A typical sensitivity curve for such a system is shown in Fig. 19. It can be deduced from this that, to minimise sensitivity, the squared ratio of frequencies $(f_1/f_2)^2$ should be as small as possible. Therefore, when designing a nanopositioning instrument, the support frame/external world interface stiffness (k_{20}) should be soft while the stage and metrology frames should be mounted on the support frame with a high level of stiffness (k_{12}).

In addition, the effects of thermal variability can be greatly influenced by mount design. With proper mounting arrangements, thermal expansions of attached structures

can be decoupled so that very little stress is transmitted between components, thus avoiding distortions [37] and error inducing relative expansion displacements of metrology components/ locations can also be controlled [36].

Two different mounting arrangements, used by precision instrument designers, will be described which allow directionally controlled thermal expansions and can decouple thermal effects.

The first, as described by Chen et al. [53], uses six point contact kinematic mounts to provide full constraint in the design of a novel precision motion stage and to decouple thermal effects. The system consists of three hemispheres on one plate contacting three pairs of roller bearings on the other plate (their axes of movement orientated at 120^0 to each other) while magnetism is used to maintain contact. A similar system is described by Hicks et al. [37] who uses V-grooves instead of roller bearings and gravity instead of magnets.
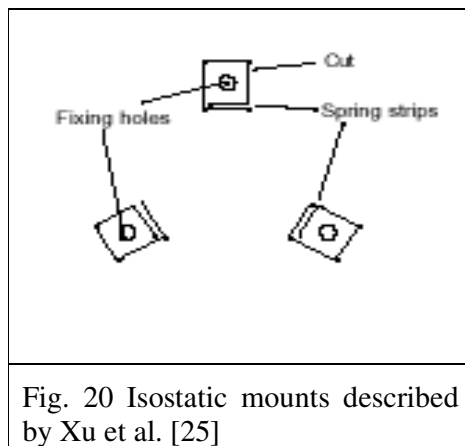
Fig. 20 Isostatic mounts described by Xu et al. [25]

Xu et al. [25], on the other hand, use a flexure based isostatic mounting arrangement in the design of an ultra precision XY positioning and scanning stage.

The advantages of this system are given as the decoupling of thermally induced stresses, the elimination of problems due to material thermal property mismatch and the maintenance of the stage datum position.

Hicks et al. [37] compare both mounting systems. According to Hicks, the main problem with kinematic mounting is that it relies on sliding contact to decouple thermal expansion effects. This would introduce unpredictable friction, which would result in the inducement of stress. Isostatic mounts are shown to be over-constraining, but stresses due to thermal expansion are properly decoupled.

With flexure mounts, a stationary datum (sweet spot) could possibly be established if the allowed line of motion of each mount meets at a single point.

2.6 Metrology

Because of the variety of possible errors and uncertainties associated with the mechanical system, reliance cannot to be placed on the commanded signal for knowledge of a stage true position. Positioning sensors are necessary for this purpose. These sensors must themselves be traceable, or otherwise be traceable through calibration via an external sensor, to measurements that are internationally accepted standards of length. Furthermore, the performance of the closed control loop in a positioning application is determined by the measurement system. Hence the measurement system is fundamentally important to the accuracy of positioning devices [37].

G(s)= positioning transfer function

H(s)= sensor transfer function

Fig. 21 Simple closed loop positioning control system presented by Hicks et al. [37]
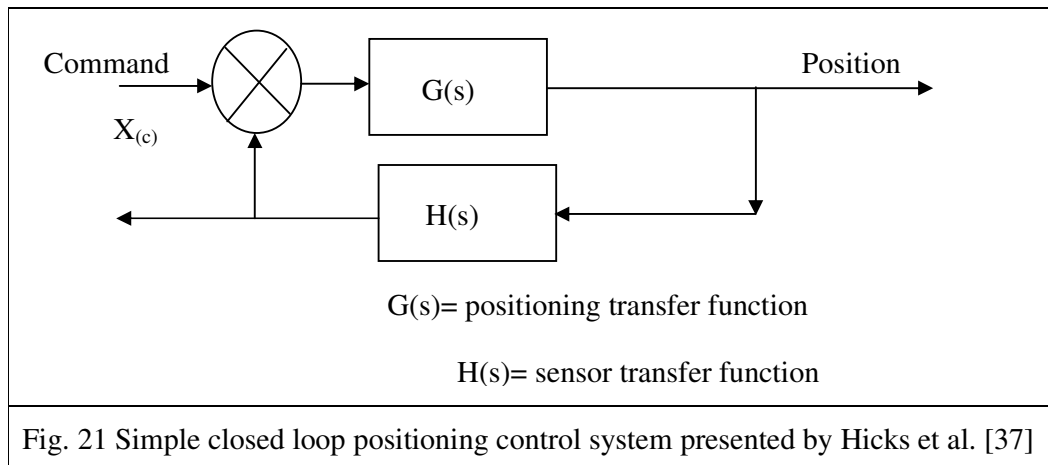
From Fig. 21, $x_p = (Gx_C)/(1 + GH)$, which reduces to $x_p = x_C/H$ when G is large. This simplified arrangement indicates that the actual position, to which the stage moves, for a given command, depends only on the sensor transfer function i.e. for closed loop control, measurement is paramount. It would appear from this that errors in the metrology system have a far more significant effect on positioning than errors in the mechanical system, but errors in metrology may not be completely divorced from those of the mechanical system.

2.6.1 Displacement sensors

Grating interferometers and capacitance sensors are commonly used for the in-process measurement of stage displacements:

2.6.1.1 Grating interferometers

Several grating interferometers have been developed that are capable of sub-nanometre measurement [9] [57] [59]. Thiel et al. [68] claim that the Heidenhain LIP382 interferential linear encoder could achieve a resolution of 31.25 pm with an interpolation error of ±50 pm.

Grating interferometers in general have several disadvantages 9; they are subject to Abbe error since the measurement axis cannot coincide with the point of interest on the stage; differential thermal expansion between the substrate material and the stage material may be difficult to avoid; and they cannot detect opposite axis error or orthogonality in multi-axis systems.

2.6.1.2 Capacitance sensing

Parallel plate capacitors are very suited for use as displacement sensors. Capacitance micrometers work by letting the displacement being measured vary the gap between the plates and then measuring the change in impedance. Hicks et al. [37] claim that displacements as small 10^{-14} m have been measured in this way.

Ideally, the capacitance C varies according to

$$C = \frac{\varepsilon_r \varepsilon_0 A}{d}$$

Equ. 12

C is the capacitance (Farads); ε_0 is the permeability of free space (electric flux density in vacuum electric field strength $=8.85419$ pFm^{-1}); ε_r is the relative permeability in medium (approximately 1.006 for air); d is the gap width between plates (m); and A is the plate area (m^2).

Capacitance varies in a parabolic rather than a linear manner with gap size. This is not a problem since the impedance does vary linearly when the applied voltage rms value and frequency remain constant.

According to Hughes [58]

$$\text{Impedance of capacitor} = \frac{V}{I} = \frac{1}{2\pi f C} \Rightarrow V \propto \frac{1}{C} \Rightarrow V \propto \frac{d}{\varepsilon_0 \varepsilon_r A} \Rightarrow V \propto d$$

Equ. 13

Where *V* is the rms voltage, *I* is rms current and *f* is the frequency.

Capacitors have very high positioning resolution, zero hysteresis, zero power dissipation at the point of measurement, high linearity (< 0.01 % is possible), insensitivity to cross-talk, simplicity and the ability to be made from very stable materials such as Invar [37] [34]. The small size of capacitance displacement sensors means that they can be located close to the stage point of interest, thus minimising Abbe and cosine error. Their effect on the dynamic behaviour of the stage is also small due to their low mass.

2.6.2   Calibration measurement

Calibration measurement refers to the traceable measurements made using an external sensor, such as an interferometer, against which the capacitance sensors are calibrated.

2.6.2.1   Laser interferometers

To measure displacement, laser interferometers use the interference pattern (alternating interference fringes) produced when a reference laser beam is combined with a beam reflected from the moving object. McCarthy [9] describes laser interferometers as being the ultimate in accurate feedback, combining very high accuracy and non-contact sensing. Yeh et al. [30] list the merits of laser interferometer as subnanometer-level resolution, long dynamic range and traceability to the primary standard of length, and therefore assert that it is a most suitable measuring tool for nanopositioning control.
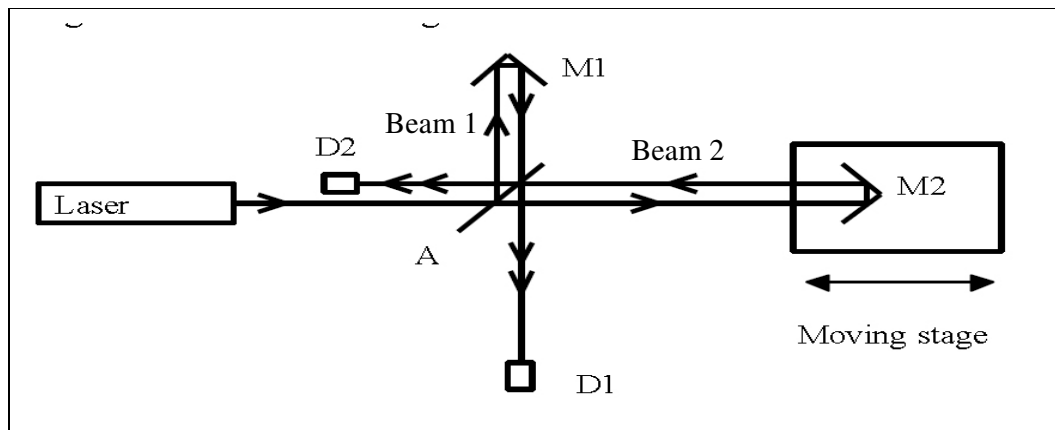
Fig. 22 Michelson single pass interferometer arrangement presented by Hicks et al. [37] *D1* = detector1, *D2* =detector2; *M1*=stationary mirror, *M2* = moving mirror; *A* = beam splitter.

There is a wide range of interferometer configurations to choose from. Variants of one such configuration, the Michelson, are used by several researchers [37] [26] [25] to measure displacements of precision position stages. The use of laser light, such as He-Ne that has extremely high wavelength stability, allow Michelson laser interferometer measurement systems to achieve high accuracy.

The basic optical arrangement of the Michelson single pass interferometer is presented by Hicks et al. [37] in Fig. 22. Both Ruijl [26] and McCarthy [9] present a two pass Michelson interferometer arrangement. This set-up, using polarising optics, causes the measuring beam to be reflected twice from the moving mirror, hence doubling the resolution (Fig. 23) when using fringe counting to determine displacement. To increase the resolution further, McCarthy [9] present a four pass Michelson interferometer arrangement (Fig. 23).
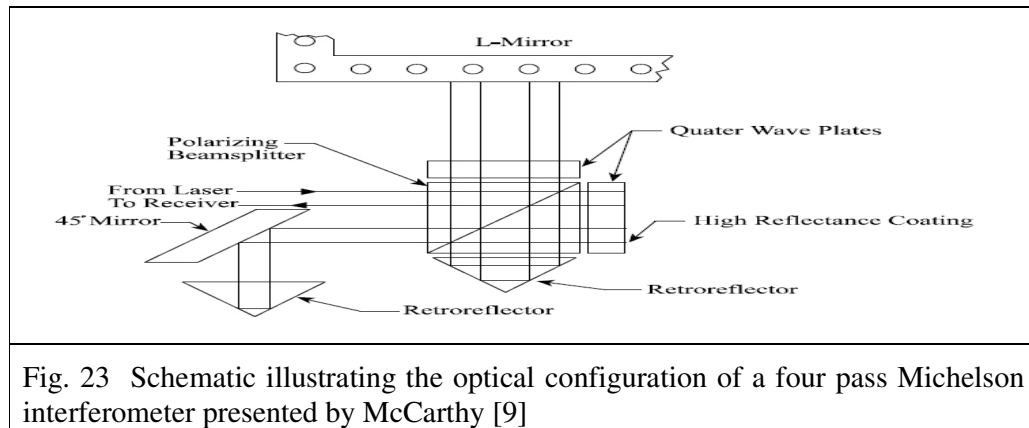
Fig. 23 Schematic illustrating the optical configuration of a four pass Michelson interferometer presented by McCarthy [9]

Alternatively, instead of counting the fringes, it is possible to interpolate along the interference pattern, but signal imperfections, in terms of non-linearity make this difficult [60]. According to Hansen et al. [61], non-linearity is often due to periodic deviation arising from misalignment, ghost reflections and less than ideal polarizing performance of the optical components. Ideally the beam splitter should divide the laser beam into two perfectly orthogonal polarized beams, one entering the measuring arm of the interferometer, while the other enters the reference arm. Polarization inefficiencies may cause part of the reference beam frequency to enter the measuring arm and part of the measuring beam frequency to enter the reference arm. Whether they are subsequently transmitted or reflected from the polarising splitter also depends on the circular polarization effect of the ¼ wave plates. As described by Schmitz et al.

[60], this leakage of component frequencies tends to produce a cyclical, non-cumulative, non-linearity with a period of one (first order) or two (second order) wavelengths of the interference pattern. Castro et al. [41] gives the typical magnitude of this error as a 5.4^0 phase error peak-to-peak. This results in a ± 4.8 nm displacement error for each 1.266 μm of stage travel.

Interpolation can be facilitated by using a Heydemann compensation [62], which is reported to be a widely used compensation method for such periodic deviations. If the reference and measuring beams are perfect sine and cosine signals of equal amplitude, then plotting the sine against the cosine of the interferogram signal would result in a circle with a radius equal to the signal amplitude with its centre at (0,0); the angle of the radius vector providing a measure of the phase difference between the interfering rays and hence a measure of displacement. Phase shifts resulting from periodic deviation cause the sine/cosine plot to be elliptical. [63]. Applying a Heydemann compensation corrects these shifts and allows interpolation of the interference pattern and sub-nanometre positional measurement [63], the resolution being limited by sensor noise. Based on a description by Kiong et al. [64], Heydemann interpolation can be applied as follows.

If the two interfering beams are described by

$$u_1 = A \sin \delta \qquad\qquad\qquad u_2 = A \sin \delta$$

Then the instantaneous phase, δ, is given by

$$\delta = \tan^{-1} \frac{u_2}{u_1}$$

Equ. 14

To facilitate fringe fractioning, a polar adjustment, σ, is then applied, $\theta = \delta + \sigma$, to give a phase range of 0 to 2π. σ is zero when u_1 and u_2 have positive values; σ is π when u_1 is negative; σ is 2π when u_1 is positive and u_2 is negative. The effectiveness of this correction is illustrated in Fig. 24.
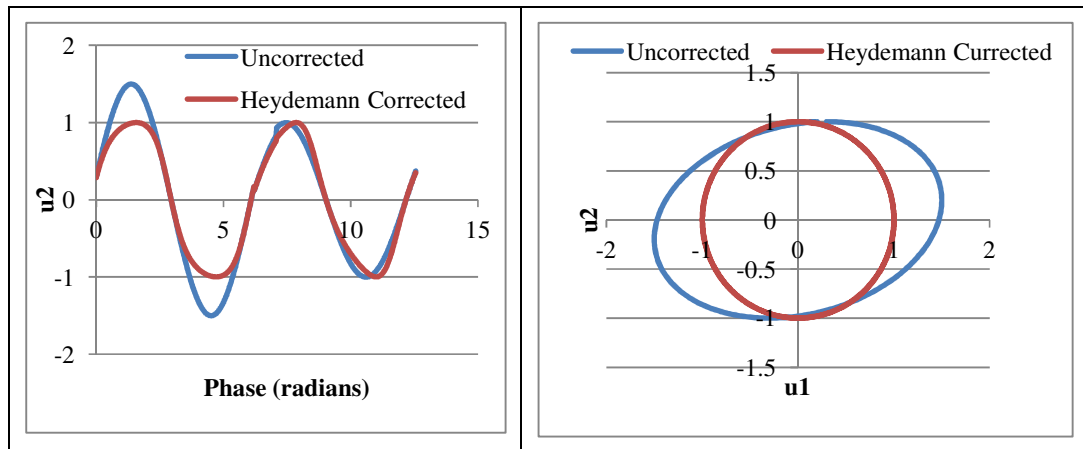
Fig. 24 Graphs illustrating the effectiveness of using a Heydemann correction for correcting for varying amplitude and non-linearity.

However several error other sources of error are associated with Michelson interferometers. According to McCarthy [9], interferometer error sources include laser wavelength variation due to environmental factors, accuracy of sensors used for measuring the environment, thermal expansion (of work piece, positioning table, base, optics, etc.), cosine error, accuracy of work piece thermal expansion coefficients, parasitic displacement of the stage, and deadpath correction accuracy. Additionally Castro et al. [41] reports timing error (the difference in time between when the interferometer records its readings and when the process sensor being calibrated records its readings) to be a source of measurement error.

2.7   Control

Thus far the requirements of a precision positioning instrument have been examined in terms of mechanical structures, metrology and possible sources of positioning error. This section looks at how the movement of such an instrument can be controlled.

In closed-loop control, the controller will move the stage to eliminate the difference between the commanded position and the measured position. Indeed, the suppliers of actuators also supply sophisticated proportional integral differential (PID) controllers which enhance steady state behaviour, improve damping and stability, minimise overshoot, eliminate hysteresis and linearise motion to the command signal. Here, the effectiveness of closed loop control in eliminating various error types and the sensitivity of such systems to external disturbances is examined.

Rankers [52] points out that the performance of the feedback section depends very much on the disturbances that act on the system. Hicks et al. [37] also look at the significance of disturbances (load fluctuation, friction, vibration, acoustic, machine dynamics) on a closed loop piezo driven positioning system. They analyse a typical closed control loop with temperature and time dependant (drift) off-sets (b_{01} applied at the command, b_{02} applied to the piezo input and b_{03} is applied between the piezo and the sensor) (Fig. 25).

Fig. 25 Closed loop control with time and temperature dependant disturbances from Hicks et al. [37].
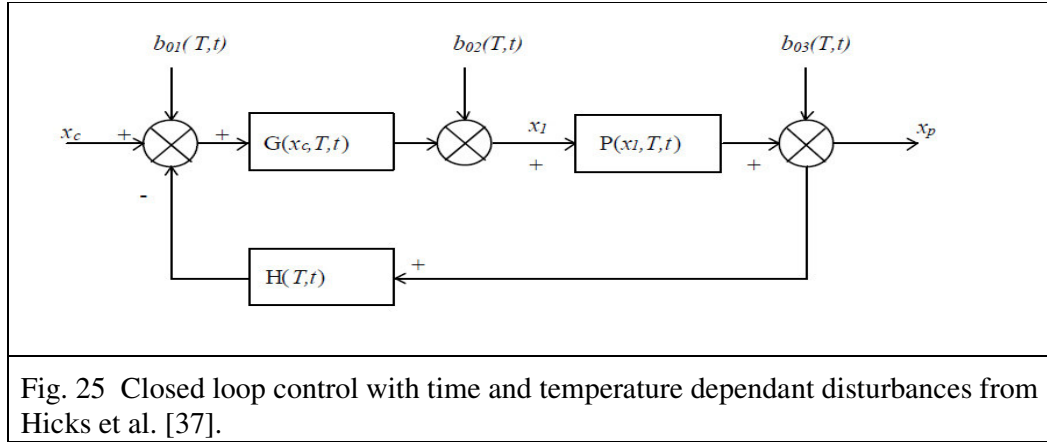
$$x_p = b_{03} + P\{b_{02} + G(x_C + b_{01} - Hx_p)\}$$

$$x_p = \frac{b_{03}}{1 + HPG} + \frac{Pb_{02}}{1 + HPG} + \frac{PG(x_C + b_{01})}{1 + HPG}$$

$x_p = x_C = b_{01}$ when G is very large and H is unity

Equ. 15

where G is the controller gain, P is the piezo transfer function, H is the measurement system transfer function.

This indicates that the true position is given as the sum of the command position plus the electronic input off-set if G is very large and H is unity. Hicks maintains that this off-set (b_{01}) is indistinguishable from the command signal (x_c) and is therefore impossible to remove. The piezo transfer function (P) and other off-sets (b_{02}), occurring between the controller and the piezo (electronic), as well as between the controller and the sensor (b_{03}) (including a possible mechanical contribution) are shown by this equation to be unimportant. If H is not unity, the final expression is

$$x_p = \frac{x_C + b_{01}}{H}$$

<div align="right">Equ. 16</div>

The implication of this is that when closed loop control is used, positioning accuracy is dependant solely on the measurement system and the indistinguishable command off-set if the controller gain can be made sufficiently large. This indicates that design effort must be targeted at eliminating or minimising the effects of all possible sources of error acting on the measurement system.

<u>Control of a contouring stage in particular</u>

According to Hicks et al. [37], the ability to follow varying commands is governed by three properties given below;

- The stiffness and mass of the stage.

Open loop control is dominated by stage resonant frequency. Hicks represents the open loop response as a mass/spring/damper arrangement for which the transfer function is given as

$$G(s) = \frac{1}{\frac{1}{\omega_n{}^2}s^2 + \frac{1}{\omega_n Q}s + 1}$$

<div align="right">Equ. 17</div>

where $\omega_n = 2\pi f_n$ = angular velocity, Q = amplification factor, f_n = resonant frequency and Q = (response at resonance)/(response at dc)

- The frequency response of the controller.

- The current output capability of the piezo drive amplifier.

2.7.1   Error mapping

Because of expected imperfections in real positioning sensors, the measured position may differ from the true position. This is usually a systematic error that can be calibrated out through a method called error mapping. Using an error map in the control of a nanopositioning stage for a micro-CMM, Chao et al. [65] report errors reduced to 0.9 μm (± 3 σ) over a 25 mm range and as little as ± 20 nm over a short range movement of 0.3 μm.

The method simply involves moving the stage over its entire range and comparing its commanded position with its true position at a number of individual locations during its stroke [9]. The relationship between the true and commanded positions is then established and is expressed a polynomial. Knowing this relationship, the commands given to the controller can then be offset accordingly so that the stage will go to a location closer to its targeted location. Harris et al. [66] indicate that several correction techniques are available.

Hicks et al. [37] present a method of mapping for a closed loop system. A measured value x_m is expressed as a power series polynomial of the true position x_p. Because the system is closed, the measured position is made equal to the command position x_c.

$$x_c = x_m = a_0 + a_1 x_p + a_2 x_p^2 + a_3 x_p^3 + a_4 x_p^4 + a_5 x_p^5 + ...$$ Equ. 18

By reversing the polynomial, a new polynomial in x_c is found which equals x_p.

$$x_p = b_0 + b_1 x_c + b_2 x_c^2 + b_3 x_c^3 + b_4 x_c^4 + b_5 x_c^5 + ...$$ Equ. 19

This is again a power series, but with different coefficients which can be related through given equations to the coefficients of the command polynomial.

Hicks goes on to explain how the coefficients matrix associated with this polynomial (found through calibration) is used to linearise the sensor output which is in turn made equal to the command so that the command is now linear with respect to the motion. This approach is used in Queensgate Ltd. [67] digital controllers.

An alternative method of correction is also suggested. Here the coefficients matrix of the control command position polynomial is applied to the command before it is issued to the controller, while the coefficients matrix of the true position polynomial is applied to the read back before displaying it.

Hicks claims that mapping errors in the order of 0.1 % with scale factor variation of 1.5 % are achievable when using fourth order mapping with linear capacitance sensors.

2.8   Discussion

It is evident from the work of researchers that a precision positioning instrument is a complex system in which the sub-systems are often inter-dependant and in which

errors in one invariably affects the others and ultimately degrades the positioning accuracy. It is also evident that individual error sources may have several different effects simultaneously and that more than one source of uncertainty may exist at any one moment.

The literature has proven to be a rich source of information on the current state of the art, possible sources of uncertainty, useful design options, procedures, principles and guidelines which will form the basis for an effective robust design and subsequently effective investigation into specification requirements. It is the significance and interdependence of these factors, as well as the effectiveness of methods by which errors and uncertainty can be diminished or their effects mitigated, that will be further investigated through the rigorous design process which will be pursued in the forthcoming chapters.

Chapter 3

3 The mechanical design of the three dimensional instrument.

3.1 Introduction

This chapter describes the application of the principles that have been identified in the review of the literature in Chapter 2. These principles are used in the iterative design of the mechanical components of the 3D nanopositioning instrument.

The mechanical geometry of the stage evolved solely to address functional requirements of the instrument. A description of its evolution, the concerns behind the key decisions and exploratory analysis results are presented here.

3.2 Design methodology

The use of a similar step-wise iterative approach to design is used in this thesis as is described by a number of prominent researchers (Elmustafa et al. [51] , Woronko et al. [51], Yeh et al. [30], Thiel [68] , Rankers [52] and others). The steps include an initial mechanical concept design, followed by mathematical analysis of this design; results based modification to the design, computer modelling and analysis, followed again by redesign. Additionally, in accordance with Rankers [52] recommendation, the process is started by specifying the criteria that will be subsequently used in the interpretation and evaluation phase.

3.3 Design principles

The following basic principles have been adhered to from the beginning of the design process and have dictated the geometry of each of the structural elements.

- The measurement and displacement axes are to coincide in accordance with the Abbe principle.

- Fundamental to the instrument design is the issue of measurement axis alignment. A capacitance sensor on each axis will measure its displacement and these will be calibrated using three Michelson interferometers. To achieve the required flexibility and to aid set-up, commercially available, optical mounts are to be used for mounting the optical components as well as the stationary capacitance plates.

- Parallel metrology is to be used, ensuring that cross-axial displacements can be sensed and compensated. This requires fixed reference planes supported on a stiff metrology frame. The force frame is to be separate from the metrology frame so as to avoid measurement errors arising from frame deformations.

- Metrology loops must be environmentally robust [52].

- Thermal fluctuations should not introduce thermal gradients, stresses, warping or un-nulled expansion, while sensitivity to external vibrations must be minimised.

3.4   Initial design decisions

Some fundamentals of the design must first be decided upon.   These decisions are based entirely on the knowledge provided in the literature (Chapter 2) and, having been made, can provide a context in which to choose a material.

As identified in Section 2.5, positioning instruments require the following mechanical structures; a stage, a guidance system, a force frame, a metrology frame, a support frame and a mounting arrangement.

The initial design decisions:

- Flexure hinges should guide the movement of the stage. Even though, as discussed in Section 2.5.2, only limited translations are possible and parasitic movement can be introduced through manufacturing limitations or assembly errors, flexures are capable of very linear, frictionless and repeatable movement.

- The stage must be as small as possible so as to minimise its weight, thus optimising its dynamic characteristics, but must also be large enough so that necessary metrology components can be mounted on it.

- Piezo stack displacement actuators are to be used on each axis. These have positioning resolution limited only by their controlling electronics and data acquisition card (DAC) bit count. As explained in Section 2.5.4, piezo actuators have inherently high stiffness, thus avoiding shortening of stroke lengths and unwanted modal resonance. Their physical size and shape allow the driving force to be applied along lines through the centre of gravity of the stage.

This avoids problems that can arise from flexibility in guidance as described in Section 2.5.4.

- To reduce the response to external vibrational disturbances, the support frame/external world interface stiffness should have low stiffness while the stage and metrology frames should be mounted on a support frame with a high level of stiffness (Section 2.5.4).

- From the literature, it is apparent that all the components should be manufactured from the same material so that structural distortion causing mismatch between thermal expansions can be avoided and that metrology loops can be easily nulled.

3.5 Material selection

Within the context of the above outlined initial mechanical design decisions, the material selection may be considered. From Section 2.5.1, the most relevant material selection criteria have already been identified as follows.

- High Young's modulus for stiff guidance and high resonance.

- The yield stress must be a multiple of the absolute maximum stress occurring due to loading. This, though, can only be decided in the context of a particular design geometry and stroke length.

- Low values of E/ρ are required for the high resonance frequencies necessary for resilience to vibrational disturbances and to facilitate the rapid movement necessary for contouring.

- Low values of α/λ and high values of $\lambda/\rho C_p$ are necessary to minimise unpredictable thermal gradients, stress and associated warping.

- Good machineability.

- Affordable.

Two possible materials which satisfy most of these criteria are Super Invar and aluminium alloy 6082 T6. Table 3 below lists their mechanical and thermal properties sourced from eFunda Engineering materials [69].

74

	Super Invar	Aluminium 6082T6	
Density	8140	2810	Kg.m^{-3}
Hardness Rockwell B	75	60	
UTS	483	228	MPa
Yield Strength	276	103	MPa
Young's Modulus	145	71.7	GPa
Poisson's Ratio	0.23	0.33	
Coefficient of Thermal Expansion	0.31	23.4	$\times 10^{-6}$ K^{-1}
Coefficient of Thermal Conductivity	10.4	173	Wm^{-1}K^{-1}
C_P	900	502.42	J.Kg^{-1}K^{-1}
E/ρ	17.81	25.52	$\times 10^6$ Nkg^{-1}m^{-1}
α/λ	3	13.5	$\times 10^{-8}$ W^{-1}
$\lambda/\rho C_p$	1.42	122.53	m^{2}sec^{-1}

Table 3   Material properties table

Super Invar must be considered here predominantly because of its very low thermal expansion coefficient, low value of α/λ, and, as claimed by Hicks et al. [37], it can be fabricated using conventional metalworking techniques. But, the material property data sheet [70] states that machining introduces stresses in the alloy which may cause variation in thermal expansion behaviour. Consequently, it is recommended that parts made from this material should be heat treated as close to finish size as possible.   It is also stated that the alloy is somewhat difficult to machine because the machined chips are gummy and stringy.

 Aluminium 6082 T6, structural grade aluminium, is a very high strength material, used for highly stressed structural parts [69]. Its low values of α/λ, high values of E/ρ and good machineability characteristics make it an attractive candidate for this project, but it is the high ultimate tensile strength (UTS) and yield strength of this particular alloy,

which render it exceptionally suitable for consideration. This is indicated by Elmustafa et al. [51], and Chu [29].

Aluminium 6082 T6 is the material of choice. Although Super Invar has a superior coefficient of thermal expansion and slightly better strength and stiffness characteristics, the aluminium alloy is less dense (a lighter stage allows faster response and exhibits higher resonance frequencies), less expensive, easier to manufacture and has superior thermal conductivity so that thermal gradients can dissipate more quickly.

3.6 The stage

The stage is the moving heart of the instrument. Contouring requires a single point at the centre of the stage to be displaced continuously with nanometre accuracy over a curved path. In a typical nanopositioning instrument, the stage carries a specimen, probe, work-piece or tool. In addition, the stage normally carries metrology components so that its position can be effectively monitored.

3.6.1 The stage size

To avoid unpredictable thermal gradients and to enhance responsiveness, while minimising overshoot, it is desirable that the stage be as small as possible. But, minimising the stage size is limited by the necessity to carry metrology components and adjustable mounts. The stage geometry is further constrained by the necessity to organise the sensor components in accordance with the Abbe principle, i.e. the measurement axes of the interferometers should be made to coincide with those of the capacitance sensors and the displacement axes of the stage (see Fig. 26 and Fig. 27).

In order to comply with these requirements, the first step to realising an effective mechanical design was to choose the individual metrology components and the appropriate mounts. A detailed description of these is presented in Chapter 4 and uncertainties arising from the choices, in the context of the metrology arrangement, are analysed in Chapter 6. The individual components were drawn in 3D (using Solid Edge software) and the part drawings were assembled into three normally orientated interferometers, the measurement axis of each being aligned with capacitance sensors and coincident at a single point.

Fig. 26 The proximity of interferometer mirrors, orthogonality bracket and capacitance components with their mounts that dictated the shape size of the stage.	Fig. 27 Three orthogonally arranged four pass interferometers with the drawn cube representing the minimum stage size.
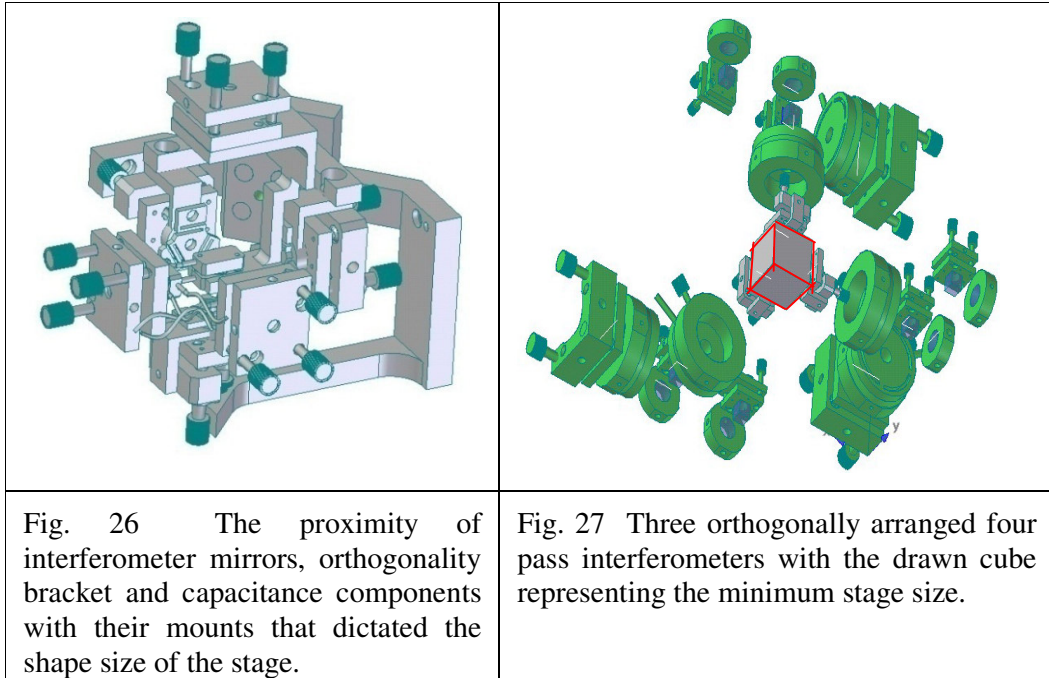
By positioning the components that are to be mounted on the moving stage as close as possible to a single central spot while not contacting or interfering with each other, as illustrated in Fig. 26, the minimum stage size and shape became apparent (represented by the cube in Fig. 27).

3.6.2   The guidance flexures

Having decided on the use of flexures for guidance, it was then necessary to choose between flexure geometries. Two flexure guidance configurations were initially considered due to their common use by researchers and their use in commercial available stages. These were compared in the context of simple single axis stage designs. The geometries of the two designs are shown in Fig. 28 and Fig. 29 . Design 1 uses notched flexures, while Design 2 is a bracketed cantilever arrangement.

Flexure geometry can affect stage stiffness, maximum stroke length, modal resonant frequencies, dynamic response times and ease of manufacture. Calculations, based on these geometries indicated that Design 2 facilitates smaller lighter stages combined with longer stroke lengths. Therefore the bracketed cantilever design was deemed to be the most suitable flexure arrangement for this project.

.

| Fig. 28 Flexure Design 1 | Fig. 29 Flexure Design 2 |
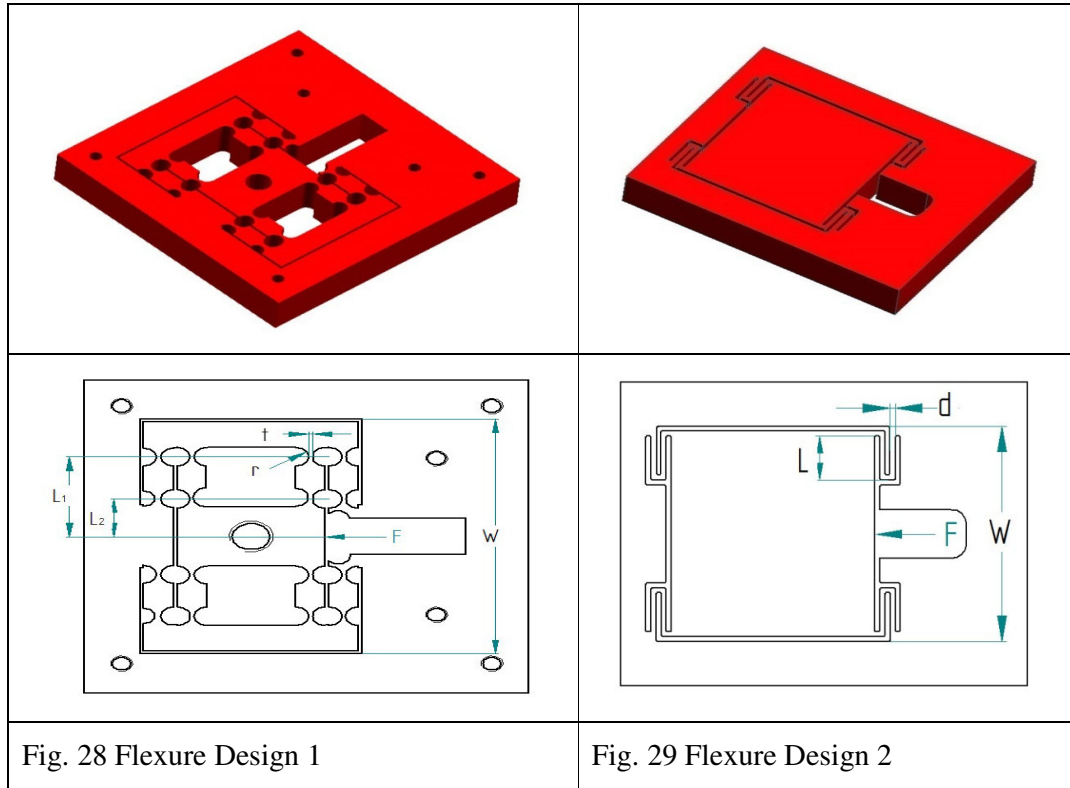
3.6.3 Early stage and force frame designs

Having defined the stage size, it was necessary to devise the initial stage flexure guidance designs for each of the three orthogonal axes. In order to effectively null thermal expansion, to minimise thermal gradients and to avoid friction, it was necessary that the flexures should be cut from a single block of material using EDM. This, when combined with the accommodation of clamping and access requirements for the wire used in the manufacturing process, presented a considerable design challenge. Several early designs with varying levels of success were drawn and examined in FEA. Four such designs are illustrated in Fig. 30.

Fig. 30 Drawings of XYZ stage designs
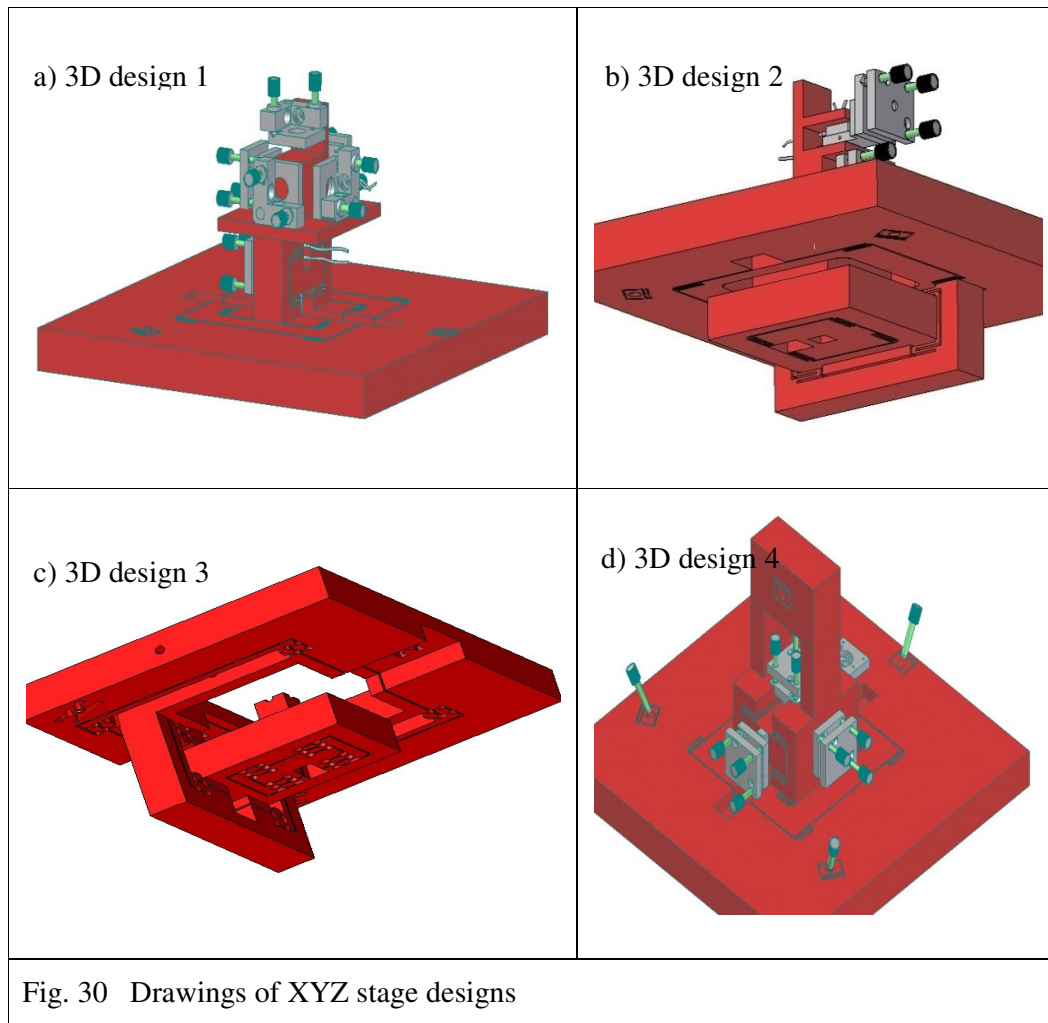
Each of the four designs has a small light stage capable of carrying the metrology components, which can be used in compliance with the Abbe principle and be manufactured by EDM from a single block of metal.

3.7 Mounting considerations

It is reported in the literature (see Section 2.5.5) that when proper mounting arrangements are not used, thermal expansion can cause stress to be transmitted between attached components and relative displacements of metrology components can cause measurement errors. To investigate these matters further in the context of an XY stage design, a finite element model was built, meshed and fully constrained at the surfaces of four holes. The temperature was then raised by 1 K.

Fig. 31 Expansion of an aluminium XY stage resulting from a 1 K rise in temperature.	Fig. 32 Expansion of a Super Invar XY stage resulting from a 1 K rise in temperature.
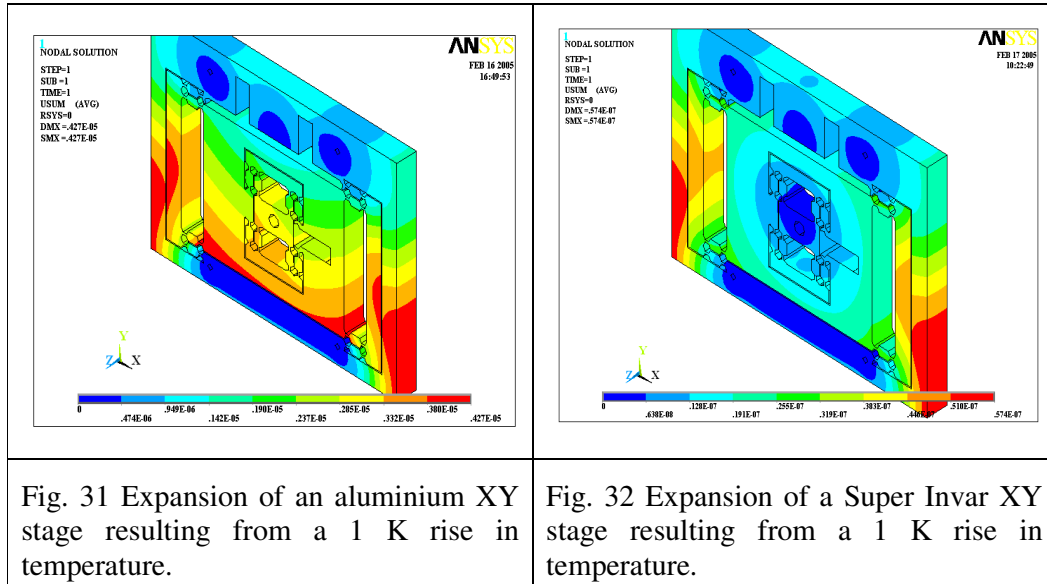
It was found that the use of the thermal expansion coefficient of aluminium ($23.4 \times 10^{-6} K^{-1}$) gives rise to the expansion pattern illustrated in Fig. 31, while using the characteristics of Super invar ($\alpha = 0.31 \times 10^{-6} K^{-1}$) gives the pattern illustrated in Fig. 32. As expected, Super Invar expanded far less than aluminium, but more significantly, it was found that the dissimilar thermal expansions interact differently with the fixed mounting arrangements of the models to give very different distortion patterns. This unexpected finding means that the displacement of the aluminium stage geometric centre is much more temperature dependant than that of the Super Invar stage. This evidence indicates that aluminium would be the wrong choice of material for precision instruments if fixed mounts are used to locate components. An improved mounting system would be necessary to facilitate the use of such a material. Flexure based isostatic mounting, described by Xu et al. [25] (Section 2.5.5), was identified as being such a system.

Isostatic mounting uses a monolithic flexure arrangement to decouple the thermal expansion effects from fixing locations. Each flexure allows motion in one direction while constraining it in all others. Three of these mounts are arranged in such a manner that their individual compliant axes intersect at a single point, as depicted in Fig. 33.

Fig. 33 Isostatic mount arrangement.
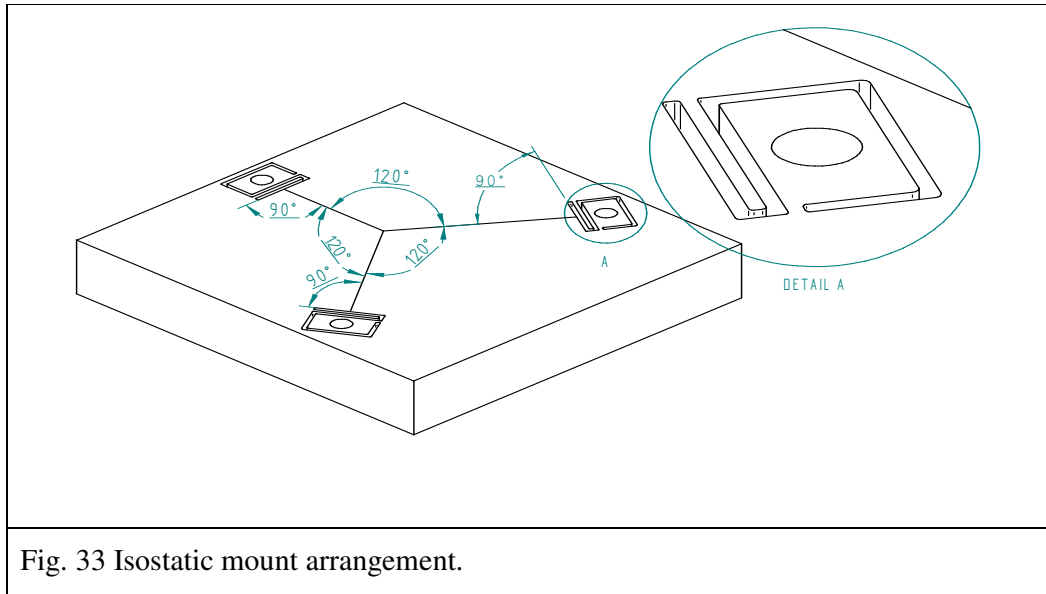
FEA was used to examine the effectiveness of an isostatic design in reducing induced stress and in maintaining a single stationary location at the centre of a stage. A simple rectangular block represented the geometry of the stage and the material characteristics specified were those of Super Invar (coefficient of thermal expansion = 0.31×10^{-6} K^{-1}). The surfaces of each hole were fully constrained and uniform thermal loads were applied.
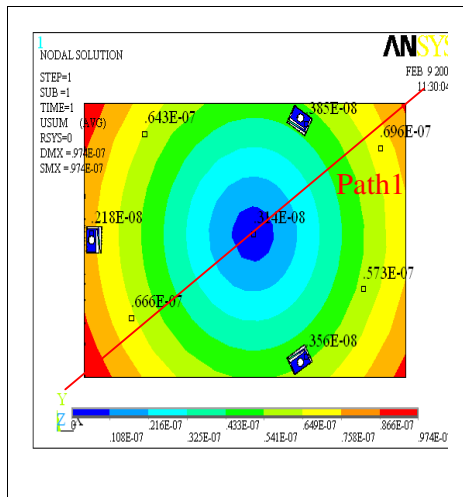
Fig.34 USUM displacements due to thermal expansion resulting from a 1 K temperature rise.
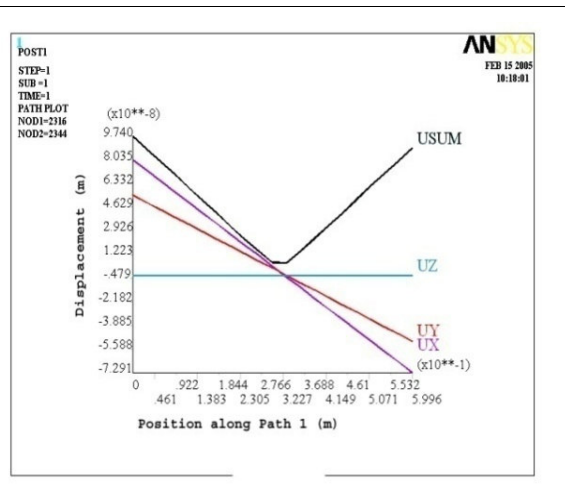
Fig.35 Graph of displacements along Path.

81

Fig.34 shows that the effect of raising the temperature of the block by 1 K is that the minimum displacement values occurred at the centre of the block and increase outwards in a directed radial manner from here. Fig.35 illustrates X, Y and Z axis displacements for points originally located on a path extending diagonally between corners (given in Fig.34). The plots indicate that minimum thermal induced displacement can be established at a chosen location.
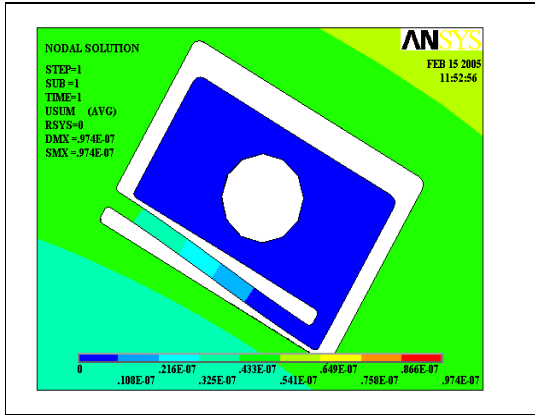
| Fig. 36 Total displacements near mount due to a 1 K temperature raise using Super Invar. | Fig. 37 Total displacements near mount due to a 1 K temperature reduction using Super Invar. |

| Fig. 38 von Mises stress near mount due to a 1 K temperature rise on a fixed mount. | Fig. 39 von Mises stress near mount due to a 1 K temperature rise. |
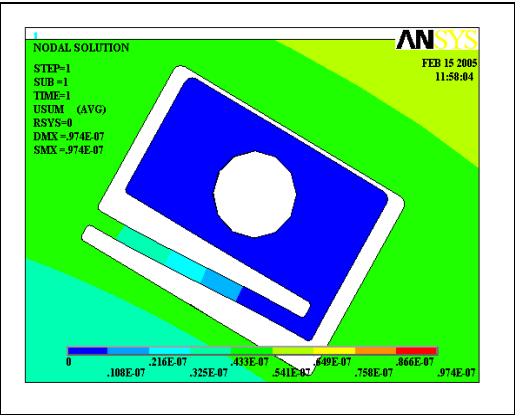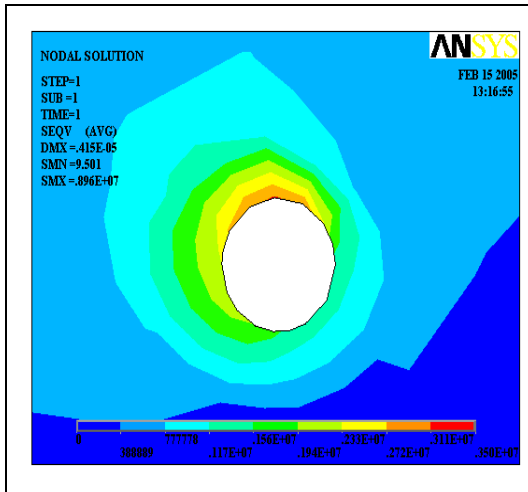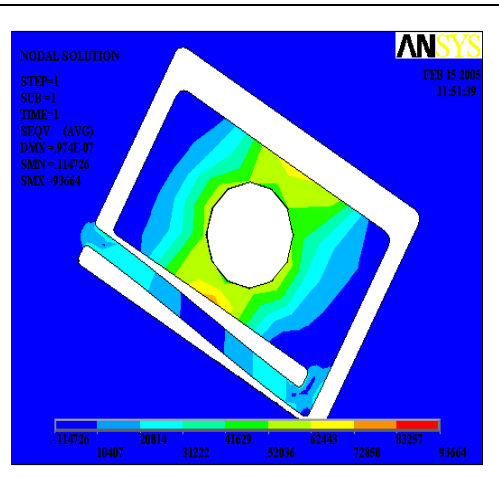
Fig. 36 and Fig. 37 illustrate the behaviour of one of the mounts under differing thermal conditions. In Fig. 36 a 1 K temperature rise has been modelled. In this case

the flexure is compressed as the material of the block expands outwards. In the case of a temperature reduction, as shown in Fig. 37, the flexure is in tension since the block material contracts towards the centre. In this way, constraint of the thermal expansion has been reduced and consequently so also has the stress at the mount.

The von Mises stress pattern, resulting from a 1 K temperature rise, induced at the isostatic mounting hole is shown in Fig. 39 and the stress induced at a fixed mount is illustrated in Fig. 38. There is a 37.4 fold reduction in the maximum stress level at the circumference of the mount hole itself, i.e. the stress which would be transferred to the supporting frame. Additionally, in the isostatic case, the stress is far more localised, leaving the instrument structures virtually stress-free.

3.7.1 The effect of isostatic mounting

Locating the working point at the instrument point of least expansion and having all parts made from material of the same coefficient of thermal expansion, allows the retention of measurement axis alignment, although the spacing between components along the axes changes as expansion of the instrument takes place.

This situation is illustrated schematically in Fig. 40. Two schematics are presented in this figure, one representing the instrument in elevation (XZ plane), the second representing a plan view (XY plane). Four circles are used to represent:

a) the stage at temperature T_1; b) the expanded stage at a higher temperature, T_2;

c) the metrology frame at T_1; and d) the expanded metrology frame at T_2.

The blue lines represent a single measurement axis in its T_1 and T_2 positions. One end of each is the point of interest on the stage, the other end is the reflective surface of the interferometer beam splitting prism. It can be seen in Fig. 40 that the measurement axis retains its orientation, although its length is increased when the instrument expands.

Fig. 40   Schematic showing that a measurement axis retains its orientation if the point of interest coincident with the points of least expansion of both the stage and metrology frame while the same thermal expansion coefficient applies to all structures.

84

Fig. 41 illustrates the FEA predicted thermal expansion pattern of a stage mounted on a base using isostatic mounts in both stage and base when a temperature rise of 1 K is modelled and the model is constrained at the centre of the base. Fig. 41 illustrates that the sweet spot, i.e. the point of interest on the stage located for least expansion in its XY plane,
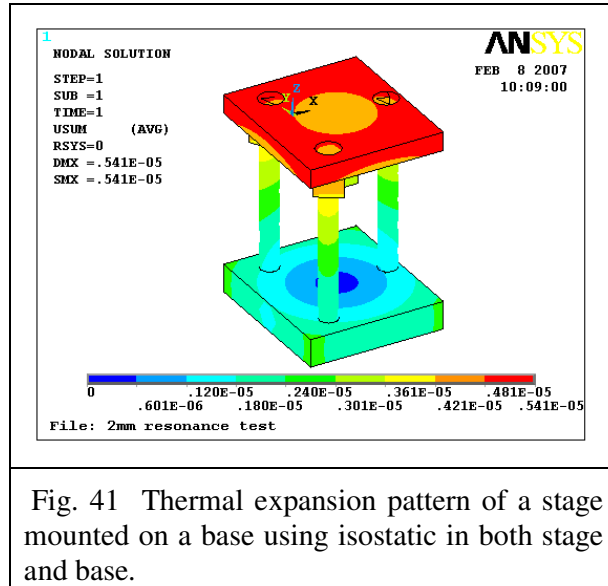
Fig. 41 Thermal expansion pattern of a stage mounted on a base using isostatic in both stage and base.

does not remain stationary, but rises vertically in the Z direction away from the base. This is consistent with the behaviour predicted in Fig. 40. As the metrology frame would behave likewise, the measurement axes can remain coincident with each other and with the stage centre of expansion.

For these reasons, the former approach of making the centre of expansion of the metrology frame coincident with that of the stage, was adopted and implemented in the design through the use of isostatic mounts.

The simple isostatic mounts described Section 3.7 produce zones of least thermal expansion centred close to the plane of the mounts. This is ideal for single axis and XY stages, but, although the arrangement works in the case of Design 3, for three axis instruments, such as Designs 1, 2 and 4, the working point may not lie in this plane. In such cases it is desirable to shift the spot of least expansion, or 'sweet spot', out of the mounting plane so as to allow the measurement axes to remain coincident with movement axes of the working point during temperatures fluctuations.

Several solutions were found to this problem. In designs 1, 2 and 4, the isostatic flexure mounts are tilted at a 30^0 to the XY plane (see Fig. 42) in order to produce a raised sweet-spot.

85

3D design 1

Tilted iso flexures

3D design 4

Tilted iso flexures

3D design 2
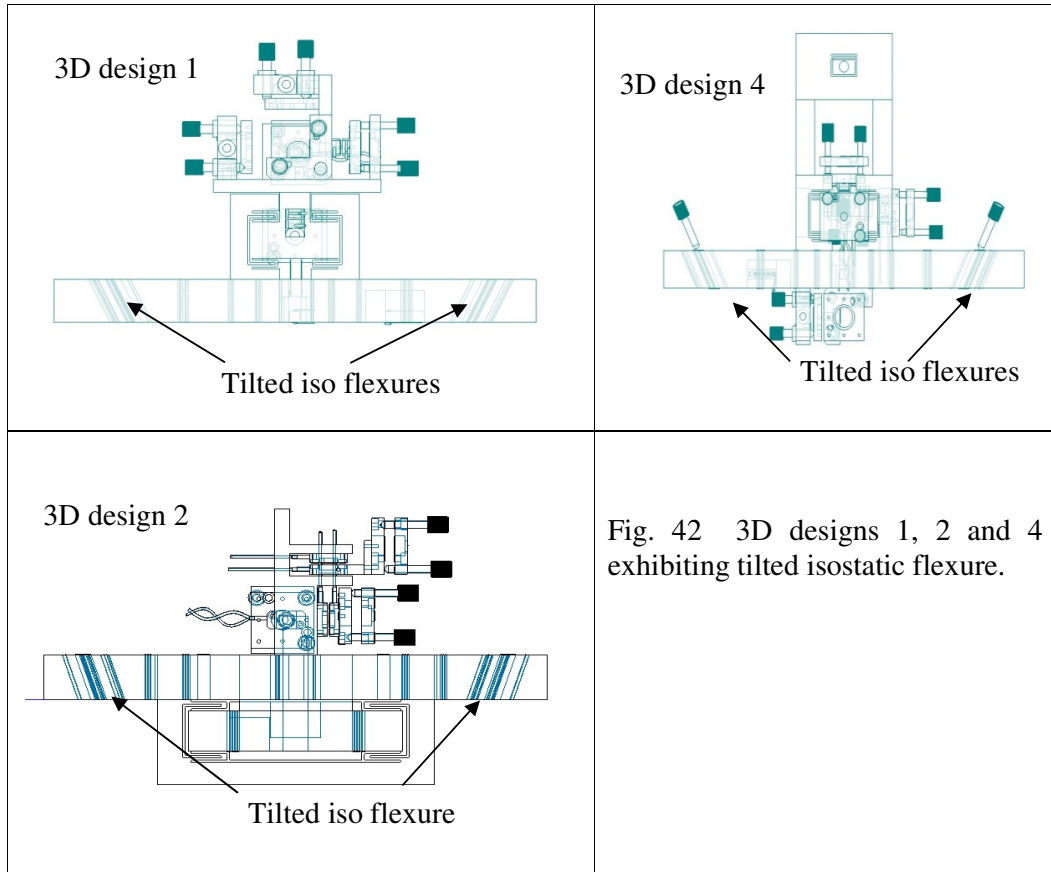
Tilted iso flexure

Fig. 42 3D designs 1, 2 and 4 exhibiting tilted isostatic flexure.
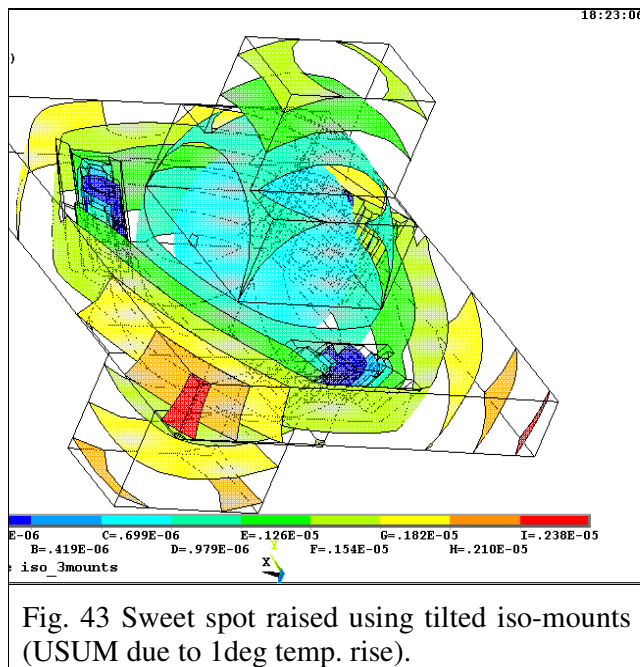
Fig. 43 Sweet spot raised using tilted iso-mounts (USUM due to 1deg temp. rise).

The hypothesis that the sweet spot could be raised by tilting the isostatic mounts was tested using FEA. Fig. 43 shows the FEA predicted pattern of thermal expansion of a simple model due to a temperature rise of 1 K. The blue spheres indicate the volumes of least expansion. The diagrams suggest that the design is very effective in positioning the sweet spot.

Sloping isostatic mounts, are expensive and difficult to manufacture (requiring special fixtures). Another, less expensive, solution accomplishes a similar effect. This design involves placing isostatic flexures in the same manner as described in Section 3.7, but now located in stiff raised columns so that half their depth coincides with the plane of the X and Y measurement axes (see Fig. 44). The vertical position of the sweet spot can be established by adjusting the depth of holes located under the columns.
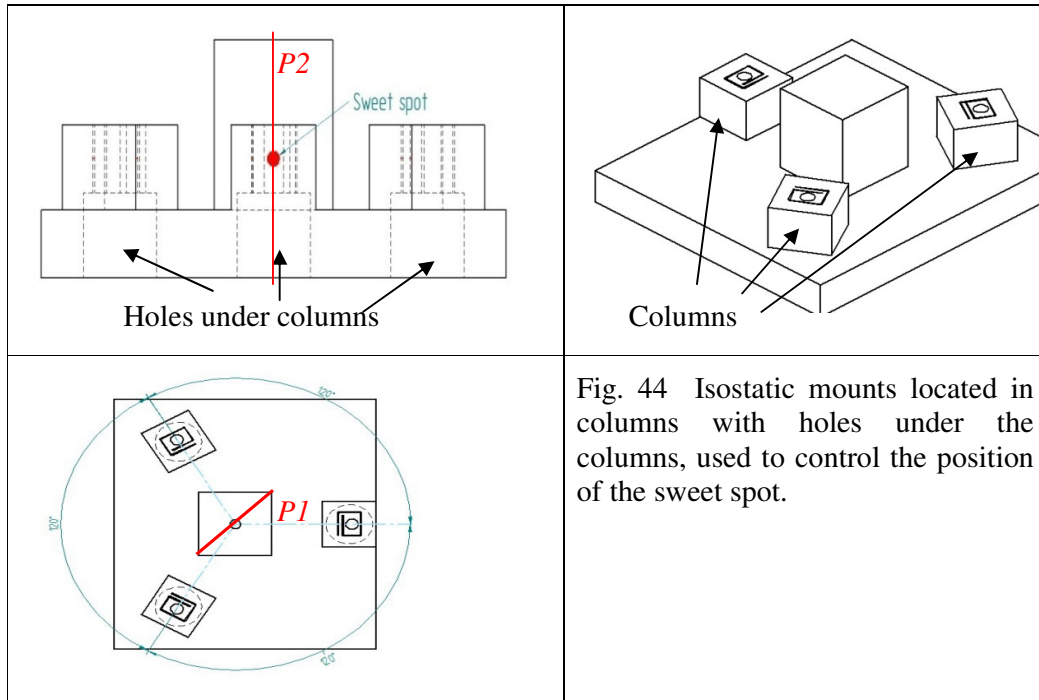
Fig. 44   Isostatic mounts located in columns with holes under the columns, used to control the position of the sweet spot.
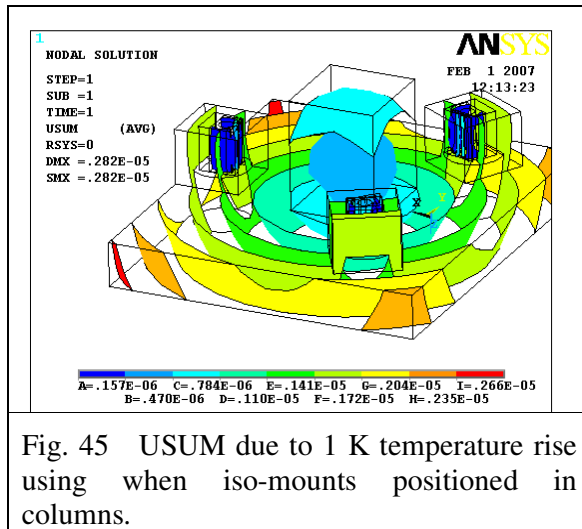
Fig. 45   USUM due to 1 K temperature rise using when iso-mounts positioned in columns.

Fig. 45 illustrates the effectiveness of the column isostatic mount approach when the temperature is modelled as 1 K higher than the nominal temperature. Again, the blue sphere represents a volume where displacements are minimised.

As explained in Section 2.5.4, to reduce the effects of external vibration disturbances, the stage and metrology frames should be mounted on a support frame with stiff linkages. As expanding material would easily compress stiff mounting flexures, a flexure thickness of 6 mm was initially chosen. The effectiveness of these mounts was then examined using FEA.
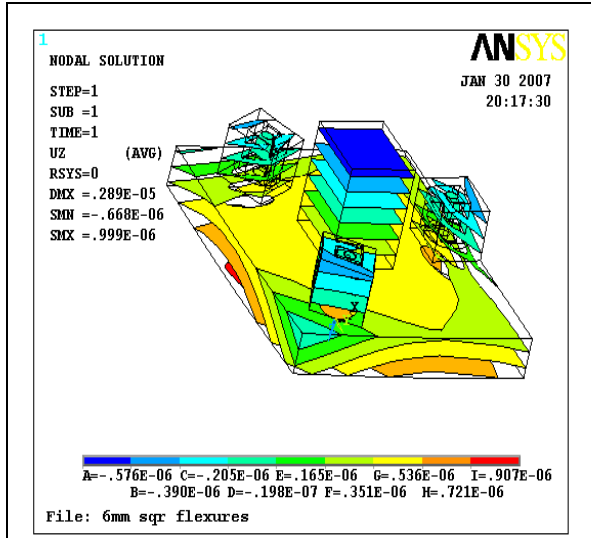
Fig. 46 Z axis displacements of the block when a 1 K rise in temperature is modelled with 6mm thick isostatic mount flexures.
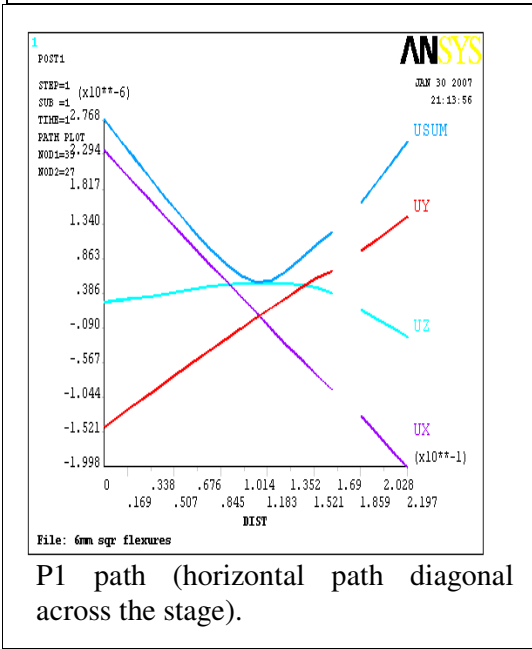
P1 path (horizontal path diagonal across the stage).
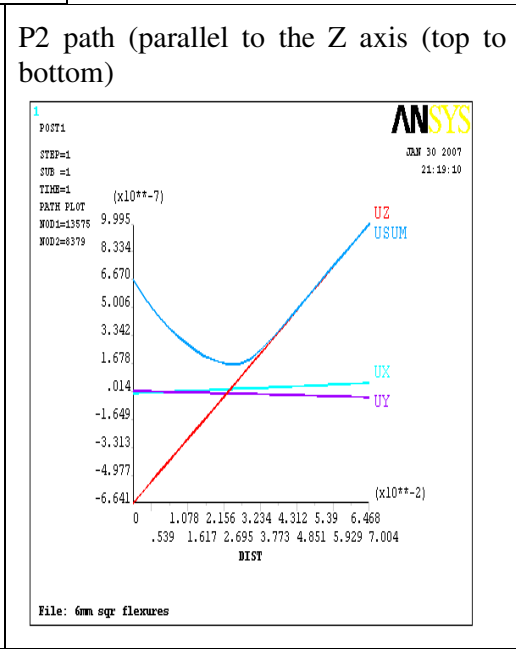
P2 path (parallel to the Z axis (top to bottom)

Fig. 47 Graphs showing the displacements of nodes located along two paths P1 and P2 (illustrated in Fig. 44 (one horizontal diagonal across the stage and the other vertical extending centrally from the top to the bottom of the stage) when 6 mm thick isostatic mount flexures are used.

Graphs are given in Fig. 47 of nodal displacements along paths running vertically from the top to the bottom of the stage (P1, Fig. 44) and running in a horizontally diagonal

across the stage (P2, Fig. 44). As expected, the average displacement curves (USUM) for each path show minimum values about the point of interest. The displacements in the Z direction of nodes along path *P2* would be expected to be constant for all nodes. Fig. 47 indicates that this is not the case. To explore this further, the Z displacements were examined separately. The isosurface image of Z direction displacements, presented in Fig. 46, illustrates the distortion introduced with a temperature rise of 1 K, though, as Fig. 48 illustrates, the maximum coupling stress is only 12.5 MN.m^{-2}.

Fig. 48 von Mises stress at the isostatic mounts due to a 1 K temperature rise when 6 mm mount flexures are used.
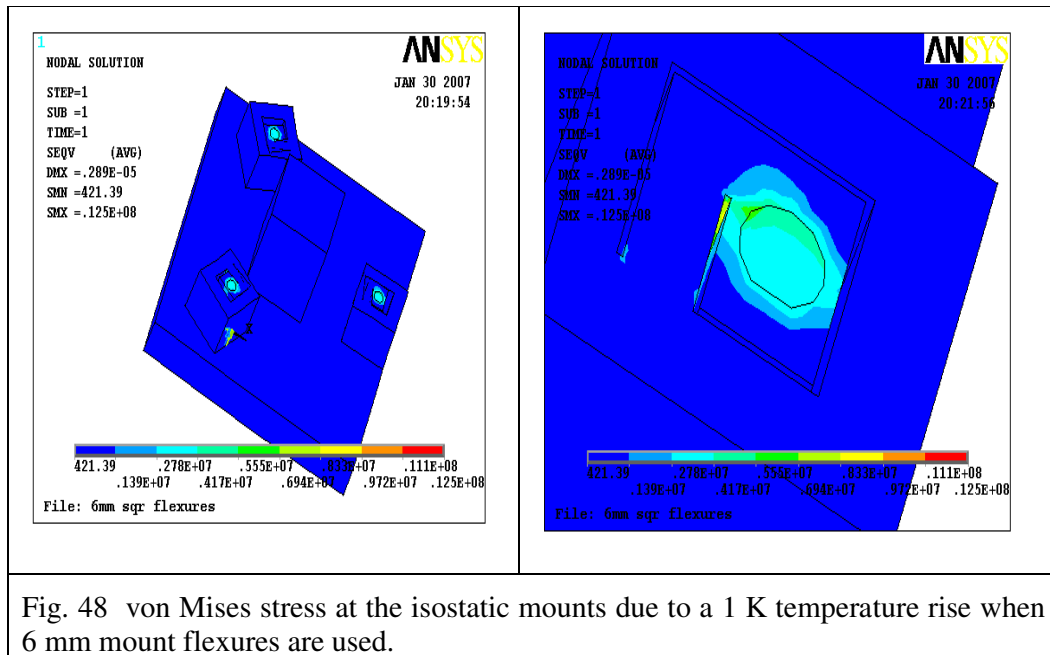
It is suspected that substantially stouter columns and a thicker base may prevent this distortion, but the space requirements to facilitate the metrology components, would prohibit this approach.

Another possible solution considered was to use a softer flexure. The model mount flexure thickness was reduced to 2 mm. Fig. 49 illustrates that the distortion has been successfully reduced while Fig. 50 indicates that the coupling von Mises stress is reduced to 5.9 MNm^{-2}. The graphs presented in Fig. 51 also indicate far less distortion, evident by linear curves when softer flexures are used. It would appear that, for improved thermal expansion characteristics, the 2 mm mount flexure is preferable.
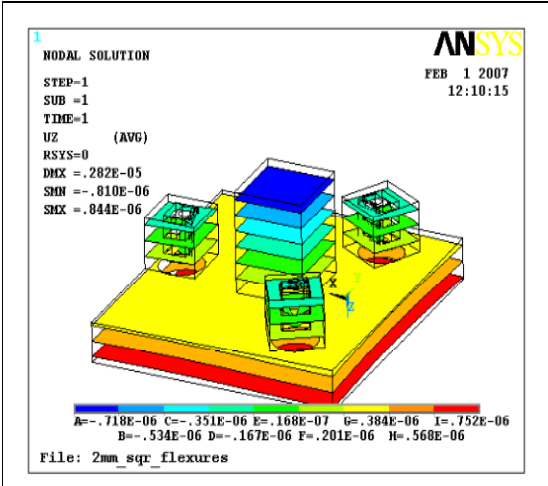
| Fig. 49 Z axis displacements of the block when a 1 K rise in temperature is modelled with 2 mm thick isostatic mount flexures. | Fig. 50 von Mises stress at the isostatic mounts due to a 1 K temperature rise when 2 mm mount flexures are used. |

| UX, UY and UZ along a vertical path through the center of the stage. | UX, UY and UZ along a horizontal diagonal path through the centre of the stage. |
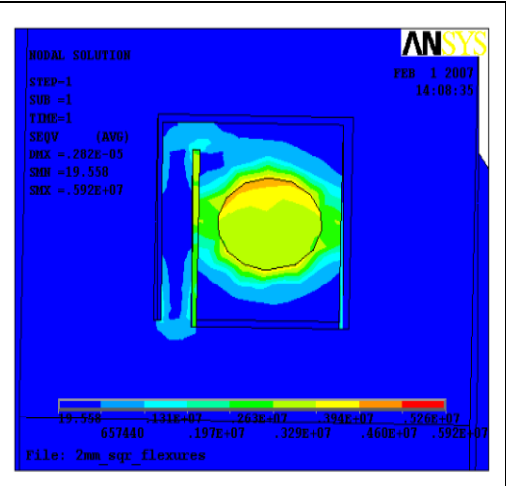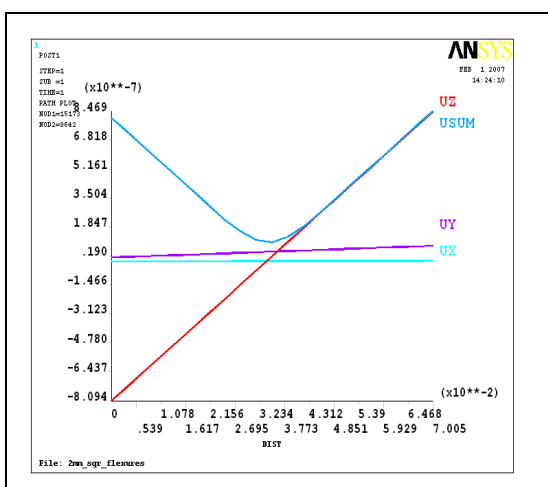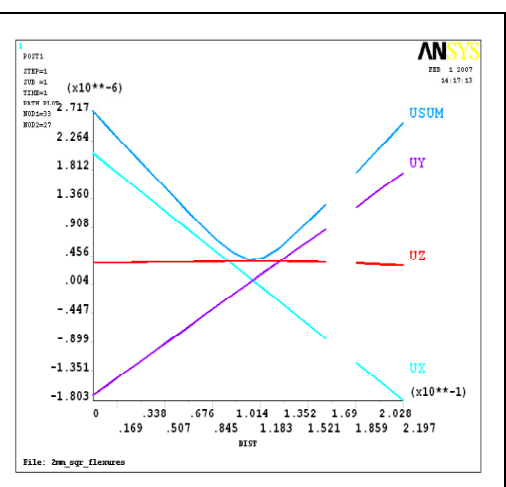
Fig. 51 Graphs showing the displacements of nodes located along paths *P1* and *P2* when 2 mm thick isostatic mount flexures are used.

Thus the stage was developed based on the guidance flexure arrangement exemplified in Design 4 with a pillar located isostatic mounting system. The finalised design is discussed Section 3.2.

3.8 The final design

3.8.1 Stage/force-frame
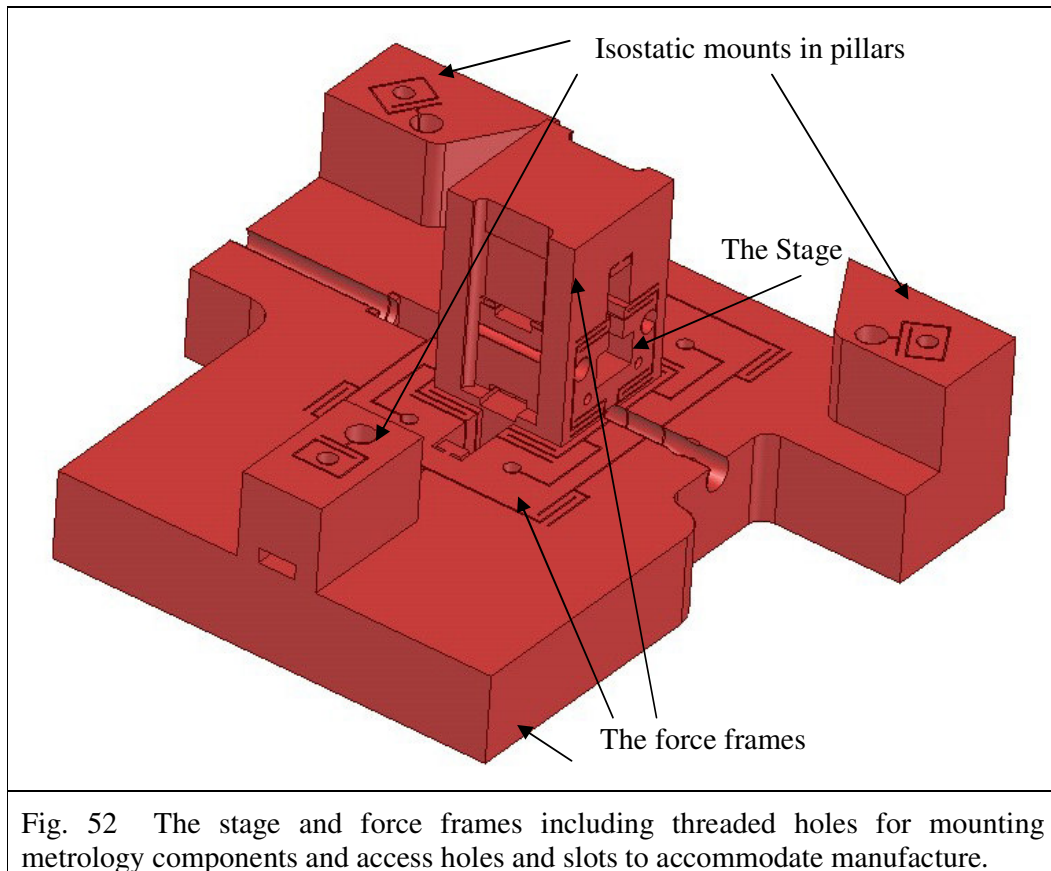
Fig. 52 The stage and force frames including threaded holes for mounting metrology components and access holes and slots to accommodate manufacture.

The design illustrated in Fig. 52 provides:

- a light responsive stage;

- insensitivity to external vibrations through stiff guidance with high principal mode resonance;

- frictionless movement;

- capability of carrying the required metrology components;

- compliance with the Abbe principle;

- minimal sensitivity to thermal expansion and minimising warping arising from mounting stresses by locating the point of least expansion at the stage working point;

- rapid thermal stabilisation by keeping the stage small and using a material of high thermal conductivity; and

- minimal parasitic displacements, rotations and resonance by arranging the driving force to act through or close to the axes' centres of gravity.

3.8.2   Dimensioning the flexures

Dimensioning the flexures involved balancing the following requirements:

- high axial compliance and off-axial stiffness;

- maximised stroke lengths;

- flexures stress below the yield stress of the material;

- the piezo remaining in contact with the stage, even at resonance;

- high guidance stiffness and resonance frequencies (required for faster response); and

- high structural and mount stiffness (for insensitivity to external vibration disturbances).

The equation for calculating the linear stiffness of a compound bracketed flexure stage, as presented by Elmustafa et al. [51], was used to calculate the stiffness of the 3D stage guidance flexures

$$k_{x,y,z} = \frac{1}{2}\left\{ \mathrm{E}b_{x,y,z}\left(\frac{d_{x,y,z}}{L_{x,y,z}}\right)^3 \right\}$$

Equ. 20

The stage axes each has four of these hinges in parallel, so

$$k_{x,y,z} = 2\left\{ \mathrm{E}b_{x,y,z}\left(\frac{d_{x,y,z}}{L_{x,y,z}}\right)^3 \right\}$$

Equ. 21

Axis	X,	Y	Z
E (GN.m^{-2})	70	70	70
$d_{X,Y}$ (mm)	2	2	2
$b_{X,Y}$ (mm)	24	24	42
M (kg)	0.662	0.307	0.088
Table 4 Initial dimensions.			

Initially the stiffness of each axis was calculated based on the first estimate dimensions given in Table 4 and plotted against a range of possible flexure lengths in Fig. 53.   The d and b dimensions were chosen, based on values calculated for the two-axis designs, in order to provide appropriate flexure compliance in a single direction for each hinge while achieving effective stiffness in all other directions.
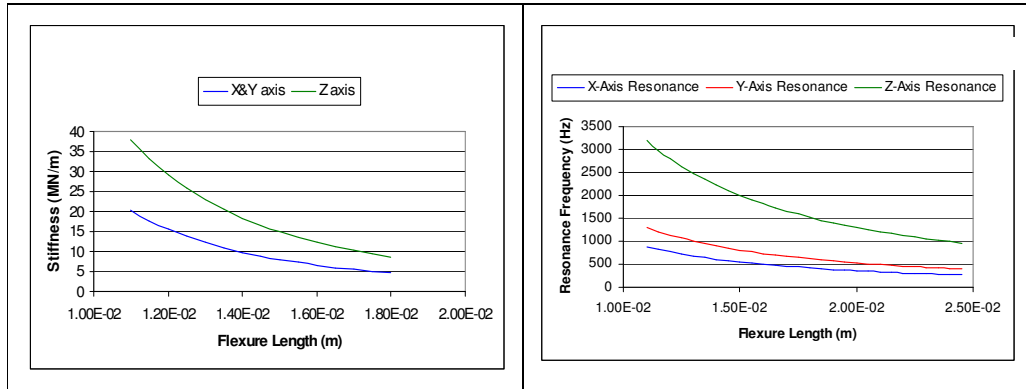
Fig. 53   Guidance flexure stiffness based on initial dimensions.

Fig. 54   Guidance flexure resonance frequencies based on initial dimensions.

The dominant modal resonance frequency for each axis is calculated using

$$ f = \frac{1}{2\pi}\sqrt{\frac{k}{m}} $$

<div align="right">Equ. 22</div>

and is plotted against flexure length in Fig. 54.   The graphs indicate that relatively high resonance is achievable for the X and Y axes for lengths ranging from 11 mm to 17 mm, while the Z axis is shown to be much stiffer with a higher resonance frequency over the entire graphed range of 11 mm to 18 mm.

As described in Section 2.5.3, a preload must be applied so that the piezo does not break contact with the stage at resonance and must be greater than the maximum

dynamic force generated due to resonance [51]. This force was calculated based on the following expression presented by Woronko et al. [51]

$$F_d = 4\pi^2 f^2 m_{eff} \frac{\Delta L}{2}$$

(Section2.5.3, [51])

where f is the oscillating frequency (Hz), ΔL is the actual stroke (m) and m_{eff} is the effective mass (Kg), while the actual stroke length is calculated by using the following equation presented by Physik Instrumente (PI) GmbH & Co [27]

$$\Delta L = \Delta L_0 \frac{K_T}{K_T + k}$$

Equ. 23

ΔL_0 and K_T being the nomina extension and stiffness of the piezo.

The required preload is created by making the gap provided for locating the piezo smaller than the retracted piezo length. The reduction in gap size below that required to accommodate the piezo can be calculated by

$$\text{gap reduction} = \frac{F_d}{k}$$

Equ. 24

| Fig. 55 Reductions in piezo accommodation gap and the corresponding preloads graphed against a range of flexure lengths for the initial flexure dimensions. | Fig. 56 Preloads graphed against a range of flexure lengths when gap reductions are 0.1 mm and 0.05 mm respectively and the initial flexure dimensions are used. |
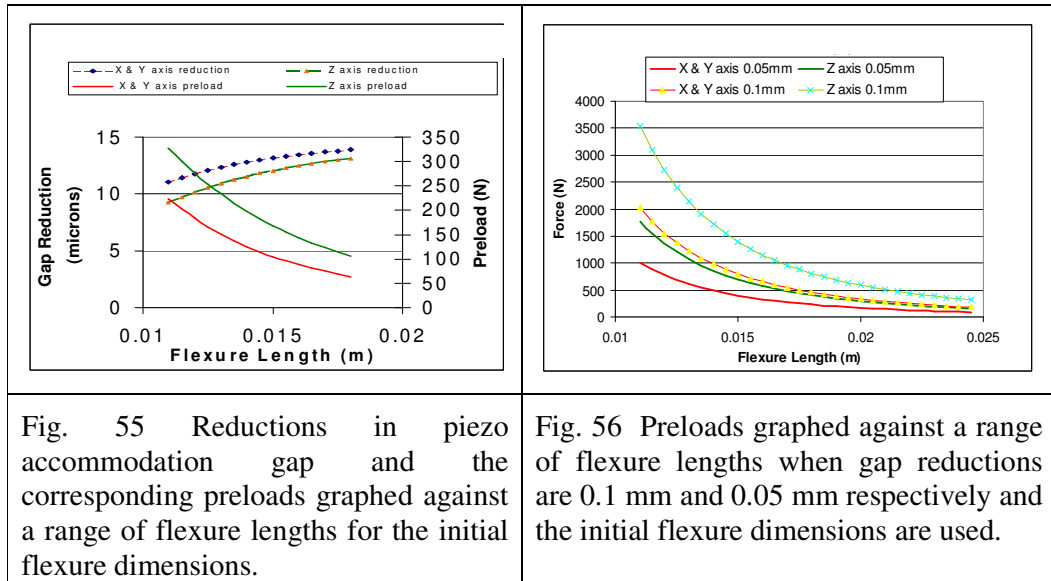
The necessary gap reductions, even with a factor of safety of two, are small (12 μm to 15 μm) as can be seen in Fig. 55. Since these are minimum values only, it was possible to choose a more manufacturing friendly gap reduction. Two sizes were examined, 0.05 mm and 0.1 mm. The preloads resulting from these reductions were calculated and plotted in Fig. 56 against a range of flexure lengths. As the maximum force that can be exerted by the chosen piezo (Physik Instrumente Co [27] PI840.1) is 1000 N, then the minimum flexure length for the two gap sizes can be deduced (Fig. 56). In the case of a 0.1 mm reduction the X and Y axis flexures must be longer than 14 mm, while the flexures of the Z axis must be at least 17 mm for the dimensions given in Table 4. This gives a 612 Hz resonance frequency for the X axes, 899 Hz for the Y axis and 1660 Hz for the Z axis. In the case of a 0.05 mm reduction, the X and Y axes flexures must be at least 12 mm while the flexures of the Z axis must be at least 14 mm long. This gives a 771 Hz resonance frequency for the X axes, 1132 Hz for the Y axis and 2221 Hz for the Z axis.

At smaller gap sizes attention to stress levels becomes more significant since the forces and stage deflections involved are much higher. The maximum stress arising from the preload and deflection loads can be calculated from Section 2.5.3, Equ. 8 [51]

$$\sigma_{max} = \frac{3Ed\delta_{max}}{L^2} \ where \ \delta_{max} \ \text{is the maximum deflection}$$
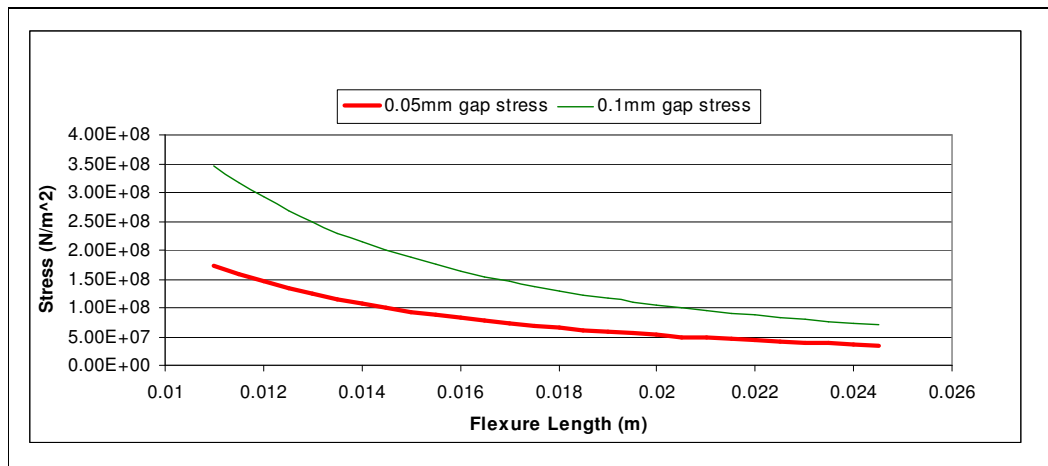
Fig. 57 Flexure stress levels at full deflection (0.05 mm and 0.1 mm piezo gap reduction).

It is apparent from Fig. 57 that flexure stress is independent from flexure depth (b dimension). Consequently the guidance flexures with the initial dimensions given in

95

Table 4, all have the same maximum stress. The stress arising from a 0.1 mm and a 0.05 mm gap reduction is plotted in Fig. 57 for a range of flexure lengths from 11 mm to 25 mm. Since the yield stress of the material is 103 MN.m^{-2}, then, if permanent deformation of the flexures is to be avoided, it can deduced from the graph that the flexures must be at least 23 mm and 15.5 mm long in the case of the 0.1 mm and the 0.05 mm reductions respectively. 23 mm flexure lengths could be acceptable for the X and Y axes, as the size of the stage need not change, but, in the case of the Z axis, would require the overall width of the stage to be increase. Additionally, from Fig. 54, the X axis resonance frequency is 290 Hz with a 23 mm long flexure, while that of the Y axis is only 427 Hz. The reduced minimum flexures lengths of 15.5 mm, associated with the 0.05 mm gap reduction, gives a more respectable resonance frequency of 525 Hz for the X axis, 772 Hz for the Y axis and 1906 Hz for the Z axis

Table 5 provides a summary of these calculated values.

	0.10 mm gap reduction			0.05 mm gap reduction		
	X axis	Y axis	Z axis	X axis	Yaxis	Z axis
Length (mm)	23	23	23	15.5	15.5	15.5
Resonance frequency (Hz)	290	427	1055	525	772	1906
Stress (MN.m^{-2})	79.4	79.43	79.4	87.4	87.4	87.4

Table 5 Summary of minimum flexure lengths required to avoid plastic deformation and the consequent resonant frequencies and stress levels for gap reductions of 0.1 mm and 0.05 mm.

The 0.05 mm gap reduction was adopted to achieve the preloads for the instrument under design, since this permitted shorter flexures and consequently smaller stage structures and higher resonant frequencies.

It was felt, that 87.4 MN.m^{-2} stress is uncomfortably close to material yield stress and so the X and Y axes flexures were lengthened to 16.5 mm. While constrained by the need to keep the stage as small as possible, a different approach was adopted for the Z axis. The Z axis flexures were in fact reduced to 14 mm and, so that the stress under preload could be maintained below the yield stress for these short flexures, the flexure thickness d was reduced to 1.5 mm with a 12 mm slot cut through the centre of the

flexures. This effectively creating eight 15 mm deep flexures acting in parallel instead of four 42 mm deep flexures. This reduced the stiffness and resonant frequency of the Z axis, balancing its responsiveness with the other axes.

The stiffness of the Z axis can now be calculated by using Equ. 25

The stiffness of the eight parallel flexure Z axis,

$$k_Z = 4\left\{\mathrm{E}b_Z\left(\frac{d_Z}{d_Z}\right)^3\right\}$$

Equ. 25
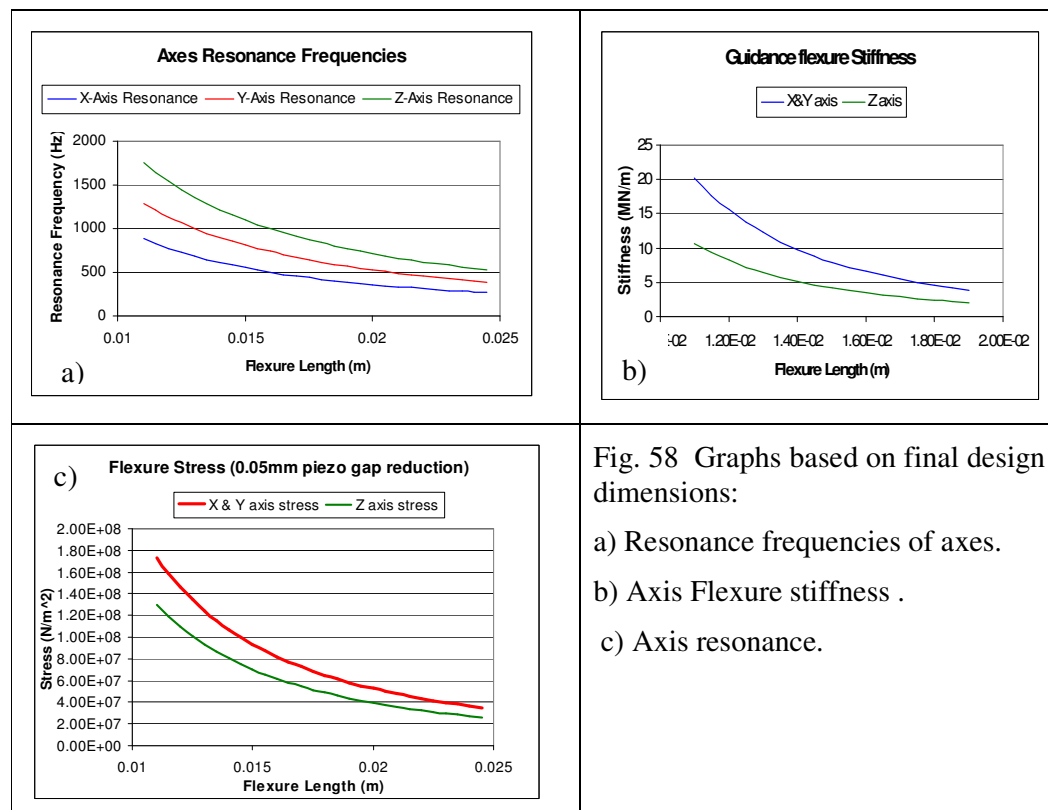
Fig. 58 Graphs based on final design dimensions:

a) Resonance frequencies of axes.

b) Axis Flexure stiffness .

 c) Axis resonance.

The chosen flexure dimensions, along with axis resonance and maximum stress levels are tabulated in Table 6.

	X axis	Y axis	Z axis
Piezo locating gap reduction (mm)	0.05	0.05	0.05
E (GN.m$^{-2)}$	70	70	70
$d_{X,Y}$ (mm)	2	2	1.5
M (kg)	0.662	0.307	0.088
Length (mm)	16.5	16.5	14
Axis stiffness (N.μm^{-1})	5.98	5.98	5.166
Resonance frequency (Hz)	478	702	1219
Stress (MN.m^{-2})	77.1	77.1	80.4
Table 6 Flexure dimensions table, including axis resonance and maximum flexure stress levels			

To verify the calculated values prior to the preparation of final drawings for manufacture, a model of the stage was built in FEA and a load of 100 N was applied initially to each axis. The resulting displacements and the stiffness of each axis are given in Fig. 59. An obvious large discrepancy between the calculated values and the FEA predictions for all axes became apparent.   It was also noticed that there appeared to be some deformation of the force frames, particularly in the case of the X and Y axes.

The calculated values given in Table 6 do not, however, take into account any deformations of the force frame or the stage itself as these are design-specific. Further FEA analysis was performed in which the colour range representing the displacements was manipulated in order to focus on the deflection of structural members. These FEA images (Fig. 61) show that the structures deform in front of and behind the expanding piezo in the case of each axis.

Fig. 59 FEA predicted displacements of the stage axes when the application of a 100 N force to each axis is modelled

a. Y axis displacement = 8.19 μm

  stiffness = 12.21 N.μm^{-1}

b. X axis displacement = 8.88 μm

  stiffness = 11.26 N.μm^{-1}

c. Z axis displacement = 8.624 μm

  stiffness = 11.6 N.μm^{-1}

Fig. 60 Deformation of the Y-axis front beam when subjected to a centrally located 100 N force. Included also is a graph of the displacement of locations along a path stretching the length of the beam.

Fig. 61 Deformation of axis structural members when subjected to 100 N force;

a) deflexion of X axis rear beam

b) deflexion of Z axis rear beam

c) deflexion of Y axis rear beam

It also became evident from FEA that the structural members against which the piezo actuators push are less rigid relative to the stiffness of the guidance flexures than anticipated. This can be deduced from Fig. 60, in which is shown the FEA predicted deformation of the beam of the Y axis against which the axis displacing force is applied. In this instance, the beam is subjected to a centrally located 100 N force. The included graph of the displacement of locations along a path stretching the length of the beam indicates that the beam is deflected 0.281 μm for an axial stage displacement of 6.56 μm. Such deflections would result in reduced stroke lengths and were regarded as a possible explanation for the difference between the calculated and FEA predicted axial stiffness values. It was also anticipated that these deflections would have implications for preload stress levels in the guidance flexures and would give rise to

hitherto unforeseen resonance modes. For these reasons it was felt important to develop a greater understanding in this area.

Fig. 62 Key to beam equation variables
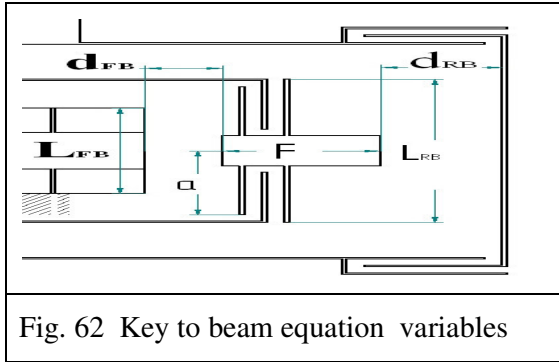
A reasonable assumption is that some structures act as beams, fixed at both ends while deflecting under centrally positioned concentrated loads. Using standard beam theory, the deflection, x_B, of a beam of length L_B, loaded at a distance a from one end, can be calculated as follows

$$x_B = \frac{2FL_B^3 Z^3 (1 - Z)^2}{3EI(1 + 2Z)^2} \quad \text{where } Z = \frac{a}{L_B}$$

and the beam stiffness,

$$k_B = \frac{F}{x_B} = \frac{3EI(1 + 2Z)^2 F}{2FL_B^3 Z^3 (1 - Z)^2}$$

when he load is central

$$k_B = \frac{192EI}{L_B^3} = \frac{192Ebd_B^3}{12L_B^3} = \frac{16Ebd_B^3}{L_B^3}$$

Equ. 26

Both the X and Y axes have two of these deformable members associated with them, one in front and one behind the piezo. Each deflects in series with the flexure hinges of its respective axis, giving a reduction in effective stiffness that can be calculated with Equ. 27. This equation is derived simply as follows.

The total piezo expansion (δtot), includes preloading and the deflection of both beams (front beam deflection δ_{FB} and rear beam deflection δ_{RB}) as well as the displacement of the stage ($\delta stage$). So

$$\delta_{tot} = \delta_{stage} + \delta_{FB} + \delta_{RB}$$

$$\frac{F}{k_{eq}} = \frac{F}{k_{stage}} + \frac{F}{k_{FB}} + \frac{F}{k_{RB}}$$

$$k_{eq} = \frac{k_{stage}k_{FB}k_{RB}}{k_{RB}k_{FB} + k_{stage}k_{RB} + k_{stage}k_{FB}}$$

<div align="right">Equ. 27</div>

Because the piezo is pushing against flexible members in series with the stage guidance flexures, the stage stroke length is shortened; giving rise to an increased apparent stiffness that can be calculated by using Equ. 28

$$\frac{1}{k_{\text{App}(XY)}} = \frac{1}{k_{stage}} - \frac{1}{k_{FB}} - \frac{1}{k_{RB}}$$

$$k_{\text{App}(XY)} = \frac{k_{stage}k_{FB}k_{RB}}{k_{RB}k_{FB} + k_{stage}k_{RB} + k_{stage}k_{FB}}$$

<div align="right">Equ. 28</div>

Since

$$F = \delta_{tot}k_{eq}$$

$$\delta_{\text{stage}(XY)} = \frac{\delta_{tot}k_{stage}k_{FB}k_{RB}}{k_{RB}k_{FB} + k_{stage}k_{RB} + k_{stage}k_{FB}}$$

$$\delta_{\text{stage}(XY)} = \frac{F}{k_{App}} = \frac{\delta_{tot}k_{stage}k_{FB}k_{RB}(k_{RB}k_{FB} - k_{stage}k_{RB} - k_{stage}k_{FB})}{k_{stage}k_{FB}k_{RB}(k_{RB}k_{FB} + k_{stage}k_{RB} + k_{stage}k_{FB})}$$

$$\delta_{\text{stage}(XY)} = \frac{\delta_{tot}(k_{RB}k_{FB} - k_{stage}k_{RB} - k_{stage}k_{FB})}{(k_{RB}k_{FB} + k_{stage}k_{RB} + k_{stage}k_{FB})}$$

<div align="right">Equ. 29</div>

Equ. 29 allows the displacement of the stage from the no-load position to be calculated when δtot is known, as in the case of preloading through the reduction in gap size. Also, by combining Equ. 8 and Equ. 29 the following expression can be used to calculate the maximum stress in the hinges under preload when the total displacement corresponds to the total piezo gap reduction.

$$\sigma_{\max XY} = \frac{3Ed_{flex}\delta_{tot}(k_{RB}k_{FB} - k_{stage}k_{RB} - k_{stage}k_{FB})}{L_{flex}^2(k_{RB}k_{FB} + k_{stage}k_{RB} + k_{stage}k_{FB})}$$

<div align="right">Equ. 30</div>

In the case of the Z axis, there is no beam in front of the piezo, while the beam to its rear is connected to the Y axis by four rectangular struts, as can be seen in Fig. 63, that come under axial tensile load when the stage is preloaded and during the normal stage displacement cycles. These rectangular struts behave effectively like four springs acting in parallel with each other, while simultaneously acting in series with the stage Z axis guidance flexures and the deflection of the beam behind the piezo. The axial lengthening of the struts for a Super Invar stage is depicted in Fig. 64 by the gradation in colour along the length of the struts.
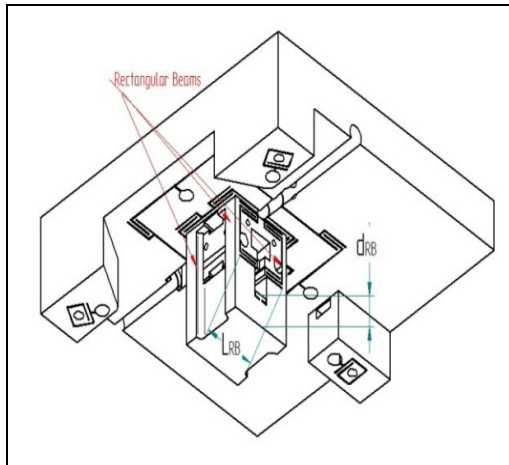
| Fig. 63 Key to Z axis beam calculations. | Fig. 64 FEA image illustrating the bending of the beam behind the piezo and the axial lengthening of the struts. |

| Fig. 65 Displacement in the Z direction of nodes along a vertical path running from the bottom to the top of one of the Z axis force frame struts.(stage modelled in Super Invar). | Fig. 66 Displacement in the X and Y direction of nodes along a vertical path running from the bottom to the top of one of the Z axis force frame struts. (stage modelled in Super Invar). |
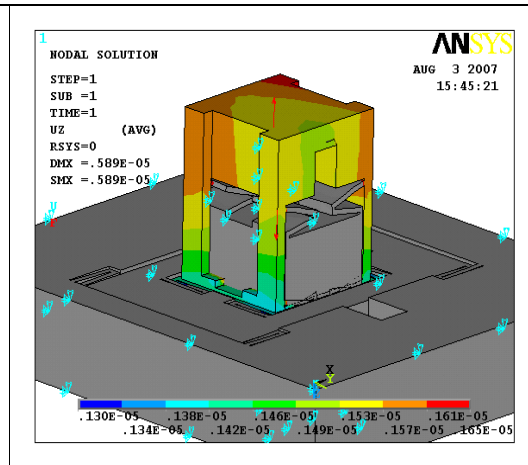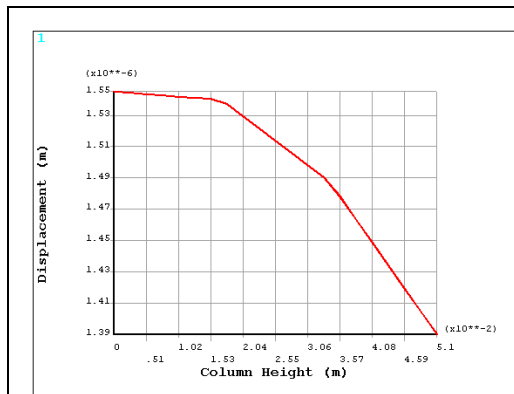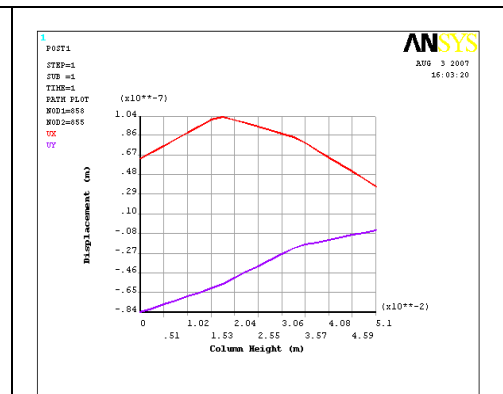
From the definition of Young's modulus

$$E = \frac{\text{stress}}{\text{strain}} = \frac{F/A}{\Delta l/l_0} = k_{strut} \frac{l_0}{A}$$

For a single strut of cross sectional area A and original length l_0 under axial load.

$$k_{strut} = \frac{EA}{l_0} = \frac{4EA}{l_0} \text{ for four identical struts in parallel.}$$

Equ. 31

It can be deduced from Fig. 65 that the FEA predicted combined axial stiffness of the four struts in aluminium is 302 N.μm^{-1} (assuming Young's Modulus for Super Invar to be 145 GN.m^{-2} and that of Aluminium to be 70 GN.m^{-2}). This is considered to be in good agreement with the calculated value of 284.1 N.μm^{-1} as the loading of the struts is not purely axial. This is witnessed by the fact that the struts bend inwards, characterised by displacements in the X and Y directions as shown in Fig. 66.

In a similar manner to that used in relation to the X and Y axes, it can be shown that

$$k_{eq(Z)} = \frac{k_{stage}.k_{RB}.k_{struts}}{k_{RB}k_{struts} + k_{stage}k_{struts} + k_{stage}k_{RB}}$$

Equ. 32

and that the Z axis stage displacement is

$$\sigma_{stage(Z)} = \frac{\delta_{tot}(k_{RB}k_{struts} - k_{stage}k_{RB} - k_{stage}k_{struts})}{(k_{RB}k_{struts} + k_{stage}k_{RB} + k_{stage}k_{struts})}$$

Equ. 33

And that the maximum stress in the Z axis guidance flexures is given by

$$\sigma_{stage(Z)} = \frac{3Ed_{flex}\delta_{tot}(k_{RB}k_{struts} - k_{stage}k_{RB} - k_{stage}k_{struts})}{L_{flex}^2(k_{RB}k_{struts} + k_{stage}k_{RB} + k_{stage}k_{struts})}$$

Equ. 34

And that the apparent stiffness of the Z axis is

$$\text{apparent flexure stiffness (Z)} = k_{app} = \frac{k_{stage}k_{struts}k_{RB}}{k_{RB}k_{struts} - k_{stage}k_{RB} - k_{stage}k_{struts}}$$

<div align="right">Equ. 35</div>

These equations were used in conjunction with the dimensions and material properties of the stage to calculate for each axis; the axis equivalent stiffness, the axis apparent-stiffness, the maximum guidance flexure stress and the expected stage displacement due to a 0.05 mm gap reduction. These values are tabulated in Table 7. Having included the structural deformations in the calculated apparent stiffness values, the values are now closer to those predicted by the FEA method, but the differences are still significant.

	X axis	Y axis	Z axis
Beam depth b_{FB}, b_{RB} (mm)	28.5	28.5	42
Front beam width d_{FB} (mm)	8.3	11.5	N/A
Rear beam width d_{RB} (mm)	13.75	49.32	17.25
Front beam length L_{FB} (mm)	30.74	54	N/A
Rear beam length L_{RB} (mm)	75	107.9	36.5
Strutt cross-sectional area A (m^2)	N/A	N/A	3.145×10^{-5}
Strutt length L_0 (m)	N/A	N/A	31
Front beam stiffness (N.µm^{-1})	308.3 (Equ. 26)	674.9 (Equ. 26)	N/A
Four Strut in parallel axial equivalent stiffness k_{struts} (N.µm^{-1})	N/A	N/A	284.1
Rear beam stiffness k_{RB} (N.µm^{-1})	3048 (Equ. 26)	196.7 (Equ. 26)	4965 (Equ. 26)
Flexure stiffness k_{stage} (N.µm^{-1})	5.98 (Fig. 58)	5.98 (Fig. 58)	5.166 (Fig. 58)
Equivalent stiffness k_{eq} (N.µm^{-1})	5.754 (Equ. 27)	5.855 (Equ. 27)	4.992 (Equ. 32)
Apparent stiffness (N.µm^{-1})	6.224 (Equ. 28)	6.111 (Equ. 28)	5.353(Equ. 35)
Stage offset for a 0.05 mm gap reduction δ_{tot} (mm)	0.0462(Equ. 29)	0.0479 (Equ. 29)	0.0482 (Equ. 33)
Stress σ_{max} (MN.m^{-2})	71.31(Equ. 30)	73.91(Equ. 30)	77.33 (Equ. 34)

Table 7 Stage dimension, calculated actual, equivalent and apparent stiffness, as well as maximum guidance flexure stress due to preloading, when the compliance of force frame structures is factored into the calculations.

NODAL SOLUTION
STEP=1
SUB =1
TIME=1
UZ   (AVG)
RSYS=0
DMX =.838E-05
SMN =-.110E-06
SMX =.192E-06

Contact deformation

-.110E-06   -.426E-07   .246E-07   .917E-07   .159E-06
     -.762E-07   -.901E-08   .581E-07   .125E-06   .192E-06
File: stage 2mm flex
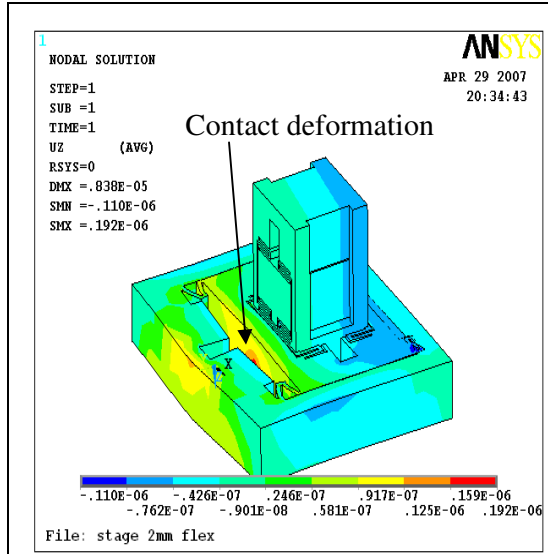
Fig. 67 Deformation arising from the application of the force at a single key point in the model.

It was suspected that the deformation arising from the manner in which the force was applied during FEA modelling could account for much of the discrepancy. This deformation is represented in Fig. 67 by a clearly visible red spot. The approach of applying the load at a single key-point was used because of its speed and convenience as compared to the alternative contact analysis. It had been assumed that this would provide a reasonable approximation to how the piezo force is transmitted to the stage through a small ball.

For proper comparison with the FEA results, the compression of the soft aluminium surface and hard steel ball tip of a piezo actuator at the point of contact must be factored into the equations.

According to Leach [71], the combined compression of both the ball and surface at the point of contact can be calculated from

$$x = \frac{(3\pi)^{2/3}}{2} F^{2/3} (V_1 + V_2)^{2/3} \left(\frac{1}{D}\right)^{1/3}$$

Equ. 36

Where x is the combined elastic compression of the ball and surface, D is the diameter of the ball. V_1 and V_2 can be calculated from

$$V_1 = \frac{1 - v_1}{\pi E_1} \qquad\qquad V_2 = \frac{1 - v_2}{\pi E_2}$$

Where v_1 is the poisson ratios of the aluminium, v_2 is the poisson ratios of the ball steel, E_1 is Young's modulus of the aluminium and E_2 is Young's modulus of the ball steel.

$$k_{ball} = \frac{F}{x} = \cfrac{F}{x = \frac{(3\pi)^{2/3}}{2} F^{2/3} (V_1 + V_2)^{2/3} \left(\frac{1}{D}\right)^{1/3}}$$

<div align="right">Equ. 37</div>

The compression can be regarded as another spring acting in series with the guidance flexure and treated as such. Factoring k_{ball} in Equ. 33 to Equ. 35, gives a more accurate estimate of the design stiffness, stage displacement and stress levels under preload. These values are presented in Table 8.

	X axis	Y axis	Z axis
Stiffness due to ball penetration k_{ball} (N.μm^{-1})	10.43	10.43	10.43
Equivalent stiffness k_{eq} (N.μm^{-1})	3.709(Equ. 27)	3.751 (Equ. 27)	3.411 (Equ. 32)
Apparent stiffness (N.μm^{-1})	15.43 (Equ. 28)	14.75(Equ. 28)	10.64 (Equ. 35)
Stage offset for a 0.05mm gap reduction δ_{tot} (mm)	0.012 (Equ. 29)	0.01272 (Equ. 29)	0.0238 (Equ. 33)
Stress σ_{max} (MN.m^{-2})	18.55 (Equ. 30)	19.62 (Equ. 30)	25.87 (Equ. 34)
FEA predicted stiffness (N.μm^{-1})	10.59	12.21	11.6

Table 8   Calculated actual, equivalent and apparent stiffness, as well as maximum guidance flexure stress due to preloading, when the compliance of force frame structures and the surface contact penetration the of a 4 mm ϕ steel ball is factored into the calculations.

It can be deduced from examining the FEA models (where the piezo action is simulated as two separate forces) that, although the material behind the piezo is deformed and deflected, unlike in the real world situation (where the piezo expands between the front and rear beams), there is no effect on the stage displacement, guidance flexure stress or apparent stiffness of the stage. For this reason, a better comparison with FEA predictions can be achieved by ignoring the rear beam deflection and any contact deformation of that beam in the calculations. This can be effected by replacing k_{RB} by k_{ball} in Equ. 27 to Equ. 35. Calculated values, based on these equations, are tabulated in Table 9.

It can be deduced from Table 9 that there is now better agreement between the values calculated by using the derived equations and the FEA values. The act of comparison has led to improved understanding of the shortcomings of the FEA model used.

	Xaxis	Yaxis	Zaxis
Stiffness due to ball penetration k_{ball} (N.μm^{-1})	10.43	10.43	10.43
Equivalent stiffness k_{eq} (N.μm^{-1})	3.78(Equ. 27)	3.76 (Equ. 27)	5.123 (Equ. 32)
Apparent stiffness (N.μm^{-1})	14.3 (Equ. 28)	14.67(Equ. 28)	10.61 (Equ. 35)
Stage offset for a 0.05mm gap reduction δ_{tot} (mm)	0.0132 (Equ. 29)	0.0128 (Equ. 29)	0.0161 (Equ. 33)
Stress σ_{max} (MN.m^{-2})	20.38 (Equ. 30)	19.74 (Equ. 30)	25.85 (Equ. 34)
FEA predicted stiffness (N.μm^{-1})	10.59	12.21	11.6

Table 9   Calculated actual, equivalent and apparent stiffness, as well as maximum guidance flexure stress due to preloading, when the compliance of force frame structures and the surface contact penetration the of a 4 mm ϕ steel ball is factored into the calculations. (Note: Deformations behind the piezo are ignored so that comparison can be made with FEA findings).

3.8.3   The metrology frame

The purpose of the metrology frame is to provide a support for the stationary interferometer optics and capacitance sensor plates. Fig. 68 is a 3D drawing showing the Abbe principle compliant arrangement of these components and their mounts. The drawing shows three two-pass interferometers (coloured yellow) with additional optional components (grey) required to change these to four-pass configurations. Three capacitor sensor plates are also included with their adjustable mounts.
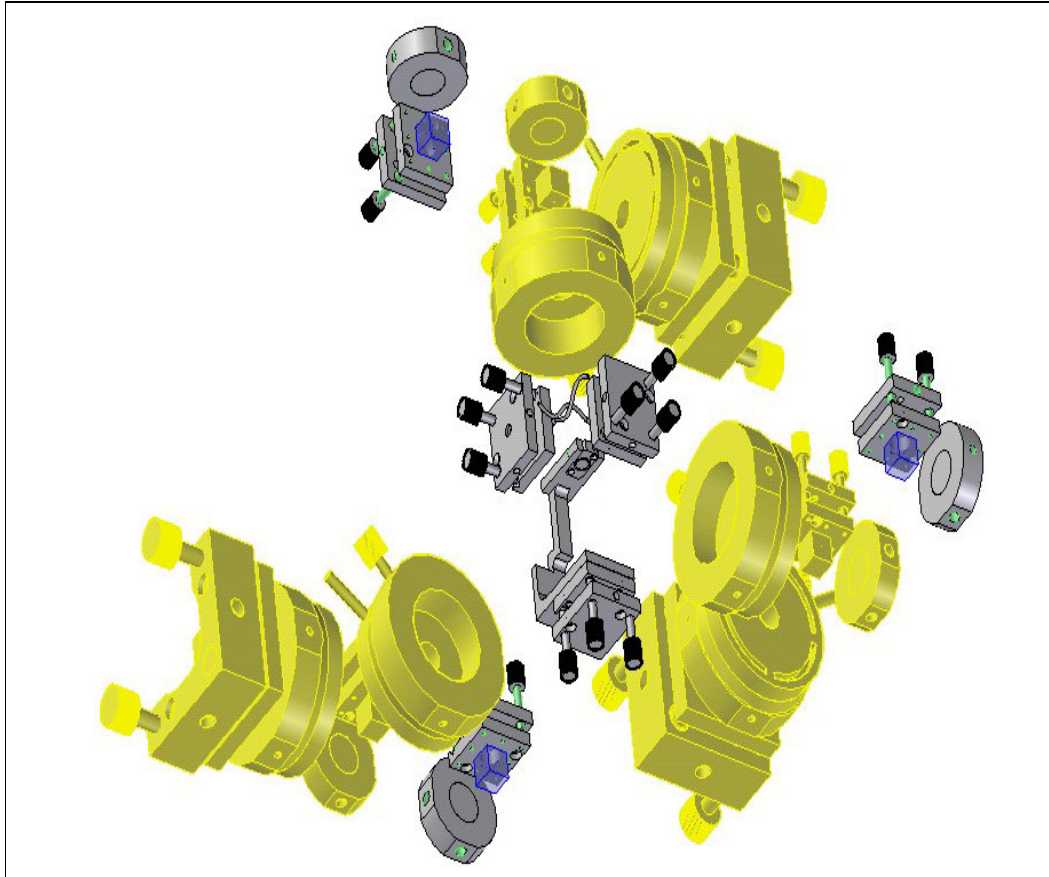
Fig. 68 Metrology components that are mounted on the metrology frame including the stationary components of three Michelson four-pass interferometers and three stationary capacitance plates along with standard adjustable mounts.

The shape of the frame evolved to facilitate the mounting of all these components and to provide high stiffness, high mass, minimum thermal off-axial displacement of components relative to those mounted on the stage and to facilitate adequate access to mount adjustment screws. Also, to minimise deadpath error (described in Section 4.3.2.1), slots are provided that allow the reference beam path lengths to be adjusted so as to equal those of the reference beams. Drawings of the designed frame and the locations of the mounted components are given in Fig. 69.

Isostatic mounting decouples this frame from the support frame expansions and from force frame deformations while at the same time allowing it to thermally expand from the vertical axis coincident with the stage sweet-spot, thus facilitating parallel metrology.

109
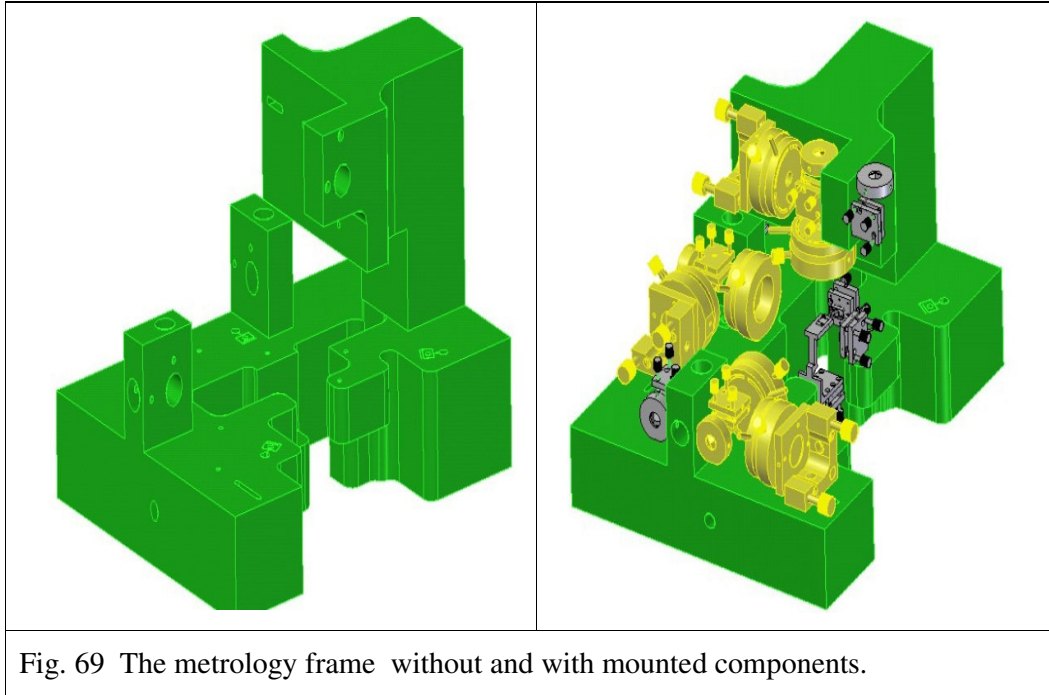
Fig. 69 The metrology frame without and with mounted components.

The frame was designed to be manufactured from a single piece of metal, but after consultation with the manufacturer, Waterford Tools Ltd., the frame was made in two parts (to be subsequently assembled with dowel pins) in order to facilitate affordable machining.

3.8.4   The support frame

This frame supports the metrology frame and stage/force frame (see Fig. 70).   As described in Section 3.7.1, short connecting rods ensure high resonance frequencies of modes dominated by horizontal translations and rotations of the supported frames. Substantial columns are used to keep the distance to each supported frame short. The columns also facilitate equalising this spacing. As explained in Section 3.8.3, equal spacing between the support frame and both the metrology frame and stage is necessary if thermally induced relative vertical displacement of metrology components is to be nulled.

Columns

stage/force frame

Metrology
frame
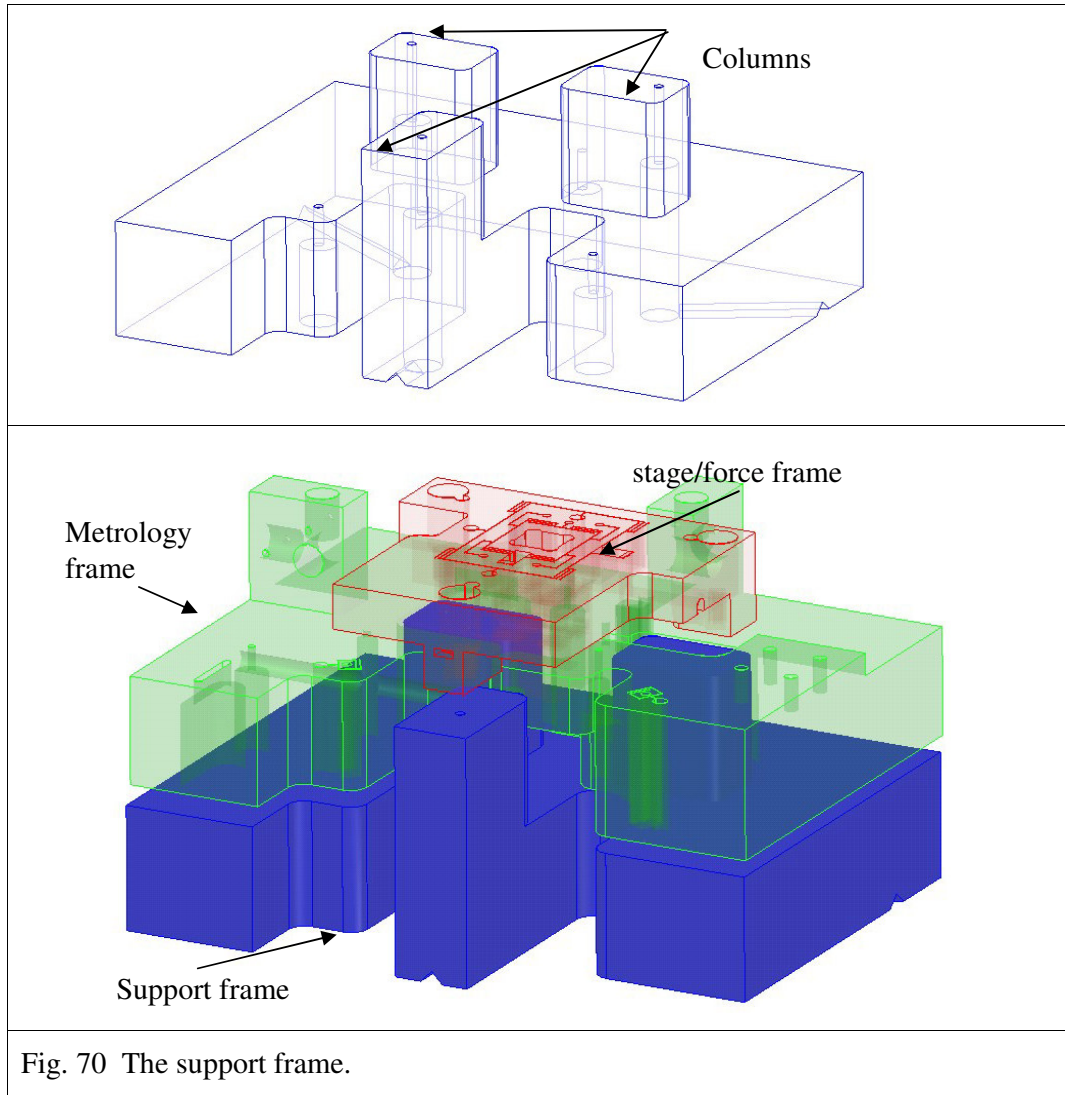
Support frame

Fig. 70 The support frame.

The support frame in turn is kinematically supported on a base plate as described in Section 2.5.5 [37]. Here, ball bearings in V grooves that are orientated at 120^0 to each other (Fig. 71) allow the support frame to expand from a vertical axis coincident with the sweet spot. This arrangement further reduces the displacement of the support pin holes in the support frame relative to those of the stage and metrology frames, thus minimising the coupling stress between structures.

111

Plan

V groove

Ball bearing

Elevation
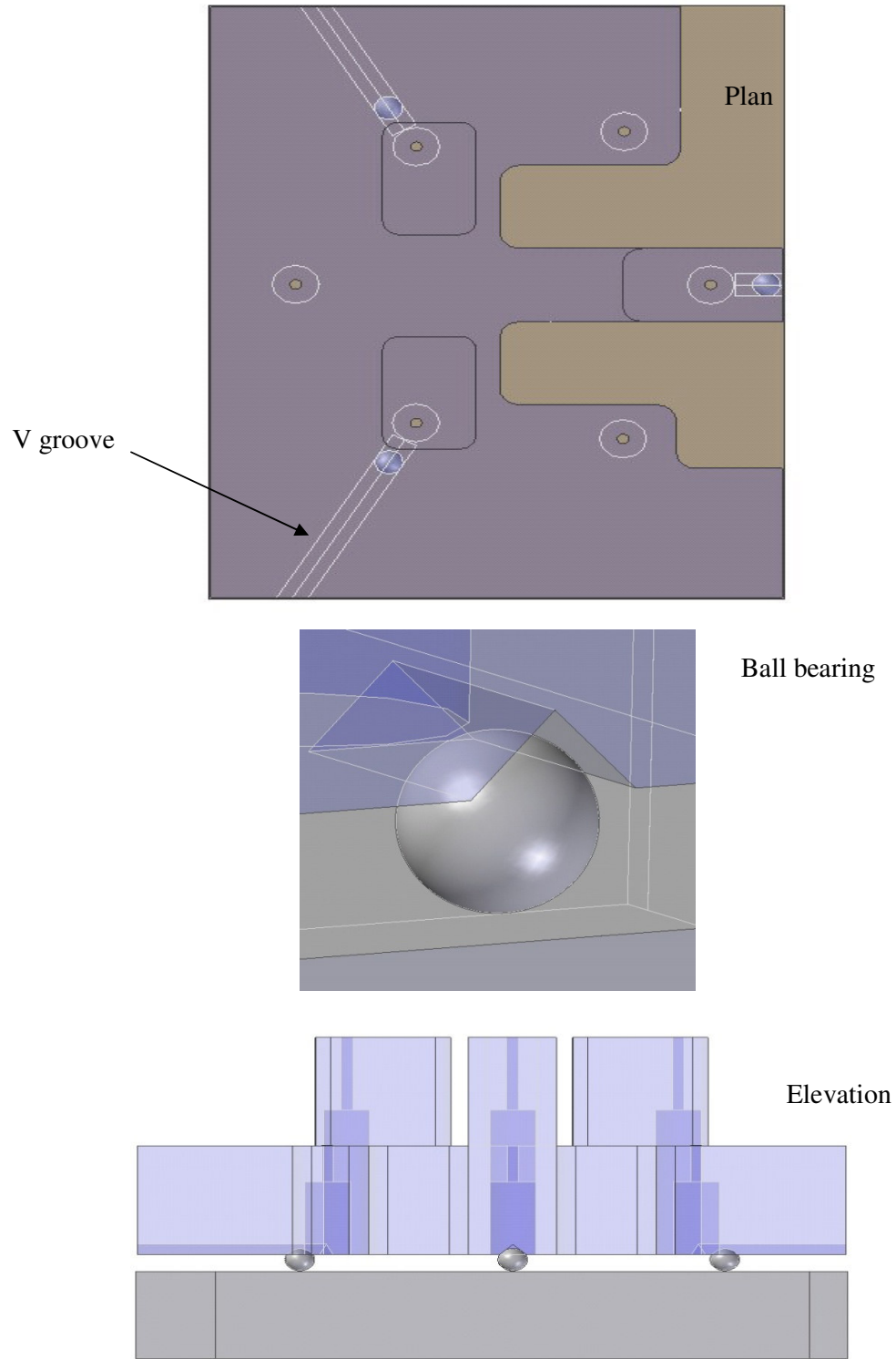
Fig. 71 Kinematic mounting arrangement used with the support plate.

3.8.5   Isostatic optical mounts

Isostatic mounting plates have also been designed to minimise the thermally induced movement of mirrors relative to the measurement axes, decouple stress and to minimise mirror distortion. Fig. 72 illustrates how one of these brackets expands when the temperature rises by a single degree Celsius.
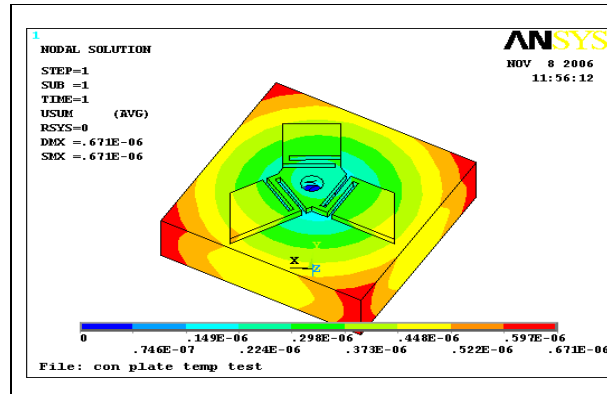
Fig. 72   Thermal expansion pattern of the Isostatic mirror mount design. due to 1 K rise in temperature.

3.9   Overview of the instrument mechanical structures

All the instrument components are to be made from aluminium 6082 T6 so as to avoid thermal mis-match and relative expansions. The low density of aluminium permits an increased resonant frequency and faster response. Calculation and FEA have shown that flexures in this material are suitable for pre-loading plus normal deflection. This material combines a low thermal expansion coefficient and high thermal conductivity which promotes short lived transient thermal gradients, rapid thermal equilibrium and minimal thermal induced stress.
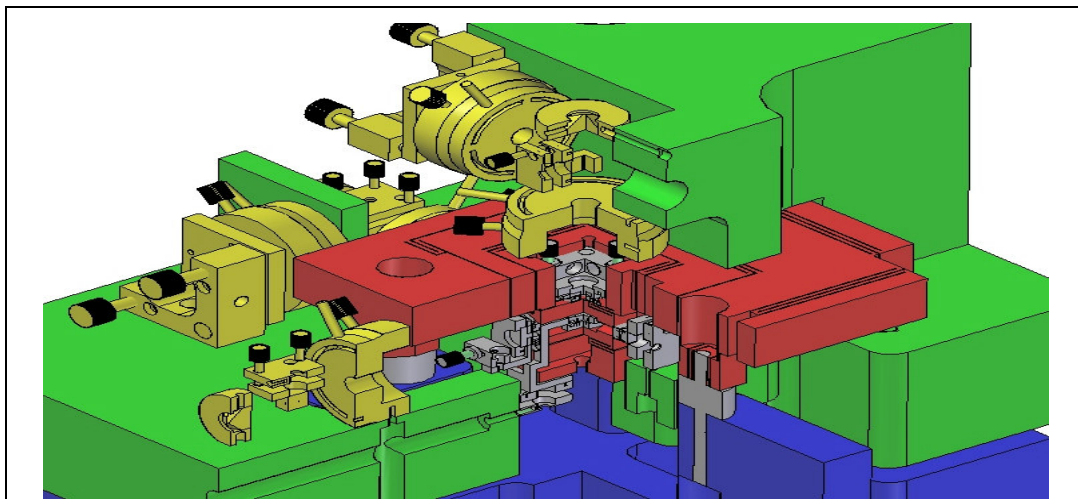
Fig. 73 Cut away view of assembled instrument

113
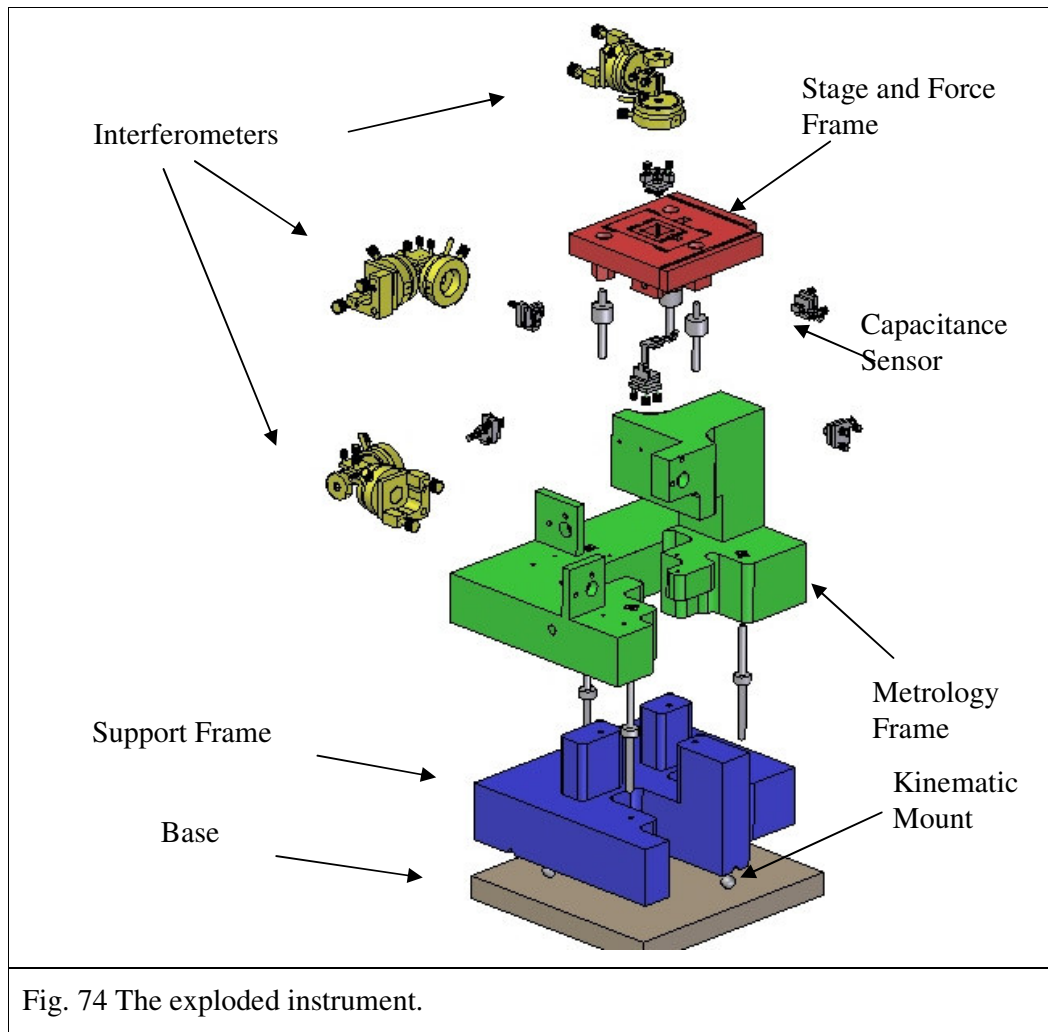
Fig. 74 The exploded instrument.

The stage has three driven orthogonal axes on each of which is mounted the moving monitoring capacitance plates and calibrating interferometer mirrors along with their adjustable mounts. Commercially available mirror mounts are used to provide the flexibility required to achieve measurement axis orthogonality and minimisation of measurement non-linearity due to mirror and capacitance plate tilting.   Additional brackets allow for measurement and movement axis alignment thus minimising Abbe and Cosine errors. Fig. 73 shows a cut away view of assembled instrument. Dedicated flexure design makes possible the essential smooth, linear and repeatable displacement, resilient to off-axial parasitic movements. The flexures connect the stage to the force frame against which the stage actuators push. A single block of material, wire eroded, is used to produce the stage and force frame structure.   The stationary metrology components are all supported on the metrology frame. In order to direct thermal

114

expansions and to minimise coupling stress, the stage/force frame and the metrology frame are each isostatically mounted through short rods onto the support frame that is in turn kinematically mounted on a flat base. Fig. 74 shows an exploded view of the instrument.

The instrument is to be operated within an environmentally controlled vacuum chamber while thermal shielding will be used to avoid hot spots and to reduce thermal gradients.

3.10 Chapter summary

This chapter was concerned with the mechanical structural components of the 3D instrument. The evolution of the stage design was described as well as that of the force frames, the guidance system, the metrology frame, the support frame and the coupling arrangements.

In conclusion, this chapter has presented a design outline of a nano-resolution positioning instrument, flexible enough to allow investigation into positioning error sources and their effects. Static, modal and transient methods of FEA are used in parallel with the theoretical approach, allowing supporting comparison and confirmation. Each of the instruments structural parts is described, outlining the key features that allow the desired functionality to be realised. Given is the theoretical rationale and methodology for calculating guiding flexure dimensions, stroke lengths, stiffness, resonance frequencies and preloads along with plotted calculated data that other researchers may find useful. The contribution to the effective and apparent stage positioning stiffness of actuator ball tip contact surface penetration and the non-rigid behaviour of stage/force frame members is quantified. Presented also is a novel use of isostatic stage mounting that has been shown through FEA to produce a raised 'sweet spot' necessary for maintaining measurement and moving axis alignment.

It must be remembered that the mechanical components form only part of a complex positioning system involving metrology, calibration, positioning control and environmental control.

Chapter 4

4   The Metrology System

4.1   Introduction

The purpose of the metrology system is to facilitate accurate measurement of the stage working point position in 3D space. Robust accurate measurement is a prerequisite to accurate positioning.

The key components of the system are displacement measurement sensors, which are calibrated using a reference measurement system. Data from the displacement sensors forms the feedback for closed loop positioning control. The metrology loops must be considered to also include component mounts and mechanical structural supports. A Cartesian coordinate system is realised by arranging the reference measurement axes normal to each other and by measuring all displacements relative to these axes.

Piezo mounted strain gauge sensors were used on an early single axis prototype stage. For reasons of error minimisation and to facilitate parallel metrology, capacitance sensors are used on the three dimensional positioning instrument developed in this thesis. These displacement sensors are calibrated to reference measurements taken with Michelson interferometers.

This chapter looks at the displacement sensors used, the interferometer reference measurement arrangements, as well as errors associated with each, and the devised set up procedures.

4.2   Displacement sensors

Due to the possible periodic errors and the consequent difficulties with interpolation between interferogram turning points, interferometers are not suitable for real time displacement measurement of a dynamic stage. For this reason small light weight linear sensors such as capacitance or strain gauge sensors were considered for use on the positioning instrument.

4.2.1   Strain gauges

The strain gauges used on the first prototype single axis stage consist of resistive films bonded to the piezo stacks and are arranged as part of a Wheatstone bridge, the output of which is made proportional to displacement. The manufacturer, PI [27] claims a resolution of greater than 1 nm and a bandwidth of 5 kHz. A National Instruments

DAQ card (DAQcard-6024), combined with LabView software [72] was used to both provide control signal inputs to an E610-SO piezo PI controller [27] and to monitor the outputs from the latter. In addition to the convenience of having the factory calibrated strain gauges packaged with the actuator, separate sensor mounts are not required and therefore, the stage size can be kept to a minimum. This allows for a lighter faster stage with less overshoot.

Fig. 75 Open loop piezo hysteresis detected using piezo mounted strain gauges.	Fig. 76 Single axis stage frequency response measured using strain gauge sensors .
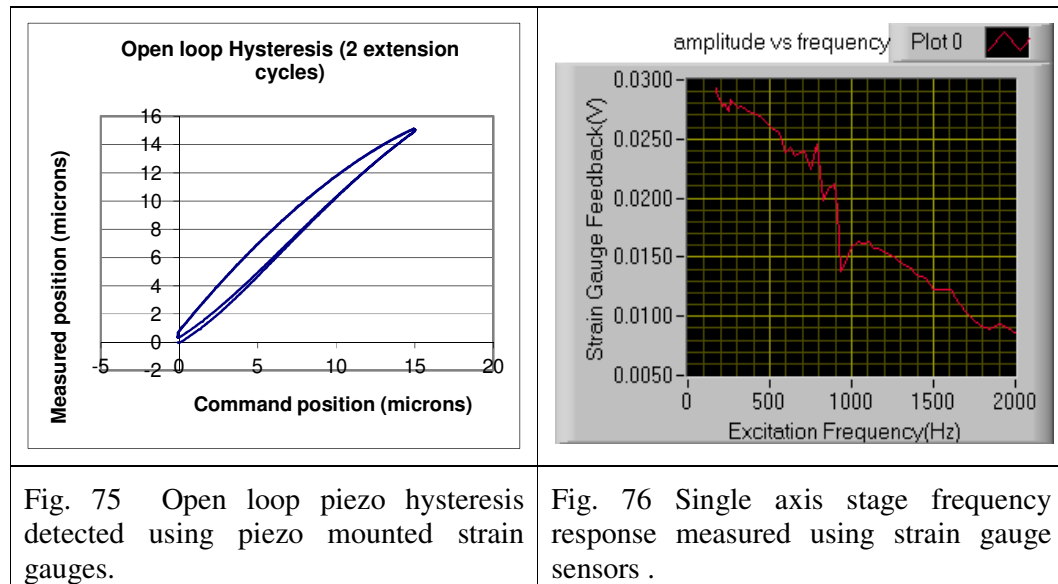
As can be seen in Fig. 75 and Fig. 76 the strain gauge sensors were successfully used to determine the open loop piezo characteristic hysteretic and frequency responses for the stage in question. There are several reasons, though, that they were not regarded as suitable for use with the 3D positioning instrument:

If stage movement were to be measured using actuator mounted strain gauges:

- additional movement arising from thermal expansion of material between the stage point of interest and the sensor would not be accounted for in the measurement;

- reduction in stage travel distance due to elastic deformation at and near the point of actuator/stage contact would not be measured by the sensor, leading to an error (predicted using FEA to be at least 220 nm);

- series metrology only may be performed, i.e. each sensor in a multi-axis system can measure only along a single axis, while the reference plane of one or more

sensors is moved by other axis actuators. Since off-axial parasitic stage displacements cannot be detected with these sensors, relative movements of measuring plains cannot be detected and hence cannot be compensated for; and

- the axis of measurement can only coincide with the movement axis if the axis of actuation coincides with the desired axis of movement. For the designed instrument this is not the case, so the Abbe principle would not be complied with.

All of these problems can be avoided or reduced by using sensors on the stage itself.

4.2.2 Capacitance sensors

Capacitance sensors consist simply of two parallel plates; one plate moves with the stage, while the other remains stationary. The stage displacements, in theory, are then inversely proportional to the change in the sensor impedance or as given in Section 2.6.1 , $V \alpha d$ (Equ. 13).

Unlike the actuator mounted strain gauge sensors, capacitor sensors can be used in parallel metrology systems [27], i.e. when used with multi-axis positioners, each can measure motion relative to a common single fixed position, even though displacements may be caused by several actuators acting along different axes. This means that parasitic cross-axial movements are measured and included in the servo-loop.

Because of their relatively small size, the moving plate can be located close to working point. This means that the unmeasured displacements associated with strain gauge sensors (due to thermal expansion, contact distortions or compressions) can be included in the measurements made using capacitors.

The general advantages of capacitance sensors have already been identified (see Section 2.6.1). The specifics of the design, relating to the three sensors used with the three axis positioning instrument, are presented in this section.

The PI Co [27] manufactured sensor model D-015.00 combined with the E509 servo-control module were chosen as they had specifications, given in Table 10, considered necessary for this application.

	Material: aluminium
	Surface area: 16.6 mm^2
	Nominal measurement distance: 15 μm
	Sensor Thermal drift: 50 ppm.K^{-1}
	Noise Factor: 0.115 $ppm.\,Hz^{-0.5}$
	Bandwidth: 0.3 kHz to 3 kHz
	Temperature drift of electronics: -30 ppm.K^{-1}
	Linearity error: < 0.05 %

Table 10   The Physik Instrumente Co [27] manufactured sensor model D-015.00 dimensions and technical data taken from the PI catalogue

4.2.3   Error sources associated with capacitance sensors

Although capacitance sensors are exceptionally well suited to measuring small displacements, several possible sources of error have been identified (see Section 2.6.1). The significance of these for the particular chosen sensor is examined here.

As will be explained, the first three topics (plate non-parallelism, stray capacitance/edge effects and plate flatness errors) all result in non-linear measurement and hence reduced accuracy. In this section, possible error magnitudes, resulting from each error source, are established for the particular PI manufactured sensor used in this project. Error source specific approaches to reducing non-linearity are also explored here, while the methodology and effectiveness, in this regard, of error mapping is explained in Section 2.7.1.

Furthermore, PI claim that an electronics based 'Integrated Linearization System' can deliver a 0.003 % linearity. This system uses a fourth order polynomial technique to compensate for errors due to stray capacitance, plate tilt and plate flatness. Measurement uncertainty is thus calculated based on the overall 0.003 % stated linearity and not on the values calculated for the individual error sources.

Plate non-parallelism

The following expression [37] is used to calculate the capacitance of a two plate sensor subjected to tilt.

$$C = \frac{2\varepsilon_r\varepsilon_0 A}{d}\left(\frac{1}{1 + \sqrt{1 - k^2}}\right)$$

<div align="right">Equ. 38</div>

when

$$k = \frac{r.\sin(2\theta)}{2d}$$

<div align="right">Equ. 39</div>

θ is the angle of tilt between the plates, r is the radius of the circular plates, ε_0 is Permitivity of free space ($= electric\ flux\ density/electric\ field\ strength = $ 8.85419 pF.m^{-1}), ε_r is the Relative Permitivity in medium ($= 1.006$ for air), d is the gap width between plates (m), A is the Plate area (m^2) and C is the Capacitance (Farads).

As can be seen in Table 10, the sensor has a surface area of 16.6 mm^2 and a nominal measurement distance of 15 µm. The calculated capacitance along with the reactance (the measure of opposition to alternating current) were plotted in Fig. 77 over the full measurement range for an assumed tilt angle of 1 mRad.
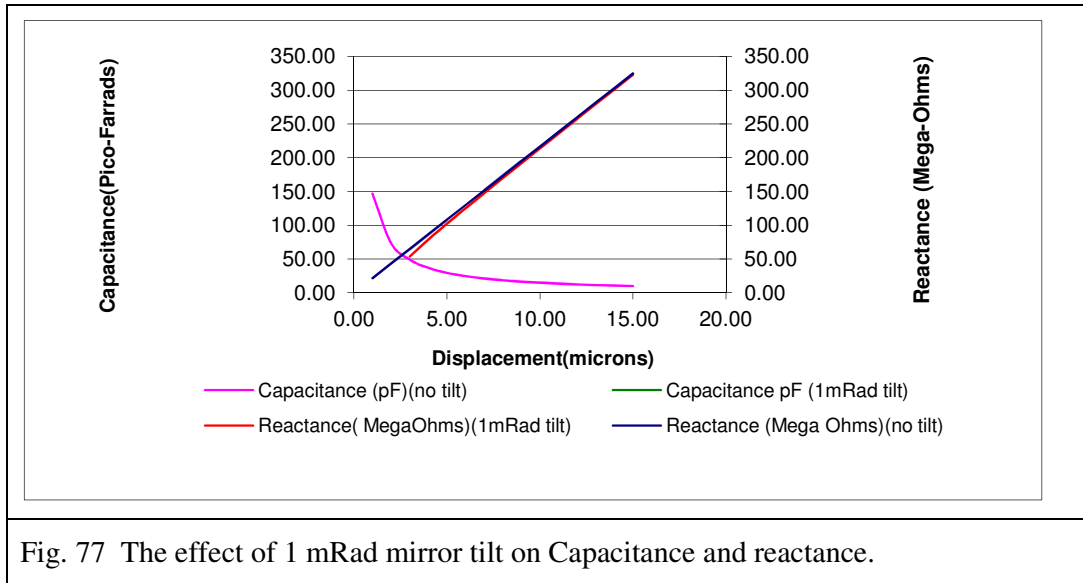
Fig. 77 The effect of 1 mRad mirror tilt on Capacitance and reactance.

With no tilt, the reactance varies linearly with displacement (ignoring other sources of non linearity such as stray capacitance etc.). As can be seen from Fig. 77, tilt causes capacitance and reactance to deviate from the values expected when the plates are parallel. The smaller the gap size, the greater the reactance deviation. At actual displacement 3 μm, the deviation is as much as 4.55 % which translates to a measurement difference of 136.5 nm.

If interferometers are used to calibrate the capacitance sensors, non-linearity errors can be minimised. Of concern then is the non-linearity of measurement between points of calibration (39.55 nm apart if calibration is done for instance using a four-pass interferometer with a laser of wavelength 632.8 nm and only peaks and troughs are counted).

| Fig. 78 Residuals due to 1 mRad tilt. | Fig. 79 The effect of tilt angle on residuals. |
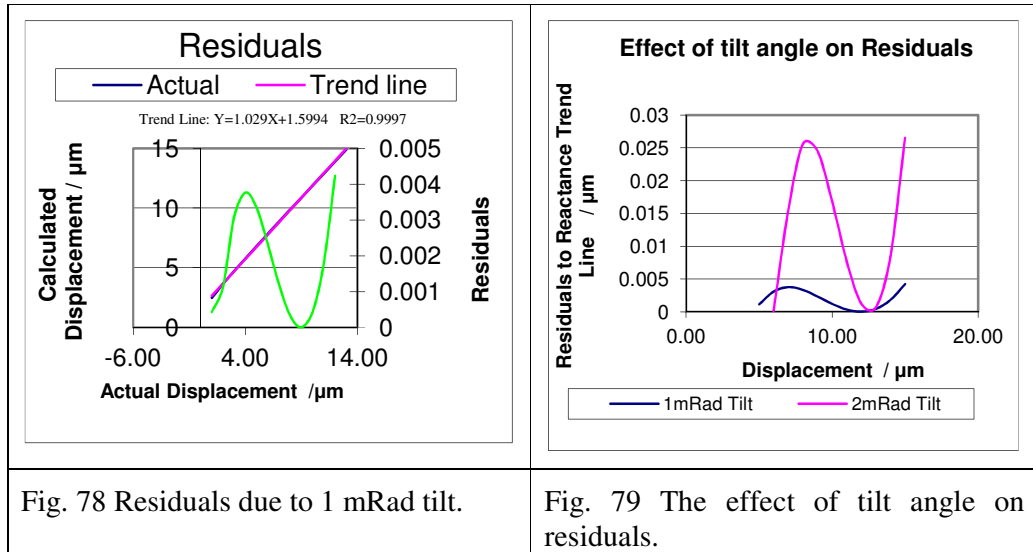
The graph in Fig. 78 shows reactance due to a 1 mRad tilt when the gap size varies over the full range. A best fit trend line was calculated using linear regression. Also plotted are the residuals. Linearity, (defined as half the peak to peak value of the residuals expressed as a percentage of the full range [37]) can be calculated from Fig. 78 to be 0.035 %. Thus a ± 5.2 nm uncertainty exists for a 15 μm stage travel. Using a four pass interferometer, calibration points can be obtained at 39.55 nm intervals. A 0.035 % linearity uncertainty would translate into a ± 0.01 nm measurement uncertainty.

As the tilt angle increases, so does the non linearity of the sensor signal. This is shown in Fig. 79. For a tilt angle of 2 mRads the non linearity increases to 0.08 %, giving a measurement uncertainty of ± 12.5 nm over the entire range or 0.03 nm using the four pass interferometer.

The measurable phenomenon of non-linearity itself can be used to reduce mirror tilt through repeated experimentation and adjustment. Its effects can be significantly reduced through interferometer calibration, the use of error mapping techniques and the PI electronics based 'Integrated Linearization System'.

Stray capacitance and edge effects

This can result from unshielded wiring and edge effects such as plate size differences or coupling with the backs of plates. Stray capacitance effectively manifests as capacitance in parallel with the capacitive sensor. Small amounts of stray capacitance can give rise to high levels of non linearity. Hicks et al [37] claim that a 75 fF stray capacitance resulting from edge effects caused a 0.1 % non linearity in a 100 μm range 10 pF capacitor sensor.

Plate flatness

Plate deviation from flatness may occur as a result of errors in manufacture or from bending of the plates due to stresses induced by incorrect mounting or thermal gradients. Irregularities in flatness can lead to non- linearity in the output of a sensor. Hick and Atherton [37] give the following expression for calculating the capacitance of a bowed capacitor plate

$$C = 2\pi\varepsilon_r\varepsilon_0 \left\{ d_{bow} - (d_0 + R)\ln\left(1 - \frac{d_{bow}}{d_0}\right) \right\}$$

Equ. 40

where $\quad d_{bow} = R - \sqrt{R^2 - r^2}$

r is the radius of the capacitor, R is the radius of the bow, d_0 is the nominal gap size, and d_{bow} is the height of bow above edges.

Unfortunately, in the case of the capacitive sensor which is to be used in this project, the radii of any plate bows present are not known. The drawing in Table 10, though, indicates a maximum deviation in inter-plate distance of 0.005 mm for a perfectly mounted capacitor. Assuming a value of 0.005 mm
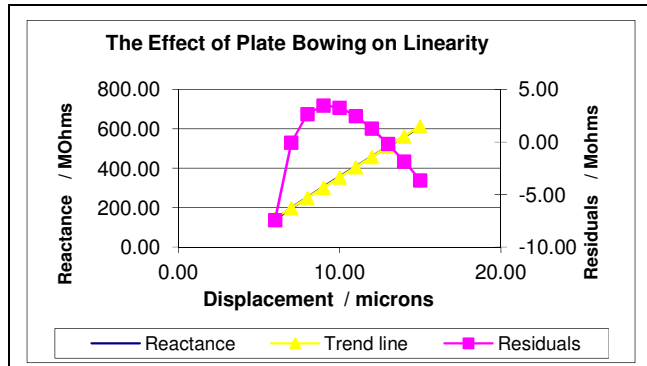
Fig. 80 The predicted effect of plate bowing on the PI D-015 capacitance sensor based on Equ. 40.

for d_0, R is calculated to be 230.0025 mm through basic geometry. The capacitance, reactance and linearity were calculated for an inter-plate gap ranging from 5 ɥm to 15 ɥm. Based on the calculated residuals as plotted in Fig. 80, the linearity is found to be 1.17 %. This translates to a possible displacement measurement error of 175 nm.

In reality, the bowing may vary with thermal gradient induced stress and mounting stresses. It is also unlikely that only one of the plates would exhibit a single bow profile across its full diameter. It is more likely that both plates would be warped in a more complex manner especially if mounting forces are culpable. The type of bowing suggested by Hicks et al. [37] is more likely to result from systematic manufacturing errors. In point of fact, the degree of non-linearity due to variation in plate flatness must be measured experimentally.

With reference to non-linearity resulting from plate distortion, the D-015 sensor has several advantages.

- It is made from aluminium, which has the same coefficient of thermal expansion as the instrument structures, thus avoiding buckling stresses arising from unequal relative thermal expansions.

- The measuring surfaces are diamond tool machined to a claimed ultra-flat mirrored surface [27].

- The Integrated Linearization System reduces non-linearity from this source.

<u>Noise</u>

Sensor signal noise gives rise to measurement uncertainty which is quantified in Section 6.2.

- Electronic noise

The PI manufactured model D-015.00 capacitive sensor is used with the servo controller E-509.C3A which supplies ± 5 V to the sensor with a selectable bandwidth of 0.3 to 3 kHz and a noise factor of $0.115 \, ppm. \, Hz^{-0.5}$. If, for instance, the sensor is used with a 2 kHz bandwidth, the true noise displacement is

$$15 \times 10^{-6} \times 0.115 \times 10^{-6} \times \sqrt{2 \times 10^{-3}} = 0.01 \, nm.$$

To keep this displacement to less than 1 nm the bandwidth must be below 336 kHz.

- Mains pickup noise

Presented in Fig. 81 are the power spectra of the background noise picked up on the sensor wires. The spikes due to mains pickup at 50 Hz and harmonics at 100 Hz and 150 Hz are clearly evident. Spikes at higher frequencies are due to unknown sources, but it is suspected that these may include power supplies.
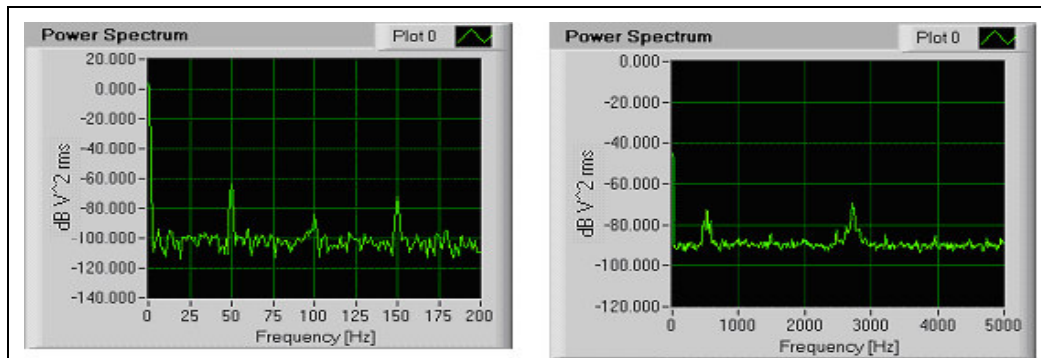
Fig. 81   Background electrical noise spectra with spikes indicating the presence of mains pickup at 50 Hz and harmonics at 100 Hz and 150 Hz.

- Quantisation noise

As explained in Section2.4.4.1, quantisation noise refers to the uncertainty in a signal resulting from the fact that a finite number of controller bits are used to represent it. According to Hicks et al. [37], the rms value of this measurement noise is given by

$$\text{Quantisation noise} = \frac{0.29 d_x}{2^N}$$

<div align="right">Equ. 41</div>

where d_x is the maximum measurement range and N is the number of bits.

A PI manufactured E-509 [27] 16 bit controller, combined with the National Instruments 16 bit data acquisition card 6036E [72] were chosen for the 3D instrument. This controller, combined with a 15 μm range actuator results in a standard measurement uncertainty due to quantisation noise of 0.07 nm.

Thermal Expansion

As described in Section 2.4.1.2 , the aluminium ($CTE = 23.4 \times 10^{-6} K^{-1}$) sensor D-015 (plate area of 16.6 mm^2) would be expected to increase its capacity by 0.0047 % per 1 K increase in temperature due solely to increased plate area. This gives rise to a possible 0.7 nm measurement error per K for the sensor nominal range of 15 μm.

The plates and their mounts have the same coefficients of thermal expansion as the instrument supporting structures, thus the expansions of the sensors along their axes of measurement are nulled within their measurement loop. Any structures between the sensor and the plane of the point of interest are also subject to thermal expansion, which is not detectable by the sensor. It is, therefore, important to locate the capacitor as close as possible to this point; uncertainties associated with these offsets are discussed in Section 6.2.

The effect of environmental variability on relative permittivity

By rearranging Equ. 12, the gap size d being measured, can be seen to be proportional to the relative permittivity (ε_r) of the air between the plates.

$$d = \frac{\varepsilon_0 \varepsilon_r A}{C}$$

Relative permittivity is calculated as 1.00832 when using the following formula presented by Hicks et al. [37]

$$(\varepsilon_r - 1) \times 10^6 = \frac{1553.9}{T} P_1 + \frac{2663.6}{T} P_2 + \frac{1295.3}{T} \left(1 + \frac{5748}{T}\right) P_3$$

<div align="right">Equ. 42</div>

where

T = temperature (300 K)

P_1=Partial pressure of CO_2 in free dry air =101.3 kPa

P_2= Partial pressure of CO_2 = 0.035 kPa

P_3= Partial pressure of water Vapour = 3.5667 kPa at 100 % relative humidity and 295 K.

Any change in temperature, pressure or humidity effects ε_r and consequently the accuracy of the measurement. Software compensation for the effects of environmental variation is described in Section 5.2.5.1, while associated uncertainties are quantified in Section 6.2.

Having examined the displacement measuring system, the next section is concerned with the referenced measurement system used for its calibration.

4.3   Reference measurement

As established in the literature (Section 2.6.2), Michelson laser interferometers are commonly used to calibrate displacement sensor systems for several recognised reasons: their measurements are inherently traceable to international standards; they are capable of high resolution; their axes can be made to coincide with the displacement axes of the point of interest, allowing compliance with the Abbe principle; measurement is achieved without contact.

Three configurations of Michelson interferometers, used by different researchers [37][26][25], are identified: these are single pass, two pass and four pass. As is outlined in Section 2.6.2, the two and four pass versions use polarising optics to cause the light beams to be reflected more than once from the moving mirror so that the measurement resolution is doubled and quadrupled respectively. The 3D positioning instrument designed for this thesis incorporates a mounting structure which allows the use of any of these configurations.

The positional accuracy of the instrument relies ultimately on the accuracy of this reference metrology system since this is used to calibrate the measurement system on which closed loop control is dependant. Some environmental, set-up and inherent error sources have been recognised in Section 2.3. In this section, the effects of each of these sources are examined and quantified, but first, the paths of the laser beam through the optics of each arrangement is explained.

4.3.1 Michelson interferometer configurations

Three Michelson interferometer configurations are described in Section 2.6.2.1, a single pass arrangement presented by Hicks et al. [37], a two pass system presented by Ruijl [26] and a four pass system, based on a system described by McCarthy et al. [9].
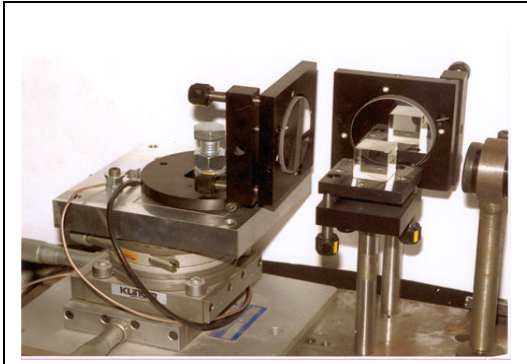
Fig. 82 The single axis prototype with mirrors, beam splitter and laser of the single pass interferometer

The basic single-pass configuration was used on the prototype single axis stage.

By counting the number of fringes (N) of the interference pattern illuminating the sensor, the moving mirror displacement was calculated using the formula

$$\Delta d = N \left(\frac{\lambda}{2} \right)$$

Equ. 43

This interferometer was successfully used to measure the stage displacement, flexure stiffness, frictional effects (Fig. 83) and the hysteretic behaviour of the piezo actuator (Fig. 84).
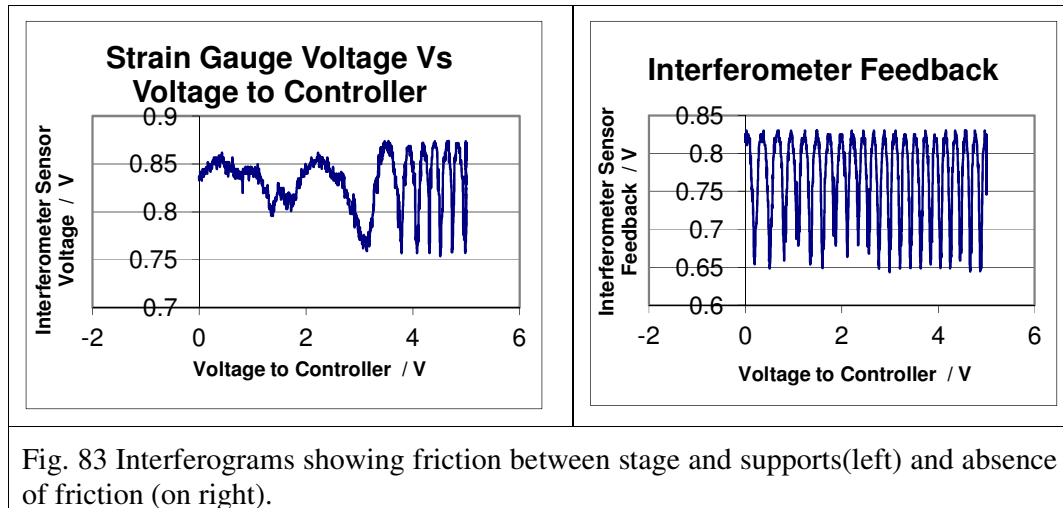
Fig. 83 Interferograms showing friction between stage and supports(left) and absence of friction (on right).
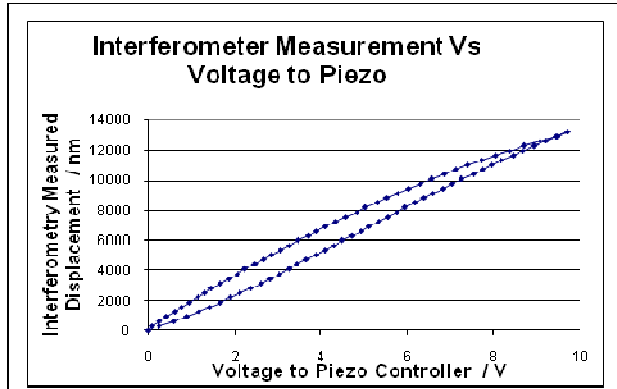
Fig. 84 presents the interferometer measured piezo hysteresis. The stage was driven through a single extension/retraction cycle and a LabView program was used to count the peaks and troughs of an interferogram to calculate the distance displaced using Equ. 43 .

Fig. 84 Interferometer measured piezo hysteresis.

The two and four pass configurations
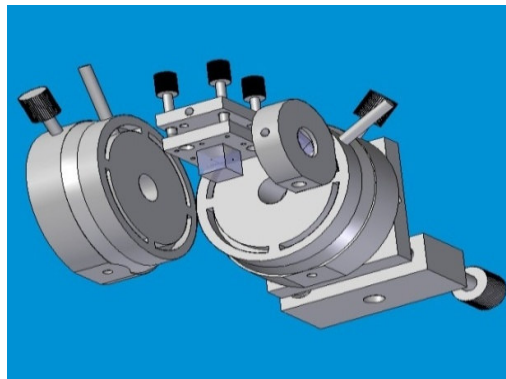
Fig. 85 Physical arrangement of a two pass Michelson interferometer stationary components with Melles Griot [38] manufactured standard optical mounts.
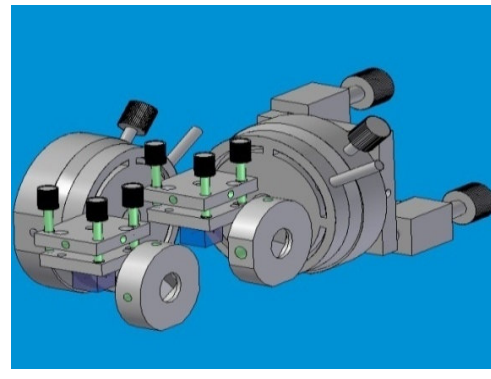
Fig. 86 Physical arrangement of a four pass Michelson interferometer stationary components with Melles Griot [38] manufactured standard optical mounts.

Fig. 85 and Fig. 86 show the mechanical mounting arrangement of the stationary components used to implement both the two and the four pass interferometers. Because of the similarities between both arrangements, it was possible to design the metrology frame to accommodate both.

4.3.2   Interferometer error sources

The accuracy of interferometer measurement can be degraded in numerous ways, many of which have been identified in Section 2.3.

The effect on the wavelength of laser light

It has been established in Section 2.4.1.2 (see Table 1) that the effect of variability in the wavelength of interferometer laser light on short range displacement measurement, resulting from environmental changes, is negligible. Nevertheless, the uncertainty of measurement, due to environmentally induced changes to the wavelength of the He-Ne laser light, is investigation and quantified in Section 6.3.1.

Expansion of mirror substrates

The expansion of interferometer mirror substrates can cause variations in the relative geometric optical path lengths. It was necessary to choose between purchasing mirrors with substrates made of aluminium (the same material as the instrument structural components) and Zerodur (having a very low thermal expansion coefficient of $\pm 0.15 \times 10^{-6}$ K^{-1}). Calculations indicated that low CTE mirror substrate material may actually introduce errors in some measuring arrangements where the supporting structures are made from material with a high CTE such as aluminium. It was found that the substrate should be chosen based on how the mirror is to be used.   Because of the particular interferometer optical arrangement designed for the thesis, Zerodur is the optimum choice in this instance.

Deadpath error
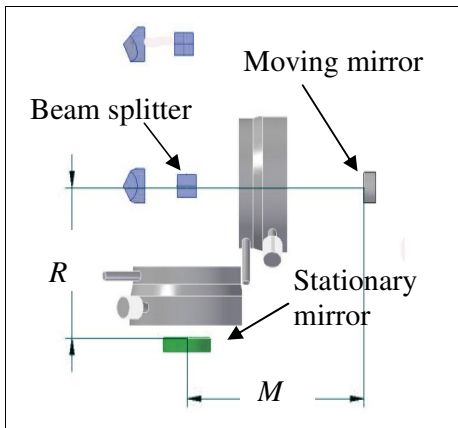
Fig. 87   Plan view of the X axis interferometer   components Deadpath length is the difference between lengths *M* and *R*.

Deadpath is described by Castro [41] as the difference in optical path length of the measurement and reference components of laser beam at the home location.   Since the instrument interferometers are structured so that the reference and measurement beams travel identical distances though the optical components, the deadpath (see Fig. 87) can be taken to be:

$$\text{deadpath} = M - R$$

Equ. 44

Any expansion which cause the deadpath distance to change would give rise to relative phase shifts between the component laser beams, thus giving rise to measurement error if uncompensated. The provision of slots on the metrology frame provides adequate flexibility so that the distances *R* and *M* can be made equal. In theory this means that deadpath error should not occur, but in reality measurement uncertainty occurs examined and quantified in Section 6.3.1.

As explained in Section 2.4.1.2, the thermal expansion of optical components can cause relative phase shifts between measurement and reference beams if the beams do not travel identical distances through media of identical refractive index. This can then be misinterpreted as stage movement. The following expression has been derived to facilitate calculation of the error

$$\text{measurement error} = \frac{1}{2}\{n|t_{ref} - t_{measure}|\alpha.\varDelta T\}$$

<div align="right">Equ. 45</div>

n is the refractive index of plate sandwich; t_{ref} is the thickness of refrence quarter wave plate; $t_{measure}$ is the thickness of measurement quarter wave plate; α is the coefficient of thermal expansion of glass; and $\varDelta T$ is the the change in ambient temperature.

If the temperature is kept constant, or if it arranged so that the optical path for each beam is identical through each media, then this problem does not arise. Using Equ. 45, it can be calculated that to keep the error below 1 nm for a temperature rise of 1K, the geometric path difference in glass must be less than 0.18 mm.

The interferometer configurations chosen for the 3D precision positioning instrument ensure that the reference and measurement beams travel through the same thickness of glass so that measurement error due to the expansion of optical components is minimised. Uncertainties associated with this error are quantified in Section 6.3.1.

4.3.2.2   Set-up errors

<u>Tilting of mirrors</u>

It has been established in Section 2.4.2.1 that measurement errors result if interferometer mirrors are not normal to each other. To improve understanding and to

further explore the effects of mirror tilt on measurement, a trigonometric expression based on Ruijl's Equ. 5 [26] and Fig. 5 is derived in Appendix B 1.

$$\text{measured translation} = \frac{x}{2}(2 + \sin\alpha\tan\alpha)$$

Equ. 46

Where x is the actual displacement and α is the angle of tilt.

Equ. 46 allows the measured translation to be calculated for given actual translation and angle of tilt. If the mirror is not tilted ($\alpha = 0$), then the measured translation equals the actual translation.

It can be deduced from Equ. 46 that a scale error of magnitude $1 + \frac{1}{2}\sin\alpha\tan\alpha$ is introduced for a given angle of mirror tilt ($\times$ 1.000152316 for a 1^0 angle of tilt). An actual translation of 15 μm would be measured as 15.00228 μm (an error of 2.28 nm) if the mirror is tilted by 1^0.

When mirror tilt is combined with irregularities of optical component reflective surfaces may result in measurement uncertainty. This is examined in greater detail in Section 6.3.2.

4.4 Mounting arrangement

Both the displacement and the reference measurement systems are arranged so as to comply with important principles, namely: the Abbe principle; correct location of sensors; adequate mount flexibility; adequate mount stiffness; low component mass; and high orthogonality.

- The Abbe principle i.e. the measurement axes should coincide with the axes of movement.

By adopting this principle, both cosine and Abbe type errors are minimised. The mechanisms of these errors are explained in Section 2.4.3.4, along with equations for calculating their magnitudes (Equ. 4 and Equ. 5).

In an effort to realise the significance of this error, the effect on cosine error of axis misalignment angles for given stage displacements is plotted in Fig. 88. Cosine error is

132

shown to increase in a non-linear fashion with relative rotation of the axes. The error is seen to be greater at longer displacements.

 Fig 89, on the other hand, looks at the effect of displacement on cosine error for given angles of axis misalignment. It can be deduced from the graph that, for a given angle, the error is directly proportional to the measured displacement.

Fig. 88 The effect of axis misalignment angle on cosine error for given stage displacements.	Fig 89 The effect of displacement on cosine error for given angles of measurement axis misalignment.
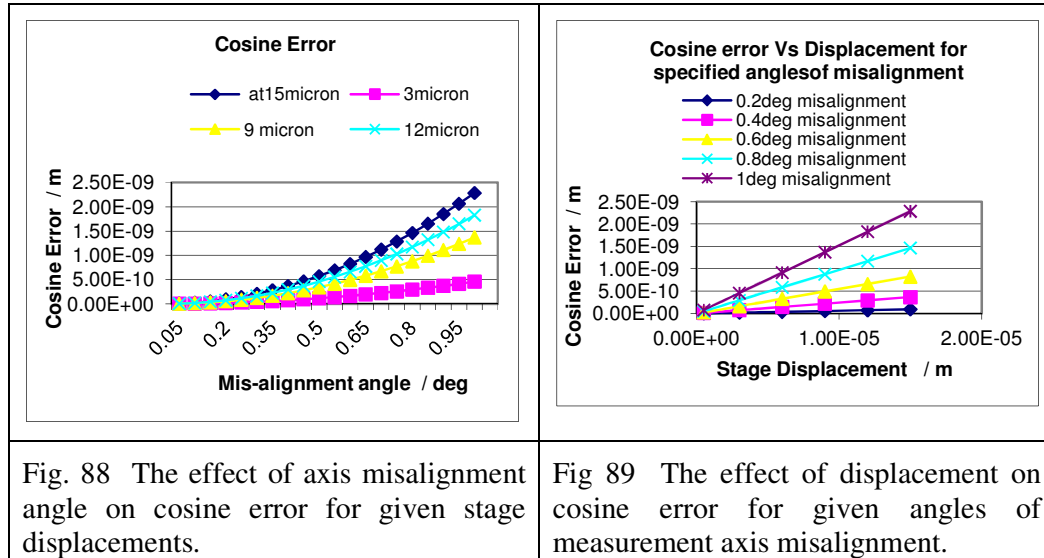
Cosine error is not regarded as being a serious problem. Measurable misalignment angles are required to cause significant measurement errors. As large a misalignment as 1^0 gives rise to a Cosine error < 2.5 nm for a stage displacement of 15 μm. The misalignment angle needs only to be < 0.65^0, for the error to be kept smaller than 1 nm (see Fig 89).

Abbe error has serious implications, however, especially for situations where stage layout dictates working at locations distant from measurement axes.   Locating a specimen work point a distance 1 cm from the measurement axis would produce an Abbe error of 174.5 nm for a parasitic rotation of as little as 0.001^0.   In fact if the Abbe error is to be kept to within 1 nm for a stage where the maximum angular rotation is 0.001^0, then the maximum offset must be less than 58 μm.

Much of the design effort in this project has been directed to ensuring that the measurement axes coincide as far as possible with the displacement axes of the 3D instrument.
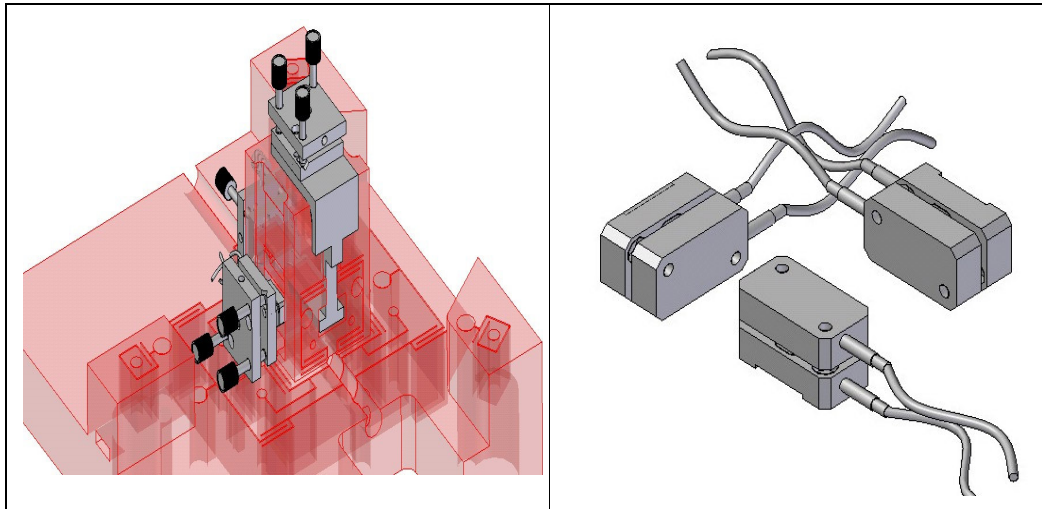
Fig. 90 The mounting arrangement and orientation of the capacitance sensors

The assembly drawings given in Fig. 90 show how the capacitance sensors are orientated so that their measurement axes are normal to each other and coincide at a single point. Fig. 91 illustrates how the interferometers are similarly arranged.
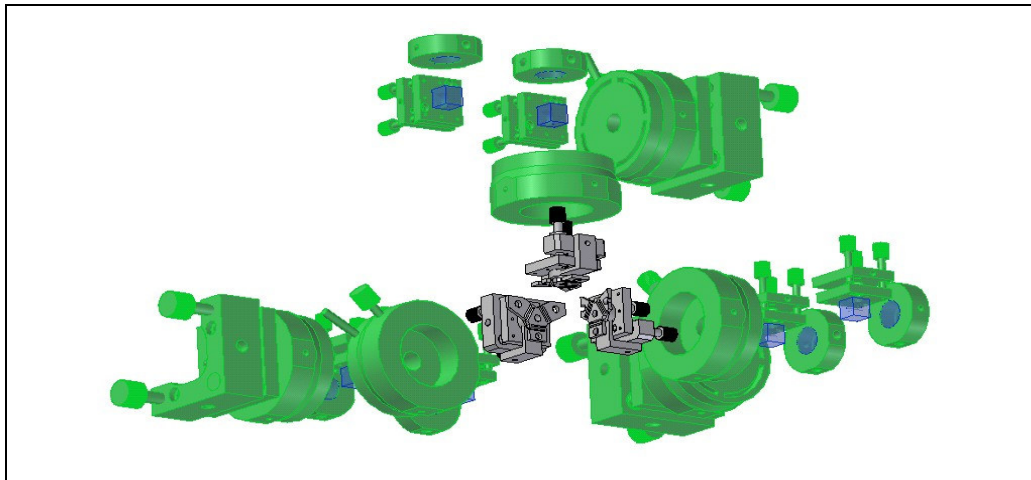
Fig. 91 Mounting arrangement and orientation of the three four pass interferometers

- The sensors should be positioned as close as possible to the point of interest.

As is explained in Section 4.2.1, when the sensor is placed at a distance from the point of interest, the sensor is not measuring the displacement of the point, but is measuring something else e.g. the expansion of the piezo. Various phenomena, such as thermal

expansion, structural deformations, or parasitic translations or rotations may cause the point of interest to be displaced differently than the point, the displacement of which is actually being measured. Because this difference is not measured, it cannot be accurately compensated for.
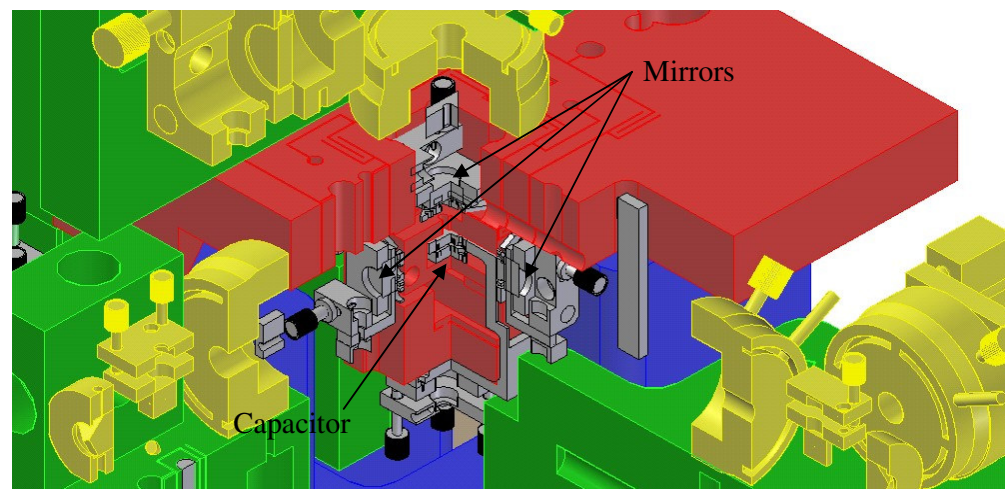
Fig. 92 Cut-away of instrument.
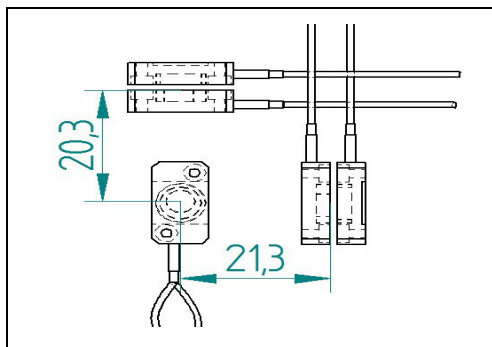
Fig. 93 Offset of X and Y capacitance sensors from the point of interest.

The instrument is designed so that all the sensors are placed as close to the XYZ centre of the stage as possible. Dimensionally small mirrors, capacitor plates and flexible mounts have been chosen for this purpose. Nevertheless, the space requirement of these components and the guidance system structural members necessitates a distance between the point of interest and the sensor positions. The cut-away section drawing of the instrument, given in Fig. 92, serves to illustrate how the metrology system components are arranged so as to balance the conflicting requirements for space, flexibility and proximity.

The resulting actual offsets of the capacitance sensors from the point of interest are shown in Fig. 93. The Z axis capacitor is at the point of interest, while the X and Y axes sensors are respectively 21.3 mm and 20.3 mm distant from it. Similarly, the offsets between the stage mounted interferometer mirrors and the point of interest is

135

given for each axis in Fig. 94 and Fig. 95. Uncertainty in position measurement is inevitable due to these unavoidable compromises.

| Fig. 94   Spacing of optical components in the Y and Z axes interferometers. (all measurements given in millimetres) | Fig. 95   Spacing of optical components in the Y and X axes interferometers. (all measurements given in millimetres) |
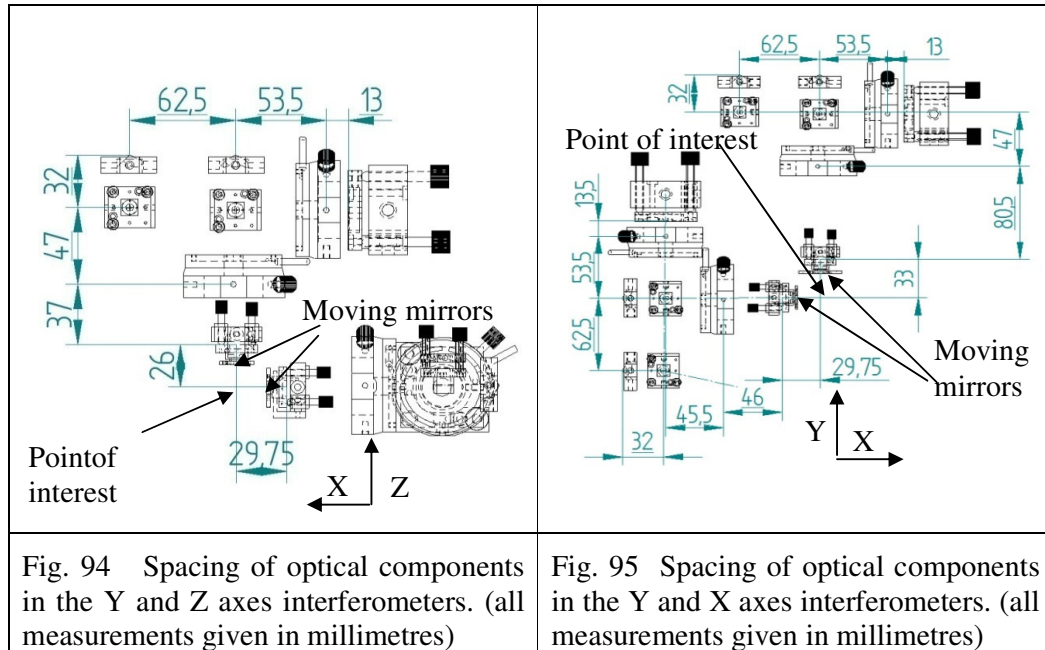
The thermal expansion of the aluminium structures lying between the point of interest and the X axis sensor, for example, is as much as 511.2 nm.K^{-1}.   Knowledge of expansions allows compensation to be implemented through the software (see Section 5.2.5.1), but uncertainty arising from component uncertainties in thermal coefficients, offset distance measurement and temperature measurement cannot be compensated, but are quantified in Section 6.3.2.

- Flexibility

As outlined in Sections 4.2.2 and 4.3.2.2, misalignments can result in measurement non-linearity and scale errors. For the components of the measurement system flexibility in adjustment is seen as necessary to affect proper alignment.   Adjustability also enables physical experimentation to be performed into the effects of misalignments.
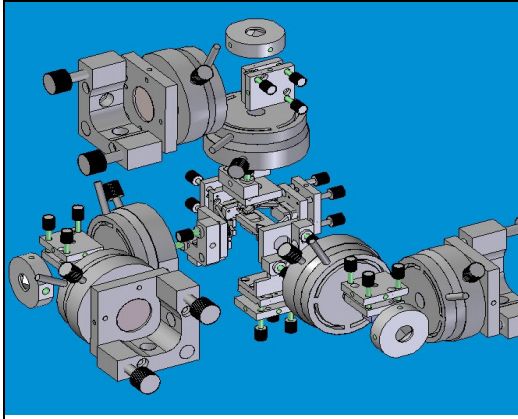
| Fig. 96 Interferometers and capacitance sensor arrangement using standard Melles Griot Inc.[38] optical mounts. | Fig. 97 Thermal expansion pattern of the Isostatic mirror mount design due to 1 K rise in temperature. |
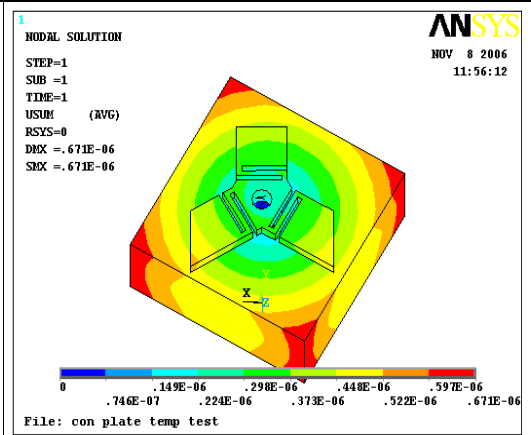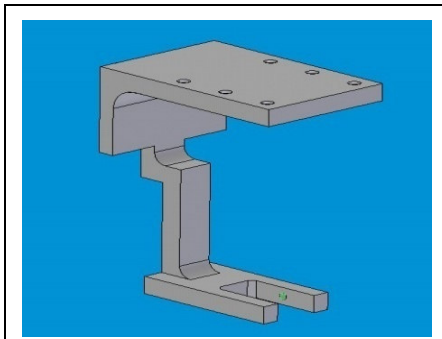
Fig. 98 Bracket for supporting Z axis target capacitance plate.

To achieve the required flexibility, standard Melles Griot manufactured [38] optical mounts are used throughout (Fig. 96). Because of the physical layout of the stage and force frame, a non-standard bracket (Fig. 98) was also required to attach the Z axis capacitance sensor target plate to its standard Melles Griot [38] manufactured adjustable mount.

Isostatic mounting plates have also been designed to minimise the thermally induced movement of mirrors relative to the measurement axes and to minimise mirror distortion by decoupling stress. Fig. 97 illustrates how one of these brackets expands when the temperature rises by a single degree: the centre of the plate remains stationary as the arms expand.

Orthogonality of measurement axes

To ensure that reference measurement axes are orthogonal requires exacting techniques and procedures at set-up [26] which are described in Section 7.2. The measurement axes of the interferometers define the Cartesian coordinate system against which movement is referenced. It is vital that all three measurement axes are orthogonal to each other so as to avoid errors in measurement and to ensure traceability and reproducibility of results.

137

An error separation method, originally presented by Ruijl [26] as a means for accurately determining the angle between axes, is described in Section 0. Because the mirrors of the 3D instrument are facing away from the working point, rather than towards it, as is the situation described by Ruijl [26], this solution is not applicable for the 3D instrument addressed in this project. The requirement for externally facing mirrors in this instance arises from the need to keep the capacitance sensors very close together in the centre of the structure, hence preventing internal facing interferometry. After considerable study and experimentation, a solution has been developed for this problem: an external orthogonality calibration system has been developed, based around a specifically designed artefact (Fig. 99).
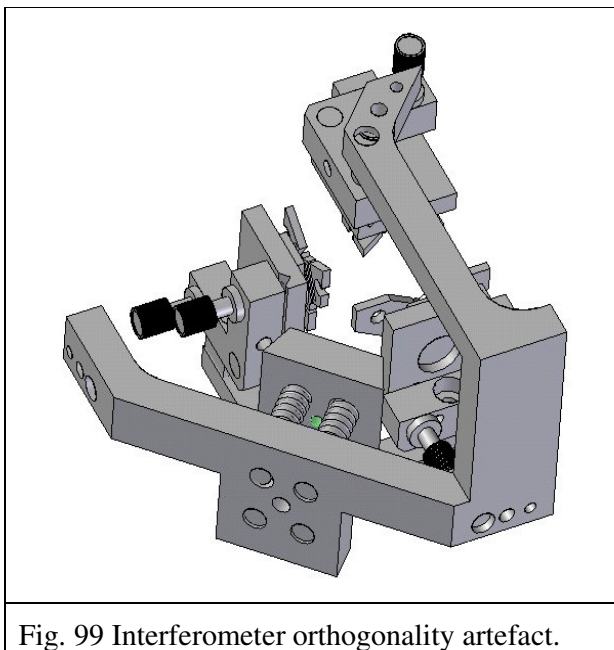
Fig. 99 Interferometer orthogonality artefact.

key aim in the development of this artefact was that it could be used with an adaptation of the standard angle error rejection procedures as presented by Ruijl [26]. This has not yet been accomplished. Because the angles of Ruijl's artefact can be ignored, knowledge of their size is not necessary. Furthermore, changes in artefact shape due to distortion do not give rise to errors. The artefact, designed to ensure the interferometer orthogonality of the 3D instrument of this thesis, though, necessitates a prior knowledge of its geometry for it to function. Unfortunately this introduces uncertainty in orthogonality because of possible errors in angular measurement and unmeasured distortions caused by mounting forces or thermal effects when in place on the instrument. This uncertainty is quantified in Section 6.4.3.

The artefact consists of an assembly of mirrors mounted in locating holes on a bracket as shown in Fig. 100. The assembly accuracy is of little significance to its effectiveness, though the angles between the mirror planes must be carefully measured subsequently and maximum care is needed in its handling and mounting thereafter.
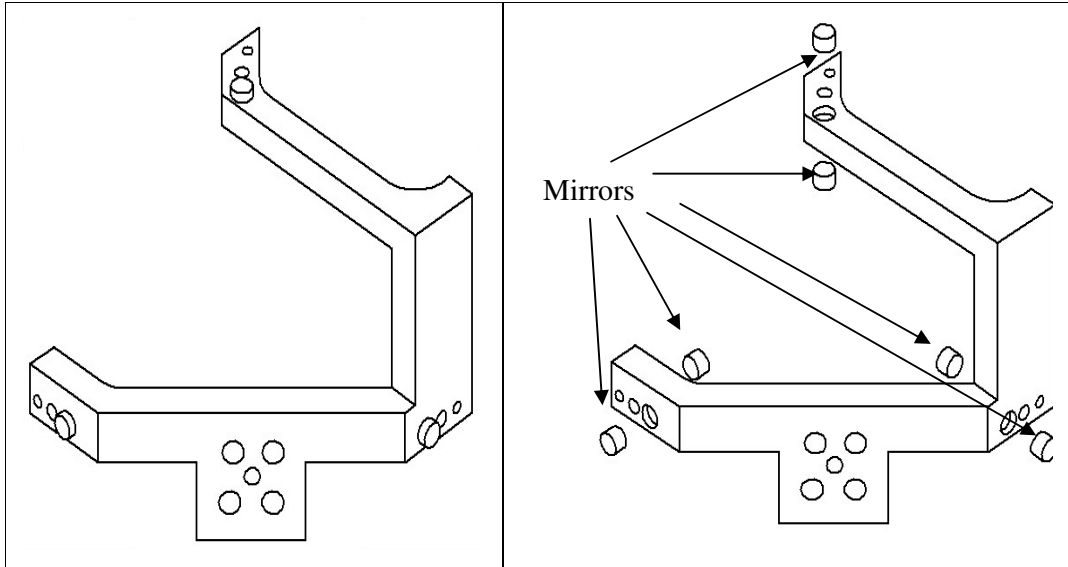
Fig. 100   The artefact designed to ensure orthogonality of the interferometer measurement axes.
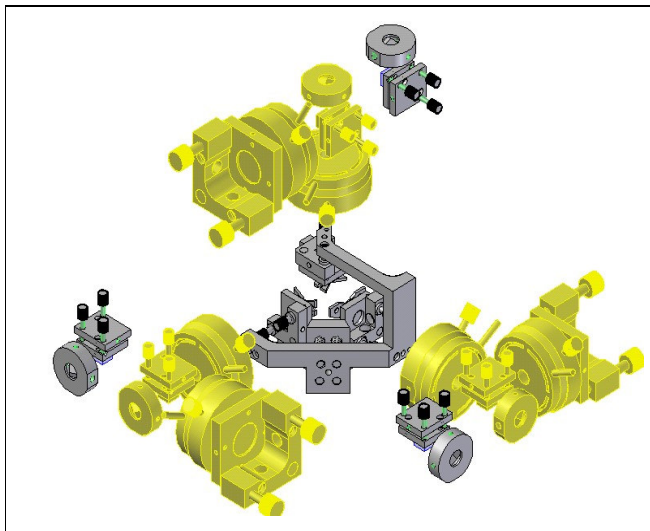
Fig. 101   Drawing of the bracket location relative to the three interferometers only for reasons of clarity (viewed from above).

Fig. 102 shows how the bracket is positioned relative to the three interferometers.

The interferometer measuring beam for each axis must scan over the surface of each of the artefact mirrors, the scanning movement being provided by piezo driven stage displacement. Access for this procedure is achieved by the provision of three holes on each arm of the artefact (Fig. 100). The outermost of these are simple holes, which allow the measurement beam to reflect from the stage mounted reference mirror of each of the interferometers. The middle holes are countersunk on the sides of the bracket closest to the stage. The artefact mirrors are mounted in the countersinks with their reflective surfaces accessible to the measuring beams. Unlike the outer holes, the innermost holes are countersunk on the sides of the bracket closest to the interferometer. Again, all these mirror surfaces are accessible to the measuring beams.

139

The limited displacement capability of the piezos, a maximum of 15 μm along each axis, is not sufficient to move the mirrors out of each others way when switching scanning from one mirror to the next. To realize greater displacements, a simple spring/screw mechanism, guided by pins, is used to provide large movement (>17 mm) in a direction approximately 45^0 to the stage X and Y axes. This movement, when combined with the geometry of the bracket itself, allows all the bracket holes to move simultaneously over a range of approximately 12 mm normal to the interferometer measurement axes. This allows the corresponding mirrors on each axis to be scanned in pairs. The described bracket movement is illustrated in Fig. 102.
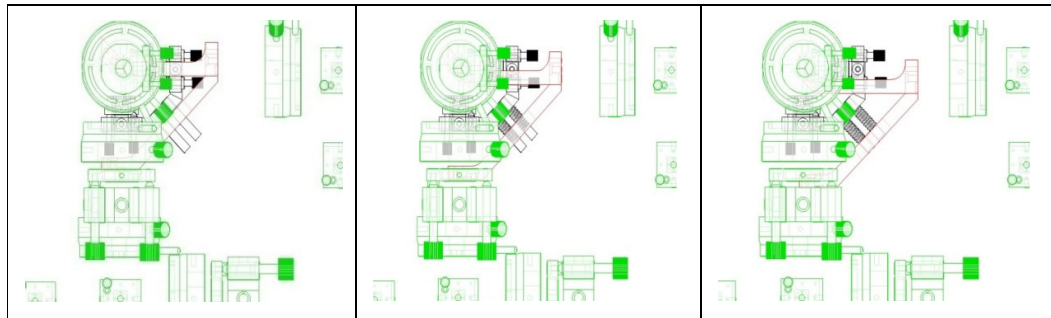
Fig. 102 The three positions of the bracket, allowing each of the bracket mirrors and the reference mirrors of the three interferometers to be scanned by their respective interferometers.
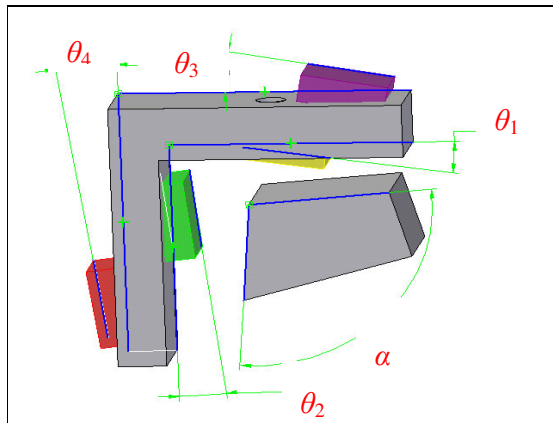
Fig. 103 Schematic showing the nominal angles of bracket mirrors

Fig. 103 presents a simplified illustration of two arms of the bracket with four mirrors (coloured blocks). The angle α represents the angle between the planes of measurement mirrors, while θ_1, θ_2, θ_3 and θ_4 are the angles subtended by the artefact mirrors and two imaginary planes which are normal to each-other. Angles x_1 to x_4 and angles y_1 to y_4, illustrated in Fig. 104 and Fig. 105 are the angles subtended by the artefact mirrors and the interferometer reference mirrors, which can be calculated based on scanning results.

140

| Fig. 104 First and second positions of bracket. | Fig. 105 Third and fourth positions of the bracket |
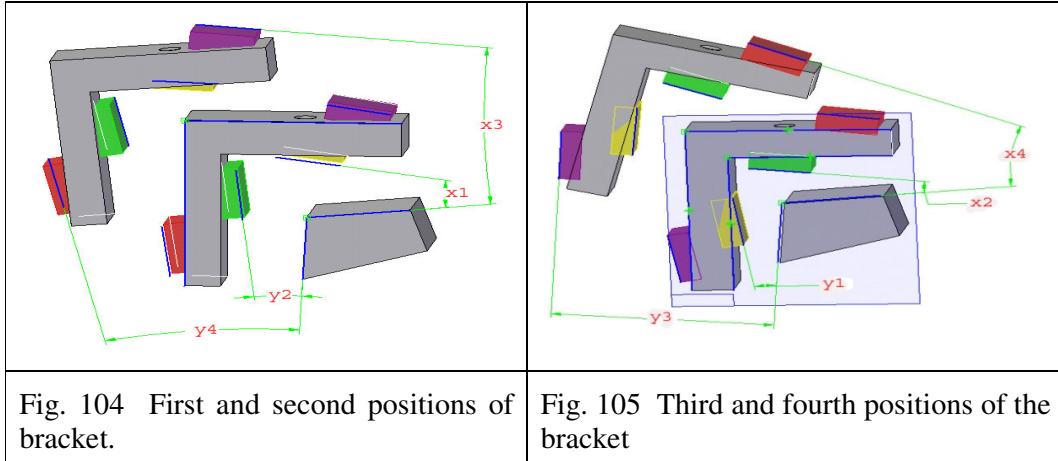
The value of α can then be calculated using the following expression

$$\alpha = \frac{1}{4}\left(\sum_{i=1}^{4} x_i + \sum_{i=1}^{4} y_i - \sum_{i=1}^{4} \theta_i\right) + 90$$

Equ. 47
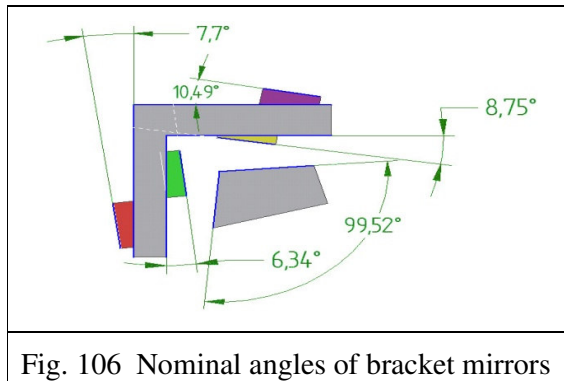
Fig. 106 Nominal angles of bracket mirrors

The following example demonstrates the effectiveness of the bracket in finding the value of α. All the angles, given in Fig. 106, Fig. 107 and Fig. 108 are randomly chosen, as are the relative positions of the bracket. These were drawn before the angles were measured.
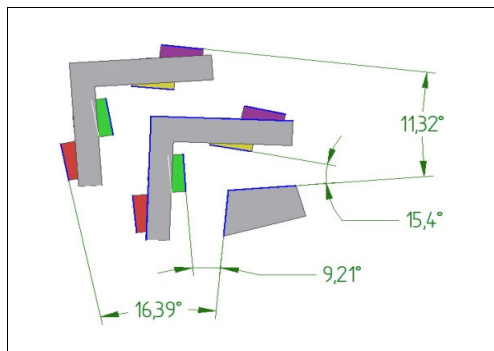
| Fig. 107 First and second positions of bracket. | Fig. 108 Third and fourth positions of the bracket. |
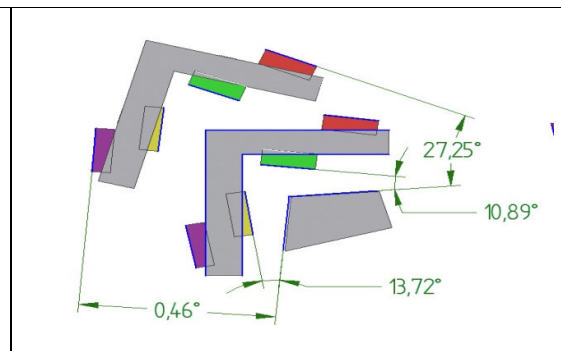
141

The results of this are tabulated in Table 11.

		A Measured Angles		B Measured Angles	Bracket Mirror angles	C Bracket Mirror angles*2	A+B-C
		Pos1&Pos2		Pos3&Pos4			
Yellow	x1	15.4	y1	13.72	8.75	17.5	11.62
Purple	x3	11.32	y3	0.46	10.49	20.98	-9.2
Gr	y2	9.21	x2	10.89	6.34	12.68	7.42
Red	y4	16.39	x4	27.25	7.7	15.4	28.24
Totals		52.32		52.32		66.56	38.08
						Angle	99.52

Table 11 Calculating the angle between interferometer axes based on the example

The drawings presented in Fig. 109 and Fig. 110 show, from different viewpoints, how the bracket is orientated to the stage and measurement axes of the interferometers.

Fig. 109 Drawing of the bracket located relative to the stage and the XY plane interferometers (viewed from below).	Fig. 110 Drawing of the bracket located relative to the stage and the three interferometers (viewed from above).
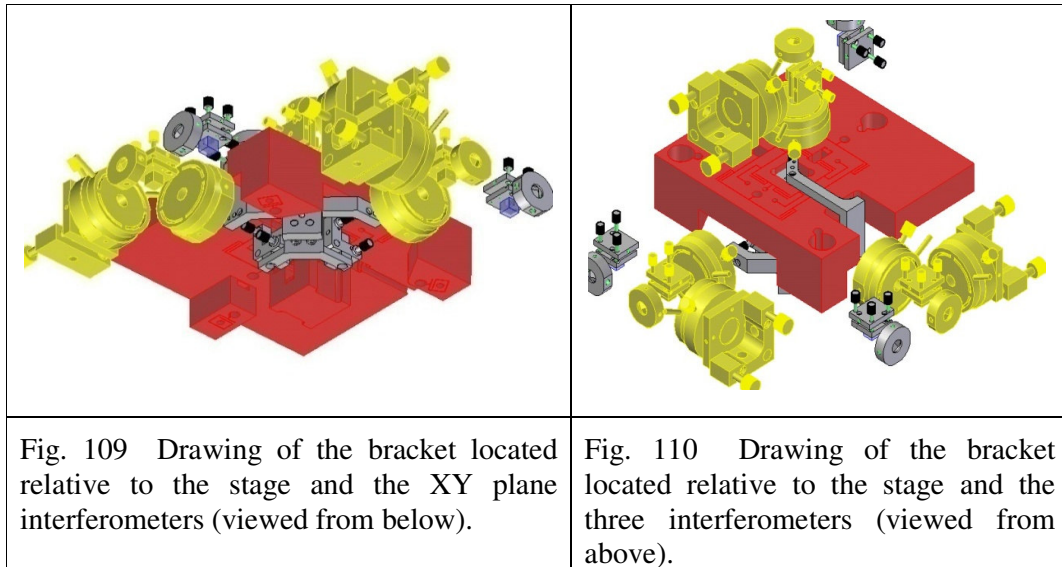
As can be seen in Fig. 104 and Fig. 105, four different positions of the bracket are necessary to obtain all the angular values used in Equ. 47. These positions can be tilted arbitrarily to each other, thus allowing this design to be considered a viable real world option. The first position can be chosen randomly and the second position is realised by translation along the guide pins. To obtain positions three and four, the bracket is flipped, i.e. it is rotated through 270^0 in the plane of the measurement axes followed by a rotation of 180^0 out of this plane. Even a cursory examination of the bracket, as illustrated in Fig. 109 and Fig. 110, would lead to the conclusion that it cannot be

flipped as described. The stage is in the way. A simple modular redesign, incorporating a detachable reversible arm for measurement of the Z to X and Z to Y axes orientations, would facilitate flipping. This configuration could be used to obtain all the data required for use in Equ. 47.

Alternatively the bracket, as presented here, can be used with the expression

$$\alpha = \frac{1}{2}\left(x_1 + x_3 + y_2 + y_4 - \sum_{i=1}^{4} \theta_i\right) + 90$$

Equ. 48

		A Measured Angles Pos1&Pos2	B Bracket Mirror anges	A-B
Yellow	x1	15.4	8.75	6.65
Purple	x3	11.32	10.49	0.83
Gr	y2	9.21	6.34	2.87
Red	y4	16.39	7.7	8.69
Totals		52.32		19.04
			angle	99.52

Table 12 Calculating the angle between interferometers based on data from the first and second positions of the bracket only and Equ. 48.

Equ. 48 was used to calculate the value of α for the previous example, when only the first two positions of the bracket are utilised. The results are tabulated in Table 12.

The two methods yield the same result. In fact they would be expected to give identical results for all theoretical examples. In actual use, though, greater accuracy would be expected when using the four positions, as the estimate would be based on more data.

Mount Stiffness

As explained by Rankers [52] (Section 2.5.5), the instrument structures (support frame, metrology, frame, stage and linkages) should be as stiff as possible. This, when combined with a soft instrument/world interface stiffness, promotes a reduced sensitivity to external vibration. With this in mind, all the structures of the 3D instrument have been designed using FEA to optimise their stiffness.

4.5 Summary and discussion

The aim of this chapter was to investigate the issues concerning the instrument measurement and calibration systems. The significance of these issues has been explored and explanations given as to how they were addressed in the physical design.

The chapter began by looking at the displacement measurement sensors. Two types were discussed: strain gauges (piezo mounted) and capacitance micrometers The sensor chosen for use in the parallel metrology system of the 3D positioner was the PI manufactured D-015 capacitor. This was further critiqued with reference to possible associated error sources.

 Having looked at the displacement measurement system, attention was then turned to the reference measurement or calibration system. Three Michelson configurations were discussed; a single pass, as presented by Hicks et al. [37], a double pass, as presented by Ruijl [26] and a four pass arrangement as described by McCarthy et al. [9]. The metrology frame was then designed to facilitate the use of all three configurations. Several error sources, capable of degrading the measurement accuracy of the interferometers were subsequently discussed and their potential magnitudes calculated in the context of the actual 3D instrument design and the actual purchased components. How these issues are addressed in the instrument design was described.

Since the orientation of the measurement axes of the interferometers define the instrument coordinate system, knowledge of their orthogonaity is vital so that displacements can be related to the Cartesian coordinate system and measurement errors are to be avoided. Presented is a description of an artifact designed specifically for determining the angles between measurement axes of the interferometers in use on the 3D instrument. Drawings (Fig. 99, Fig. 100, Fig. 101 and Fig. 102) of the artifact, along with equations (Equ. 47 and Equ. 48) for calculating the angle and examples (Table 11 and Table 12) of how it may be used are included in the description.

Several error sources associated with the design of the 3D instrument, along with their possible magnitudes, have been identified in this chapter. These are regarded as errors only if uncompensated. Error compensation is thus recognised as an important intrinsic part of the control strategy described in the following chapter. Associated though, with these error sources are uncertainties which cannot be compensated. It is these uncertainties that are examined in detail and, quantified in Chapter 6.

Chapter 5

5   Command and Control

5.1   Introduction

Having discussed the mechanical and metrology systems, this chapter describes the third major system essential for precision positioning, i.e. the control system. It is this that determines the manner in which the movement accuracy of the stage is to be achieved.

A series of inter-dependant programs, developed especially for this thesis using LabView and Mathcad software, is presented. These programs allow the following.

- Calibration of the axial capacitance sensors with respect to the appropriate interferometers.

- Linearisation of the capacitance measurement to the reference measurement through error mapping.

- Implementation of compensation for environmentally induced bias during both calibration and operation.

- Transformation of the Cartesian coordinates of desired locations to instrument axial coordinates and calculation of the Cartesian coordinates of measured positions.

- Formulation the sequential commands required for three dimensional contouring over circular and linear paths as well as over spherical or planer surfaces.

Standard second order analysis of the system leads to provisional controller settings and illustrates the effectiveness of closed loop proportional integral (PI) control in achieving optimal dynamic response characteristics and allows these characteristics, across all axes, to be compared and balanced.

In the context of the research question, the control system design and analysis facilitates the identification of some parameters that should be included in the specification of a typical precision positioning instrument while it is shown that the bias effects of other parameter variability can be substantially nullified through software or physical design.

5.2   The system

Stage movement is affected by three piezo actuators (Type PI840.1, made by Physik Instrumente Co [27]), each acting along separate near orthogonal axes and individually controlled by means of a three channel PI controller (E-509.C3A PZT sensor and controller module combined with the E-503 amplifier module).   Displacement feedback to the controller is via three PI D-015 capacitance sensors, one on each axis. The capacitance sensors are calibrated against two pass Michelson interferometer displacement measurements.   The schematic diagram in Fig. 111 illustrates the flow of data/information within the control system that was designed for this particular instrument and the interdependence of its key constituents.   As can be deduced from the schematic, several programs are integral to the system.

a) A 'Calibration program' to calibrate the capacitance sensors with respect to the interferometers.

b) A 'Command program' to generate the sequential commands necessary for a variety of movement scenarios.

c) A 'Mapping program' to determine the error mapping function for each axis and to generate the coefficients for use in modifying the command and feedback signals.

d) A 'Driving program' to efficiently output the command sequence to the controller.

e) A 'Monitoring program' to track the position of the moving stage.

Each of these programs was developed specifically for this thesis using LabView and Mathcad software packages. In addition to their primary functions, as listed above, these programs also realize compensation for specific biases. Compensations are affected in this control system for the biases in measurement and consequently positioning, arising from changes in environmental variables and set-up alignments, all of which are identified and described in Chapter 4.

The following compensations are implemented.

- Bias in the wavelength of the laser light due to differences in environmental variables (temperature, pressure and humidity) from NTP.

- Biases due to differences between the instrument coordinate system and the Cartesian system, arising from any non-orthogonality of the instrument interferometer measurement axes at set-up.

- Non-linearity of the capacitance measurements relative to those of the interferometers substantially arises from non-parallelism of the capacitance plates and misalignment of the capacitance measurement axes with the reference axes. This set of biases is characterised at calibration in terms as a fourth order mapping function which is subsequently used to compensate for measured positions during monitoring and to compensate target positions (when the function is used in its reverse form).

- Biases in capacitance measurement arising from thermal expansion/contraction of the plates and changes in relative permittivity arising from environmental variable differences between values at calibration and those at the time of operation.

- Bias due to thermal expansion of the offset distances of the axis sensors from the point of interest arising from differences in temperature between those at calibration and those at the time of operation.

Other biases, associated with various possible sources of error also exist. These are not compensated within the control system designed here, as they are expected to be effectively nulled within the metrology system through careful design of spatial positioning and material selection as described in Chapter 4.

Each of the programs is described in the following section and is available in operating form.

Control Schematic

Error Mapping Function Program Xc=f(Xp)

Error Mapping MathLab Program

Callibration Program (LabView)

Environmental Data

Command Program (LabView)

A coefficients Files

Command Files

Error Mapping Function Program Xp=f(Xc)

B coefficients Files

Interferometer Feedback

Environmental data & Axis Orthogonality

PI Controller

Driving Program Environmental compensation

Monitoring Program Environmental compensation

Piezo Actuator

PI Controller

Capacitance Feedback

Piezo Actuator

Capacitance Feedback

Position

Position

Calibration Only

In process control

Fig. 111 Schematic of the control and calibration system.

149

5.2.1   The Mapping program

Error mapping is used in this system (see Fig. 111) to linearise the command position relative to the true position in a similar manner to that described by Hicks et al. [37] and used by Queensgate Instruments Ltd. [67] in their digital controllers (see Section 2.7.1).

The Mapping program was written in Mathcad software specifically for this project. It automatically and simultaneously reads from the most recent calibration data files, generated by the Calibration program (Section 5.2.2), for each of the axes. Fourth order polynomial regression is used to determine the coefficients of the power series function describing the true position, x_p, (interferometer measured) in terms of the command position, x_c (capacitance measured position when closed loop control is used)

$$x_p = b_0 + b_1 x_c + b_2 x_c^2 + b_3 x_c^3 + b_4 x_c^4 + b_5 x_c^5 + \cdots$$

<div align="right">Equ. 49</div>

The coefficients of this mapping function (the b coefficients in Equ. 49) are calculated by the Mapping program each time the instrument sensors are recalibrated and are stored to three tab-delimited files, one for each axis. Hence the coefficients are specifically related to the alignment conditions pertaining to each individual axis at the time of their calibration.

Solely to test the functionality of this the Mapping program, a mapping function was established for measurement data files that had been generated by the Calibration program for the single axis prototype stage driven over its entire range. In Fig. 112 the original interferometer sensor against strain gauge voltages are shown as well as a graph showing the displacements measured by the interferometer against the same displacements measured by the calibrated strain gauge.
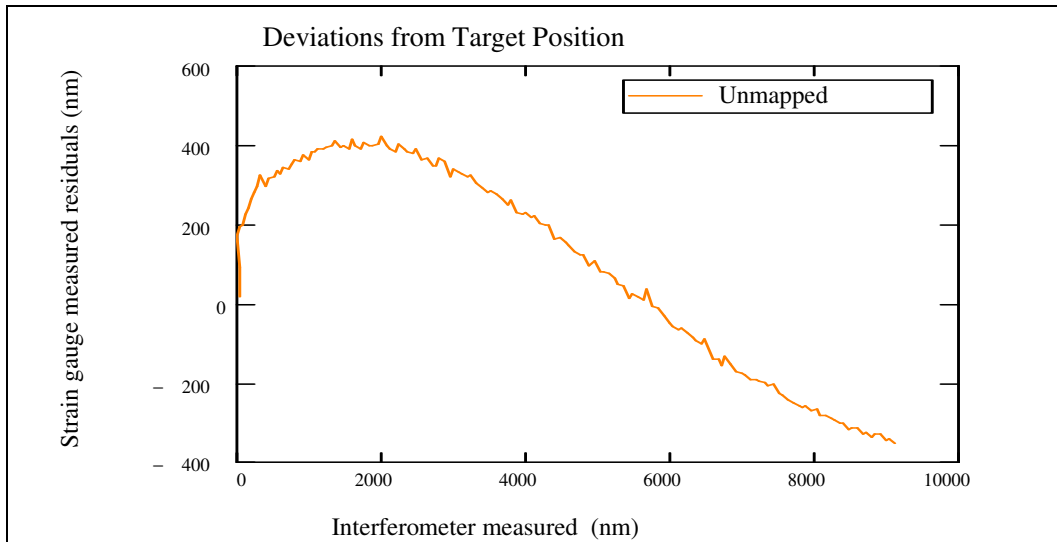
Fig. 112 Feedback interferometer Vs strain gauge voltages when the prototype single axis stage was displaced and the corresponding displacement measurement graph.

The following coefficients were found for this set of data

$$b\_coefficients = \begin{pmatrix} b_0 \\ b_1 \\ b_2 \\ b_3 \\ b_4 \end{pmatrix} = \begin{pmatrix} 179.023 \\ 1.312 \\ -1.125 \times 10^{-4} \\ 1.213 \times 10^{-8} \\ -4.47 \times 10^{-13} \end{pmatrix}$$
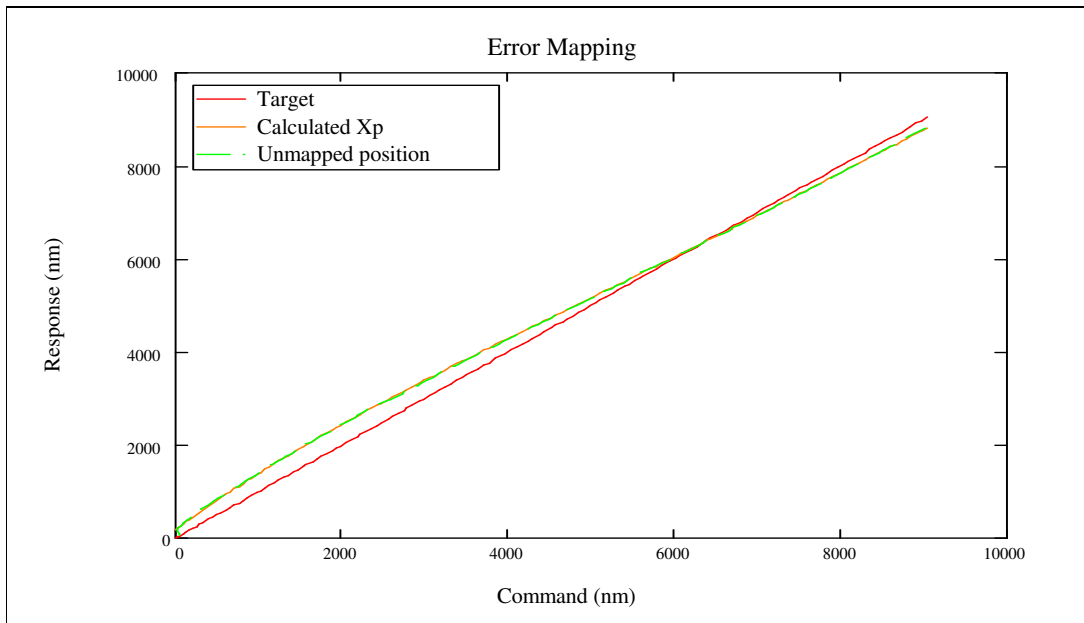
Fig. 113 Comparison of calculated x_p to the true position.

Using these coefficients and Equ. 49 with the full range of strain gauge measured data, the corresponding set of x_p values were calculated. As can be deduced from Fig. 113, the calculated x_p values are a good fit for the interferometer measured data. This is an indication that the coefficients are accurate and that Equ. 74 can be used to successfully map capacitor measured position data for the purpose of monitoring.

The series is now reversed and a fourth order polynomial expression is found for the command position, x_c, in terms of the true position, x_p

$$x_c = x_m = a_0 + a_1 x_p + a_2 x_p^2 + a_3 x_p^3 + a_4 x_p^4 + a_5 x_p^5 + \cdots$$

Equ. 50

Having determined coefficients for this series (a coefficients), they are automatically saved to three tab-delimited files.

$$a\_coefficients = \begin{pmatrix} a_0 \\ a_1 \\ a_2 \\ a_3 \\ a_4 \end{pmatrix} = \begin{pmatrix} -102.27 \\ 0.665 \\ 1.088 \times 10^{-4} \\ -9.708 \times 10^{-9} \\ 2.663 \times 10^{-13} \end{pmatrix}$$

x_c was then calculated using and the previously calculated x_p values and the a coefficients with Equ. 50. The target position, the mapped command, the mapped position and the unmapped position can be compared in Fig. 114. The target is the desired stage position. The mapped command is the set of commands that should be applied to the controller in order to compensate the non-linear relationship between the reference and in-process sensors, while the mapped position is the true position resulting from these mapped commands. It can be deduced from Fig. 114 that the true position is effectively linearised relative to the target position.

Using this program, the true position of the stage after a given command can be expected to be closer to the target position. The next section describes how the quality of this mapping can be quantified.
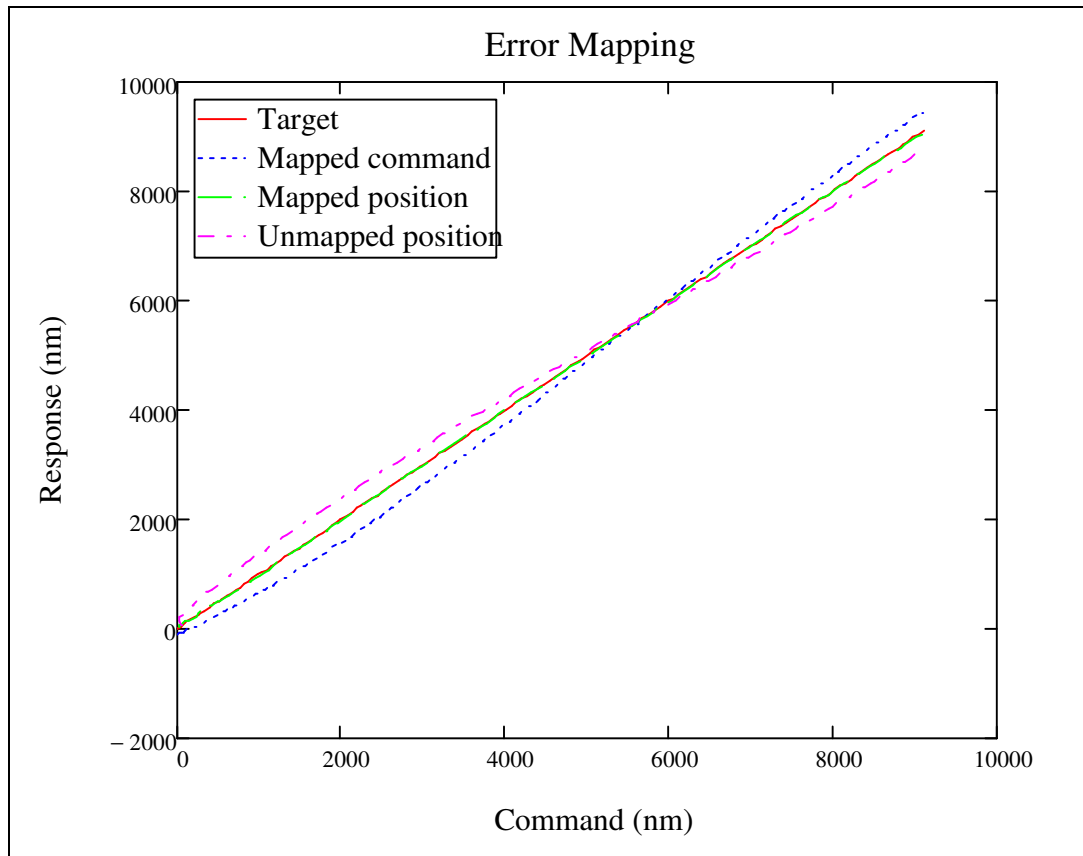
Fig. 114 Graph showing the effect of mapping on the commands and on resulting stage position.

The effectiveness of mapping

Inaccuracies in the regression coefficients give rise to errors in mapping. The difference (residuals) between the set of target positions and the mapped and unmapped positions is shown in Fig. 115. The mapping error is defined by Hicks as half the peak to peak range of the residual curve and expressed as a percentage of the full range displacement. From the previously used data (Fig. 115) it can be shown that the residuals can be reduced from 6.77 % in the unmapped case to 0.62 % in the mapped case for this particular set of calibration data.

Fig. 115 Comparison between the mapped and unmapped deviations from commanded positions.
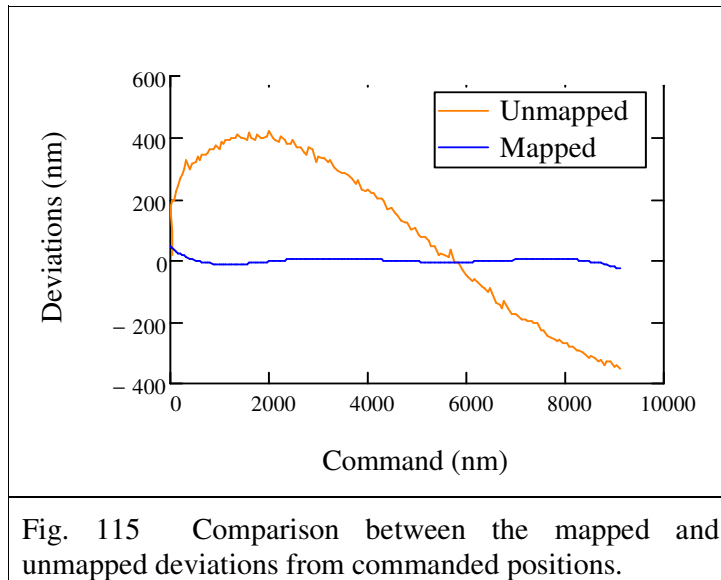
The positioning error is defined by Yeh et al. [30] as the root mean square of the difference between the actual positions and the preset command positions through the entire positioning range. Thus it can be deduced from Fig. 115 that for the single axis stage, the standard error is reduced from σ = 200 nm for the unmapped data to σ = 3 nm for the mapped positions.

Fig. 116 Comparison between the scale factor of mapped and unmapped positions.
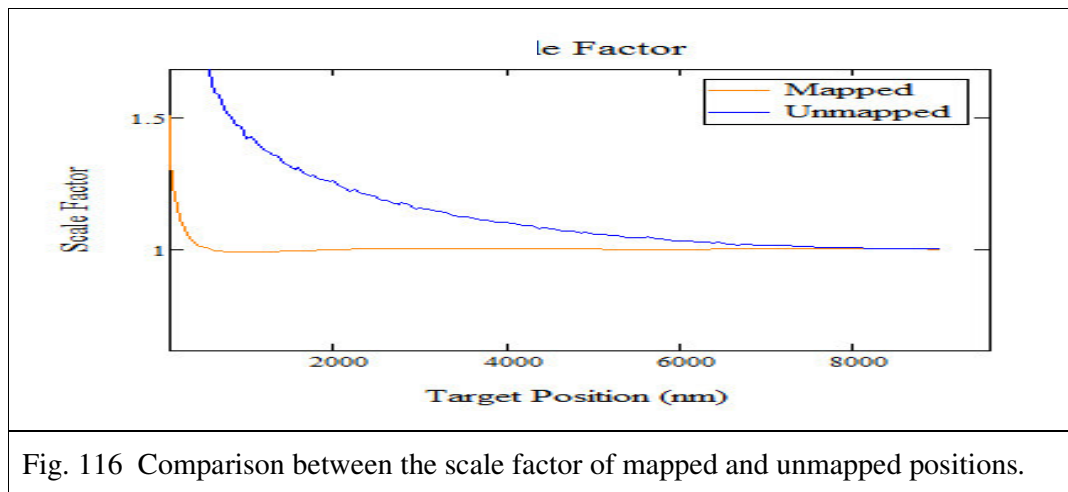
The scale factor (the ratio of true position to target position) for this data is shown in Fig. 116. It can be seen to vary significantly for unmapped data over the full range of displacement. This means that the actual movement error resulting from an unmapped command will substantially depend on the position of the stage at the instant of the command. Mapping can be seen in Fig. 116 to significantly improve the scale factor.

For the mapped commands, the scale factor deviates little from unity (Std Dev = 0.008 after 2 μm stage travel). Thus the use of the calibration data from the single axis prototype stage indicates that mapping could deliver a high level of positional improvement.

154

In addition to generating the mapping coefficients, the Mapping program also calculates values for the mapping error, the positioning error and the scale factor for each axis. This facilitates monitoring the quality of the mapping at calibration.

5.2.2   The Calibration program

As can be seen from Fig. 111 there is a need to calibrate the capacitance sensors with respect to the reference interferometers. In order to achieve this within the overall system, a Calibration program was developed using LabView software. This program simultaneously reads the feedback voltage from the capacitance sensors and the interferometers.   A description is given in Section 4.3.1 of how Michelson interferometers are used to measure displacement. Consistent with this description, the peaks of the interferograms are located and counted as the stage is driven over the full range of each axis and the displacement of the stage is calculated. This measured reference value is then compared to the voltage feedback from the capacitance sensor. A capacitor sensitivity volts.nm^2 value is thus obtained.
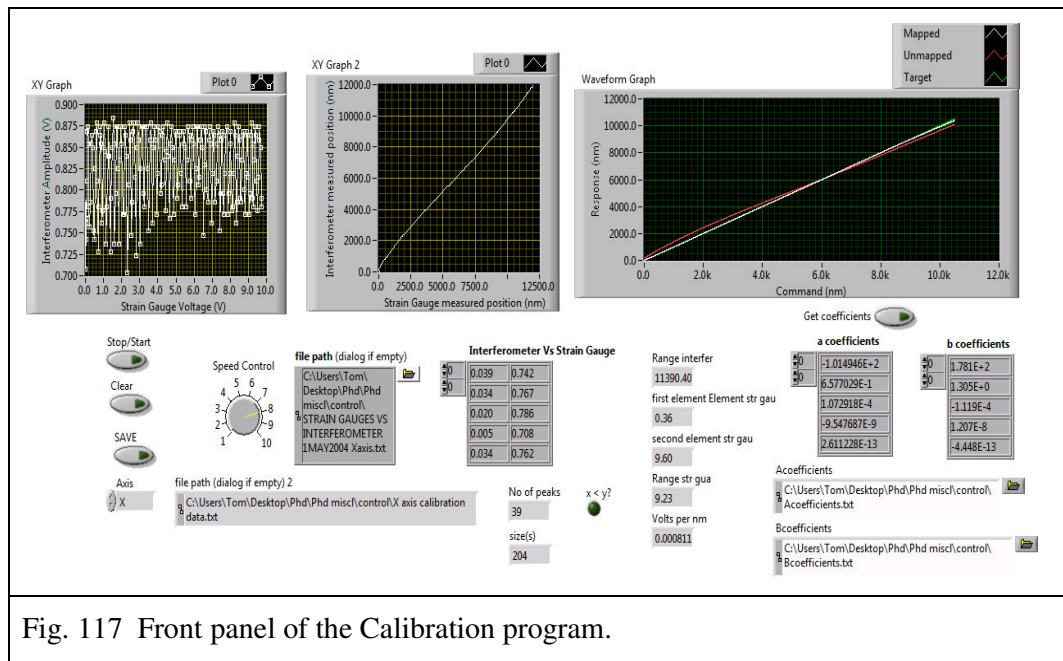
Fig. 117 Front panel of the Calibration program.

The positions of the stage, as indicated by the peaks of the interferometer, and the equivalent positions, as measured by the calibrated capacitance sensor, are compiled into a single array and saved to a tab-delimited file. Three of these files are generated,

one for each axis, and are accessed by the Mapping program (see Fig. 111 and Section 5.2.1). The front panel of the Calibration program is shown in Fig. 117.

The axis control (bottom left hand side) on this panel allows each axis (X, Y and Z) to be calibrated individually. This dictates which sensors are addressed, the files in which the calculated measurements are stored and which mapping coefficient files are read.

The panel presents three graphs. On the left hand side is a graph of interferometer sensor voltage against capacitance sensor voltage. The centre graph shows the relationship between calculated interferometer measured positions and the calibrated capacitor measured positions. If the relationship is linear, this graph should be a straight line through the origin. The third graph (top right hand side) presents plots of the target, unmapped and mapped positions. The mapped positions are calculated using the most recent mapping coefficients generated by the Mapping program for the axis in question. This allows the effectiveness of the mapping functions to be visually assessed for each axis at calibration. Shown also on this panel are the file paths to where the calibrated data is to be saved and to where the most recent mapping coefficients are stored.

As with the Mapping program, testing the functionality of the calibration program was accommodated by real parallel interferometer and strain gauge feedback voltage values, taken as the single axis prototype stage was driven over its entire range (Fig. 112).

The usefulness of interferometers as reference displacement measurement devices depends on the correct wavelength value being used in the calculations. Environmental variation affects this value and since the resulting biases can be predicted, as is discussed in Section 6.3.1, compensation can be applied.

5.2.2.1 Interferometer wavelength compensation for environmental factors

At normal temperature and pressure (atmospheric pressure = 101.325 kPa, relative humidity = 50 %, air temperature = 293.15 K), the wavelength of He-Ne laser light is 632.8 nm. Relative changes in λ are calculated for environmental changes using the National Institute of Standards and Technology (NIST) 'Engineering Metrology Toolbox' [3] and are tabulated in Table 1.

Change from NTP	1 K Rise in Temp	1 kPa rise in Pressure	1 % rise in Humidity
Change in λ (Air) nm	6.02×10^{-4}	-1.7×10^{-3}	5×10^{-6}
Relative change in λ (ppm)	0.951	2.68	0.0076

Table 13 Relative changes in λ calculated for environmental changes using NIST 'Engineering Metrology Toolbox' [3]

The environmental conditions may differ from NTP at the time of calibration. Having assumed that the relationship between the wavelength of the He-Ne laser light and the environmental variability is linear over the range of these differences, Equ. 51 is used as a compensating factor within the Calibration program

$$W = 362.828268\{1 + \left(0.951 \times 10^{-6}(T_C - T_{NTP})\right) + \left(-2.68 \times 10^{-6}(P_C - P_{NTP})\right) + \left(0.0076 \times 10^{-6}(RH_C - RH_{NTP})\right)\}$$

Equ. 51

Where W is the compensated wavelength, T_C is the temperature at calibration, P_C is the atmospheric pressure at calibration, RH_C is the relative humidity at calibration, T_{NTP} is the temperature at normal temperature and pressure, P_{NTP} is the atmospheric pressure at normal temperature and pressure, RH_{NTP} is the relative humidity at normal temperature and pressure.

5.2.3 The Mapping Function program

The Mapping Function program is a sub-program written in LabView for this thesis that is used within the Command and the Monitoring programs. In the context of the Command program (see Section 5.2.4) , the purpose of the Mapping Function program is to apply the error mapping to command signals prior to outputting mapped command signals (x_c) to the controller. It accomplishes this by passing the command values through the reversed mapping function (Equ. 50), having first read the a-coefficient files appropriate to the axis being driven. In the Monitoring program (see Section 5.2.5) the Mapping Function program is used to convert the mapped positions, as measured by the capacitance sensors, to the true positions (x_p), i.e. the measurement of the position that would be obtained when using the calibrating interferometer. Here the

capacitor measurement values are passed through the mapping function (Equ. 49) using the set of *b*-coefficients that is read from the files appropriate for the axis being monitored.
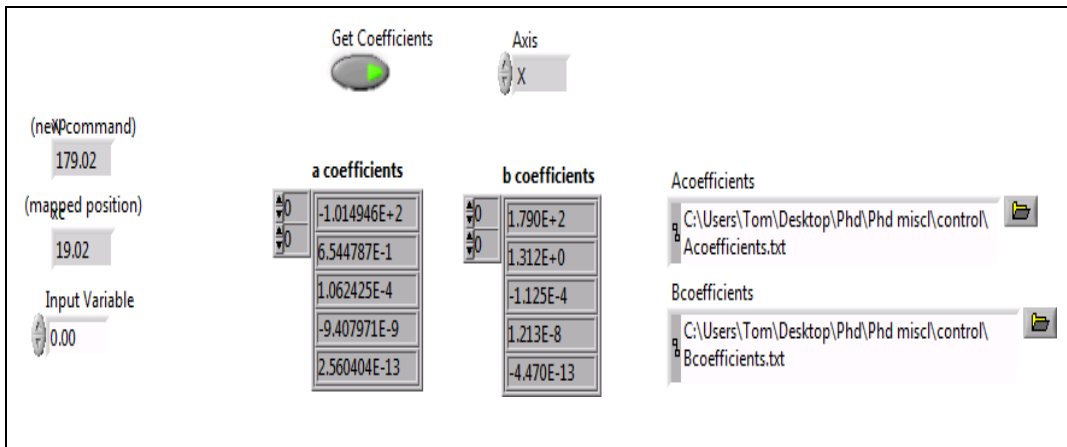
Fig. 118 Front panel of the Error Mapping Function program.

Since this is used as a sub-program, its front panel is not generally seen by an operator.

5.2.4   The Command program

This program was written for this thesis in LabView software and generates the command sequences that enable the stage to be used for contouring in 3D space. The program is written to calculate the Cartesian coordinates of the points describing lines, circles, spheres and flat planes. As explained in Section 5.2.3, within the Command Program, the appropriate error mapping is applied to all the individual X, Y and Z coordinate values by means of the Mapping Function sub-program. Environmental compensation is not applied in this program since the generated coordinates are stored to files that may be used by the Driving program later under possible different conditions.

Circular contouring

The ability of instruments to tightly follow small radii circular paths is a common method of assessing the performance of contouring instruments [73]. To facilitate effective comparisons with the work of other researchers in the future, it is desirable that this instrument should also have this ability. For this reason the Command program allows a circle to be defined by entering its radius, the coordinates of its center and its desired resolution. The resolution simply defines the separation of

158

adjacent points along the X and Y axes. The program then calculates the coordinates of all the points on the circle, using the following common equation of a circle, centre (h, k) and radius r that is given by

$$r^2 = (x - h)^2 + (y - k)^2$$

<div align="right">Equ. 52</div>

Fig. 119 shows the Circle tab of the command program. It illustrates an example of a circle with centre at (3 µm, 3 µm) with a radius of 3 µm.
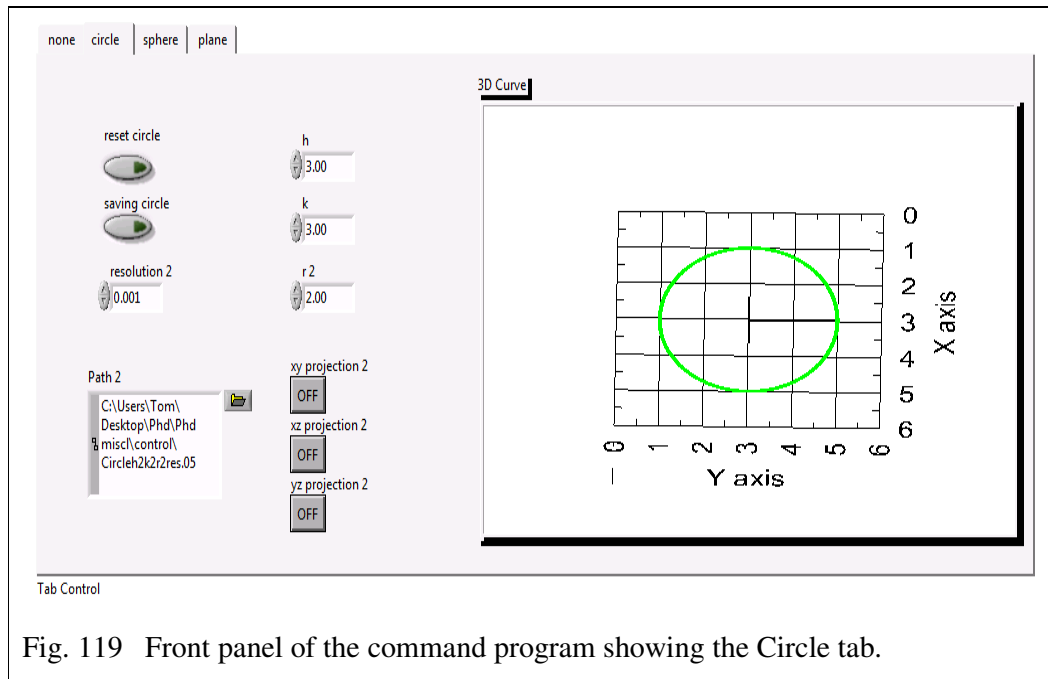
Fig. 119   Front panel of the command program showing the Circle tab.

As well as allowing the operator to enter values for the radius, the resolution, and the coordinates of the center (h, k), the panel provides graphical feedback to the operator and allows satisfactory coordinates to be saved to a selectable tab-delimited spreadsheet file.

<u>Spherical contouring</u>

The instrument can also be commanded to scan over a spherical surface. As in the case of the circle, the radius of the sphere, the location of its centre and the desired resolution combined can define the spherical path.
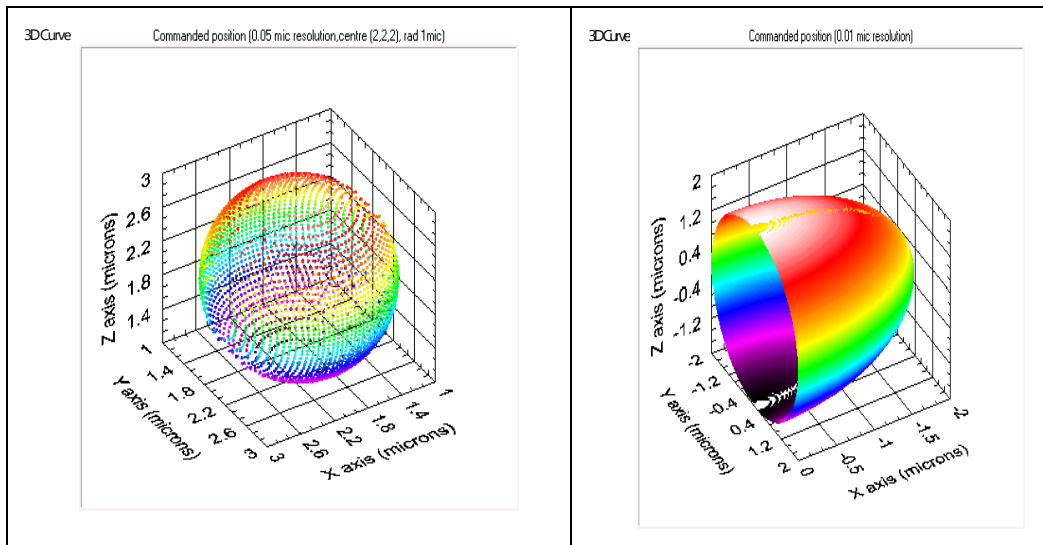
Fig. 120 3D graphs of point coordinates generated to command the stage over spherical surfaces when the resolution is set to 0.05 μm and 0.001 μm.

The coordinates of the points constituting the surface of spheres are generating by creating a series of consecutive circles separated by a distance equal to the defined resolution, their radii forming a semi-circle.   Fig. 120 illustrates spherical surfaces using resolutions of 0.05 μm (top) and 0.001 μm (bottom). It can be deduced that a much smoother surface is possible with a higher resolution.

Linear paths
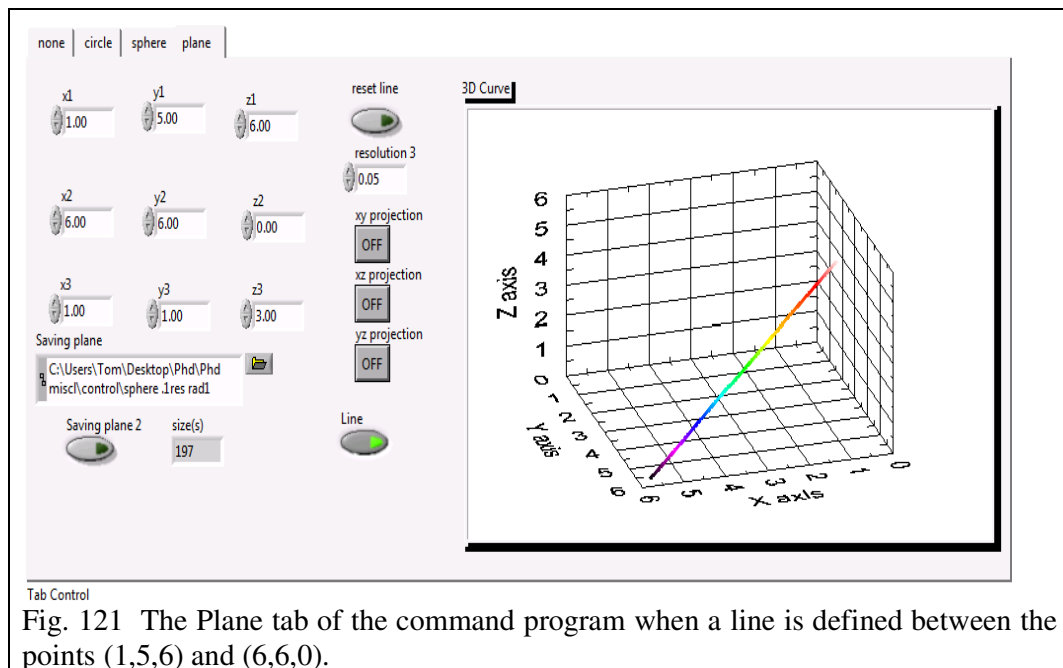
Fig. 121 The Plane tab of the command program when a line is defined between the points (1,5,6) and (6,6,0).

The stage may also be commanded to follow linear paths through 3D space that are defined by the coordinates of their end points. For smooth paths and scanning, the stage is commanded to step different distances along each axis when moving between individual points.

Flat Planes
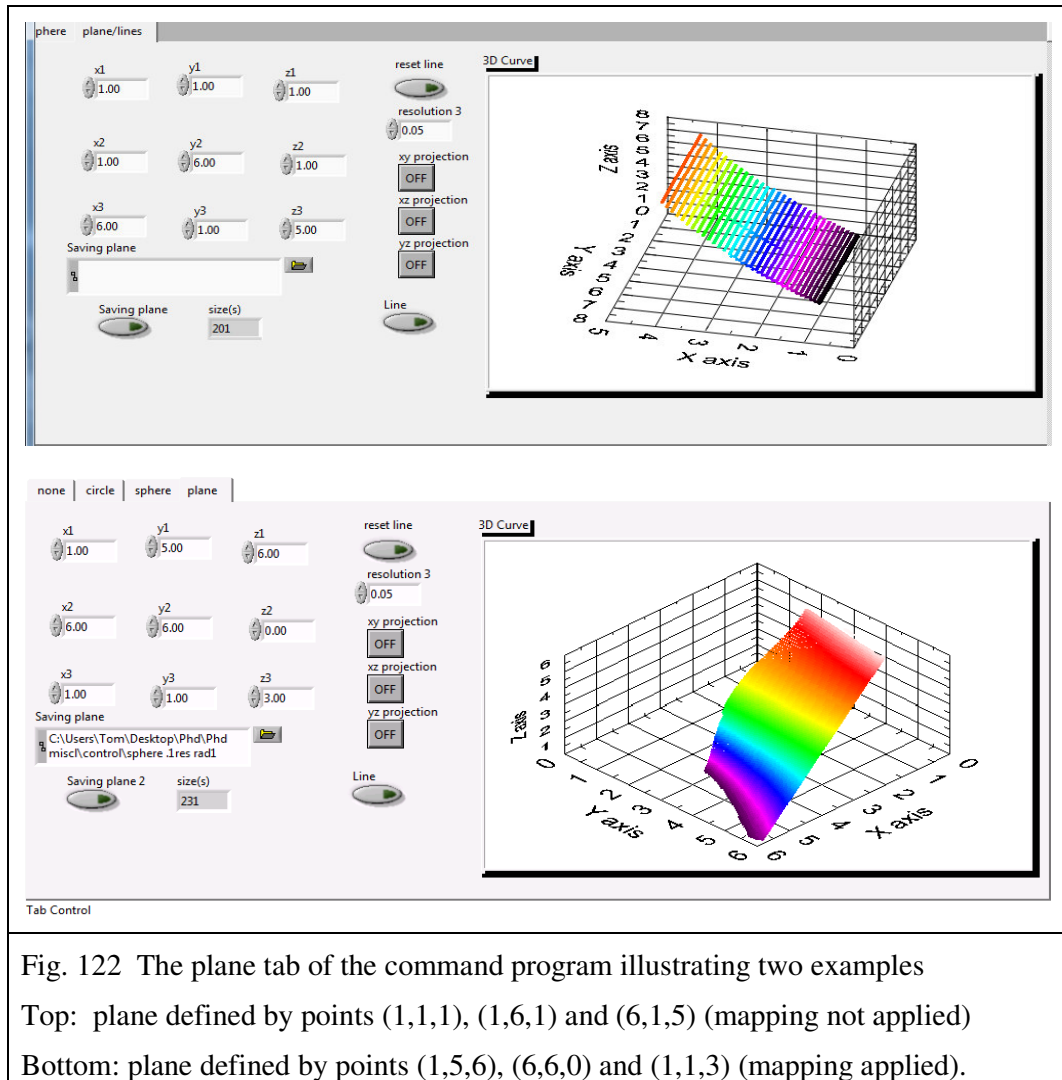
Fig. 122 The plane tab of the command program illustrating two examples

Top: plane defined by points (1,1,1), (1,6,1) and (6,1,5) (mapping not applied)

Bottom: plane defined by points (1,5,6), (6,6,0) and (1,1,3) (mapping applied).

A Boolean switch on the front panel allows the operator to choose between lines and planes.   A plane is defined by the coordinates of three points, $(x1,y1,z1)$, $(x2,y2,z2)$ and $(x3,y3,z3)$ along with a desired resolution. The points forming the plane surface are sequenced so that the stage scans backwards and forwards in straight parallel lines over the surface of the plane containing the three defining points. The front panel Plane tab

161

is illustrated in Fig. 122, with two examples of such planes. The bottom example shown in the figure appears to be curved. This is due to the effect of mapping and would result in the stage actually scanning over a flat plane.

The tab allows the entry of the coordinates of the three points and to save the coordinates to a tab-delimited file.

5.2.5 The Driving and monitoring programs

The Driving program and the Monitoring program are LabView programs written for this thesis. The Driving program is used to drive the stage through a sequence of movements having first allowed an operator to recall the coordinate files created previously by the Command program (see Section 5.2.4) , while the Monitoring program allows for the monitoring of the stage position. Compensation for differences in environmental variables from those existing at the time of calibration, as well as compensation for non-orthogonality of the instrument measurement axes are applied to the point coordinates prior to outputting the command signals to the PI controllers and prior to viewing of stage measured positions. These programs have similar front panels, one of which is shown in Fig. 123.
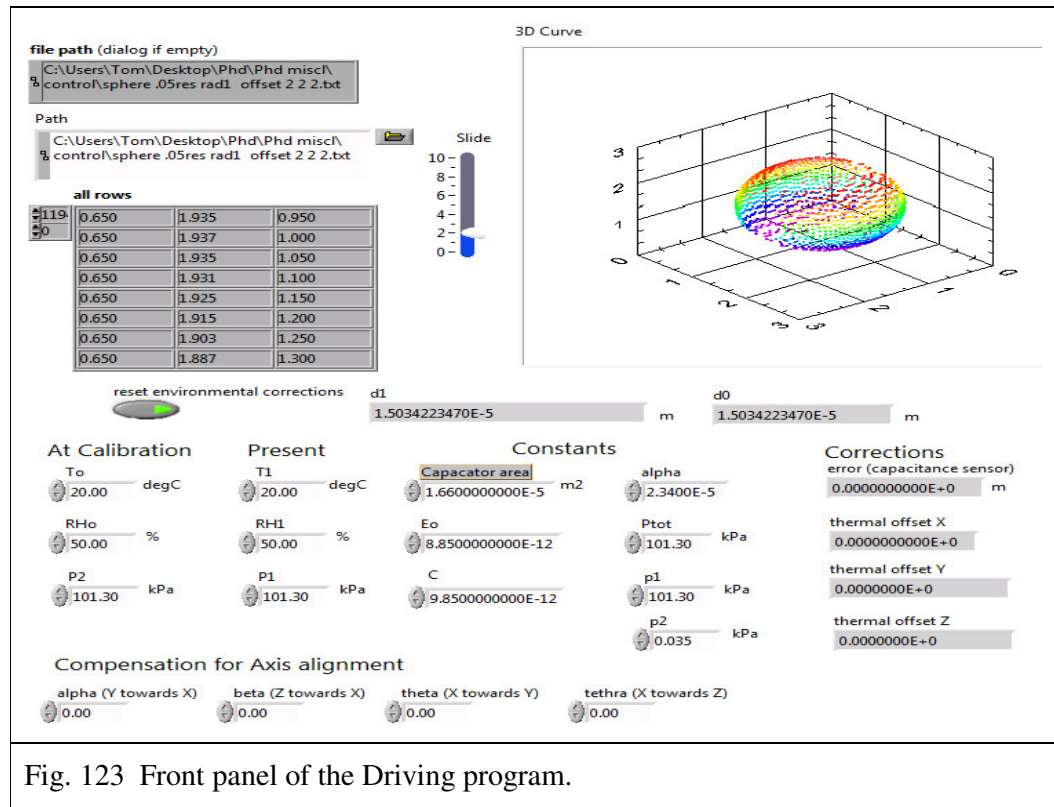
Fig. 123 Front panel of the Driving program.

Although the commands have already been error mapped in the command program, the mapping must be reversed for monitoring purposes using the Mapping Function program as described in Section 5.2.3.

5.2.5.1 Compensation for environmental changes

As explained in Chapters 3 and 4, the instrument has been successfully designed so as to avoid predictable sources of error while Chapter 6 examines and quantifies uncertainties for which compensation is not possible. The errors that are compensated in the command and monitoring programs are those that are not corrected elsewhere.

Compensation for the combined effect of sensor offset and thermal variability

This error depends on the size of the offset and hence is different for each axis. The error is simply calculated by

$$error = \alpha(T1 - T0).\,offset$$

Equ. 53

Where *T1* is the temperature at the time of operation (K) and *To* is the temperature at the time of calibration (K).

Compensation for errors in capacitance measurement resulting from environmental changes

The capacitance sensors are calibrated prior to operation using the calibration program as described in Section 5.2.2. Any changes in temperature, pressure or humidity from the time of calibration to the time of operation may result in measurement and displacement errors. To apply the correct compensation, it is necessary to identify how these variables combine to effect capacitor displacement measurement.

$$C = \frac{\varepsilon_r \varepsilon_0 A}{d}$$

Equ. 12, Section 2.6.1

From Equ. 12 it can be deduced that compensation must be applied for any changes to the area of the plates, to the relative permittivity of the air between the plates and to gap size arising from differences in environmental conditions from time of calibration.

Plate area and gap size

Theoretically, thermally induced changes in plate thickness do not result in gap reduction as the sensors and their mounts are made from material of the same coefficient of thermal expansion as the metrology frame, stage and mounting frame. Expansion, and contraction, of these structures null those of the sensor and need no compensation, although uncertainties resulting from tolerances in the coefficients must be considered (Section 6.2).

Changes in plate area, on the other hand, are not nullified and hence compensation must be applied. A compensating factor or relative change in plate area, x, may be calculated using Equ. 54

$$x = \frac{A1}{A0} = \frac{\pi(r + r\alpha(T1 - T0)^2)}{\pi r^2} = \left(1 + \alpha(T1 - T0)\right)^2$$

Equ. 54

If $A1$ is the plate area at the time of operation, Ao is the plate area at the time of calibration, α is the coefficient of thermal expansion of the plate material (m^{-1} K^{-1}), r is the plate radius, and x is the relative increase in area.

The Relative Permitivity

Temperature, atmospheric pressure and relative humidity all affect the relative permittivity as can be deduced from equations Equ. 55, Equ. 56 and Equ. 57. Rearranging Equ. 42 (Section 4.2.3) taken from Hicks et al. [37] the Relative Permitivity, ε, can be calculated from

$$\varepsilon = \frac{1553.9\frac{p1}{T} + 2663.6\frac{p2}{T} + \frac{1259.3}{T}\left(1 + \frac{5748}{T}\right)p3}{1 \times 10^6} + 1$$

Equ. 55

T is the temperature (300 K), $p1$ is the partial pressure of CO_2 in free dry air (101.3 kPa), $p2$ is the partial pressure of CO_2 (0.035 kPa), $p3$ is the partial pressure of water vapour (3.5667 kPa at 100% relative humidity and 295 K)

And

$$p3 = RH\left(\frac{e}{100}\right)$$

Equ. 56

where e is the vapour pressure (Pa) and can be calculated using as follows

$$e = \frac{a0 + T\left\{a1 + T\left(a2 + T\left(a3 + T(a4 + (a5 + a6))\right)\right)\right\}}{1000}$$

where

$T = 26.85$	$P1 = 101.3$	$P2 = 0.035$
$a0 = 6.107799961$	$a1 = 4.436518521 \times 10^{-1}$	$a2 = 1.428745805 \times 10^{-2}$
$a3 = 2.650648471 \times 10^{-4}$	$a4 = 3.031240396 \times 10^{-6}$	$a5 = 2.034080948 \times 10^{-8}$
$a6 = 6.136820929 \times 10^{-11}$		

Combining Equ. 54, Equ. 55, Equ. 56 and Equ. 57 give an expression (Equ. 58) by which the error in measurement due to the combined effects of environmental changes on the capacitance sensors may be calculated. The same error is applicable to all axes.

$$d_1 = \left\{ \frac{\frac{1}{T1}\left(1553.9\frac{Ptot + P1 - P0}{Ptot} + 2663.6\left(P2\left(\frac{Ptot + P1 - Po}{Ptot}\right)\right) + 1259.3\left(1 + \frac{5748}{T1}\right)\right)}{1 \times 10^6\, C} + \frac{1}{C} \right\}$$

$$\times\, \varepsilon_0 A\{1 + 2\alpha(T1 - T0) + \alpha^2(T1 - T0)^2\}$$

$$d_0 = \frac{1}{C}\left\{ \left\{\frac{1553.9\frac{p1}{T0} + 2663.6\frac{p2}{T0} + \frac{1259.3}{T0}\left(1 + \frac{5748}{T0}\right)RH0}{1 \times 10^6} \right\} \times \left\{\frac{\left\{a0 + T\left\{a1 + T\left(a2 + T\left(a3 + T(a4 + (a5 + a6))\right)\right)\right\}\right\}}{10000}\right\} + 1 \right\} \varepsilon_0 A$$

$$\text{Error} = d_1 - d_0$$

The significance of the possible environmentally induced biases can be deduced from Equ. 58 (1.4 nm.K^{-1} due to thermal expansion of the particular capacitance plates, 9 nm.K^{-1} due to thermally induced changes to relative permitivity, 0.06 nm.(%RH)$^{-1}$ due

to the effect of %humidity on relative permittivity and –0.8 nm.(kPa)$^{-1}$ due to the effect of changing pressure on relative permittivity).

These capacitance measurement biases are calculated in both the driving and monitoring programs. The biases are then subtracted from the mapped command positions in the case of the Driving program while they are added to the capacitance measured positions in the case of the Monitoring program.

5.2.5.2   Corrections for reference axis non-orthogonality

The measurement axes of the calibrating interferometers may not be orthogonal. If command and measured positions are assumed to be in terms of the Cartesian coordinate system, without cognisance of possible interferometer measurement axis angular offsets, then considerable positioning errors could result.

The diagrams in Fig. 124 illustrate how all the instrument axes may tilt away from the Cartesian ideal to a greater or lesser extent. If the variables X, Y and Z are the Cartesian coordinates of a single point, then $X1$, $Y1$ and $Z1$ are the instrument coordinates of the same point. β is the angle that the instrument Z axis makes with the Cartesian Z axis in the direction of the X axis, τ is the angle the instrument X axis is tilted towards the Z axis, while α is the tilt angle of the Y axis in the direction of X axis and θ is the angle by which the X axis tilts towards the Y axis. The tilts of the Y axis towards Z axis and that of the Z axis towards the Y axis could also be considered, but are not necessary in order for positions described in one system to be translated to the other.

The specially designed bracket described in Section 4.4 in conjunction with the 'Angular measurement' program allows the angles between the instrument measurement axes to be effectively measured.
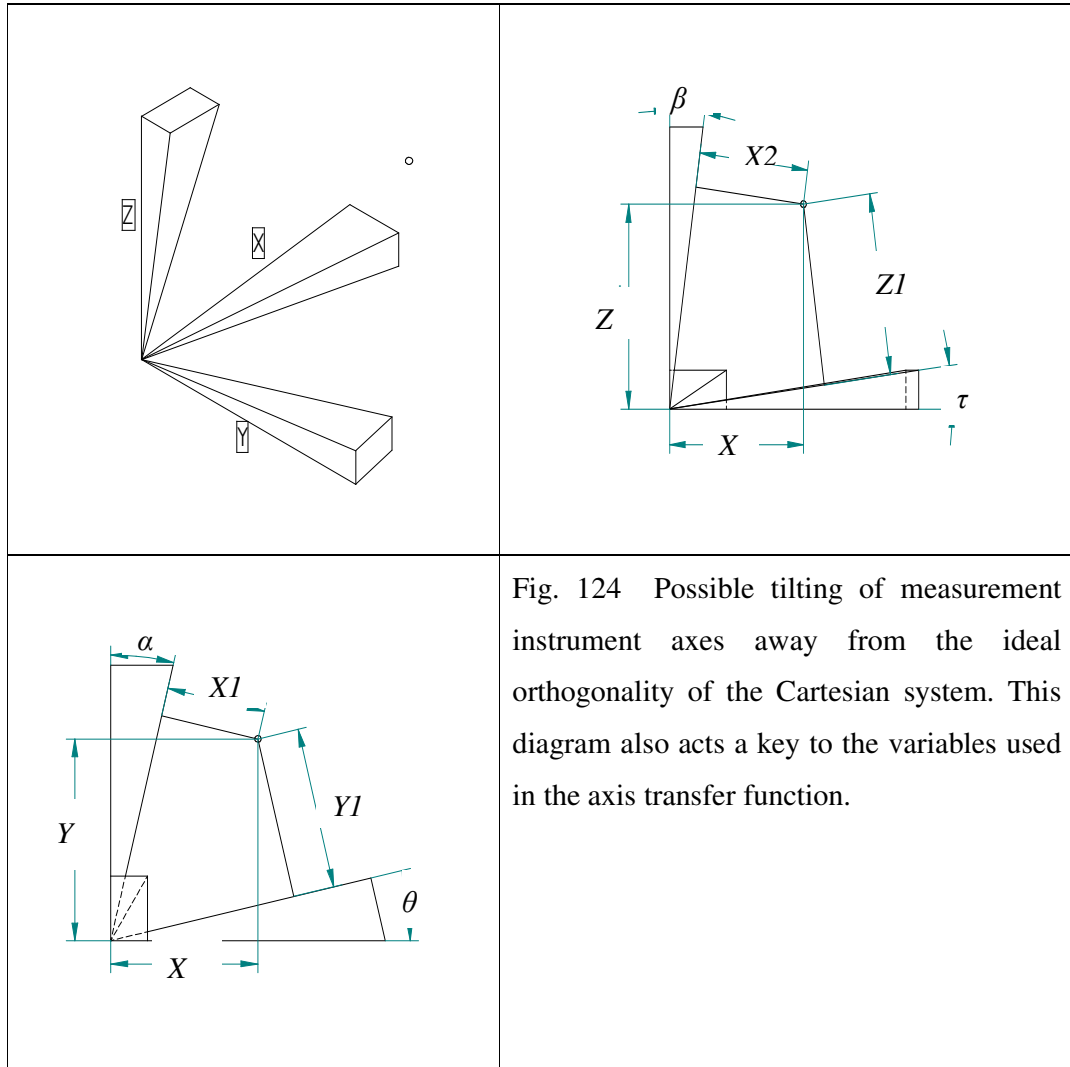
Fig. 124 Possible tilting of measurement instrument axes away from the ideal orthogonality of the Cartesian system. This diagram also acts a key to the variables used in the axis transfer function.

The position coordinates recalled from file by the 'Driving program' and having been previously generated in the 'Commands' program, are in terms of the Cartesian system. These are translated to instrument coordinates via the following functions (Equ. 59)

$$x1 = x \cos(\alpha) - y \sin(\alpha)$$
$$y1 = y \cos(\theta) - x \sin(\theta)$$
$$z1 = z \cos(\tau) - x \tan(\tau)$$

<div align="right">Equ. 59</div>

These equations are based on trigonometry of the diagrams in Fig. 124.

The positions measured using the capacitance sensors are measured relative to the instrument coordinates. These are translated into Cartesian coordinates in the

<div align="center">167</div>

'Monitoring' program via the following functions that are also based on the trigonometry of the diagrams of Fig. 124;

$$x = \frac{\frac{y1 \sin \alpha}{\cos \theta} + x1}{\cos \alpha - \tan \theta \sin \alpha}$$

Equ. 60

$$y = \frac{\frac{x1 \sin \theta}{\cos \alpha} + y1}{\cos \theta - \tan \alpha \sin \theta}$$

Equ. 61

$$z = \frac{\frac{z1 \sin \beta}{\cos \beta} + x2}{\cos \beta - \tan \tau \sin \beta}$$

Equ. 62

This chapter has so far looked at the use of LabView and MathCad programs, tailor written for this thesis, to calibrate the capacitance sensors, to generate the command sequences for contouring or scanning, to apply error mapping in order to reduce non-linearity and to compensation for environmental changes and non-orthogonal measurement axes. Since contouring is a system requirement, it is now necessary to consider the dynamic behavior of the stage with a view to its optimization.

5.3 Dynamic behaviour

The response of the stage to a step input should be rapid, exhibiting no overshoot, while subsequently it should reach steady state at the position commanded in as short a time as possible. In this section, each axis of the stage is analyzed in order to predict the open-loop response, the results of which are used to determine provisional PI controller tuning settings. The closed-loop response, using these settings, is then predicted.

5.3.1 The open loop system

The experimentally obtained open loop step response of the single axis stage is given in Fig. 125. The Fig. 125 plot indicates a slightly under damped second order system.

It can be deduced from the plot that the % overshoot is approximately 14 % and by rearranging the standard equation for calculating % overshoot (Equ. 63), the value of the apparent damping ratio for this stage can be estimated to be as large as approximately 0.53.

$$\%OS = 100e^{-\left(\zeta\pi\sqrt{1-\zeta^2}\right)}$$

$$\zeta = \sqrt{\frac{(\ln|\%OS|)^2}{(\ln|\%OS|)^2 + \pi^2}}$$

Equ. 63
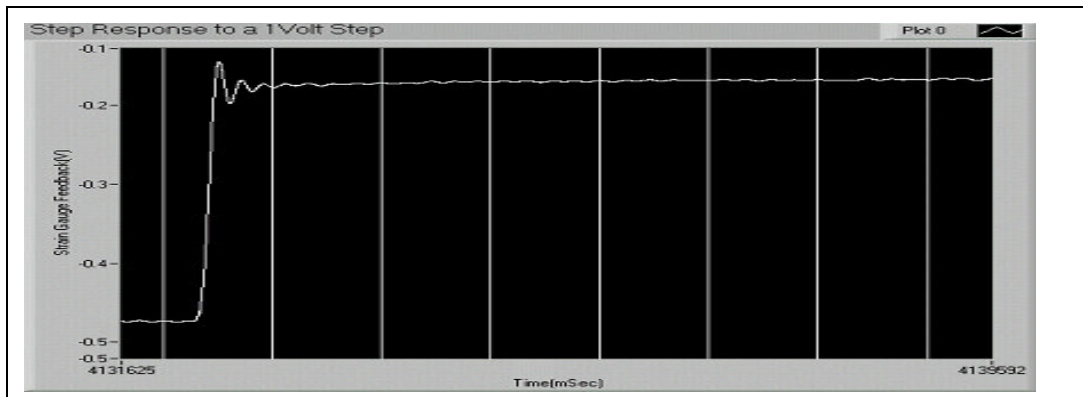
Fig. 125 The open loop step response of the single axis prototype stage

As discussed in Section 2.7, Hicks et al. [37] represent the open loop response of a monolithic flexure guided stage as a mass/spring/damper arrangement for which the transfer function is given as

$$G(s) = \frac{1}{\frac{1}{\omega_n{}^2}s^2 + \frac{1}{\omega_n Q}s + 1}$$

(Equ. 17, Section 2.7)

$$where \quad Q = \frac{\text{response at resonance}}{\text{response at dc}}$$

Also, since $Q = \dfrac{1}{2\zeta}$, the transfer function can be written as

$$G(s) = \cfrac{1}{\cfrac{1}{\omega_n{}^2}s^2 + \cfrac{2\zeta}{\omega_n}s + 1}$$

<div align="right">Equ. 64</div>

where ζ is the damping ratio and the system resonant frequency can be calculated using the following standard formula

$$f_0 = \frac{1}{2\pi}\sqrt{\frac{k_T}{m_{eff}}}$$

<div align="right">(Equ. 22, Section 3.8.2)</div>

f_0 is the natural frequency of the freely oscillating piezo (18 kHz for the piezo in question), k_T is the stiffness of the piezo stack (57 kN(μm)$^{-1}$ for the piezo in question), m_{eff} is the total effective mass (including the effective mass of the piezo, the mass of the stage, the mass of the mirrors, capacitors, mounts etc.).

Using an inverse LapLace transform the equivalent differential equation in the time domain can be shown to be

$$\frac{\mathrm{d}^2x}{\mathrm{d}t^2} + 2\zeta\omega_n\frac{\mathrm{d}x}{\mathrm{d}t} + \omega_n^2 x = 0$$

<div align="right">Equ. 65</div>

This equation is the common equation that describes a damped freely oscillating (not driven) mass suspended by a spring or, in effect, a stage suspended by flexures, the damping being provided by the material itself. Monolithic flexure guided stages are resonant and virtually undamped, having damping ratios of approximately 0.06 [27].

According to the actuator suppliers, Physik Instrumente [27], the voltage on the piezo after a switching event is given by

$$u(t) = u_0 + u_{PP}\left(1 - e^{-t/RC}\right)$$

<div align="right">Equ. 66</div>

where $u(t)$ is the voltage at time t, u_0 is the initial voltage, u_{PP} is the peak to peak drive voltage, R is the resistance in the drive circuit, and C is the piezo actuator capacitance.

The transfer function for the power supply/piezo capacitance is based on the laplace transform of Equ. 66 as follows

$$L\left(1 - e^{-\frac{t}{RC}}\right)s = \frac{1}{s} - \frac{1}{s + \frac{1}{RC}} = \frac{1}{s}\left(\frac{\frac{1}{RC}}{s + \frac{1}{RC}}\right)$$

<div align="right">Equ. 67</div>

Fig. 126 Step response of power supply and piezo actuator
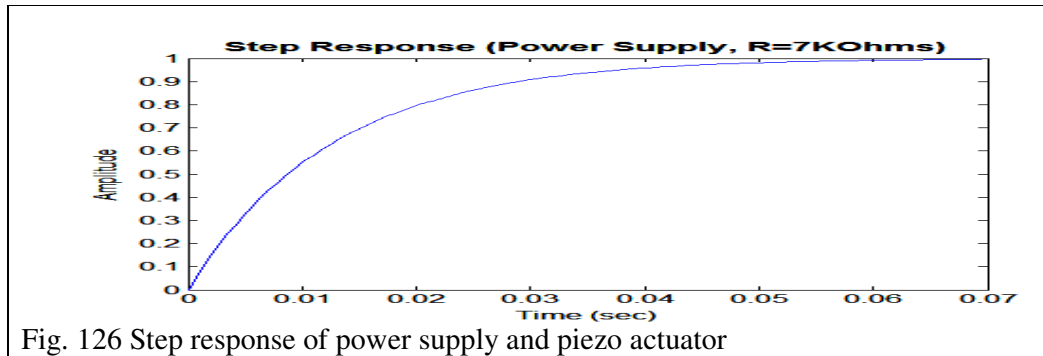
Since the E-610 controller amplifier driving electronics has variable resistance up to 10 kΩ and given that the P-841.10 actuator has an electrical capacitance of 1.8 μF, then, using the transfer function of Equ. 67, the expansion of the free piezo can be expected to exhibit the first order response illustrated in Fig. 126. Fig. 126 illustrates the strong influence of the capacitance of the piezo stack and the drive capacity of the electronics on the slew time of the stage.

The open loop transfer function derived for the combination of the power supply/actuator with the mass/spring damper arrangement of the stage and flexures is shown in Fig. 127.

Fig. 127 Open loop transfer function for the combined power supply, piezo actuator, stage and flexures
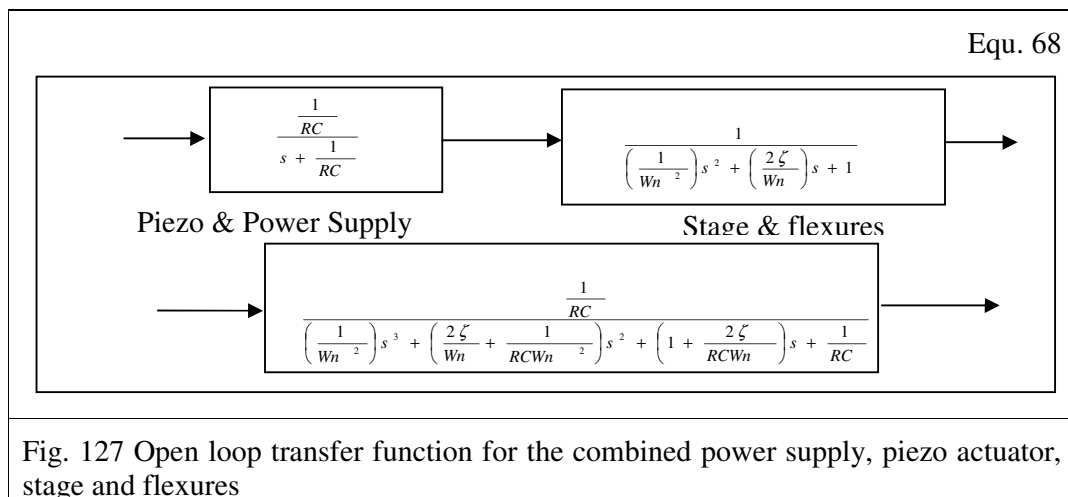
The step response based on this function is given in Fig. 128. The plot indicates an under-damped response with an overshoot of approximately 11 %.

These calculations are based on variables that are subject to error and uncertainty. The piezo, for example, is specified with a stiffness of 57 N.$(\mu m)^{-1}$ ± 20 %. In this context, the predicted response is regarded as being in reasonable agreement with the experimental step response results depicted in Fig. 125.
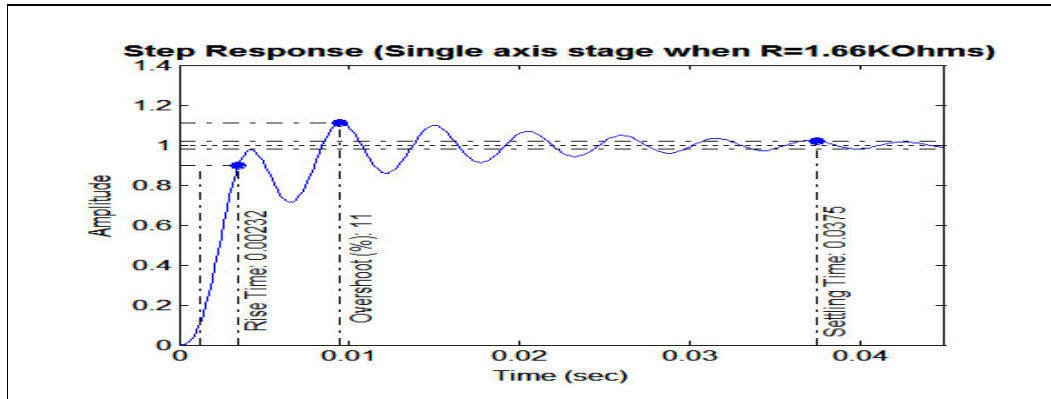
Fig. 128 Predicted open loop response of the single axis prototype stage, based on the transfer function given in Fig. 127 and assuming the power supply driving electronics to have a resistance of 10 kΩ and the stage/flexures to have a damping ratio of 0.06 with a resonant frequency of 181 Hz.

As the same actuators and controllers are used to drive each of the three instrument axes, expected systematic differences in the predicted open loop responses are due only to the different mechanical properties of the axes. Tabulated in Table 14 are the mass, stiffness, natural frequencies and damping ratios for each 3D instrument axis as well as for the single axis prototype stage. The indicated mass values are inclusive of the stage structures and the metrology components, while the stiffness values are those previously calculated and tabulated in Table 6. Using these values with Equ. 22, the indicated axial natural frequencies were calculated.

	Single axis prototype stage	X axis	Y axis	Z axis
Mass (kg)	0.7	0.812	0.457	0.238
Stiffness (N.μm^2)	0.91	5.98	5.98	5.166
Wn (Hz)	181.46	431.9	475.72	741.5
Table 14 Data used in the open and closed loop transfer functions				
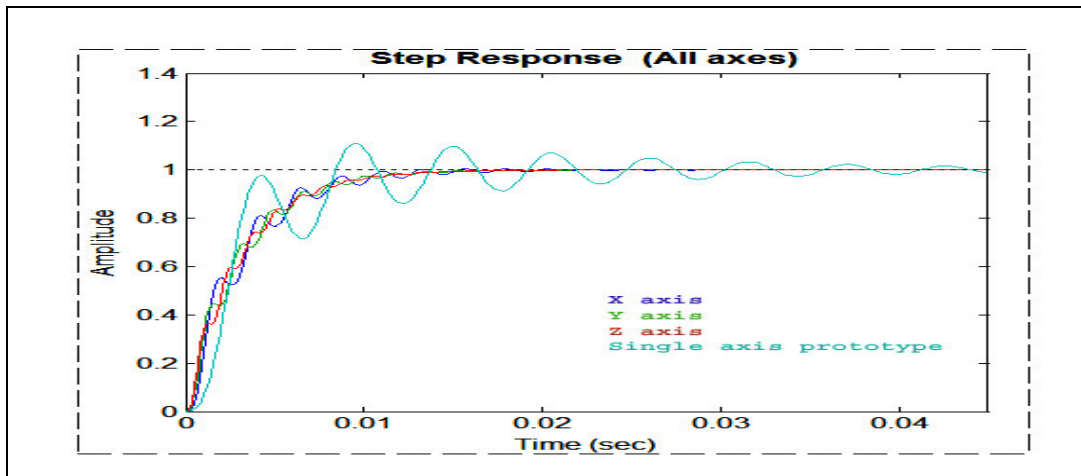
Fig. 129 The predicted open loop step response

Plots given in Fig. 129 and Fig. 130 show the predicted dynamic step and Bode response of each axis based on the data of Table 14 and the open loop transfer function (Equ. 68).
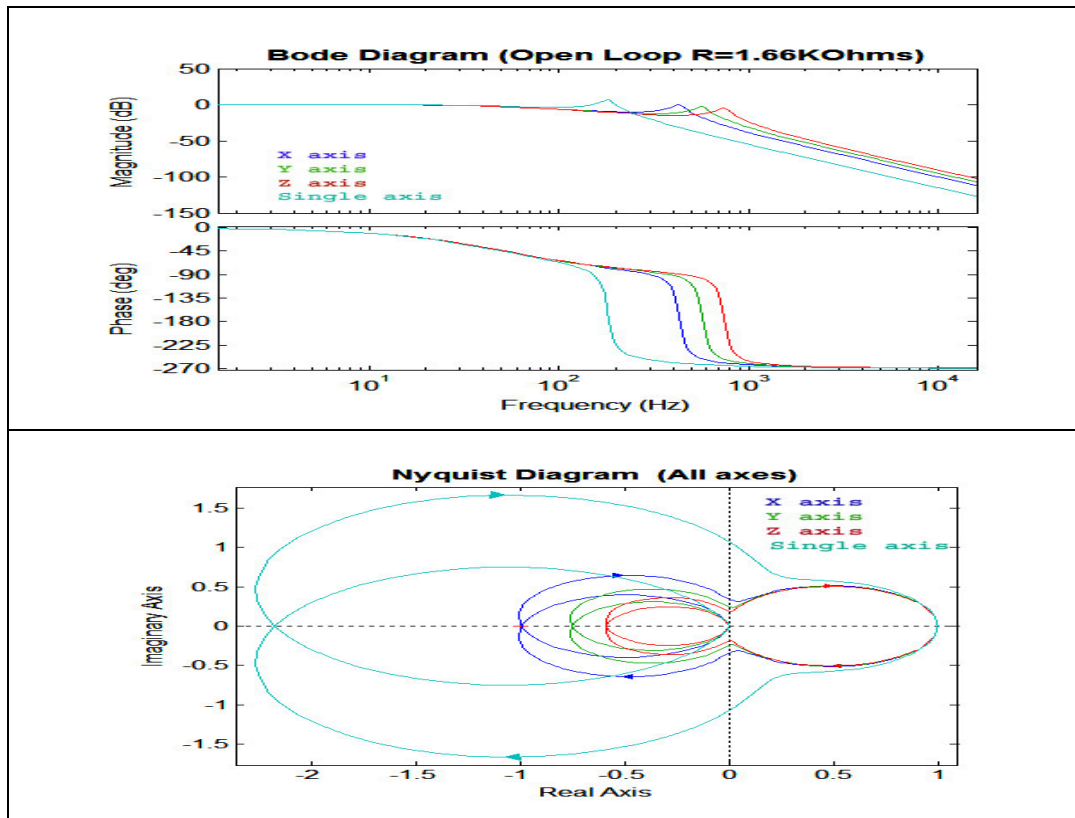
Fig. 130 Open loop bode and nyquist plots for each axis.

173

The phase and gain margins, the common indicators of stability, were calculated for each axis using MathLab. These, along with the % overshoot, rise time and settling time characteristic parameter values are tabulated in Table 15.

	% Overshoot	Rise Time (ms)	Settling Time (ms)	Gain Margin (dB)	Phase Margin (deg)
Single Axis prototype	11	2.3	37.5	-6.77 at 185 Hz	-44.05 at 200 Hz
X axis	0.42	5.4	12.6	0.05 at 435 Hz	1.44 at 435 Hz
Y axis	0.02	5.8	12.7	2.46 at 579 Hz	-180 at 0 Hz
Z axis	0	6.7	11.6	4.61 at 745 Hz	-180 at 0 Hz

Table 15 Predicted open loop characteristics.

The step response curves (Fig. 129) indicate each axis to be underdamped, with differing overshoot levels and settling times, while the Bode plot indicate the instrument axes to be stable (the gain 0 dB crossover frequencies are smaller than those at the phase -180^0 crossovers). Additionally, the Nyquist plots do not encircle the point (-1, 0).

This is not the case for the single axis prototype stage. It is predicted that this becomes unstable near its resonance frequency as is illustrated by its Bode plot (Fig. 131).
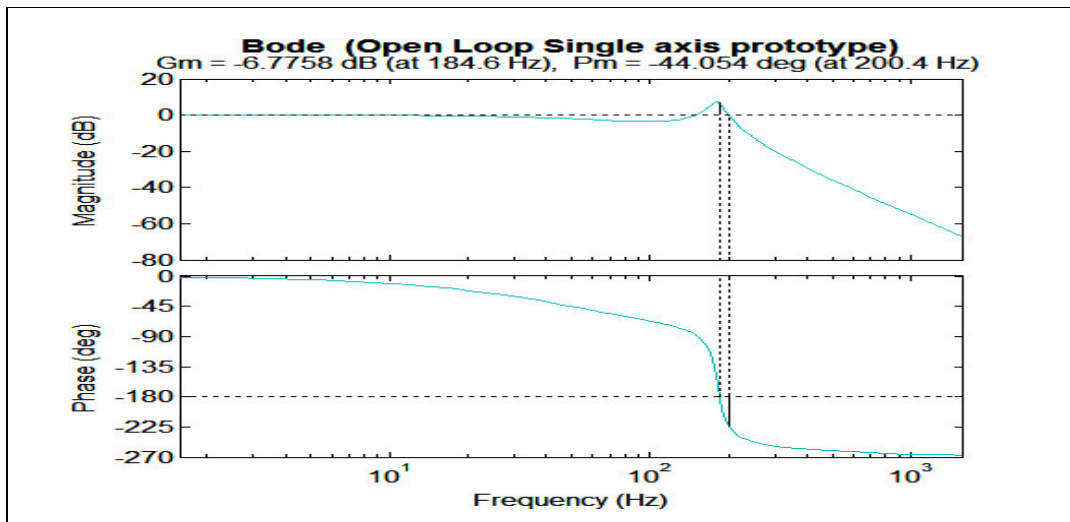
Fig. 131 Bode plot of the open loop response of the single axis, indication loss of control near its natural frequency.

174

The analysis of the open loop system indicates that the 3D instrument axes are much more stable than the single axis stage. This is due to the higher stiffness values of their flexures and consequent higher resonant frequencies. Moreover, the instrument axes are extremely well balanced. The stage moves at approximately the same speed along each axis, resulting in rise times that differ from each other by as little as 1.3 ms.μm^{-1} and all settle to within 2 % of their final position within 1.1 ms of each other. Even though these are excellent characteristics for a 3D stage operating in open loop, piezo hysteresis has not been factored into the model and the step response curve (Fig. 129) indicate that the movement of the stage is not smooth and although the maximum %overshoot is only 0.42 % (for the X axis), it represents an overshoot of 4.2 nm(μm)$^{-1}$ step (significant in the context of nanopositioning). In order to eliminate hysteresis, to increase the speed of response, to reduce the settling times and to eliminate overshoot, closed loop response must be used.

5.3.2   The closed loop system

The closed loop control system is schematically described in Fig. 132. In addition to blocks representing the power supply, the piezo, the stage and flexures, this diagram also includes blocks representing a proportional integral controller, a notch filter and a position senor.

Fig. 132 Schematic of the closed loop system
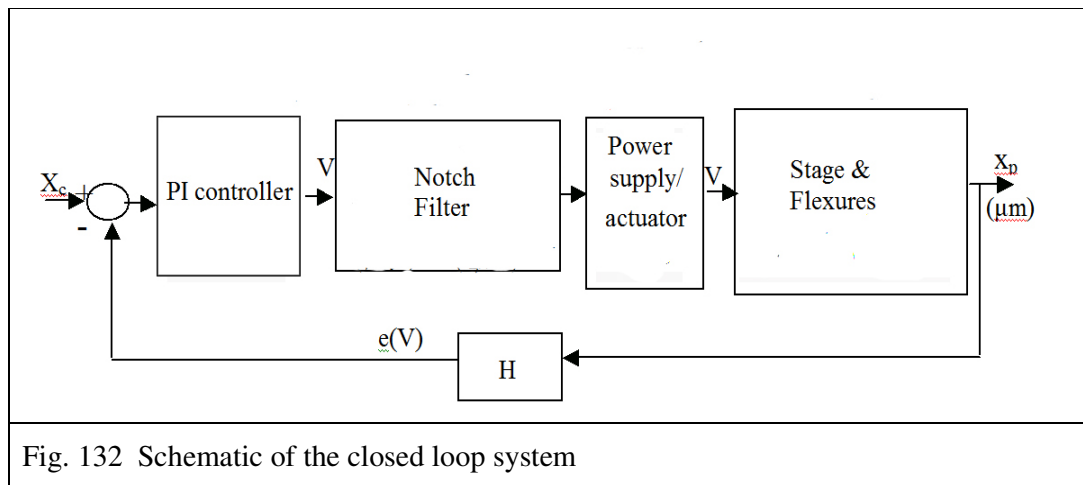
<u>The proportional integral controller</u>

In the time domain, the action of this PI controller can be mathematically represented as

175

$$x_p = x_c = k_c \left(e(t) + \frac{1}{T_i} \int e(t) dt \right)$$

<div align="right">Equ. 69</div>

where $e(t)$ is the difference between the desired position (x_C) and the measured position (x_p) while k_c is the controller gain and T_i is the integral time.

In the s-domain, this becomes

$$L \left(x_c + k_c \left(e(t) + \frac{1}{T_i} \int e(t) dt \right) \right) s = k_c \left(1 + \frac{1}{T_i s} \right) = \frac{k_c(T_i s + 1)}{T_i s}$$

<div align="right">Equ. 70</div>

The notch filter

The purpose of the notch filter is to prevent damaging oscillations at the resonant frequencies of the individual axes. The transfer function used here (Equ. 71), representing the action of the notch filter, is the same as that presented by R. Glöß [74]. It can be deduced from Equ. 71 that its contribution to the system is to place zeros at s equal to $\pm j\omega$. These are close to and effectively neutralize the poles generated by the plant at resonance.

$$\frac{V_{out}}{V_{in}} = \frac{\frac{1}{\omega_n^2} s^2 + 1}{\frac{1}{\omega_n^2} s^2 + \frac{1}{\zeta \omega_n} s + 1}$$

<div align="right">Equ. 71</div>

The system transfer function

The schematic in Fig. 133 represents arrangement of the closed loop system and illustrates the relationship between the constituents and the flow of data.
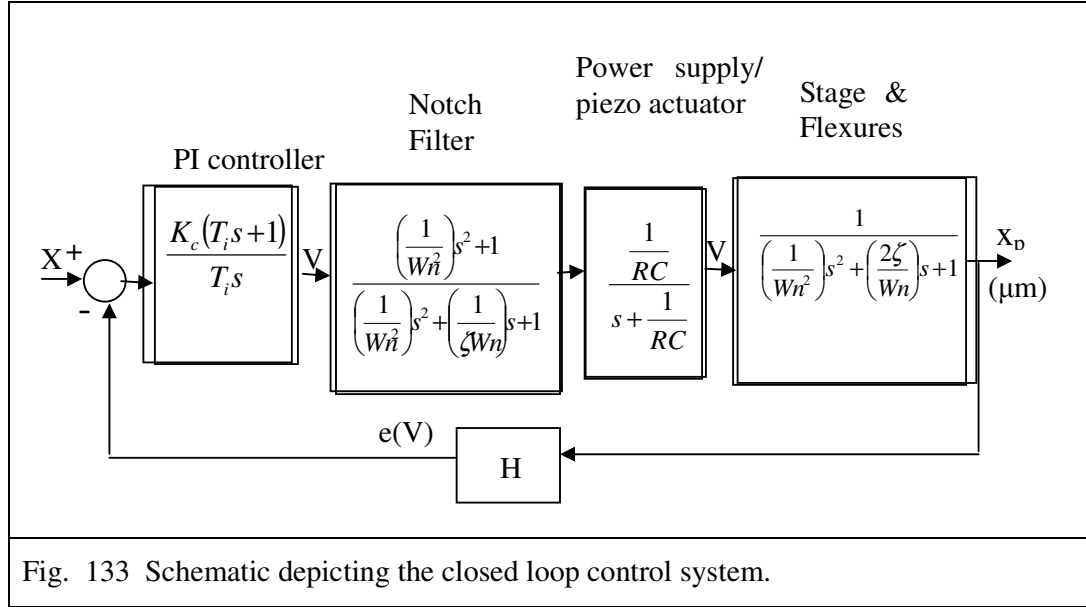
Fig. 133 Schematic depicting the closed loop control system.

$$\frac{Xp}{Xc}$$

$$= \frac{\left(\frac{K_c T_i s + K_c}{T_i s}\right)\left(\frac{1 + \left(\frac{1}{\omega_n^2}\right)s^2}{1 + \left(\frac{1}{\omega_n \zeta_n}\right) + \left(\frac{1}{\omega_n^2}\right)x^2}\right)\left(\frac{\frac{1}{RC}}{s + \frac{1}{RC}}\right)\left(\frac{K_p}{\left(\frac{1}{\omega_n^2}\right)s^2 + \left(\frac{2\zeta}{\omega_n}\right)s + 1}\right)}{1 + H\left\{\frac{K_c T_i s + K_c}{T_i s}\left[\left(\frac{1 + \left(\frac{1}{\omega_n^2}\right)s^2}{1 + \left(\frac{1}{\omega_n \zeta_n}\right) + \left(\frac{1}{\omega_n^2}\right)s^2}\right)\left(\frac{\frac{1}{RC}}{s + \frac{1}{RC}}\right)\left(\frac{K_p}{\left(\frac{1}{\omega_n^2}\right)s^2 + \left(\frac{2\zeta}{\omega_n}\right)s + 1}\right)\right]\right\}}$$

Equ. 72

The value of the integral times used (Ti) are simple multiples of the rise times of the open loop axial response curves, summarized in Table 15. This approach is based loosely on the standard 'Direct Synthesis' method for tuning PI controllers where

$$K_c = \frac{T_p}{K_p(\theta_p + T_c)} \quad \text{and} \quad T_i = T_p$$

Equ. 73

where Kc is the controller gain, Kp is the process gain, θp is the process dead time (zero seconds), Tc is the closed loop constant (approximately = the settling time), Tp is the process time constant (time to 63 % of change in set-point).

$K_c \approx 1/K_P$, therefore, $T_P \approx T_c$. So, $Ti \approx T_P$. The open loop rise time (2.3 ms for the X axis) was thus taken as a first approximation of the integral time. The value of Ti was

then refined through a trial and error approach. A *Ti* value of 0.003 s was eventually chosen as the overshoot was reduced to 0.13 %. Larger values would eliminate overshoot, but at the expense of longer rise times.

The systematic experimental approach of the Ziegler-Nichols method, for example, may be more effective for the purpose of instrument commissioning. Indeed the manufacturers of the controller provide concise instructions as to its tuning. Although the tuning parameters determined in this analysis may provide good initial approximations as to the optimum settings, the experimental approach bypasses the parameter uncertainties associated with the analysis. On the other hand, the model based tuning method used here allows for pre-build theoretical analysis of the dynamic behaviour of the stage, a worthwhile and necessary phase in the design of any precision contouring instrument.

The dynamic response of the closed loop system was predicted using Equ. 72, the measured and calculated data given in Table 14 and the parameter values summarized in Table 16. Included in Table 16 are the characteristic gains of the controller (*Kc*) and that of the plant (*Kp*), the resistance of the power electronics (*R*), the capacitance of the piezo stack (*C*), the damping ratios of the plant (ζ) and of the notch filter (ζn) as well as the calculated natural frequencies (*Wn*). *Kc*, *R* and *C* are obtained from the controller manual while the ζ and ζn values are based on information obtained directly from the manufacturers, Physik Instrumente [27]. *Kp* is calculated by dividing the calculated maximum axial stroke length (see Section 3.8.2) by the output controller voltage (100 V), while the previously calculated *Wn* value is taken from Table 14.

	Kc	*Kp*	*H*	*Ti* (ms)	*R* (kΩ)	*C* (μF)	ζ	ζn	*Wn* (Hz)
X axis	10	0.136	1	3	1.66	1.8	0.06	0.6	431.9
Y axis	10	0.136	1	3	1.66	1.8	0.06	0.6	575.7
Z axis	10	0.138	1	3	1.66	1.8	0.06	0.6	741.5
Table 16 The values used to predict the closed loop response of the three axes.									

| Fig. 134 Nyquist plots for the three instrument axes | Fig. 135 Root locus for the three instrument axes |
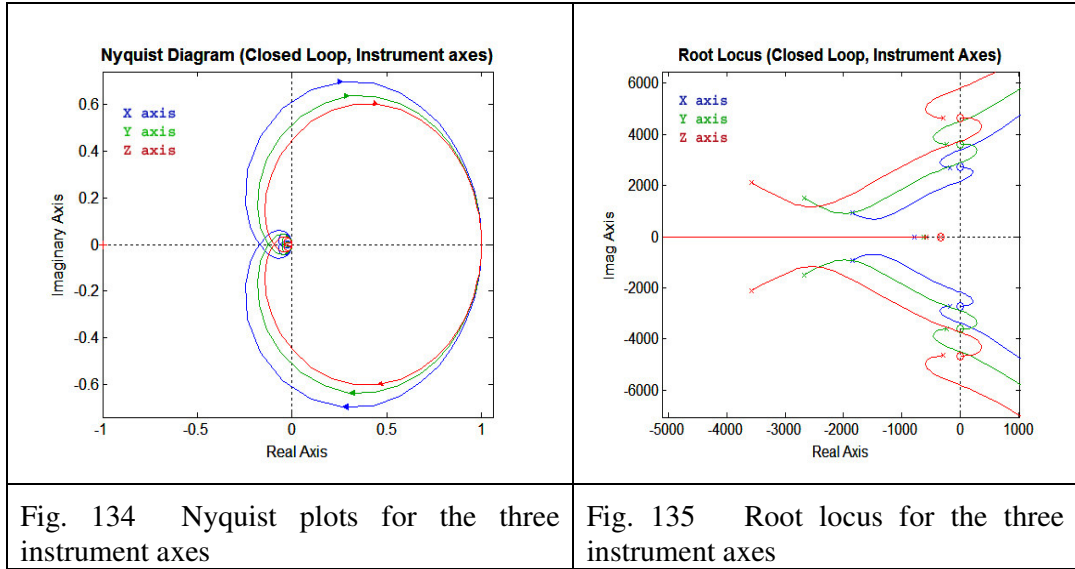
Fig. 134 and Fig. 135 show the Nyquist and root locus plots for all three axes. In accordance with the Nyquist criterion for stability, the point (-1,0) is not encircled in the Nyquist plot, while the root locus plot shows that all the poles and zeros are on the left hand side of the s plane. It can be deduced from these observations that the designed system is stable.

The expected step response for each axis is illustrated in Fig. 136 and the key response parameters are tabulated in Table 17. It can be deduced from the step response graphs that a smooth rapid (< 7.2 ms to reach 1 μm) response can be attained. Additionally, each of the stage axes are predicted to move at almost the same speed since the range of settling times is only 0.68 ms for a 1 μm step.

Fig. 136 Predicted step response of the close loop response
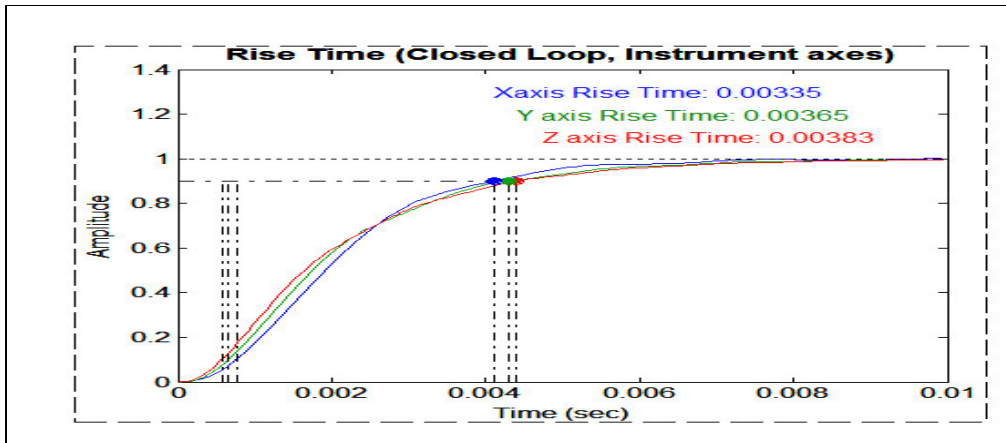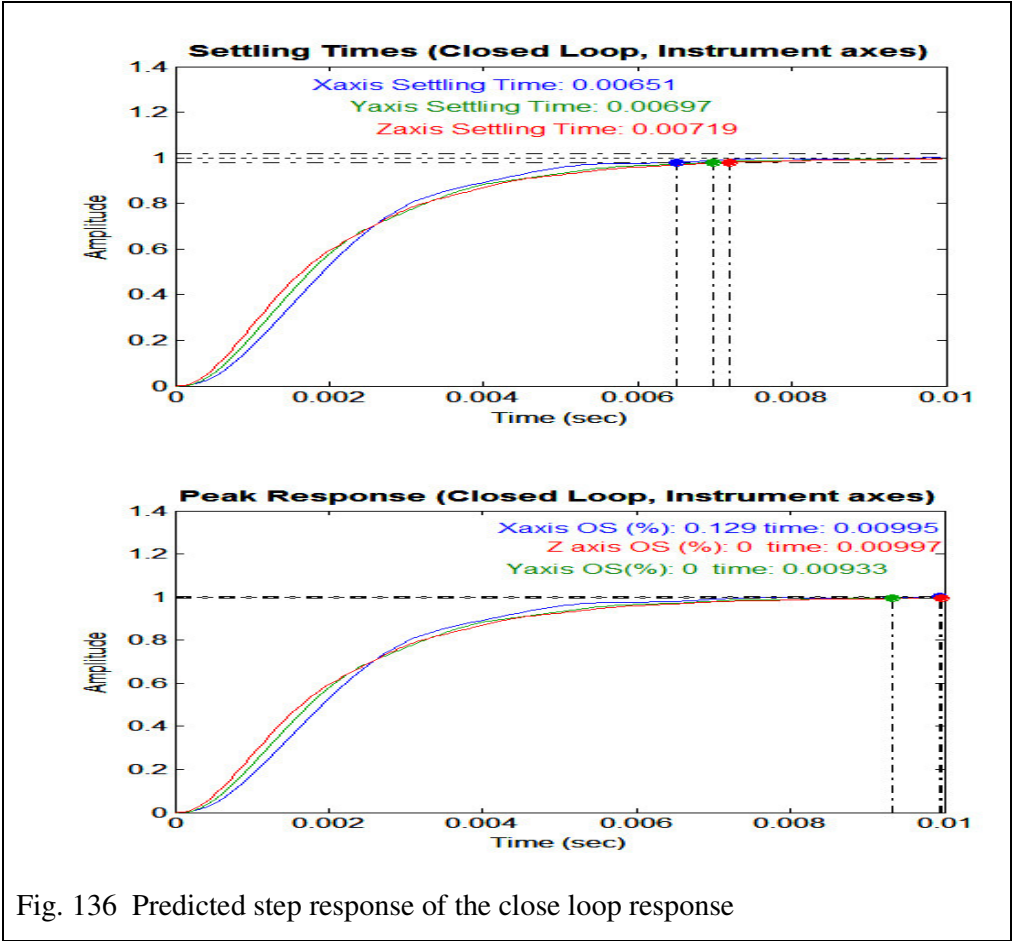
	Rise Time (ms)	% Overshoot	Settling Time (ms)	Gain Margin (dB)	Phase Margin (deg)	Bandwidth (Hz)
X axis	3.35	0.129	6.51	14.46 at 346 Hz	180 at 0 Hz	120
Y axis	3.65	0	6.97	18.18 at 461 Hz	180 at 0 Hz	94.5
Z axis	3.83	0	7.19	20.48 at 594 Hz	180 at 0 Hz	89.9
Table 17 Expected instrument axis step response parameters.						

Bode Diagram (Closed Loop, Instrument axes)

Bode Diagram (Closed Loop, X axis)
Gm = 15.329 dB (at 346.1 Hz), Pm = -180 deg (at 0 Hz)
Bandwidth Frequency (Hz): 107,
Magnitude (dB): -2.99

Bode Diagram (Closed Loop, Y axis)
Gm = 18.185 dB (at 461.2 Hz), Pm = 180 deg (at 0 Hz)
Bandwidth Frequency (Hz): 94.5
Magnitude (dB): -3

Bode Diagram (Closed Loop, Z xis)
Gm = 20.481 dB (at 594.08 Hz), Pm = 180 deg (at 0 Hz)
Bandwidth Frequency (Hz): 89.9
Magnitude (dB): -3

Fig. 137 The bode plots for each axis shown individually, in order that the gain and phase margins can be deduced

181

The stability indicators (the gain and phase margins), as well as the band width (assumed to be the frequency at which the magnitudes is –3 dB) are taken from the individual axis bode plots given in Fig. 137 and are also tabulated in Table 17.

The theoretical analysis carried out in Section 5.3 yields system information critical to the design of the contouring stage and forms part of the iterative design process. It showed that by using well tuned notched closed loop control with the designed mechanical system, an axially balanced smooth rapid response with no overshoot and short settling times is possible. If this proved not to be the case, redesign of either the mechanical or control system would have been necessary.

The Table 16 parameters have associated uncertainties, but it is possible to use methods described in GUM [23] to estimate the quality of predictions subject to these uncertainties. For the purposes of this thesis, this is not considered necessary since uncertainties in prediction are replaced by uncertainties in metrology when subsequent physical tuning and experimentation is used. Matters pertaining to these uncertainties are addressed in Chapter 6.

5.4   Summary and discussion

The schematic diagram presented in Fig. 111 illustrates the command and control system required to facilitate the highly accurate and precise positioning and monitoring of the stage. The chapter describes how a suite of control programs that were written specially for this thesis, enable automated sensor calibration, environmentally induced bias compensations, instrument/Cartesian coordinate axis transformations along with positioning/command linearisation. The functionality of the individual interdependent LabView and Mathcad programs has been outlined in Section 5.2 and soft copies of the actual programs are presented.

Section 5.3 examines the system axial dynamic characteristics. By modelling the stage and flexures as mass/spring/dampers and the piezo actuators as charging capacitors, the open loop transfer functions are identified and the step response for each axis is predicted. The transfer function is then derived for the closed loop arrangement of the mechanical stage/actuator and power supply coupled with a proportional integral controller and a notch filter. By using appropriate parameter and PI tuning values, overshoot is avoided, while rise and settling times are minimized.

The theoretical analysis of the systems dynamic behaviour served two purposes: (a) the requirement of the design process to establish that the instrument is capable of precision contouring and (b) the need, in order to answer the research question, to establish the essential parameters to be included when specifying such a system.

In conclusion, the command and control system described in this chapter provides for robust, flexible and accurate positioning/monitoring. But even though the instrument performance is optimised and potential error biases have been compensated for wherever possible, uncertainties associated with error sources still exist. Addressing the issue of these uncertainties is the subject of the next chapter.

Chapter 6

6 Uncertainty in the Metrology System

6.1 Introduction

In this chapter the component uncertainties associated with the measurement systems designed for this thesis are investigated and quantified, thus leading to the calculation of a combined instrument measurement uncertainty. An uncertainty table is constructed similar to that presented by Castro [41] and in accordance with the NIST guidelines [3] as described in Section 2.3 of this thesis.

The concept of uncertainty is succinctly described by Figliola et al. [75] as follows:

"Measurement error is the difference between the true value of the variable and the measured value assigned, but the true value is not known, therefore instead of actual error, we estimate probable error. It is this estimate which is called uncertainty in the measured value. It is the interval about the measured value within which we suspect that the true value must fall."

To avoid ambiguity and misinterpretation, the evaluation and expression of measured results have been normalised by the ISO in their 'Guide to expression of Uncertainty in Measurement', (GUM) [23]. NIST followed this with a practical set of guidelines (TN1297) [3] for implementing GUM.

According to the NIST TN1297, the uncertainty of a result can be grouped into two categories, 'A' and 'B'.

- Type A: these are evaluated by statistical methods (through sampling and analysis). Each component of uncertainty is expressed as a standard uncertainty u_i.

- Type B: these are evaluated by other means e.g. previously measured data, manufacturers' specifications, calibration reports etc. Each component of uncertainty is expressed as a standard uncertainty u_j.

It is suggested that Type A evaluation should be used where possible, but the guide also indicated that Type B uncertainty evaluations could be more accurate if it is only possible to acquire samples of inadequate size.

Type B uncertainties are used throughout this chapter, as it would be impractical and inefficient to carry out appropriate experimentation to determine the standard

185

uncertainties associated with displacement sensors, temperature sensors, pressure sensors, length measurement through the use of vernier callipers, machining processes such as EDM and milling, material expansion coefficients, optical mount tilt adjustment, etc.

As directed by the NIST reference, since the resolutions, quoted in manufacturers' specifications, are multiples of estimated standard deviations of test data, the standard uncertainty is obtained by dividing by the appropriate multipliers. The multiplier depends on the type of distribution of measurements at testing and the confidence level used when stating the resolution range.

For a quantity that has a rectangular distribution (values equally probable within limits) and the limits set to include all probable outcomes (100% confidence)

$$u_j = {a}/{\sqrt{3}} \quad where \quad a = {(a_+ - a_-)}/{2} \quad a_+ \text{ is the upper limit}, a_- \text{ is the lower limit}$$

Equ. 74

For a quantity modelled by a triangular distribution with limits which give 100 % confidence

$$u_j = {a}/{\sqrt{6}}$$

Equ. 75

For a normally distributed quantity with limits at ± 3 standard deviations (99.73 % confidence)

$$u_j = {a}/{3}$$

Equ. 76

Virtually no manufacturer provides information about how the tolerance limits are calculated, but it is indicated in NIST that distributions may be assumed. It is suggested that a rectangular distribution should be the default distribution used if no further information is available.

Standard uncertainties u_i and u_j can be combined using the law of propagation of uncertainty to give u_c.

$$u_c^2(y) = \sum_{i=1}^{N} \left(\frac{\partial f}{\partial x_i}\right)^2 u^2(x_i) + 2 \sum_{i=1}^{N-1} \sum_{j=i+1}^{N} \frac{\partial f}{\partial x_i} \frac{\partial f}{\partial x_j} u(x_i, x_j)$$

$$= \sum_{i=1}^{N} \left(\frac{\partial f}{\partial x_i}\right)^2 u^2(x_i) \quad \text{when } x_i \text{ and } x_j \text{ are not correlated}$$

Equ. 77

f is defined as a functional relationship, describing a measurement process that contains all quantities that can contribute to a significant uncertainty. y is an estimate of the quantity being measured, given by

$$y = f(x_1, x_2, x_3 \ldots x_N)$$

where quantities, x_i, are estimates of quantities, X_i, that determine the measurand, Y.

Expanded uncertainty, U, is obtained by multiplying u_c by a coverage factor, k (which has a value 2 by convention) i.e.

$$U = k u_c$$

Equ. 78.

($k = 2$ gives 95 % confidence while $k = 3$ gives > 99 % confidence)

Then the true value, Y, can be confidently believed to lie within the interval about the measurement

$$(y - U) < Y < (y + U)$$

The expanded uncertainty, U, for the metrology systems in this thesis has been estimated in a methodical manner similar to that described by von Martens [102].

According to GUM [23], the interdependence of effects arising from temperature, pressure and humidity often have negligible interdependence and can be assumed to be uncorrelated. Furthermore, for this thesis, correlations of common influences are avoided by introducing the influences as independent input quantities [23].

The following steps are adopted

- Every effort has been made to identify each effect that influences the measurement result.

- Functions have been derived which relate the effects to the measurement.

- A standard uncertainty u_j has been estimated for each uncertainty component, based on component suppliers' data sheets, known or assumed distributions and the partial derivatives of the above mentioned functions (the sensitivity coefficients).

Combined uncertainties have been calculated in accordance with the law of propagation of uncertainty Equ. 77, as described in GUM.

- The expanded uncertainty, U, for the instrument metrology is then the combined uncertainty multiplied by a coverage factor. When using B type uncertainty, Kirkup [76] demonstrates that the number of degrees of freedom, v, used for determining the magnitude of a coverage factor, is infinity. Therefore it is reasonable, based on the t-distribution, to choose $k = 2$ for a confidence interval of 95 % or $k = 3$ for a confidence limit of 99 %.

- any term in the equation with an infinite number of degrees of freedom is zero.

The displacement of the stage geometric centre relative to its home position at the time of calibration is the quantity to be measured. Capacitance sensors on each axis measure the stage displacement. Two pass Michelson interferometers are used to calibrate the capacitance sensors. Systematic errors associated with both in-process and calibration sensing have been identified in Sections 4.2.2 and 4.3.2. Mechanical nulling of the effects of these error sources is implemented where possible, as described in Chapter 3, while software compensation for these systematic errors is described in Sections 5.2.5.1 and 5.2.5.2. Uncertainty is associated with all corrections.

Having described the meaning of uncertainty and the standard method by which the measurement uncertainties are to be determined and expressed throughout this chapter, the component sources of uncertainty are now identified for this treatment. A cause and effects diagram is presented in Fig. 138 that outlines the manner in which uncertainty is propagated in the instrument metrology system. The structure of this chapter is guided by this propagation.

188
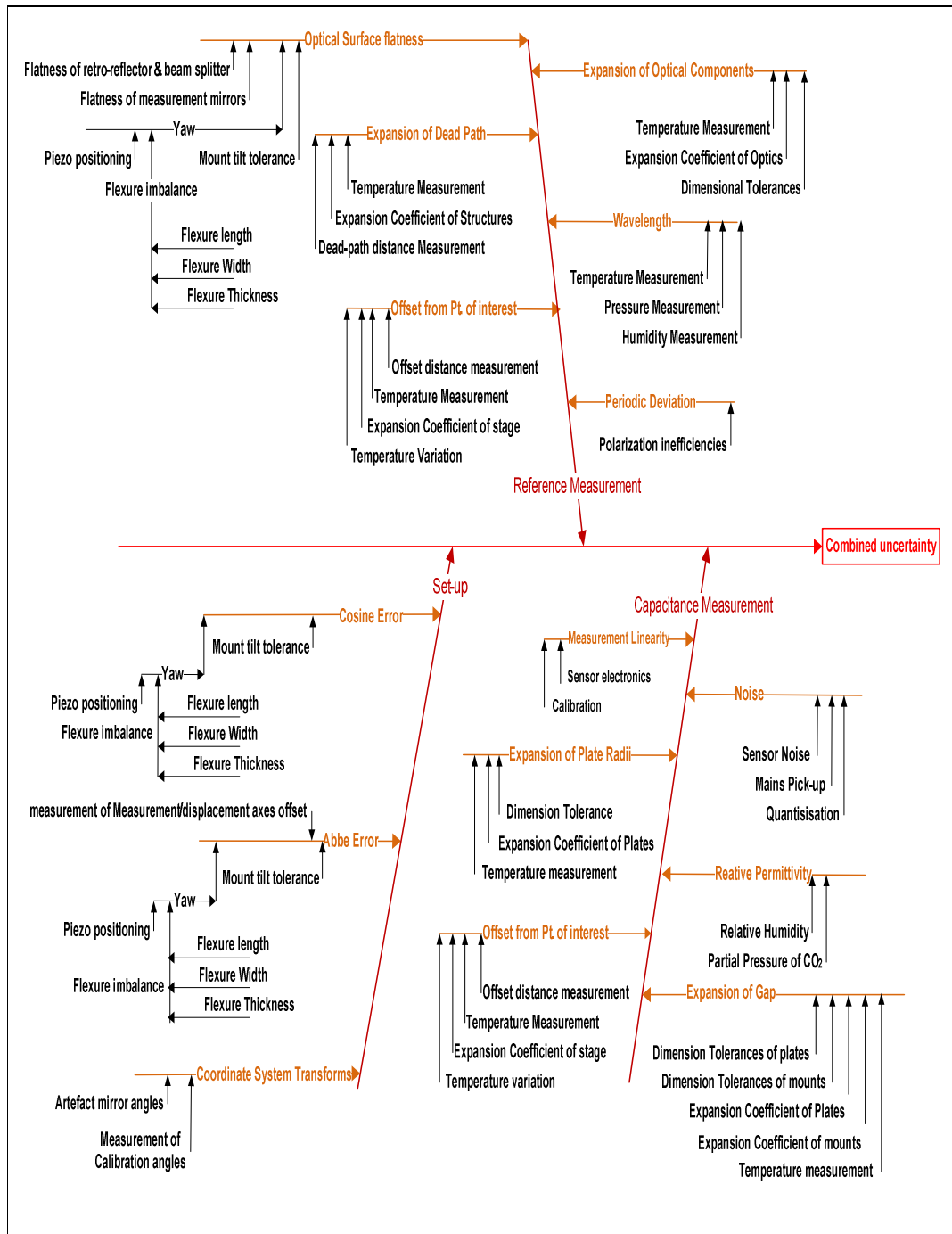
Fig. 138   Cause and effect diagram showing how uncertainty in instrument measurement is caused by a range of component uncertainties

Uncertainties associated with the capacitance measurement system are examined initially, followed by those associated with the interferometer based reference measurement system and finally the mounting arrangement for both.

189

6.2   Error sources associated with the capacitance sensors

Each axis of the stage has been designed to incorporate P-841.10 piezo actuators that are manufactured by Physik Instrumente (PI). These have a maximum unrestrained travel range of 15 µm, though the stage stroke length is somewhat shorter as a result of guidance flexure stiffness.   The capacitance sensors must be capable of accurate measurement over this range of movement.

6.2.1   Measurement linearity

As stated in Section 4.2.3, PI [27] claim that an electronics based Integrated Linearization System can deliver a 0.003 % linearity when used with their capacitance sensors. For a 15µm measurement range, a 0.003 % linearity translates to a measuring accuracy of ± 0.45 nm. Assuming a rectangular distribution, the standard measurement uncertainty due to non-linearity is

$$u_{NLC} = \frac{0.45 \times 10^{-9}}{\sqrt{3}} = 0.26 \times 10^{-9} \, m$$

When the capacitance sensor is calibrated by a single pass Michelson interferometer configuration as described in Section 4.3.1, the standard uncertainty then becomes

$$u_{NLC} = \frac{0.003\Delta}{(100)\sqrt{3}} \Rightarrow u_{NLC} = \frac{0.003\lambda}{2N_P(100)\sqrt{3}} = 0.006 \times 10^{-9} \; N_P^{-1} m$$

<div align="right">Equ.79</div>

where $\Delta = \frac{\lambda}{2N_P}$, the distance that the stage travels between calibration points and N_P is the number of passes of the measurement ray through the interferometer, while λ is the wavelength of the He-Ne laser light. Note that this value is halved if a double pass interferometer is used.

6.2.2   Noise

Electronic noise

The PI manufactured model D-015.00 capacitive sensor is used with the servo controller E-509.C3A which supplies ±5 V to the sensor with a selectable bandwidth of

0.3 to 3 kHz and a noise factor of $0.115ppm/\sqrt{Hz}$. If for instance, it is used with a 2 kHz bandwidth, the true noise displacement is $15 \times 10^{-6} \times 0.115 \times 10^{-6} \times \sqrt{2 \times 10^3} = 0.01$ nm. Because this is an rms value with no dc component, it is assumed to equal the standard deviation of displacements due to Gaussian white noise, i.e. standard measurement uncertainty due to sensor noise = 0.01 nm

Mains pickup noise
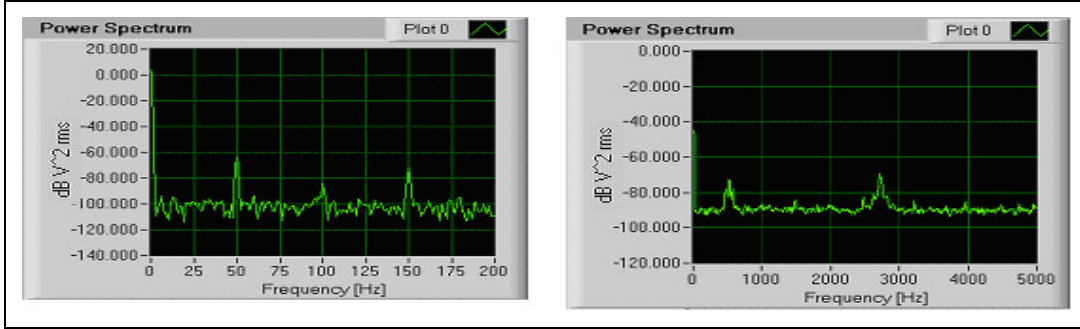
Fig. 139 Power spectra of noise in shielded sensor cable.

The V_{rms} value of the mains pickup is calculated as follows:

Using the sensor cable noise shown in Fig. 139

$$V_{rms} = \log^{-1}\left(\frac{-65}{20}\right) = 0.56 \times 10^{-3}$$

The rms value, being equivalent to the standard deviation of the noise when there is no dc component, translates to a standard measurement uncertainty of 0.84 nm when measuring displacement with a capacitance sensor of nominal range 15 μm and output of ± 5 V.

Quantisation noise

As explained in Section 2.4.4.1, this refers to the uncertainty in a signal resulting from the fact that a finite number of controller bits are used to represent it. According to Hicks et al. [37], the rms value of this measurement noise is given by

$$Quantisation\ noise = \frac{0.29d_x}{2^N}$$

Equ. 80

where d_x is the maximum measurement range and N is the number of bits.

191

Therefore for a stage with a 15 μm range and a PI manufactured E-509 [27] 16 bit controller, combined with the National Instruments 16 bit data acquisition card 6036E [72], the standard measurement uncertainty due to quantisation noise would be 0.07 nm.

The combined uncertainty noise can now be calculated in accordance with GUM [23]

$$u_{noise} = \sqrt{0.01^2 + 0.84^2 + 0.07^2} = 0.843 \text{ nm}$$

Equ. 81

This measurement uncertainty applies to all three axes.

6.2.3 Thermal expansion of capacitance plates

The uncertainty of measurement due to plate expansion depends on the following component uncertainties: uncertainty of temperature measurement, uncertainty of the plate material coefficient of thermal expansion, uncertainty of manufacturing tolerance:

Standard uncertainty due to temperature measurement

$$\text{Std. uncertainty temperature sensor}(u_{\Delta T}) = \frac{0.15}{\sqrt{3}} = 0.86 \text{ K}$$

Equ. 82

The GE Sensing/Thermoetrics [80] thermistor sensor, MC65, used for measuring the ambient temperature about the instrument, has a stated tolerance of ± 0.15 K. Assuming a rectangular distribution of temperature measurements, the standard measurement uncertainty of this component can be calculated as follows:

Standard uncertainty due to the coefficient thermal expansion (CTE) of the aluminium plates

As explained by NIST [3], the CTE of materials vary with temperature and book values are usually only averages of temperature ranges of 80 K or more. Furthermore, the range is not often provided, and when it is, there can be a bias between the average value given and the true value at the required temperature. This bias can be in the order of a few percent for a narrow averaging range, but can be greater than 10 % for wide ranges. PI states that the sensor is made of Aluminium, but does not give a CTE value. According to Bosch [77], the thermal expansion coefficient is accurate only to

±15 % for aluminium. Taking the CTE to be 24 µm.m⁻¹.K⁻¹ i.e. that of the stage material (aluminium 6082 T6) and assuming a rectangular distribution, the uncertainty in CTE can be estimated as follows

$$\text{Std. uncertainty due to CTE } (u_{Al\ \alpha}) = \frac{(24 \times 10^{-6})(0.15)}{\sqrt{3}} = 2.0785 \times 10^{-6} \text{ K}^{-1}$$

Equ. 83

Uncertainty due to manufacturing tolerance

The manufacturing tolerance for the plate diameter is 4.6 ± 0.01 mm.

$$\text{Std. uncertainty due to radius tolerance } (u_r) = \frac{0.01 \times 10^{-3}}{\sqrt{3}} = 5.774 \times 10^{-6} \text{ m}$$

The combined uncertainty in the radius due to plate expansion can now be calculated in accordance with the ISO GUM [23]

$$\text{radial thermal expansion} = \Delta r = \alpha(\Delta T)r$$

Equ. 84

where α is the thermal expansion coefficient (K⁻¹), T is the ambient temperature (K), and r is the radius (m)

$$u_{C/Rad} = \sqrt{\frac{\partial(\Delta r)^2}{\partial(\Delta T)}(u_{\Delta T})^2 + \frac{\partial(\Delta r)^2}{\partial(\alpha_{Al\ \alpha})}(u_{Al\ \alpha})^2 + \frac{\partial(\Delta r)^2}{\partial(r)}(u_r)^2}$$

Equ. 85

$$u_{C/Rad} = \sqrt{(\alpha r)^2(u_{\Delta T})^2 + ((\Delta T)r)^2(u_{Al\ \alpha})^2 + (\alpha(\Delta T))^2(u_r)^2} = 6.735 \times 10^{-9} \text{ m}$$

Equ. 86

Rearranging Equ. 12, the gap size d being measured, is expressed as a function of the plate radius, r as follows:

$$d = \frac{\varepsilon_0 \varepsilon_r \pi r^2}{C}$$

Equ. 87

The combined uncertainty in the measurement due to thermal expansion of the plates is

$$u_{MC/rad} = \sqrt{\left(\frac{\partial d}{\partial r}\right)^2 \left(u_{C/rad}\right)^2}$$

<div align="right">Equ. 88</div>

$$u_{MC/rad} = \sqrt{\left(\frac{2\varepsilon_0\varepsilon_r\pi r}{C}\right)^2 \left(u_{C/rad}\right)^2} = 0.09 \text{ nm}$$

<div align="right">Equ. 89</div>

6.2.4   Thermal expansion of plate separation distance

For accurate measurement, the capacitor plate separation distances should vary in tandem with thermal expansion of the separation distances between the stage centre and metrology reference planes. Using sensors and sensor mounts made of materials that have the same stated thermal expansion coefficient as the stage and metrology frame means that software compensation is not necessary. Nevertheless, because the materials are unlikely to be made in the same batch or even supplied by the same manufacturer, uncertainties associated with their expansion coefficients must be considered.
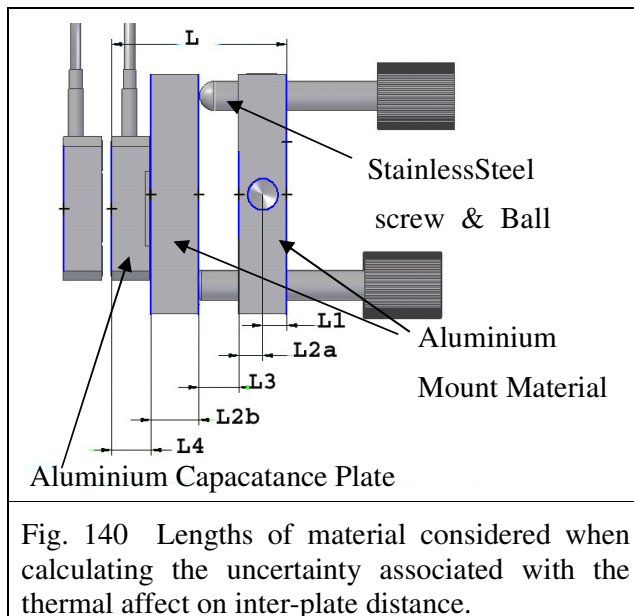
Fig. 140 presents a drawing of one of the capacitance sensors with its mount. The sensor and mount are both made of aluminium, but the separation distance between the mount base plate and its tilting plate is bridged by stainless steel bearing tipped screws. Presented also in this drawing are the dimensions considered in the calculation of this uncertainty.

StainlessSteel screw & Ball

Aluminium Mount Material

Aluminium Capacatance Plate

Fig. 140   Lengths of material considered when calculating the uncertainty associated with the thermal affect on inter-plate distance.

When $L2 = L2_a + L2_b$ and ΔT is the change in temperature from that at calibration

Δ = Actual expansion $-$ Measured expansion = $(\alpha s. L. \Delta T) - \{(L1. \alpha s. \Delta T) +$
$L2.\alpha2\Delta T + L3.\alpha3\Delta T + L4.\alpha4\Delta T$

$= \Delta T. \{(L - L1). \alpha s - (L2. \alpha2 + L3. \alpha3 + L4. \alpha4)\}$

$= \Delta T. \{(L2 + L3 + L4). \alpha s - (L2. \alpha2 + L3. \alpha3 + L4. \alpha4)\}$

Equ. 90

Since $L = L1 + L2 + L3 + L4$, and consequently $L - L1 = L2 + L3 + L4$

The combined uncertainty in gap size may be obtained as follows:

$$ug = \sqrt{\begin{array}{c} \left(\frac{\partial\Delta}{\partial L2}\right)^2 (uL2)^2 + \left(\frac{\partial\Delta}{\partial L3}\right)^2 (uL3)^2 + \left(\frac{\partial\Delta}{\partial L4}\right)^2 (uL4)^2 \\ + \left(\frac{\partial\Delta}{\partial\alpha s}\right)^2 (u\alpha s)^2 + \left(\frac{\partial\Delta}{\partial\alpha s}\right)^2 (u\alpha2)^2 + \left(\frac{\partial\Delta}{\partial\alpha3}\right)^2 (u\alpha3)^2 + \left(\frac{\partial\Delta}{\partial\alpha4}\right)^2 (u\alpha4)^2 \end{array}}$$

$u_{MC/gap}$

$$= \sqrt{\begin{array}{c} \Delta T^2(\alpha s - \alpha2)^2(uL2)^2 + \Delta T^2(\alpha s - \alpha3)^2(uL3)^2 + \Delta T^2(\alpha s - \alpha4)^2(uL4)^2 \\ + \Delta T^2(L2 + L3 + L4)^2(u\alpha s)^2 + \Delta T^2(L2)^2(u\alpha2)^2 \\ + \Delta T^2(L3)^2(u\alpha3)^2 + \Delta T^2(L4)^2(u\alpha4)^2 \end{array}}$$

Equ. 91

The component uncertainty uL4 depends on the sensor manufacturer's stated tolerance for this dimension (±0.005 mm as per Table 10).

$$uL4 = \frac{5 \times 10^{-6}}{\sqrt{3}} = 3 \times 10^{-6}$$

Equ. 92

The component uncertainties *uL2* and *uL3* must be based on measurement of the dimensions *L2* and *L3* since the mount manufacturer (Melles Griot) does not state tolerances. Using vernier callipers (resolution ±0.01 mm) for this purpose and assuming a rectangular distribution of measurements; the outcome is a dimensional uncertainty calculated as follows:

$$uL3 = uL4 = \frac{0.01 \times 10^{-3}}{\sqrt{3}} = 5.77 \times 10^{-6} \text{ m}$$

Equ.93

195

The uncertainty in the coefficient of thermal expansion of the stainless steel bearing tipped screw ($u\alpha3$) is based on a ± 10 % tolerance for the coefficient, for reasons explained in Section 6.2.3 and (NIST) [3]. When a rectangular distribution is assumed, the component uncertainty $u\alpha3$ may thus be calculated as

$$u\alpha3 = \frac{0.1 \times 17 \times 10^{-6}}{\sqrt{3}} = 0.98 \times 10^{-6} \text{ K}^{-1}$$

Equ. 94

The variable values used to calculate the measurement uncertainty associated with the effect of thermal expansion of the gap between capacitance plates are tabulated in Table 18.

$L2$ (mm)	7.5	$uL2$(μm) (Equ.93)	5.77
$L3$ (mm)	4	$uL3$ (μm)(Equ.93)	5.77
$L4$ (mm)	4	$uL4$ (μm)(Equ. 92)	3
αs (K^{-1})	24×10^{-6}	$U\alpha s$ (K^{-1}) (Equ. 83)	2.0785×10^{-6}
$\alpha2$ (K^{-1})	24×10^{-6}	$u\alpha2$ (K^{-1}) (Equ. 83)	2.0785×10^{-6}
$\alpha3$ (K^{-1})	17×10^{-6}	$u\alpha3$(K^{-1}) (Equ. 94)	0.98×10^{-6}
$\alpha4$ (K^{-1})	24×10^{-6}	$u\alpha4$ (K^{-1}) (Equ. 83)	2.0785×10^{-6}

Table 18   Variable values used to calculating the uncertainty associated with the thermal expansion of inter-plate distance.

When used with Equ. 91, these values result in a measurement uncertainty dependant on the temperature deviation from the temperature at calibration (ΔT).   This relationship is illustrated in Fig. 141.
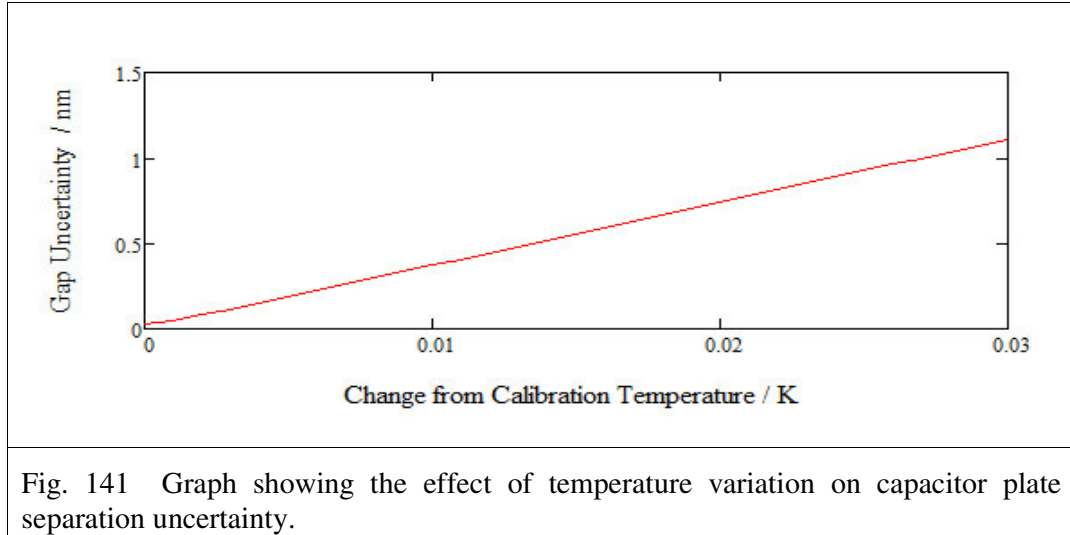
Fig. 141　Graph showing the effect of temperature variation on capacitor plate separation uncertainty.

It can be deduced from Fig. 141 that for this uncertainty to remain below 1 nm, the temperature variation must be maintained below 0.027 K. This necessitates the use of a very accurate temperature sensor such as the GE Sensing/Thermoetrics [80] supplied AS115 (resolution ± 0.002 K) for monitoring the ambient temperature about the instrument.

If the temperature deviation is maintained below 0.002 K, the uncertainty in gap size can be kept as low as 0.1 nm and the combined uncertainty in sensor measurement due to temperature variation can be calculated as follows:

$$u_{MC/T} = \sqrt{\left(u_{MC/rad}\right)^2 + \left(u_{MC/gap}\right)^2} = 0.09 \text{ nm}$$

Equ. 95

This estimate of uncertainty relates only to the measurement of the distances between the sensor plates. Any structures between the sensor and the plane of the point of interest are also subject to thermal expansion that is not detectable by the sensor. Uncertainties associated with these offsets are discussed in Section 4.4 and are quantified for each axis in Section 6.4.

6.2.5　The effect of environmental variability on relative permittivity

As explained in Section 4.2.3, Equ. 42 [37] describes the relationship between capacitor relative permittivity and environmental factors

197

$$(\varepsilon_r - 1) \times 10^6 = \frac{1553.9}{T}P_1 + \frac{2663.6}{T}P_2 + \frac{1295.3}{T}\left(1 + \frac{5748}{T}\right)P_3$$

T is the temperature, P_1 is the Partial pressure of CO_2 in free dry air (=101.3 kPa), P_2 is the Partial pressure of CO_2 (kPa), P_3 is the Partial pressure of water Vapour (kPa). Rearranging Equ. 42, leads to

$$\varepsilon_r = \left\{\frac{1553.9}{T}P_1 + \frac{2663.6}{T}P_2 + \frac{1295.3}{T}\left(1 + \frac{5748}{T}\right)P_3\right\} \times 10^{-6} + 1$$

From this, it can be deduced that uncertainty in ε_r and consequently uncertainty in measurement depends on component uncertainties in temperature, relative humidity, and atmospheric pressure. In accordance with GUM, the uncertainty in relative permittivity is given by

$$u_{\varepsilon_r} = \sqrt{\frac{\partial(\varepsilon_r)}{\partial T}^2 (u_T)^2 + \frac{\partial(\varepsilon_r)}{\partial(P_2)}^2 \left(u_{P_2}\right)^2 + \frac{\partial(\varepsilon_r)}{\partial P_3}^2 \left(u_{P_3}\right)^2}$$

$u_{\zeta r}$

$$= \sqrt{\begin{aligned} &\left\{\left(\frac{-1553.9P_1}{T^2} - \frac{2663.6P_2}{T^2} - \frac{1259.2P_3}{T^2} - \frac{(2)(1259.2)(5748)P_3}{T^2}\right) \times 10^{-6}\right\}^2 u_T^2 \\ &+ \left(\frac{2663.6 \times 10^{-6}}{T^2}\right)^2 u_{P2}^2 + \left(\frac{1259.2}{T} + \frac{(1259.2)(5748)}{T^2}\right)^2 u_{P3}^2 \end{aligned}}$$

Equ. 96

Uncertainty in temperature

As described previously in this Section, the use of the thermistor sensor, MC65, (tolerance ± 0.15 K) and assuming a rectangular distribution implies that the standard measurement uncertainty of this component can be calculated to be 0.086 K.

Uncertainty in the relative humidity

The partial pressure of water vapour, P_3, is related to the relative humidity (easily measurable) through the following common expression

$$P_3 = \frac{(RH)e}{100}$$

Equ. 97

198

where RH is the % relative humidity, e is the vapour pressure (Pa) and $T = 300$ K.

e can be calculated using Equ. 98 [104] (this gives $e = 2.665$ Pa at 300 K)

$$e = a_0 + T\left(a_1 + T\left(a_2 + T\left(a_3 + T(a_4 + T(a_5 + Ta_6))\right)\right)\right)$$

Equ. 98

$a_0 = 6.107799961$ $a_3 = 2.650648471\times10^{-4}$ $a_6 = 6.136820929\times10^{-11}$

$a_1 = 4.436518521\times10^{-1}$ $a_4 = 3.031240396\times10^{-6}$ $T = 295$ K

$a_2 = 1.428945805\times10^{-2}$ $a_5 = 2.034080948\times10^{-8}$

Having calculated values for P_3 using Equ. 97 and Equ. 98 for values of % RH, ranging from 90 % to 100 %, the corresponding relative permittivity values were calculated.

Fig. 142 Graph of calculated %Relative Humidity Vs Partial Pressure of Water Vapour	Fig.143 Graph of calculated %Relative Humidity Vs Relative Permittivity
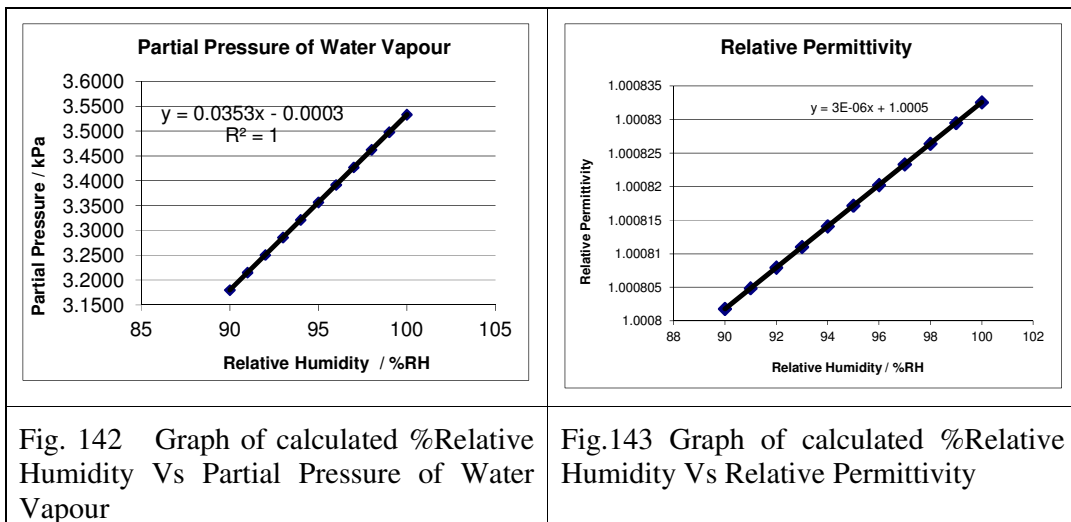
The % RH was graphed against calculated relative permittivity values and a first order trend line was applied to the calculated values. The slope of this line is 3×10^{-6}, indicating that there is a 3 ppm effect on measurement per % RH. This translates to a 0.045 nm.(%RH)$^{-1}$ for a 15 μm displacement.

The HS12P [80] humidity sensor has a stated accuracy of ± 5 % RH. As in the case of the thermistor, a rectangular distribution is also assumed here. Thus, the standard uncertainty in the partial pressure of water vapour can be calculated as follows

Std. uncertainty in water vapour $u_{P3} = \sqrt{\left(\frac{\partial P_3}{\partial (RH)}\right)^2 u_{RH}^2}$

$$u_{P3} = \sqrt{\left(\frac{e}{100}\right)^2 \left(\frac{5}{\sqrt{3}}\right)^2} = 0.076 \text{ Pa}$$

<div align="right">Equ. 99</div>

The uncertainty in the partial pressure of CO2 in air

The Bosch manufactured BMP085 digital barometer [78], used for measuring the atmospheric pressure at the instrument, has a stated accuracy of $\pm$ 0.2 kPa. Assuming a partial pressure of CO_2 of 35 Pa at NTP and a rectangular distribution of pressure measurements, the standard uncertainty of the partial pressure of CO_2 can be calculated as follows:

$$\text{Std. uncertainty due to partial pressure of } CO_2 = \left(\frac{0.035}{101.3}\right)\left(\frac{0.2}{\sqrt{3}}\right) = 0.04 \text{ Pa}$$

<div align="right">Equ. 100</div>

The uncertainty in relative permittivity can at this stage be calculated using Equ. 96

$$u_{\varepsilon_r} = \sqrt{\begin{array}{c} \left(3.712 \times 10^{-6}\right)^2 (.086)^2 + \left(29.596 \times 10^{-9}\right)^2 (4 \times 10^{-5})^2 \\ + \left(84.618 \times 10^{-6}\right)^2 (0.076 \times 10^{-3})^2 \end{array}} = 31.93 \times 10^{-6}$$

Based on Equ. 87,

$$\text{measurement uncertainty due to } \varepsilon_r = \sqrt{\left(\frac{\partial d}{\partial \varepsilon_r}\right)^2 u_{\varepsilon_r}^2} = \sqrt{\left(\frac{\varepsilon_0 A}{C}\right)^2 u_{\varepsilon_r}^2} = 0.47 \text{ nm}$$

<div align="right">Equ. 101</div>

This uncertainty in measurement applies to each of the three axes.

6.3   Reference measurement

6.3.1   Interferometer error sources

Although interferometers provide a means of highly accurate and traceable calibration for the capacitance sensors, several reference measurement error sources are addressed in this thesis. Biases are minimised through considered design of the metrology loops and software based disturbance compensation, but uncertainties associated with these compensations remain and must be quantified.

<div align="center">200</div>

6.3.1.1   Sensor noise

A Thorlabs Inc. PDA155 photodetector is used to detect the brightness of the interferogram. This sensor has a stated maximum noise level of 2 mV rms with a 0 to 10 V output. The true noise displacement can be estimated by using

$$x = \frac{\lambda}{4\pi}\sin^{-1}\frac{y}{5}$$

where x is moving mirror displacement in nanometers and y is the sensor output in volts. This gives x to be 0.02 nm when y is 2 mV. Because the noise is quoted as an rms value with no dc component, it is assumed to equal the standard deviation of displacements due to Gaussian white noise, i.e. the standard measurement uncertainty due to sensor noise is 0.02 nm.

6.3.1.2   The effect of environmental variation on the wavelength of laser light

The laser light wavelength varies with the refractive index of air. The effect of environmental deviation from NTP on the refractive index is calculated using the NIST 'Engineering Metrology Toolbox' [3] and are tabulated in Table 19. Compensation for these changes is implemented in the Calibration program as described in Section 5.2.2.1.

	NTP	1 K Rise in Temp	1 kPa rise in Pressure	1 % rise in Humidity
Refractive Index of Air	1.000271375	1.00027042	1.000274056	1.000271364
λ (Air) nm	632.828268	632.82887	632.82657	632.828273
Relative change in λ (ppm)	1	0.951	2.68	0.0076
Uncertainty of calculation	0.03×10^{-6}	0.031×10^{-6}	0.031×10^{-6}	0.031×10^{-6}

Table 19 Effect of environmental factors on the wavelength of He-Ne laser light.

The uncertainties of wavelength calculations given in the bottom row of Table 19 are expanded uncertainties, all having a coverage factor of two.   The magnitude of the calculation uncertainties are regarded as negligable in the context of this project, since,

for example, the uncertainty in calculating the relative change in λ due to temperture change, translates to 2×10^{-11} nm uncertainty in λ.

Uncertainty in displacement measurement, arising from this error source, is also dependant on several other component uncertainties that must be first quantified; in temperature measurement, in environmental pressure measurement and in humidity measurement.

Uncertainty in temperature measurement

The GE Sensing/Thermoetrics [80] thermistor sensor, MC65, used for measuring the ambient temperature about the instrument, has a stated tolerance of ± 0.15 K. Assuming a rectangular distribution of temperature measurements, the standard uncertainty in wavelength due to temperature measurement can be calculated as follows:

$$\text{Std. uncertainty in } \lambda \text{ correction due to temperature sensor } u_{\Delta T}$$

$$= \frac{0.951 \times 10^{-6} \times 0.15}{\sqrt{3}} = 0.082 \text{ ppm. K}$$

Equ. 103

The uncertainty in environmental pressure measurement

The Bosch manufactured BMP085 digital barometer [78] used for measuring the atmospheric pressure at the instrument has a stated accuracy of ±0.2 kPa. Assuming a rectangular distribution of pressure measurements, the standard uncertainty in wavelength due to pressure measurement can be calculated as follows

$$\text{Std. uncertainty in } \lambda \text{ correction due to pressure sensor } u_{\Delta P} = \frac{2.68 \times 10^{-6} \times 0.2}{\sqrt{3}}$$

$$= 0.309 \text{ ppm. kPa}$$

Equ. 104

The uncertainty due to humidity measurement.

As stated previously in Section 6.2, the GE Sensing/Thermoetrics [80] Type HS12P humidity sensor, used for measuring the relative humidity about the instrument, has a stated accuracy of ± 5 % RH. Again assuming a rectangular distribution for humidity

measurements, the standard uncertainty in wavelength due to humidity measurement can be calculated as follows:

$$\text{Std. uncertainty in } \lambda \text{ correction due to humidity sensor } u_{\Delta H} = \frac{0.0076 \times 10^{-6} \times 5}{\sqrt{3}}$$

$$= 0.022 \text{ ppm.}\%$$

<div align="right">Equ. 105</div>

<u>The uncertainty in displacement measurement</u>

The stage displacement is related to the wavelength of the interferometer laser light by

$$\text{Measured displacement } (Md) = \frac{n\lambda u_j}{2N_P}$$

<div align="right">Equ. 106</div>

where n is the number of counted wavelengths of the interferogram, N_P is the number of times that the measurement beam is reflected from the reference mirror and u_j is the appropriate relative change in λ as per Table 19. The combined uncertainty in measured displacement, Md, due to environmentally induced laser wavelength uncertainties can now be calculated in accordance with GUM [23] as follows:

$$u_{C/WL} = \sqrt{\left(\frac{\partial(Md)}{\partial(\Delta T)}\right)^2 (u_{\Delta T})^2 + \left(\frac{\partial(Md)}{\partial(P)}\right)^2 (u_P)^2 + \left(\frac{\partial(Md)}{\partial(H)}\right)^2 (u_H)^2}$$

<div align="right">Equ. 107</div>

$$u_{C/WL}$$

$$= \sqrt{\left(\frac{n\lambda}{2N_P}\right)^2 (0.082 \times 10^{-6})^2 + \left(\frac{n\lambda}{2N_P}\right)^2 (0.309 \times 10^{-6})^2 + \left(\frac{n\lambda}{2N_P}\right)^2 (0.022 \times 10^{-6})^2}$$

<div align="right">Equ. 108</div>

For stage displacement L, n is calculated by

$$n = \frac{2N_P L}{\lambda}$$

<div align="right">Equ. 109</div>

$$u_{C/WL} = \sqrt{(L)^2(0.082 \times 10^{-6})^2 + (L)^2(0.309 \times 10^{-6})^2 + (L)^2(0.022 \times 10^{-6})^2}$$

$$= 0.3205 \times 10^{-6} \, L$$

<div align="right">Equ. 110</div>

This is the standard uncertainty of the wavelength compensation and translates to an uncertainty of 0.005 nm for a stage movement of 15 μm. It applies to each of the three axes and is in agreement with that calculated by Castro et al. [41].

6.3.1.3   Deadpath error

While dead path errors are minimised through the use of a flexible mounting arrangement, uncertainty exists as a result of the inter-component distance measurement resolution, uncertainty of the thermal expansion coefficient value for the supporting structures and uncertainty due to temperature measurement.

Temperature measurement uncertainty

Again a standard temperature measurement uncertainty of 0.086 K is calculated, as in Section 6.2, when using the MC65 thermistor sensor (tolerance ±0.15   K) and assuming its stated tolerance is based on a rectangular distribution.

Deadpath length measurement

 Since the mirror location can be adjusted by means of mount screws, it is the accuracy of the deadpath measurement that contributes to its expanded uncertainty. The use of digital vernier callipers is seen as a practical approach to measuring these distances, giving a measurement tolerance of ±0.01 mm. This is possibly somewhat optimistic, though, due to difficulties of accessibility. Assuming a rectangular distribution, the uncertainty in offset distance can be estimated to be:

$$\text{Std. uncertainty due to deadpath measurement } u_{L/DP} = \frac{0.01 \times 10^{-3}}{\sqrt{3}}$$

$$= 5.77 \times 10^{-6} \, \text{m}$$

<div align="right">Equ. 111</div>

Thermal expansion coefficient uncertaint

The material bridging the deadpath is in all cases aluminium alloy 6082 T6, so the standard uncertainty in CTE is 2.0785×10^{-6} K^{-1} as explained in Section 6.2.3.

The change in interferometer measurement due to a change in deadpath distance (L_{DP}) arising from thermal expansion is calculated by the equation

$$\Delta(DP) = \alpha_{DP} L_{DP} T$$

Equ. 112

$$u_{DP} = \sqrt{\left(\frac{\partial(\Delta DP)}{\partial T}\right)^2 (u_T)^2 + \left(\frac{\partial(\Delta DP)}{\partial \alpha_{DP}}\right)^2 \left(u_{\alpha_{DP}}\right)^2 + \left(\frac{\partial(\Delta DP)}{\partial L_{DP}}\right)^2 \left(u_{L_{DP}}\right)^2}$$

Equ. 113

The measurement uncertainty is the same for each axis. It can be quantified in accordance with GUM [23]

$$u_{DP} = \sqrt{(\alpha_{DP} L_{DP})^2 (u_T)^2 + (L_{DP} T)^2 \left(u_{\alpha_{DP}}\right)^2 + (\alpha_{DP} T)^2 \left(u_{L_{DP}}\right)^2} = 0.14 \text{ nm}$$

Equ. 114

assuming L_{DP} to be 0.01 mm (the measurement resolution of the vernier callipers)

By accommodating a minimal deadpath distance, the design of the instrument has been successful in minimising the uncertainty associated with this error source.

6.3.1.4   Expansion of optical components

It is explained in Section 4.3.2.1 how the thermal expansion of optical components can cause relative phase shifts between measurement and reference beams that may be misinterpreted as measured stage movement. This error is described by Equ. 45 (see Section 4.3.2.1) and is minimised by ensuring that the beams travel identical distances through media of identical refractive index.

The arrangements of the two pass and four pass Michelson interferometers, though, mean that the beams pass through two separate quarter wave plates, thus giving rise to a possible source of error and uncertainty. Both of these are Melles Griot [38] manufactured 02 WRM 011 plates of glass/mica/glass sandwich construction with

diameters of 10 ± 0.25 mm and overall optical axis thickness of 2.5 mm. (the thermal expansion of the mica is taken to be the same as the glass).

$$\text{Measurement error } (Me) = \frac{1}{2}\{n|t_{ref} - t_{meas.}|\alpha.\Delta T\}$$

Equ. 45

where n is the refractive index of the plate sandwich, t_{ref} is the ¼ wave plate thickness in the interferometer reference arm, $t_{meas.}$ is the ¼ wave plate thickness in the interferometer measurement arm, α is the CTE of glass, ΔT is the change in ambient temperature.

The uncertainty in measurement, arising from optical components expansion, is dependant on several component uncertainties: in temperature measurement, in optical material expansion coefficient, in manufacturing tolerance and in the given refractive index of media.

Standard uncertainty due to temperature measurement

The standard temperature measurement uncertainty is again 0.086 K since the same thermistor sensor (MC65) is used as in Section 6.2..

Standard uncertainty due to the coefficient of thermal expansion (CTE) of the glass used in the 1/4wave plate.

Melles Griot [38] gives a CTE of 7.1×10^-6 K^-1 (averaged over the thermal range of 243.15 K to 343.15 K) for the glass BK7 (a Borosilicate glass). Although an uncertainty is not provided for this coefficient, NIST [3] states that the CTE for Borosilicate glass, averaged over the range 273.15 K to 373.15 K, has an uncertainty of greater than 10 % with a coverage factor, k = 2. Using this information, a standard uncertainty BK7 is estimated as follows

$$\text{Std. uncertainty due to CTE } u_\alpha = \frac{(7.1 \times 10^{-6})(0.05)}{\sqrt{3}} = 0.204 \times 10^{-6} \text{ K}^{-1}$$

Equ. 115

Uncertainty due to manufacturing tolerance

As already stated, the manufacturing tolerance for the plate thickness along the optical axes is an estimate based on the given tolerance on the plate diameter, 10 ± 0.25 mm.

206

For the nominal 2.5 mm plate thickness, the tolerance is estimated to be 2.5 ± 0.125 mm.

$$\text{Std. uncert. due to plate thickness tolerance } u_t = \frac{0.125 \times 10^{-3}}{\sqrt{3}} = 72.168 \times 10^{-6} \text{ m}$$

The combined uncertainty due to relative expansion of the ¼ wave plates can now be calculated in accordance with the ISO GUM [23]:

$$u_{C/EOP} = \sqrt{\left(\frac{\partial(Me)}{\partial(\Delta T)}\right)^2 (u_{\Delta T})^2 + \left(\frac{\partial(Me)}{\partial \alpha}\right)^2 (u_\alpha)^2 + \left(\frac{\partial(Me)}{\partial t}\right)^2 (u_t)^2}$$

<div align="right">Equ. 116</div>

$$u_{C/EOP}$$

$$= \sqrt{\left(\frac{(n)(t)(\alpha)}{2}\right)^2 (0.086)^2 + \left(\frac{(n)(t)(\Delta T)}{2}\right)^2 (0.204 \times 10^{-6})^2 + \left(\frac{(n)(\alpha)(\Delta T)}{2}\right)^2 (72.168 \times 10^{-6})^2}$$

$$= 0.393 \text{ nm}$$

<div align="right">Equ. 117</div>

This value represents measurement uncertainty when the temperature at instrument calibration differs from STP by 1K. Fig. 144 illustrates how this varies with temperature difference.

Fig. 144 The effect of temperature change on ¼ wave plate expansion uncertainty.
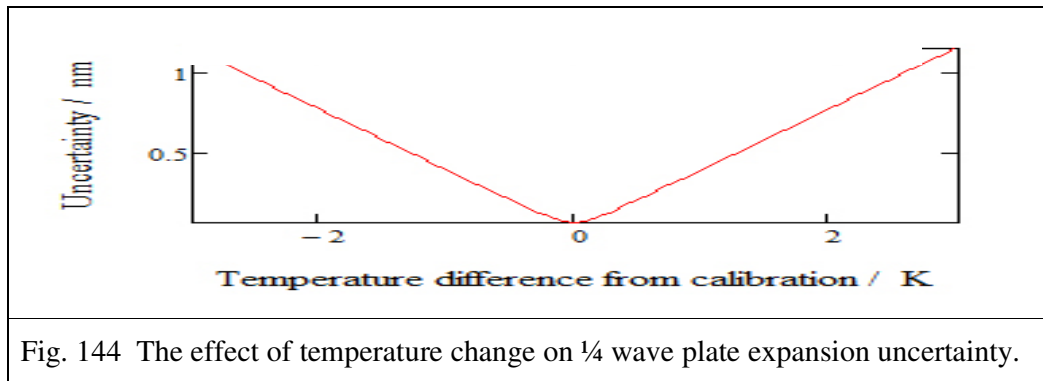
This uncertainty is the same for all axes and is fixed, being independent of distance measured.

6.3.1.5 Periodic deviation

Although various models have been reported in the literature to predict and compensate this error, none have been applied in this thesis. Castro et al. [41] report a ±4.2 nm

non-linearity error for a similar interferometer and assume a 'U' shaped distribution (because the error is periodic). The uncertainty associated with this error is thus;

$$u_{PD} = \frac{4.2 \times 10^{-9}}{\sqrt{2}} = 2.3 \text{ nm}$$

<div align="right">Equ. 118</div>

6.3.2   Set-up errors

6.3.2.1   Tilting of mirrors (effect on scale factor)

The effects of mirror tilt on measurement are explored in Section 4.3.2.2, and an expression (Equ. 46) is given, based on Ruijl's [26] Equ. 5 and Fig. 5 (see Appendix B 1 for the derivation).

$$\text{Measured tranlation} = \frac{L_m}{2}(2 + \sin(\alpha).\tan(\alpha))$$

where x is the actual displacement and α is the angle of tilt.

<div align="right">(Equ. 46, Section 4.3.2.2)</div>

From this it can be deduced that mirror tilt introduced a scale error of magnitude

$$\text{Scale error} = 1 + \frac{1}{2}\sin(\alpha)\tan(\alpha)$$

Uncertainty of the scale factor and, therefore, uncertainty in interferometer measurement, is dependant on the uncertainty of the tilting angle.   This is determined predominantly by the interferometer set-up procedure that is described in Section 7.2. The procedure establishes mirror orthognality through the adjustment of the moving mirrors until satisfactory circular fringe patterns are obtained as this only occurs when all the mirrors and beam splitter are correctly aligned. Increasing deviation from perfect alignment causes the visible fringe shapes to change from circles to distorted circles and eventually to parallel straight line fringes of equal thickness. According to Hecht [79], the angle of mirror tilt can be calculated by measuring the fringe separation.

$$\propto = \frac{\lambda}{2\Delta x'} = \frac{\lambda}{2(r_2 - r_1)}$$

<div align="right">Equ. 119</div>

where λ is the wavelength of laser light and $\Delta x'$ is the the distance between fringes.

To find $\Delta x'$, the radii of at least two fringes, r_1 and r_2, must be measured. If vernier callipers is used to make these measurements, the uncertainty in the length of each radius is

$$ur_1 = ur_2 = \frac{0.01 \times 10^{-3}}{\sqrt{3}} = 5.774 \times 10^{-6} \text{ m}$$

Uncertainty in mirror tilt angle, u_α, may be calculated in accordance with the GUM [23] as follows:

$$u_\alpha = \sqrt{\left(\frac{\partial \alpha}{\partial r_1}\right)^2 ur_1{}^2 + \left(\frac{\partial \alpha}{\partial r_2}\right)^2 ur_2{}^2 + \left(\frac{\partial \alpha}{\partial \lambda}\right)^2 u\lambda^2}$$

Equ. 120

$$u_\alpha = \sqrt{\left(-\frac{2\lambda}{(2r_2 - 2r_1)^2}\right)^2 ur_1{}^2 + \left(\frac{2\lambda}{(2r_2 - 2r_1)^2}\right)^2 ur_2{}^2 + \left(\frac{1}{2r_2 - 2r_1}\right)^2 u\lambda^2}$$

Equ. 121

Again from Hecht [79], values may be calculated for the fringe radii as follows for fixed optical spacing and path differences

$$r_m = L\sqrt{\frac{m\lambda}{d}}$$

Equ. 122

Where r_m is the radius of the mth fringe; λ is the wavelength of the laser light; d is the difference in length between the reference and measurement arms of the interferometer; while L is the sum of the distances from the reflecting surface of the beam splitter to the moving mirror and to the screen.

For λ = 632.83 nm, L = 20 cm and d = 15×10^{-6} m; by using Equ. 122, the average spacing from the first to the tenth fringe can be calculated to be 8.868 mm.

$$u_\alpha = \sqrt{\begin{array}{c}(-4.0103 \times 10^{-5})^2(5.7735 \times 10^{-6})^2 + (4.0103 \times 10^{-5})^2(5.7735 \times 10^{-6})^2 \\ + (5.63804)^2(4.8075 \times 10^{-12})\end{array}}$$

$$= 3.285 \times 10^{-10} rad = (1.883 \times 10^{-8})°$$

The maximum error in α when the outer fringe radius r_2 is measured as $r_2 + 0.01$ mm, while r_1 is measured as $r_1 - 0.01$ mm, is calculated using Equ. 119 as

$$\alpha = 2\left(\frac{632.83 \times 10^{-9}}{2 \times 8.868 \times 10^{-3}} - \frac{632.83 \times 10^{-9}}{2(8.868 \times 10^{-3} + 0.01 \times 10^{-3})}\right) = 80 \times 10^{-9} \text{ rad}$$
$$= (4.605 \times 10^{-6})^\circ$$

The change in measurement due to scale factor induced by this tilt is given by

$$L = L_m \sin(\alpha).\tan(\alpha)$$

Equ. 123

In accordance with the GUM [23], the combined uncertainty in measurement due to mirror tilting about the two axes, normal to the direction of measurement, is

$$u_{Tilt/M} = \sqrt{2\left(\frac{\partial L}{\partial \alpha}\right)^2 (u_\alpha)^2}$$

Equ. 124

$$u_{Tilt/M} = \sqrt{2\left\{\frac{L}{2}\left(\frac{\tan \alpha}{\cos \alpha} + \sin \alpha \tan \alpha\right)\right\}^2 \{1.8883 \times 10^{-8}\}^2} = 1.6 \times 10^{-20} \text{ m}$$

Equ.125

The resolution of the adjustable mount is another factor considered in relation to interferometer alignment. Using the Melles Griot [38] 07 MHT model mirror mount, an angular resolution of 20 arc sec (0.333^0) is achievable based on a 2^0 rotation of the adjustment screw. For tilt about a single axis, the angular positioning uncertainty is

$$\text{Std. uncertainty in tilt angle adjudtment} = \frac{0.166}{\sqrt{3}} = 0.096^0$$

Equ. 126

This would translate into a measurement uncertainty of over 5 nm. Fortunately the positioning limitation of the mount can be overcome by adopting a method of iterative forward/backward adjustment combined with fringe analysis. This facilitates the extremely low level of uncertainty predicted using Equ.125. This uncertainty in interferometer measurement is common to all the axes.

6.3.2.2   Tilting of mirror (varying optical path effects)

A tilted mirror in the measuring arm of the interferometer causes the measuring beam optical path to continuously vary when the mirror is translated on a stage. Consequently the beam reflects from different locations on the moving mirror, the beam splitter and the reflective surfaces of the retro-reflector. As explained in Section 4.3.2.2, any variation in flatness of any of these surfaces would result in errors.

To establish an estimate for the measurement uncertainty resulting from this phenomenon, it is first necessary to establish the ranges over which the rays traverse the surfaces.

Fig. 5 illustrates the ray path through a plane mirror laser interferometer when a tilted measuring mirror is translated as presented by Ruijl [26].   Fig. 145 presents a slightly simplified version of this diagram. Illustrated, though, in Fig. 145 are the ranges (*A, B, C, D* and *E*) on each surface from which the measurement ray is reflected as the measurement mirror is displaced along a path coincident with the axis of measurement. The hypothetical situation depicted in this schematic involves a mirror incorrectly orientated at set-up.

Fig. 145 The reflections of the measurement ray as it travels through a two pass interferometer with a tilted measurement mirror.	Fig. 146 Schematic of measurement beam reflections as the beam travels through a two pass interferometer with a tilted measurement mirror resulting from parasitic stage rotation.
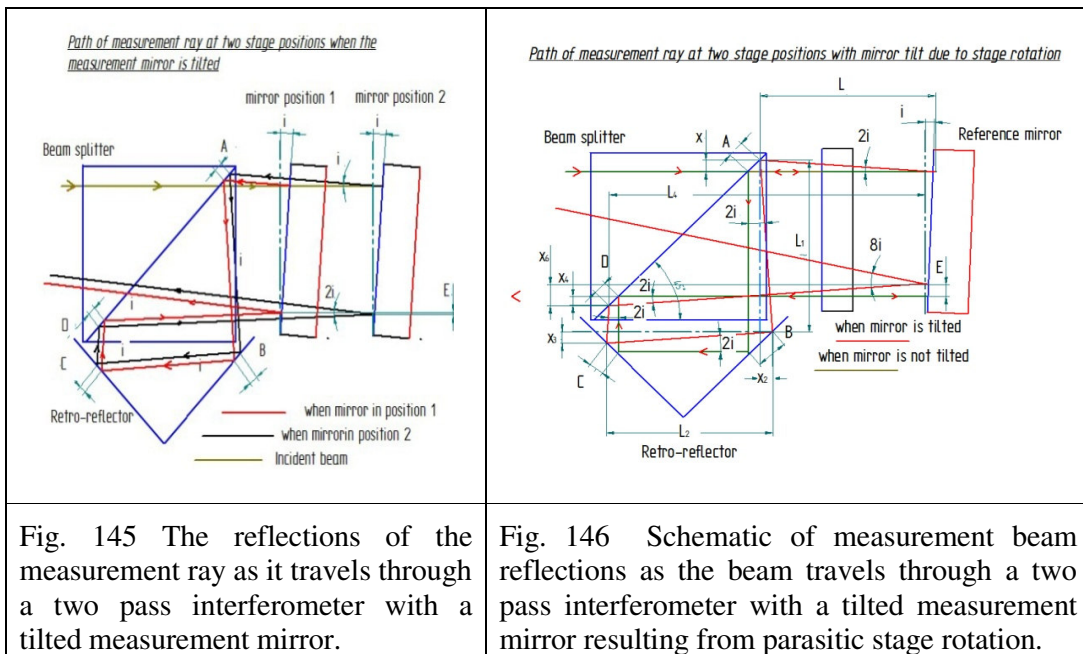
Fig. 146 is the corresponding schematic for the second hypothetical situation, where the mirror tilt results from the parasitic displacements of its translation stage. In both

diagrams, relative reflection angles are indicated as multiples of the angle of incidence of the incident ray on the moving mirror, but inter-component distances are not to scale. It can be seen from these diagrams that the magnitude of the range lengths differ from each other, but the actual magnitudes cannot be deduced, as they depend not only on the angle of tilt, but also on the spacing of optics.   These spacing distances are given in Fig. 147 for the X, Y and Z axis interferometers designed for use in the positioning instrument.
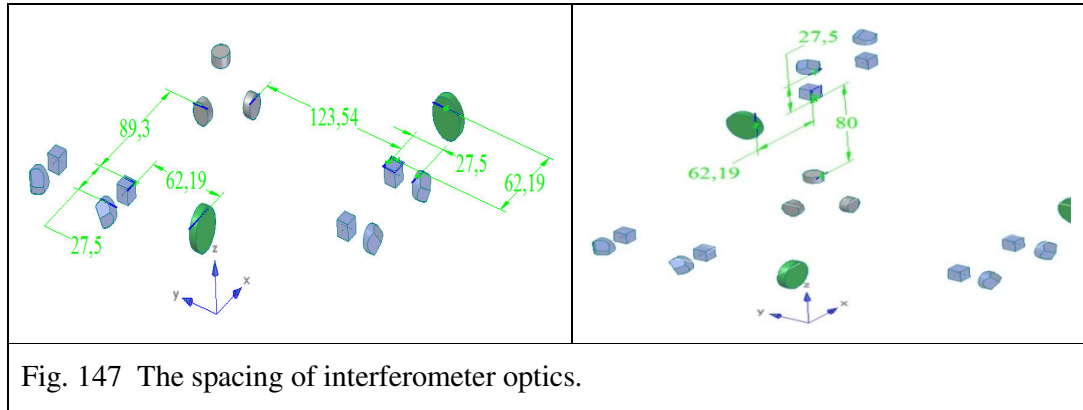
Fig. 147 The spacing of interferometer optics.

Calculation of measurement uncertainty due to mirror tilt as depicted in Situation 1 (Fig. 145)

The mirror tilting considered here arises from mirror alignment adjustment, the uncertainty of which is calculated earlier in this section to be $(4.605 \times 10^{-6})^{\circ}$.

The retro-reflector (02CCG001) and polarising beam splitter (03PBS043) are used on the 3D instrument. These are manufactured by Melles Griot [38] and in both cases the flatness of the reflecting surfaces is given as $\pm\lambda/4$.

$$\text{Std. uncertainty in flatness } u_{FL \, (ret \, ref\_bs)} = \frac{\lambda}{4\sqrt{3}}$$

Equ. 127

For the stage mounted Melles Griot [38] plane mirror (02MLE009), the flatness of the reflecting surfaces is given as $\pm \lambda/20$.

$$\text{Std. uncertainty in flatness } u_{FL \, (M)} = \frac{\lambda}{20\sqrt{3}}$$

Equ. 128

212

Expressions must now be derived to describe the relationships between measurement, flatness tolerance, reflection range lengths, optical arrangement geometry and the angles of mirror tilt.

Fig. 148 The geometry of beam reflection resulting in length A.	Fig. 149 Corner cube reflection surface flatness form assumed for the purpose of deriving relationships.
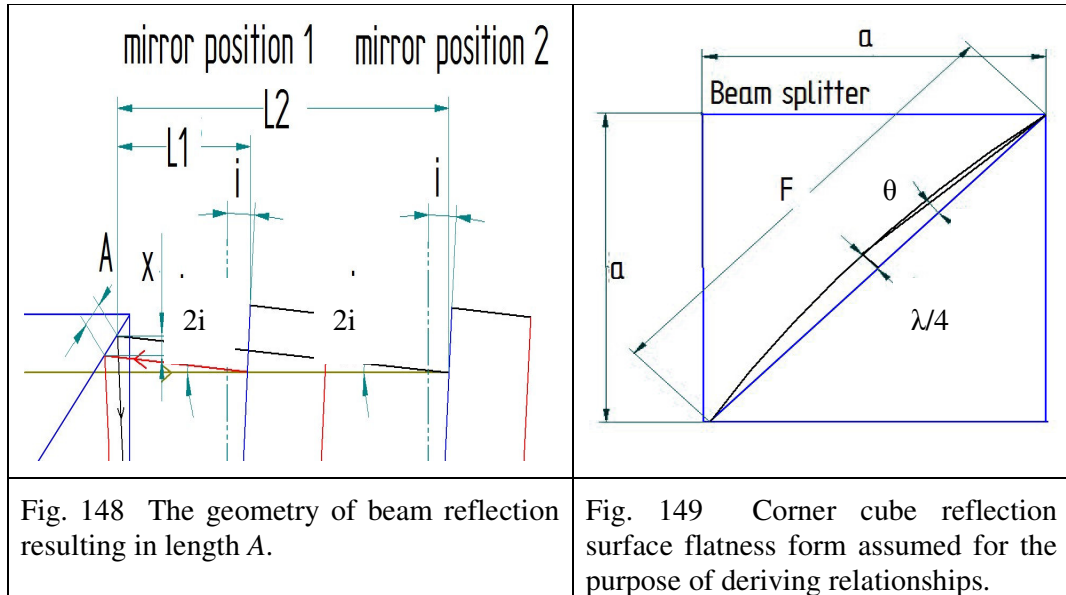
$x = (L2 - L1)\tan 2i$

$A = \sqrt{2(\Delta L \tan 2i)^2}$ by Pythagoras where ΔL is the stage displacement.

Equ. 129

$\theta = tan^{-1}\{F_L/F/2\} = \tan^{-1}(2F_L/F)$

Equ. 130

$\theta = \tan^{-1}\{(\lambda/4)/(F/2)\} = \tan^{-1}(\lambda/2F)$

Equ. 131

From Fig. 149, it can be deduced that the length of the reflecting surface of the beam splitter cube is given by $F = \sqrt{2a^2}$. Since the polarising beam splitter 02MLE009, has a stated peak to peak flatness of $\lambda/4$ at 632.8 nm, the following expression can be written for θ.

For the range over which the beam is reflected and using a similar triangle, $\tan \theta = t_A/A$, where t_A is change in measurement due to flatness tolerance. From this

$$t_A = A \tan \theta = \frac{A\lambda}{2F} = \frac{\lambda}{2\sqrt{2a^2}}\sqrt{2(\Delta L \tan 2i)^2} = \frac{\lambda(\Delta L)\tan 2i}{2a}$$

<div align="right">Equ. 132</div>

$$\text{or } t_A = A \tan \theta = \frac{2AF_L}{F} = \frac{2F_L}{\sqrt{2a^2}}\sqrt{2(\Delta L \tan 2i)^2} = \frac{2F_L(\Delta L)\tan 2i}{a}$$

<div align="right">Equ. 133</div>

where F_L is the stated flatness tolerance of the surface.

From Fig. 151, it can be seen that $|A| = |B|$

$$B = \sqrt{2(\Delta L.\tan(2i))^2}$$

<div align="right">Equ. 134</div>

| Fig. 150 Length B. | Fig. 151 Schematic of possible retro-reflector flatness deviation. |
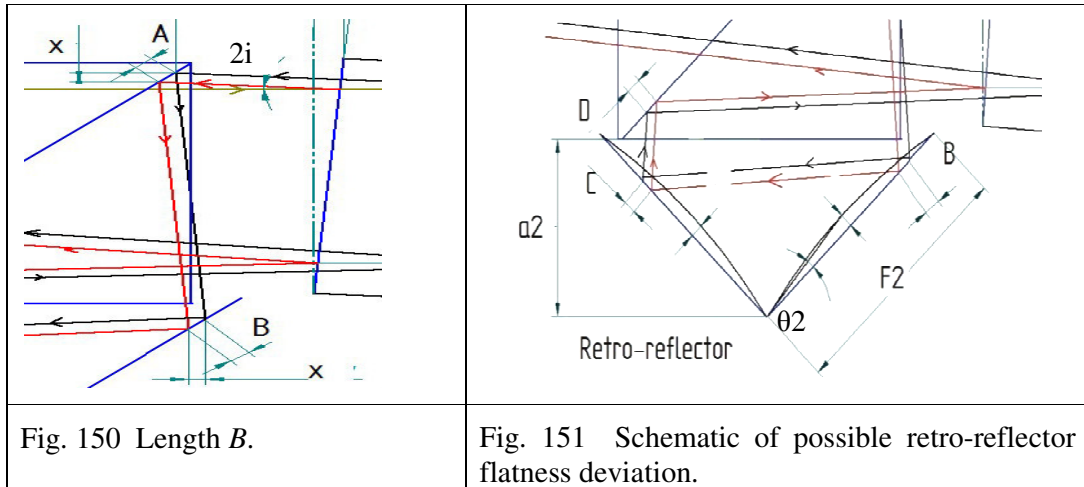
From Fig. 151, it can also be deduced that $F_2 = \sqrt{2a_2^2}$ and that $\tan\theta_2 = 2F_L/F_2 = \lambda/2F_2$ since the retro-reflector used on the 3D instrument is the Melles Griot [38] manufactured 02CCG001, having a stated peak to peak flatness of $\lambda/4$ at 632.8 nm.

For the range over which the beam is reflected (length B), $\tan\theta = t_B/B$, where t_B is change in measurement due to flatness tolerance of the retro-reflector. From this,

$$t_B = B \tan\theta = \frac{B\lambda}{2F_2} = \frac{\lambda}{2\sqrt{2a_2^2}}\sqrt{2(\Delta L \tan 2i)^2} = \frac{\lambda(\Delta L)\tan 2i}{2a_2}$$

<div align="right">Equ. 135</div>

or $t_B = B \tan\theta = \dfrac{2BF_L}{F_2} = \dfrac{2F_L}{\sqrt{2a_2{}^2}}\sqrt{2(\Delta L \tan 2i)^2} = \dfrac{2F_L(\Delta L)\tan 2i}{a_2}$

<div align="right">Equ. 136</div>

It can be deduced from Fig. 145: $|A| = |D|$ and $|B| = |C|$, so $t_A = t_D$ and $t_B = t_C$.

By using the Pythagoras theorem with the stated dimensions of the beam splitter 02MLE009, the values of dimension a can be calculated to be 14.142 mm, while in a similar manner, a_2 can be calculated for the 02CCG001retro-reflector to be 11.3 mm. Assuming possible rotations about two axes that are normal to the direction of measurement, $u_{mFlt,}$ the uncertainty in measurement due to the combined uncertainties in flatness and tilt angle, can be calculated as follows

$$u_{m\,Flt}{}^2 = 2\left\{\left(\frac{\partial t_A}{\partial i}\right)^2 u_i^2 + \left(\frac{\partial t_B}{\partial i}\right)^2 u_i^2 + \left(\frac{\partial t_C}{\partial i}\right)^2 u_i^2 + \left(\frac{\partial t_D}{\partial F_L}\right)^2 u_i^2 + \left(\frac{\partial t_A}{\partial F_L}\right)^2 u_{FL}^2 \right.$$
$$\left. + \left(\frac{\partial t_B}{\partial F_L}\right)^2 u_{FL}^2 + \left(\frac{\partial t_C}{\partial F_L}\right)^2 u_{FL}^2 + \left(\frac{\partial t_D}{\partial F_L}\right)^2 u_{FL}^2 \right\}$$

<div align="right">Equ. 137</div>

$$u_{m\,Flt} = \sqrt{4\left(\frac{1}{a_1^2} + \frac{1}{a_2^2}\right)\left\{\left(\frac{\lambda(\Delta L)}{\cos^2 2i}\right)^2 u_i^2 + (2\Delta L \tan 2\alpha)^2 u_{FL}^2\right\}} = 0.2 \text{ nm per deg tilt}$$

<div align="right">Equ. 138</div>

This can only be regarded as an estimate of uncertainty since the actual flatness profiles of the surfaces are not available for the individual mirrors, retro-reflectors or prisms.

Calculation of measurement uncertainty due to mirror tilt as depicted in Situation 2 (Fig. 146)

Now, the situation schematically depicted in Fig. 146, where the mirror tilts with the parasitic displacements of its translation stage, is examined. As before, expressions for the reflection range lengths $A,\ B,\ C,\ D$ and E are first derived in terms of the angle of stage rotation. Since the same retro-reflector and polarising cube is used as in the previous instance, $\tan\theta = 2F_L/F_1 = \lambda/2F_1$, based on Fig. 149, while $\tan\theta_2 = 2F_LF2{=}\lambda2F2$, based on Fig. 151.
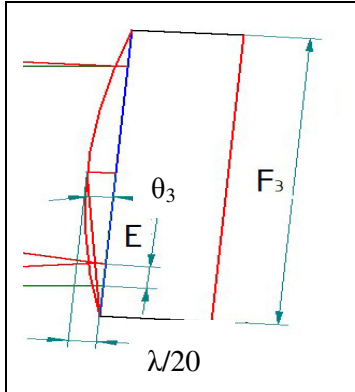
Fig. 152 Reference mirror deviation from flatness.

In the previous instance, the beam is always reflected from the same spot on the reference mirror, so flatness deviation of this mirror has negligible effect on measurement. In this situation, though, the rotation of the translating mirror causes the beam to scan over its surface. Consequently its flatness may effect displacement measurement and must be given consideration. For the Melles Griot [38] manufactured 02MLE009 mirror, with a stated flatness of $\lambda/20$ peak to peak, it can be deduced from Fig. 152 that

$$\tan \theta_3 = \frac{2F_{L3}}{F_3} = \frac{\lambda}{10F_3}$$

Equ. 139

Where F_{L3} is the flatness of the mirror used on the instrument.
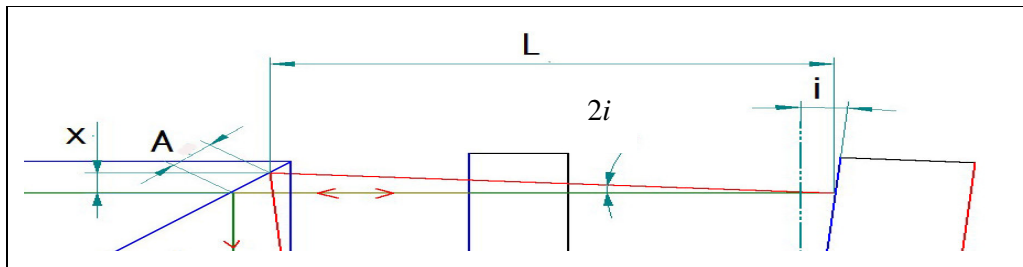
Fig. 153 Light beams reflected from the tilted translated mirror and from the same mirror in the non-tilted home position.

From Fig. 153, $x = L \tan 2i$ and $A = \sqrt{2x^2} = \sqrt{2(L \tan 2i)^2}$

Equ. 140

From Fig. 154;

$$x_2 = L_1 \tan 2i \quad and \quad B = A + \sqrt{2x_2^2}$$

$$B = \sqrt{2(L \tan(2i))^2} + \sqrt{2(L_1 \tan(2i))^2} = \sqrt{2}(L + L_1) \tan 2i$$

Equ 141

Since $x_3 = L_2 \tan 2i$, $C = B - \sqrt{2(L_2 \tan(2i))^2} = \sqrt{2}(L + L_1 - L_2) \tan 2i$

Equ 142

216
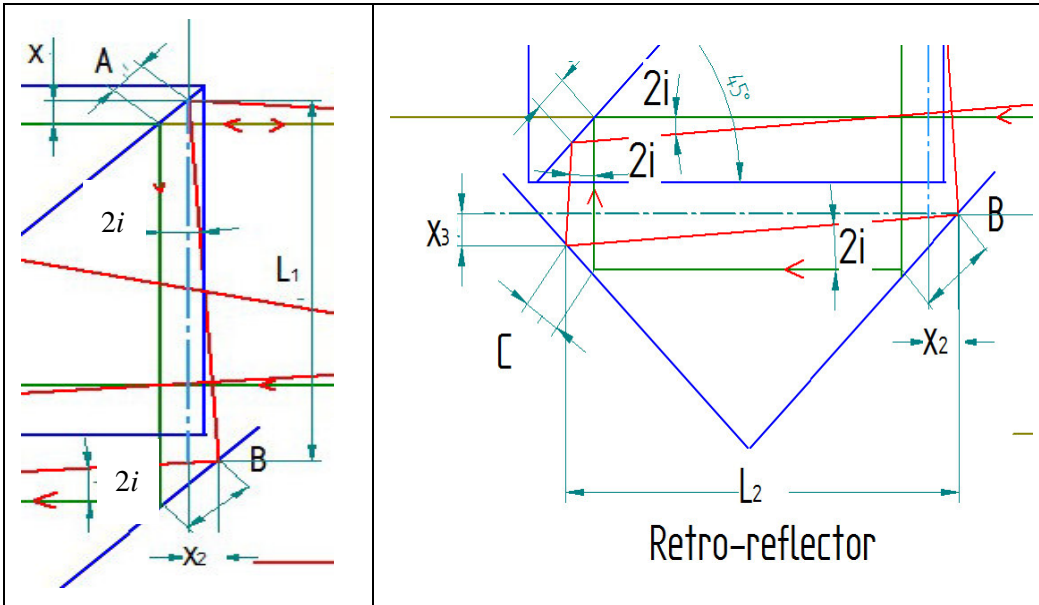
| Fig. 154 Lengths *A* and *B*. | Fig. 155 Lengths *B* and *C*. |

| Fig. 156 Lengths *C* and *D*. | Fig. 157 Lengths *D* and *E*. |
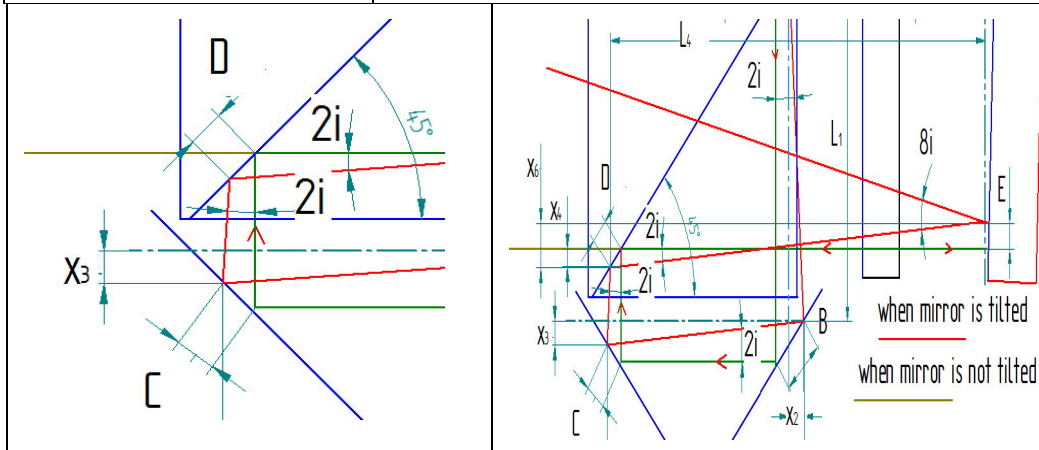
Similarly it can be shown, based on Fig. 156   that

$$D = C - \sqrt{2(L_3 \tan(2i))^2} = \sqrt{2}(L + L_1 - L_2 - L_3)\tan 2i$$

<div align="right">Equ. 143</div>

And from Fig. 157 $x_6 = L_4 \tan 2i \;\; and \;\; E = (x_6 - x_4)/\cos i \;\; and \;\; D^2 = 2x_4^2$

$$x_4 = \sqrt{\tfrac{1}{2}D^2} = \sqrt{\tfrac{1}{2}\left(\sqrt{2}(L + L_1 - L_2 - L_3)\tan 2i\right)^2}$$

and hence

$$E = \frac{\left\{ L_4 \tan 2i - \sqrt{\frac{1}{2}\left(\sqrt{2}(L + L_1 - L_2 - L_3)\tan 2i\right)^2} \right\}}{\cos i}$$

$$= \frac{\tan 2i}{\cos i}(-L - L_1 - L_2 - L_3 + L_4)$$

<div align="right">Equ. 144</div>

The laser traverses the measurement mirror an extra distance in addition to range E since the mirrors are placed distant from the point of interest about which the stage rotates as shown in Fig. 159. If L_5 is the offset distance, then the laser traverses the mirror surface an additional $L_5.\tan(i)$ as can be deduced from the schematic of Fig. 159
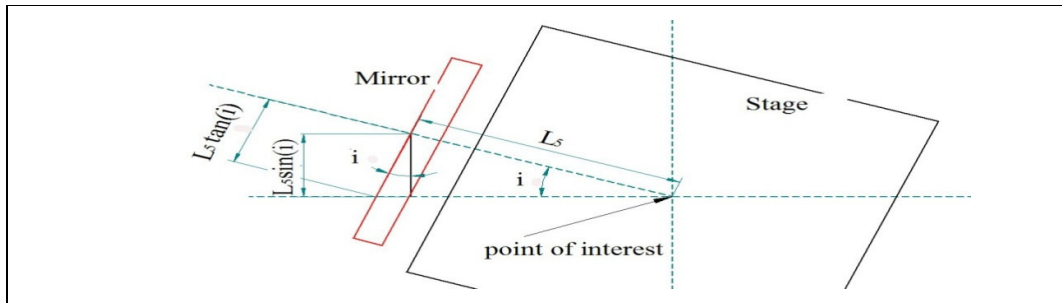
Fig. 158 Schematic showing how the offset distance L_5 causes the laser to scan over the measurement mirror.
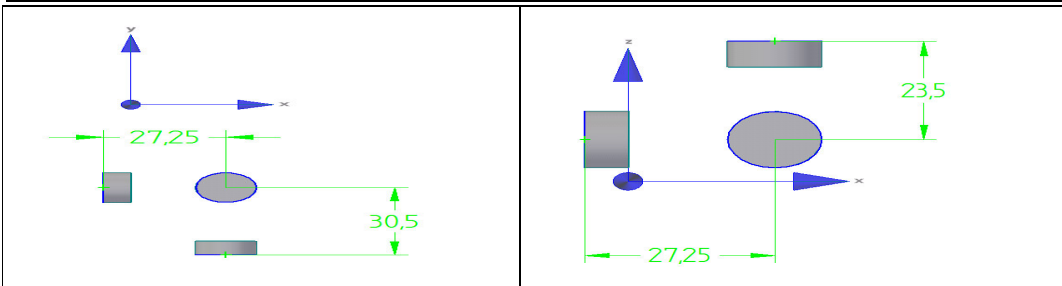
Fig. 159   Placement of measurement mirrors relative to the point of interest.

$$\text{additional distance scanned} = \frac{L_5 \sin i}{\cos i} = L_5 \tan i$$

<div align="right">Equ. 145</div>

$$E_2 = \frac{\tan 2i}{\cos i}(-L - L_1 - L_2 - L_3 + L_4) + L_5 \tan i$$

$$t_A = A \tan \theta = \frac{A\lambda}{2F} = \frac{\lambda}{2\sqrt{2a^2}}\sqrt{2(L \tan 2i)^2} = \frac{\lambda(L) \tan 2i}{2a}$$

$$\text{or} \quad t_A = A \tan \theta = \frac{2AF_L}{F} = \frac{2F_L}{\sqrt{2a^2}}\sqrt{2(L \tan 2i)^2} = \frac{2F_L(L) \tan 2i}{a}$$

$$t_B = B \tan \theta = \frac{B\lambda}{2F_2} = \frac{\lambda}{2\sqrt{2a_2{}^2}}\sqrt{2}(L + L_1) \tan 2i = \frac{\lambda(L + L_1) \tan 2i}{2a_2}$$

$$\text{or} \quad t_B = B \tan \theta = \frac{2BF_L}{F_2} = \frac{2F_L}{\sqrt{2a_2{}^2}}\sqrt{2}(L + L_1) \tan 2i = \frac{2F_L(L + L_1) \tan 2i}{a_2}$$

$$t_C = C \tan \theta = \frac{C\lambda}{2F_2} = \frac{\lambda}{2\sqrt{2a_2{}^2}}\sqrt{2}(L + L_1 - L_2) \tan 2i = \frac{\lambda(L + L_1 - L_2) \tan 2i}{2a_2}$$

$$\text{or} \quad t_C = C \tan \theta = \frac{2CF_L}{F_2} = \frac{2F_L}{\sqrt{2a_2{}^2}}\sqrt{2}(L + L_1 - L_2) \tan 2i$$

$$= \frac{2F_L(L + L_1 - L_2) \tan 2i}{a_2}$$

$$t_D = D \tan \theta = \frac{D\lambda}{2F} = \frac{\lambda}{2\sqrt{2a^2}}\sqrt{2}(L + L_1 - L_2 - L_3) \tan 2i$$

$$= \frac{\lambda(L + L_1 - L_2 - L_3) \tan 2i}{2a}$$

or $\quad t_D = D \tan\theta = \dfrac{2DF_L}{F_2} = \dfrac{2F_L}{\sqrt{2a^2}}\sqrt{2}(L + L_1 - L_2 - L_3)\tan 2i$

$$= \dfrac{2F_L(L + L_1 - L_2 - L_3)\tan 2i}{a}$$

<div align="right">Equ. 154</div>

$$t_E = E\tan\theta_3 = \dfrac{E\lambda}{10F_3}\dfrac{\tan 2i}{\cos i}(-L - L_1 + L_2 + L_3 + L_4 + L_5)$$

<div align="right">Equ. 155</div>

or $\quad t_E = E\tan\theta_3 = \dfrac{2EF_{L3}}{F_3} = \dfrac{2F_{L3}}{F_3}\dfrac{\tan 2i}{\cos i}(-L - L_1 + L_2 + L_3 + L_4 + L_5)$

<div align="right">Equ. 156</div>

$$u_{tilt}^2 = \left(\dfrac{\partial t_A}{\partial i}\right)^2 u_i^2 + \left(\dfrac{\partial t_B}{\partial i}\right)^2 u_i^2 + \left(\dfrac{\partial t_C}{\partial i}\right)^2 u_i^2 + \left(\dfrac{\partial t_D}{\partial i}\right)^2 u_i^2 + \left(\dfrac{\partial t_E}{\partial i}\right)^2 u_i^2 + \left(\dfrac{\partial t_A}{\partial F_{FL}}\right)^2 u_{FL}^2$$

$$+ \left(\dfrac{\partial t_B}{\partial F_{FL}}\right)^2 u_{FL}^2 + \left(\dfrac{\partial t_C}{\partial F_{FL}}\right)^2 u_{FL}^2 + \left(\dfrac{\partial t_D}{\partial F_{FL}}\right)^2 u_{FL}^2 + \left(\dfrac{\partial t_E}{\partial F_{FL}}\right)^2 u_{FL}^2$$

<div align="right">Equ. 157</div>

The uncertainty in the angle of tilt, u_i, in this instance may arise from the component uncertainties of

- piezo force alignment with the desired axis of stage motion; and

- flexure stiffness imbalance, resulting from manufacturing tolerances.

	Parasitic yaw about the displacement axes:		
	X axis	Y axis	Z axis
X mirror			
Y mirror			
Z mirror			
Table 20 Mirror tilt axes (in red) arising from parasitic yaw along movement axes.			

Tilting of a measurement mirror may stem from parasitic yaw movement in more than one axis.   Table 20 shows the relationship between stage parasitic yaw in each of the displacement axes to mirror rotations.   From Table 20 it can be deduced that

Combined uncertainty in X axis mirror tilt, $u_{tilt\ Y} = \sqrt{(u_{iX})^2 + (u_{iY})^2}$

Combined uncertainty in Y axis mirror tilt, $u_{tilt\ Y} = \sqrt{(u_{iX})^2 + (u_{iY})^2}$

Combined uncertainty in Z axis mirror tilt, $u_{tilt\ Z} = \sqrt{(u_{iZ})^2}$

Equ. 158

It should also be noted that yaw in the Z axis causes the X axis mirror to tilt normal to the tilt caused by yaw in X and Y axes. This would result in the measurement rays to travel in a different manner through the optics.

Piezo force alignment

A misaligned piezo force would tend to distort the flexures in a complex manner. The piezos are confined by pre-loaded locations between very parallel faces, thus ensuring that any angular deviations from the desired axial motion are small.
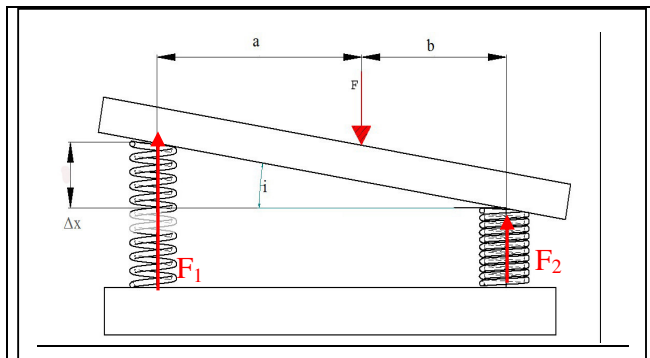
Fig. 160 Unsymmetrical piezo action, resulting in unclerical flexure compression.

Nevertheless, misplacement of the piezo actuators may cause them to act along paths which are not equi-distant between flexures.   This can result in flexures closest to the piezos compressing more than those further away (Fig. 160), thus causing parasitic rotations as the stage translates. The resulting uncertainty in mirror tilt arises from the uncertainty in positioning actuators, which is dependant on the resolution of the vernier callipers used in their placement. Before the uncertainty in the tilt angle resulting from piezo positioning errors can be calculated, it is first necessary to derive an expression to relate the actuator position to the angle of stage rotation. The piezo force, F, the flexure reaction forces ($F1$ and $F2$), the distance of the piezo force from the individual flexures (a and b), as well as the inter-flexure differential displacement (Δx) are all

221

illustrated in Fig. 160. It can be deduced from Fig. 160, by regarding the moments to be at equilibrium for a stage commanded a distance S that

$$i = \tan^{-1}\left\{\frac{S\left(\frac{a}{b} - 1\right)}{a + b}\right\}$$

<div align="right">Equ. 159</div>

uncertainty in tilt due to piezo positioning $u_{ia} = \sqrt{\left(\frac{\partial i}{\partial a}\right)^2 u_a}$

<div align="right">Equ. 160</div>

If $u = S\left(\frac{a}{b} - 1\right)$, $i = \tan^{-1}\frac{u}{(a + b)}$ and $\frac{di}{da} = \frac{di}{du} \cdot \frac{du}{da}$

$$\frac{di}{da} = \frac{\frac{S}{b}}{(a + b)^2 + u^2} = \frac{\frac{S}{b}(a + b)}{(a + b)^2 + S^2\left(\frac{a}{b} - 1\right)^2}$$

Note: $a + b$ is the distance between the springs and is, therefore, treated as a constant.

Assuming a rectangular distribution, the uncertainty in offset distance, a, can be estimated to be

Std. uncertainty in piezo positioning $u_a = \dfrac{0.01 \times 10^{-3}}{\sqrt{3}} = 5.77 \times 10^{-6}\ m$

Therefore the uncertainty in tilt due to piezo positioning is:

$$u_{ia}^2 = \left(\frac{\frac{S}{b}(a + b)}{(a + b)^2 + S^2\left(\frac{a}{b} - 1\right)^2}\right)^2 \left(\frac{0.01 \times 10^{-3}}{\sqrt{3}}\right)^2$$

<div align="right">Equ.161</div>

Flexure stiffness imbalance

To avoid stage parasitic rotation and the resulting interferometer mirror tilt, flexure pairs should be symmetrically stiff. Otherwise, a softer flexure would compress more than its twin. The dimensions, which effect the flexure stiffness, are cantilever length (*L*), cantilever thickness (*d*) and flexure depth (*b*), representatives of which are indicated in Fig. 161. Uncertainty in any of these dimensions translates into stage

rotation uncertainty that gives rise to measurement uncertainty, since the interferometer measurement mirrors and capacitance plates, mounted on the stage, are also tilted. Before deriving an expression for flexure non-symmetry induced mirror tilt uncertainty, it is necessary to derive expressions, which relate each of the flexure dimensions to the angle of mirror tilt.
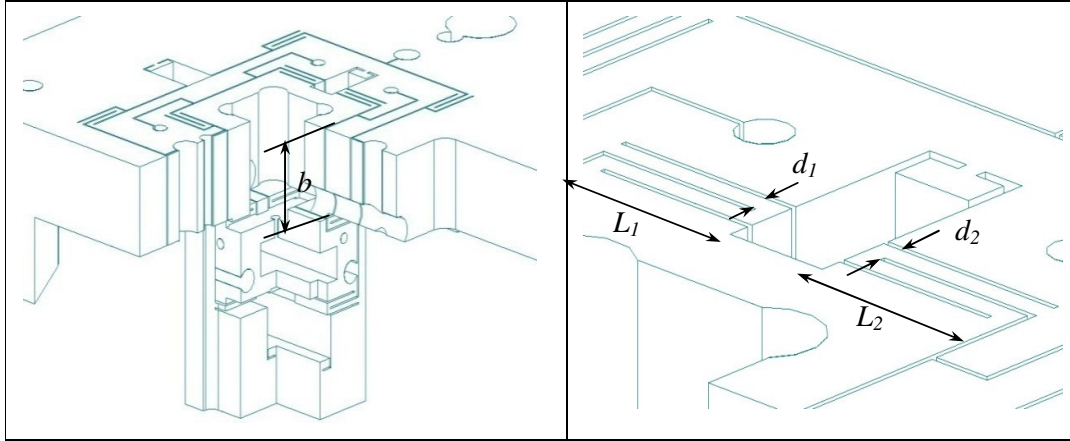
Fig. 161   Cut-away drawing of the stage showing the flexure dimensions critical to their stiffness.

As explained in Section 3.8.2, each flexure consists of two bracketed cantilevers in series and hence has a linear stiffness of $k = \frac{1}{2}Eb\left(\frac{d}{L}\right)^3$.   The combined flexure stiffness on one side of the stage is given by

$$k_t = \frac{1}{2}Eb_{t=1}\left(\frac{d_{t=1}}{L_{t=1}}\right)^3 + \frac{1}{2}Eb_{t=2}\left(\frac{d_{t=2}}{L_{t=2}}\right)^3$$

Equ. 162

while the combined stiffness of corresponding flexures on the other side is

$$k_P = \frac{1}{2}Eb_{P=1}\left(\frac{d_{P=1}}{L_{P=1}}\right)^3 + \frac{1}{2}Eb_{P=2}\left(\frac{d_{P=2}}{L_{P=2}}\right)^3$$

Equ. 163

Both the X and Y axes of the instrument are guided by four of these flexures acting in parallel, two on either side of the actuator. Thus

223

$$k_t = \sum_{t=1}^{2} \frac{1}{2} E b_t \left(\frac{d_t}{L_t}\right)^3 \qquad\qquad k_P = \sum_{P=1}^{2} \frac{1}{2} E b_P \left(\frac{d_P}{L_P}\right)^3$$

<div align="center">Equ. 164   Equ. 165</div>

The Z axis is guided by eight flexures acting in parallel, four on either side of the actuator. For this axis

$$k_t = \sum_{t=1}^{4} \frac{1}{2} E b_t \left(\frac{d_t}{L_t}\right)^3 \qquad\qquad k_P = \sum_{P=1}^{4} \frac{1}{2} E b_P \left(\frac{d_P}{L_P}\right)^3$$

<div align="center">Equ. 166   Equ. 167</div>

Fig. 162 Symmetrical piezo location ($a = b$), but non-symmetrical flexure compression caused by non-symmetrical flexure stiffness ($K_t \neq K_p$).
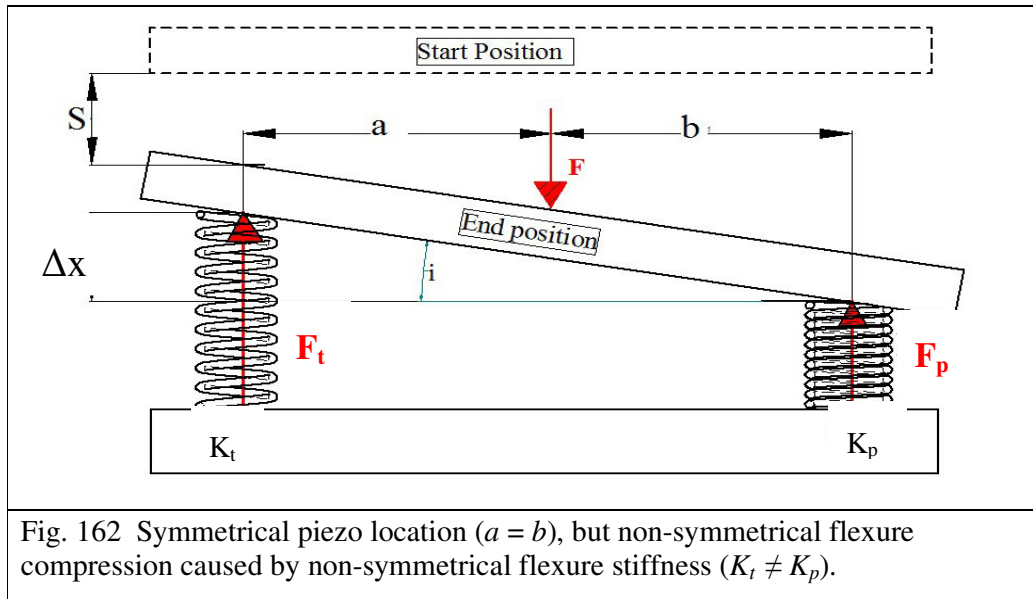
The schematic diagram, Fig. 162, illustrates a situation where a stage is commanded a distance S, but, because of the lack of flexure stiffness symmetry ($Kt \neq Kp$), parasitic rotation occurs. One side of the stage travels a distance Δx further than the other side, even though the reaction forces Ft and Fp are close to equal when i is small. In this instance, it is assumed the piezo is perfectly centred between the flexure guides i.e. a = b. It can be deduced from Fig. 162 that

$$i = \sin^{-1}\left\{ \frac{S\left(\frac{k_t}{k_P} - 1\right)}{a + b} \right\}$$

If N is the number of flexures guiding the axis in question (four in the case of the X and Y axes, and eight in the case of the Z axis), then the axial tilting angles can be calculated by using the following.

$$i = \sin^{-1} \frac{S\left(\frac{\sum_{t=1}^{\frac{N}{2}}\left\{\frac{1}{2}Eb_t\left(\frac{d_t}{L_t}\right)^3\right\}}{\sum_{P=1}^{\frac{N}{2}}\left\{\frac{1}{2}Eb_P\left(\frac{d_P}{L_P}\right)^3\right\}} - 1\right)}{a + b}$$

uncertainty in tilt due to flexure depth u_{ib}

$$= \sqrt{\sum_{t=1}^{N/2}\left(\frac{\partial i}{\partial b_t}\right)^2 (u_{bt})^2 + \sum_{p=1}^{N/2}\left(\frac{\partial i}{\partial b_p}\right)^2 (u_{bp})^2}$$

While examining the uncertainty in b_t and b_p, it is assumed that the d and L dimensions remain constant for all the guidance flexures. Initially the thickness of a single flexure ($t = 1$) is examined

$$\text{if } u = \left(\frac{\sum_{t=1}^{1}\left\{b_t\left(\frac{d_t}{L_t}\right)^3\right\}}{\sum_{P=1}^{\frac{N}{2}}\left\{b_P\left(\frac{d_P}{L_P}\right)^3\right\}} - 1 \right) = \left(\frac{\sum_{t=1}^{1}\{b_t\}}{\sum_{P=1}^{\frac{N}{2}}\{b_P\}} - 1 \right), i = \sin^{-1}\frac{Su}{a + b}$$

and remembering that $a + b$ is a constant, then

$$\frac{\partial u}{\partial b_{t=1}} = \frac{1}{\sum_{P=1}^{\frac{N}{2}}\{b_P\}} \quad and \quad \frac{\partial i}{\partial u} = \frac{1}{\sqrt{\left(\frac{a + b}{S}\right)^2 - u^2}}$$

225

$$\frac{\partial i}{\partial b_{t=1}} = \frac{1}{\sum_{P=1}^{\frac{N}{2}}\{b_P\}\sqrt{\left(\frac{a+b}{S}\right)^2 - u^2}} = \frac{1}{\sum_{P=1}^{\frac{N}{2}}\{b_P\}\sqrt{\left(\frac{a+b}{S}\right)^2 - \left(\frac{\sum_{t=1}^{1}\{b_t\}}{\sum_{P=1}^{\frac{N}{2}}\{b_P\}} - 1\right)^2}}$$

<div align="right">Equ. 171</div>

The uncertainty in the flexure thicknesses is dependant on the accuracy of the manufacturing process, milling in this instance, which has been specified at $\pm$ 0.005 mm. Assuming a rectangular distribution, the uncertainty in flexure depth can be estimated as follows.

$$\text{Std. uncertainty in flexure depth } u_b = \frac{0.005 \times 10^{-3}}{\sqrt{3}} = 2.886 \times 10^{-6} \text{ m}$$

<div align="right">Equ.172</div>

The uncertainty in tilt angle due to uncertainty in the depth of a single flexure is thus

uncertainty $u_{ib(t=1)}$

$$= \sqrt{\left(\left(\sum_{P=1}^{\frac{N}{2}}\{b_P\}\sqrt{\left(\frac{a+b}{S}\right)^2 - \left(\frac{\sum_{t=1}^{1}\{b_t\}}{\sum_{P=1}^{\frac{N}{2}}\{b_P\}} - 1\right)^2}\right)^{-2}\left(\frac{0.005 \times 10^{-3}}{\sqrt{3}}\right)^2}$$

<div align="right">Equ.173</div>

The uncertainty in tilt angle due to the combined uncertainty in the depth of all the flexures of a given axis guide is thus

uncertainty $u_{ib(t=1)}$

$$= \sqrt{2\sum_{t=1}^{N/2}\left\{\left(\left(\sum_{P=1}^{\frac{N}{2}}\{b_P\}\sqrt{\left(\frac{a+b}{S}\right)^2 - \left(\frac{\sum_{t=1}^{\frac{N}{2}}\{b_t\}}{\sum_{P=1}^{\frac{N}{2}}\{b_P\}} - 1\right)^2}\right)^{-2}\left(\frac{0.005 \times 10^{-3}}{\sqrt{3}}\right)^2\right)\right\}}$$

<div align="right">Equ. 174</div>

It is next necessary to derive an expression to relate mirror tilt to uncertainty in flexure length. Again the tilt angle is given by

<div align="center">226</div>

$$i = \sin^{-1} \frac{S\left(\frac{\sum_{t=1}^{\frac{N}{2}}\left\{b_t \left(\frac{d_t}{L_t}\right)^3\right\}}{\sum_{P=1}^{\frac{N}{2}}\left\{b_P \left(\frac{d_P}{L_P}\right)^3\right\}} - 1\right)}{a + b}$$

<div align="right">Equ. 170</div>

While examining the uncertainty in Lt and Lp, it is assumed that the d and b dimensions remain constant for all the flexures. Initially the length of a single flexure $L_{t=1}$ is examined.

$$\frac{\partial i}{\partial L_{t=1}} = \frac{-3}{L_t^4 \sum_{p=1}^{4}\{L_p^{-3}\}\sqrt{\left(\frac{a+b}{S}\right)^2 - \left(\sum_{t=1}^{\frac{N}{2}}\left(\frac{L_t^{-3}}{\sum_{P=1}^{\frac{N}{2}}\{L_p^{-3}\}}\right) - 1\right)^2}}$$

Uncertainty in L is dependant on the accuracy of the manufacturing process, EDM in this instance, which has been specified at ±1 μm. Assuming a rectangular distribution, the uncertainty in flexure length can be estimated to be

uncertainty in flexure depth $u_L = \dfrac{1 \times 10^{-6}}{\sqrt{3}} = 0.577$ μm

<div align="right">Equ. 175</div>

The uncertainty in tilt angle due to uncertainty in the length of one flexure is thus

uncertainty $u_{iL(t=1)}$

$$= \sqrt{(-3)^2 \left(L_{t=1}^4 \sum_{t=1}^{4}\{L_p^{-3}\}\sqrt{\left(\frac{a+b}{S}\right)^2 - \left(\sum_{t=1}^{\frac{N}{2}}\left(\frac{L_t^{-3}}{\sum_{P=1}^{\frac{N}{2}}\{L_p^{-3}\}}\right) - 1\right)^2}\right)^{-2} \left(\frac{1 \times 10^{-6}}{\sqrt{3}}\right)^2}$$

<div align="right">Equ. 176</div>

uncert. in tilt due to flexure length $u_{iL} = \sqrt{\sum_{t=1}^{N/2}\left(\frac{\partial i}{\partial L_t}\right)^2 (u_{Lt})^2 + \sum_{p=1}^{N/2}\left(\frac{\partial i}{\partial L_p}\right)^2 (u_{Lp})^2}$

<div align="right">Equ. 177</div>

The uncertainty in tilt angle due to the combined uncertainty in the length of all the flexures of a given axis guide is may be calculated using Equ. 176. uncertainty $u_{iL(t)}$

$$= \sqrt{2\sum_{t=1}^{N/2}\left\{(-3)^2\left(L_{t=1}^4\sum_{t=1}^{4}\{L_p^{-3}\}\sqrt{\left(\frac{a+b}{S}\right)^2-\left(\sum_{t=1}^{\frac{N}{2}}\left(\frac{L_t^{-3}}{\sum_{P=1}^{\frac{N}{2}}\{L_p^{-3}\}}\right)-1\right)^2}\right)^{-2}\left(\frac{1\times10^{-6}}{\sqrt{3}}\right)^2\right\}}$$

<div align="right">Equ. 178</div>

An expression is now derived to relate mirror tilt uncertainty to uncertainty in flexure thickness. Again, using

$$i=\sin^{-1}\frac{S\left(\frac{\sum_{t=1}^{\frac{N}{2}}\left\{b_t\left(\frac{d_t}{L_t}\right)^3\right\}}{\sum_{P=1}^{\frac{N}{2}}\left\{b_P\left(\frac{d_P}{L_P}\right)^3\right\}}-1\right)}{a+b}$$

<div align="right">Equ. 170</div>

While finding the partial derivatives for i with respect to dt and dp, it is assumed that the b and L dimensions remain constant for all the guidance flexures. Initially the width of a single flexure ($dt = 1$) is examined. It can be deduced that

$$\frac{\partial i}{\partial d_{t=1}}=\frac{3d_{t=1}^2}{\sum_{p=1}^{\frac{N}{2}}\{d_p^3\}\sqrt{\left(\frac{a+b}{S}\right)^2-\left(\left(\frac{\sum_{t=1}^{\frac{N}{2}}\{d_t^3\}}{\sum_{P=1}^{\frac{N}{2}}\{d_p^3\}}\right)-1\right)^2}}$$

<div align="right">Equ. 179</div>

As in the case of the flexure length and thickness, uncertainty in d_t and d_p is dependant on the accuracy of the manufacturing process (EDM), so

uncertainty $u_{id(t=1)}$

$$= \sqrt{(3d_{t=1}^2)^2 \left(\sum_{p=1}^{\frac{N}{2}} \{d_p^3\} \sqrt{\left(\frac{a+b}{S}\right)^2 - \left(\left(\frac{\sum_{t=1}^{\frac{N}{2}}\{d_t^3\}}{\sum_{P=1}^{\frac{N}{2}}\{d_p^3\}}\right) - 1\right)^2}\right)^{-2} \left(\frac{1 \times 10^{-6}}{\sqrt{3}}\right)^2}$$

Equ. 180

uncertainty in tilt due to flexure depth u_{id}

$$= \sqrt{\sum_{t=1}^{N/2} \left(\frac{\partial i}{\partial d_t}\right)^2 (u_{dt})^2 + \sum_{p=1}^{N/2} \left(\frac{\partial i}{\partial d_p}\right)^2 (u_{dp})^2}$$

Equ. 181

The uncertainty in tilt angle due to the combined uncertainty in the depth of all the flexure members of a given axis guide is thus

uncertainty u_{id}

$$= \sqrt{2 \sum_{t=1}^{N/2} \left\{ (3d_{t=1}^2)^2 \left(\sum_{p=1}^{\frac{N}{2}} \{d_p^3\} \sqrt{\left(\frac{a+b}{S}\right)^2 - \left(\left(\frac{\sum_{t=1}^{\frac{N}{2}}\{d_t^3\}}{\sum_{P=1}^{\frac{N}{2}}\{d_p^3\}}\right) - 1\right)^2}\right)^{-2} \left(\frac{1 \times 10^{-6}}{\sqrt{3}}\right)^2 \right\}}$$

Equ. 182

The combined uncertainty in mirror tilt due to the component uncertainties in flexure dimensions and piezo positioning can now be calculated as

$$u_i = \sqrt{(u_{ia})^2 + (u_{ib})^2 + (u_{iL})^2 + (u_{id})^2}$$

Equ.183

The uncertainty in measurement arising from uncertainties in tilting of the measurement mirror and uncertainties in the flatness of reflection surfaces can now be calculated from

$u_{tilt/flatness}^2$

$$= \left(\frac{\lambda(L)}{a \cos^2 2i}\right)^2 (u_i)^2 + \left(\frac{\lambda(L + L_1)}{a_2 \cos^2 2i}\right)^2 (u_i)^2 + \left(\frac{\lambda(L + L_1 - L_2)}{a_2 \cos^2 2i}\right)^2 (u_i)^2$$

$$+ \left(\frac{\lambda(L + L_1 - L_2 - L_3)}{a \cos^2 2i}\right)^2 (u_i)^2$$

$$+ \left(\frac{10\lambda F_3(-L - L_1 + L_2 + L_3 + L_4 + L_5)(\cos i \sec^2 2i + \sin i \tan 2i)}{(10F_3 \cos i)^2}\right)^2 (u_i)^2$$

$$+ \left(\frac{2(L) \tan 2i}{a}\right)^2 (u_{FL})^2 + \left(\frac{2(L + L_1) \tan 2i}{a_2}\right)^2 (u_{FL})^2 + \left(\frac{2(L + L_1 - L_2) \tan 2i}{a_2}\right)^2 (u_{FL})^2$$

$$+ \left(\frac{2(L + L_1 - L_2 - L_3) \tan 2i}{a}\right)^2 (u_{FL})^2$$

$$+ \left(\frac{2F_{L3}}{F_3} \frac{\tan 2i}{\cos i}(-L - L_1 + L_2 + L_3 + L_4 + L_5)\right)^2 (u_{FL})^2$$

Equ. 184

Variables	Interferometer measurement axes		
(mm)	X axis	Y axis	Z axis
L	90.55	124.79	81.25
L_1	30	30	30
L_2	7.5	7.5	7.5
L_3	22.5	22.5	22.5
L_4	98.05	132.29	88.75
L_5	27.25	30.5	23.5
a	10	10	10
a_2	11.3	11.3	11.3
F_3	10	10	10
Offset of mirror	27.25	30.5	23.5
$a + b$	28.5	89.4	21.5
d_t, d_P	2	2	1.5
b_t, b_P	27	27	15
L_t, L_P	15.5	15.5	13.5

Table 21 Variable values, used for calculating uncertainty, based on dimensions taken from the instrument design drawings and manufacturer specifications.

	X axis	Y axis	Z axis
Standard tilt uncertainty (u_{ia})(deg) due to Piezo positioning Equ.161	2.132×10^{-7}	2.167×10^{-8}	3.747×10^{-7}
Standard tilt uncertainty (u_{ib}) (deg) due to flexure width Equ. 174	8.092×10^{-9}	2.58×10^{-9}	1.599×10^{-8}
Standard tilt uncertainty (u_{id}) (deg) due to flexure thickness Equ. 182	4.558×10^{-7}	1.453×10^{-7}	5.696×10^{-7}
Standard uncertainty (u_{iL}) (deg) due to flexure length Equ. 176	2.612×10^{-5}	8.325×10^{-6}	3.264×10^{-5}
Combined uncertainty in axis yaw (u_i) Equ. 184	3.735×10^{-5}	8.977×10^{-6}	5.63×10^{-5}

Table 22 Uncertainty in stage yaw due to component uncertainties of piezo positioning and non-symmetry of guiding flexures.

Table 21 lists the values of the variables used in, Equ. 178, Equ. 182 and Equ. 184. These are taken from the instrument design drawings and the manufacturer specifications of the interferometer optical components used.   The individual component uncertainties, based on these variables values, are then tabulated in Table 22.

	u_{iX}	u_{iY}	u_{iZ}
Uncertainty in mirror tilt angle (deg)	3.735×10^{-5}	8.977×10^{-6}	5.63×10^{-5}

Table 23 Combined uncertainty in mirror tilt angle calculated by using Equ. 120 and based on Table 20 and Table 22.

Given in Table 23 is the combined uncertainty in mirror tilt arising from piezo positioning and flexure imbalance, while Table 24 presents the resultant uncertainty in interferometer measurement. Note that the uncertainty in yaw appears to equal the uncertainty in mirror tilt. This is because, as shown earlier in this section, it is possible to be highly certain with regards to interferometer mirrors set-up alignment ($u\alpha$ = 188×10^{-8} deg).

	$u_{meas/tiltX}$	$u_{meas/tiltY}$	$U_{meas/tiltZ}$
Uncertainty in interferometer measurement due to mirror tilt (using Equ. 184) (nm)	0.205	0.307	0.187
Table 24 Calculated measurement uncertainty arising from mirror tilt.			

Other component uncertainties, such as thermal expansion of offsets, could have been considered in the estimation of $u_{tilt/flatness}$, but their possible contribution to its magnitude was considered to be negligible.

6.4   Mounting arrangement

As described in Chapter4, the instrument has been designed in accordance with the following key principles.

- The Abbe principle i.e. the measurement axes should coincide with the axes of movement.

- The sensors should be positioned as close as possible to the point of interest.

Nevertheless, uncertainties arise that are associated with both Abbe error and the thermal expansion of material bridging the offsets of both capacitance sensors and interferometer measurement mirrors from the point of interest.

6.4.1   Uncertainty due to the offset of the measurement mirrors.

The physical size of the measurement mirrors and their mounts prevent their placement at the stage point of interest. Likewise, two of the capacitance sensors must also be spatially located distant from this point. Thermal expansion of the material bridging the consequent offsets is compensated in the control software when the operational temperature differs from that at calibration. However, displacement measurement uncertainty still arises. Its magnitude depends on its component uncertainties that are associated in particular with temperature measurement, thermal expansion coefficients and measurement of the offset distances.

<u>Temperature measurement uncertainty</u>

Unlike in Section 6.2, where a GE Sensing/Thermoetrics [80] MC65 thermistor sensor (resolution ±0.1 K) could be used to give a sub-nanometre displacement uncertainty associated with thermal expansion of capacitance plates, the more accurate AS115 temperature standard sensor (resolution ±0.002 K) must be used in this instance for measuring the ambient temperature about the instrument. The significance of this sensor selection can be deduced from Fig. 164. The standard temperature measurement uncertainty when using this sensor can be calculated as follows

Std uncertainty due to temperature sensor $u_{\Delta T} = \dfrac{0.002}{\sqrt{3}} = 1.155$ K

<div align="right">Equ.185</div>

(Assuming a rectangular distribution of measurements)

<u>Thermal expansion coefficient uncertainty</u>

The material bridging the offsets is in all cases aluminium alloy 6082 T6 which has a stated CTE of 24 μm(m)$^{-1}$K^{-1}. Again, as explained in Section 4.3.2.1, the uncertainty in CTE can be calculated to be 2.0785×10^{-6} K^{-1}.

<u>Offset distances</u>

The offset distances given in Fig. 94 and Fig. 95 are merely approximate indicators of true component positions, since the mirror location can be varied by means of adjustment screws. As with the deadpath measurement, it is the accuracy of the digital vernier callipers offset measurement (±0.01 mm) that contributes to uncertainty. Unlike the flexibly mounted mirrors, the target capacitance plates are fixed to the stage material. Offset distances can thus be taken directly from the drawing. Uncertainty in offset accuracy is consequently dependant on the drawing tolerance of ±0.01 mm. Assuming a rectangular distribution, the uncertainty in offset distance can be estimated to be:

Std. uncertainty in offset measurement $u_{OS} = \dfrac{0.01 \times 10^{-3}}{\sqrt{3}} = 5.77 \times 10^{-6}$ m

<div align="right">Equ. 186</div>

The change in offset distance due to thermal expansion is calculated by the equation

$$\Delta(OS) = \alpha_{OS}L_{OS}T$$

where α_{OS} is the thermal expansion coefficient of the bridging material, L_{OS} is the offset distance of the mirror or capacitor and ΔT is the difference in temperature at operation from that at calibration. The uncertainty in the magnitude of this change can be quantified in accordance with the GUM [23] as follows.

$$u_{M/\Delta OS} = \sqrt{\left(\frac{\partial(\Delta OS)}{\partial(T)}\right)^2 (u_T)^2 + \left(\frac{\partial(\Delta OS)}{\partial \alpha_{OS}}\right)^2 \left(u_{\alpha(OS)}\right)^2 + \left(\frac{\partial(Me)}{\partial L_{OS}}\right)^2 (u_{OS})^2}$$

$$u_{M/\Delta OS} = \sqrt{(\alpha_{OS}L_{OS})^2 (u_T)^2 + \left(L_{OS}(T_1 - T_0)\right)^2 \left(u_{\alpha(OS)}\right)^2 + \left(\alpha_{OS}(T_1 - T_0)\right)^2 (u_{OS})^2}$$

	X axis	Yaxis	Z axis
Capacitance offset (mm) from Fig. 93	20.3	21.3	0
Mirror offset (mm) from Fig. 94 and Fig. 95	29.75	33	26
Measurement uncertainty due to mirror offset $u_{M/\Delta OS}$ (nm) using Equ. 186	0.824	0.914	0.72
Measurement uncertainty due to capacitor offset $u_{C/\Delta OS}$ (nm) using Equ. 189	0.56	0.59	0
Table 25 Offset distance of measurement mirrors and capacitance sensors from stage point of interest along with the resultant uncertainties.			

For the Z axis the uncertainty is seen to be less significant as the capacitance sensor is located at the point of interest. The uncertainty of compensations increases as operating temperatures deviate from the temperature at calibration. In Fig. 163 a graph is presented of calculated Z axis $u_{M/\Delta OS}$ versus operating temperature, given a temperature of 293.15 K at calibration. To ensure an uncertainty of less than 1 nm for this axis, this temperature difference cannot be more than 0.0125 K. Similar curves have been calculated for the X and Y axes. The significance of the temperature sensor resolution effect on the magnitude of $u_{M/\Delta OS}$ is plotted in Fig. 164. It can be deduced

that the sensor must have a resolution of less than 0.0026 K to achieve sub-nanometre uncertainty in measurement compensation. On the other hand, it can be deduced from Fig. 165 that a digital vernier with an apparently large tolerance of ±0.01 mm is adequate for measuring the offset distances during assembly.
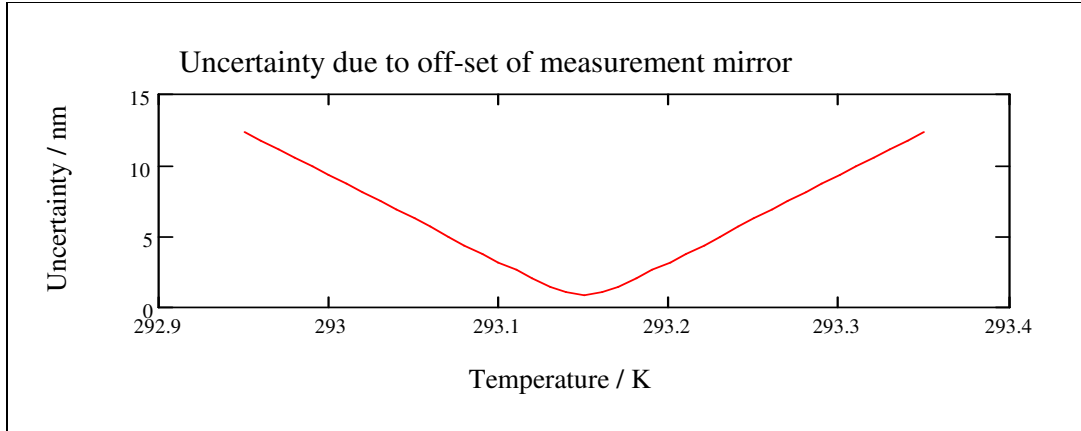
Fig. 163   Z axis positional uncertainty versus operating temperature, when the temperature at calibration is 293.15 K.
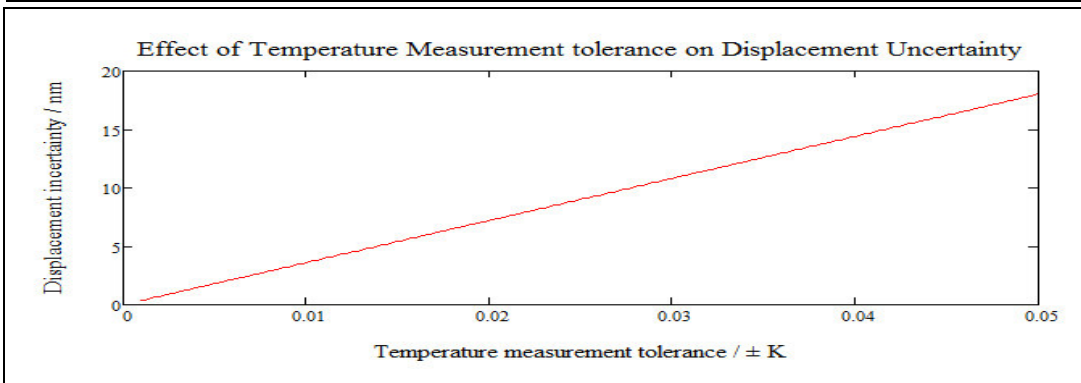
Fig. 164   The effect of temperature sensor resolution on the magnitude of displacement uncertainty arising from the component uncertainty $u_{M/\Delta OS}$.
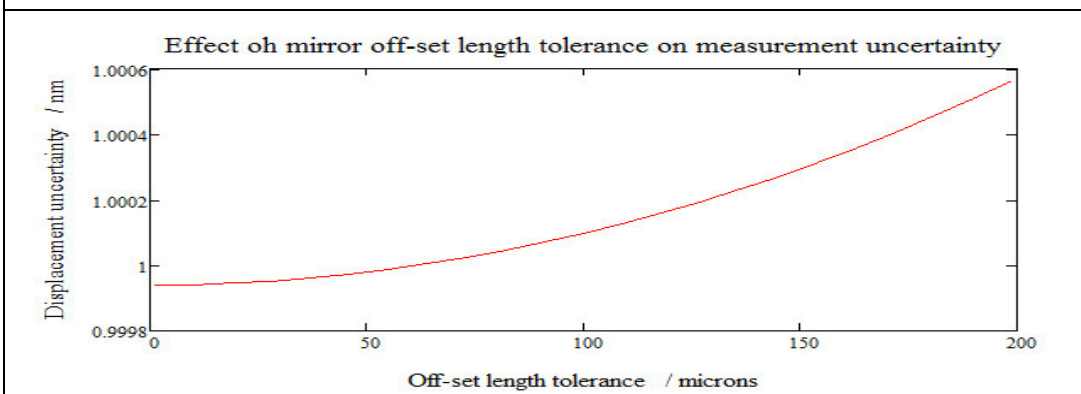
Fig. 165 Z axis positional uncertainty versus tolerances in mirror off-set distance measurement.

6.4.2 Cosine and Abbe uncertainty

Cosine error

As explained in Section 2.4.3.4, cosine error is the difference between the actual distance travelled by a stage and the measured value attributed to its displacement; the difference arising from a misalignment between the movement and measurement axes. It is proposed to achieve appropriate alignment resolution through carefully deigned rigorous set-up procedures, involving the use of a specially designed jig and a decoupling plate. These procedures are described in detail in Section 7.2.

Uncertainty in cosine error, u_{CE}, results from uncertainty in the angle, u_θ, which exists between the measurement axes and the movement axes

$$u_{CE} = \sqrt{\left(\frac{\partial CE}{\partial \theta}\right)^2 u_\theta^2}$$

Equ. 190

where CE is the cosine error, θ is the angle between the measurement axis and movement axis. From Equ. 4 (Y_m being the measured displacement)

$$u_{CE} = \sqrt{\left(\left(\frac{\tan \theta}{\cos \theta}\right) Y_m\right)^2 u_\theta^2}$$

Equ. 191

The uncertainty in the deviation angle, u_θ, is established through the interferometer set-up procedure that is described in Section 7.2. The procedure involves driving, consecutively, the stage along the two axes normal to the one being measured and adjusting the orientation of the moving axis in question until cross-talk is eliminated. The T40 model autocollimator (manufactured by Micro Radian Instruments [81]), having an angular resolution of 0.1 arc sec., is used to optimise this alignment. Assuming a rectangular distribution of auto collimator measurements, uncertainty in alignment may be calculated as

$$u_{collimator} = \frac{(0.1/60)}{\sqrt{3}} = 0.001°$$

For the X axis, uncertainty in the alignment angle, θ, may be calculated from

$$u_{\theta X} = \sqrt{u_{collimator}{}^2 + u_{yaw\ in\ Y}{}^2 + u_{yaw\ in\ Z}{}^2} \qquad \text{Equ. 192}$$

For the Y axis, uncertainty in the alignment angle, θ, may be calculated from

$$u_{\theta Y} = \sqrt{u_{collimator}{}^2 + u_{yaw\ in\ X}{}^2 + u_{yaw\ in\ Z}{}^2} \qquad \text{Equ. 193}$$

For the Z axis, uncertainty in the alignment angle, θ, may be calculated from

$$u_{\theta Z} = \sqrt{u_{collimator}{}^2 + u_{yaw\ in\ X}{}^2 + u_{yaw\ in\ Y}{}^2} \qquad \text{Equ. 194}$$

Taking the axial yaw uncertainties from Table 23, uncertainties in axial alignment ($u_{\theta X}$, $u_{\theta Y}$ and $u_{\theta Z}$) are calculated to be 0.001 deg for all axes.

This translates, using, Equ. 190, to an insignificant cosine uncertainty. A less expensive autocollimator such as the model 50 [81] would result in a very acceptable cosine uncertainty of 0.02 nm, but the same measurements would result in an Abbe error of 1.6 nm.

Abbe Error

The mechanism by which Abbe error occurs has been described in Section 2.4.3.4 where the following expression is given.

$$Abbe\ Error = \Delta . \sin{(\alpha)}$$

(Equ. 5, Section 2.4.3.4)

From Equ. 5 it can be deduced that the uncertainty associated with Abbey error depends on the component uncertainties of offset distance, Δ, and deviation angle α.

Although the offset distance of the point of interest from the measurement axis, Δ, is made to equal zero in the design of the instrument, implementation of this in the real physical instrument relies on the set-up resolution. To achieve sub-nanometre Abbe uncertainty a micrometer with a resolution 2 μm is required to set the offset distance. The uncertainty in Δ, $u\Delta$, is thus

$$u\Delta = \frac{2 \times 10^{-6}}{\sqrt{3}} = 1.155 \times 10^{-6}\ m$$

Equ.195

Uncertainty in the deviation angle, u_α, may be taken to be identical to that used in the calculation of the uncertainty in cosine error, u_{CE}, i.e. $u_\alpha = 0.001°$ for all axes.

$$\text{uncertainty in Abbe error } u_{AE} = \sqrt{\left(\frac{\partial AE}{\partial \Delta}\right)^2 u_\Delta^2 + \left(\frac{\partial AE}{\partial \propto}\right)^2 u_\propto^2}$$

$$= \sqrt{(\sin \propto)^2 u_\Delta^2 + (\Delta \cos \propto)^2 u_\propto^2} = 0.04 \text{ nm}$$

<div align="right">Equ. 196</div>

6.4.3 Uncertainty in coordinate system transforms

The positional commands, referenced to the Cartesian coordinate system, are translated to a set of commands that are referenced to the 'instrument coordinate system' by a set of transform equations (Equ. 59) that are implemented through the driving program as described in Section 5.2.5.2. Measured stage positions are subsequently changed from 'instrument coordinates' to Cartesian coordinates by the monitoring program, using the transform equations Equ.   60, Equ. 61 and Equ. 62.   Uncertainties in these transformations effect positioning uncertainty and are dependent on the component uncertainties associated with the angular measurement of the interferometer axis orientation.

Therefore, it is first necessary to establish the angular measurement uncertainty. A novel artefact, described in Section 4.4 and illustrated in Fig. 100, allows the angles between the instrument measurement axes to be effectively measured. As explained in Section 4.4, it consists of an assembly of mirrors mounted on an adjustable bracket and, when used with Equ. 48, allows the angles between the co-planer interferometers, α, to be found.

$$\alpha = \frac{1}{2}\left\{x_1 + x_3 + y_2 + y_4 - \sum_{i=1}^{i=4} \theta_i\right\} + 90$$

<div align="right">Equ. 48</div>

where θ_i is the angle that the ith artifact mirror$_i$ subtends to one of two mutually normal axes, as illustrated in Fig. 103, while x_1, x_3, y_2, and y_4 are the angles between the individual artifact mirror surfaces and those of the interferometer measurement mirrors as illustrated in Fig. 104. Uncertainty in the angle α can be calculated using

$$u_{\propto} = \sqrt{\begin{array}{l} \left(\dfrac{\partial \propto}{\partial x_1}\right)^2 u_{x1}^2 + \left(\dfrac{\partial \propto}{\partial x_3}\right)^2 u_{x3}^2 + \left(\dfrac{\partial \propto}{\partial y_2}\right)^2 u_{y2}^2 + \left(\dfrac{\partial \propto}{\partial y_4}\right)^2 u_{y4}^2 \\ + \left(\dfrac{\partial \propto}{\partial \theta_1}\right)^2 u_{\theta1}^2 + \left(\dfrac{\partial \propto}{\partial \theta_2}\right)^2 u_{\theta2}^2 + \left(\dfrac{\partial \propto}{\partial \theta_3}\right)^2 u_{\theta3}^2 + \left(\dfrac{\partial \propto}{\partial \theta_4}\right)^2 u_{\theta4}^2 \end{array}}$$

Equ.197

$$\left(\frac{\partial \propto}{\partial x_1}\right) = \left(\frac{\partial \propto}{\partial x_3}\right) = \left(\frac{\partial \propto}{\partial y_2}\right) = \left(\frac{\partial \propto}{\partial y_4}\right) = \left(\frac{\partial \propto}{\partial \theta_1}\right) = \left(\frac{\partial \propto}{\partial \theta_2}\right) = \left(\frac{\partial \propto}{\partial \theta_3}\right)\left(\frac{\partial \propto}{\partial \theta_4}\right) = \frac{1}{2}$$

Angle x_1 is obtained by subtracting the tilt of the X axis measurement mirror (i_x) from that of the artifact *mirror1* (m_1), both angles being measured in the XY plain.

$$x_1 = m_1 - i_x$$

The uncertainty in x_1 is calculated from

$$u_{x1} = \sqrt{\left(\frac{\partial x_1}{\partial m_1}\right)^2 u_{m1}^2 + \left(\frac{\partial x_1}{\partial i_x}\right)^2 u_{ix}^2}$$

Equ. 198

Since m_1 and i_x are measured in the same manner.

$$\frac{\partial x_1}{\partial m_1} = \frac{\partial x_1}{\partial i_x} = 1 \quad and \quad u_{m1} = u_{ix} = u_i$$

$$u_{x1} = \sqrt{2(1)^2 u_i^2} = \sqrt{2}.\, u_i$$

$$u_{\propto} = \sqrt{4\left(\frac{1}{2}\right)^2 \left(\sqrt{2}\, u_i\right)^2 + 4\left(\frac{1}{2}\right)^2 u_i^2} = \sqrt{3} u_i$$

Equ. 199

Location coordinate monitoring uncertainty

As when aligning the movement and measurement axes, the T40 model autocollimator (manufactured by Micro Radian Instruments) is used to measure the mirror orientations. By assuming a rectangular distribution of auto collimator measurements, angular uncertainty is again given by

$$u_{collimator} = \frac{(0.1/60)}{\sqrt{3}} = u_i$$

239

and uncertainty in orthogonality measurement can now be calculated as $u_\alpha = 0.0017^o$

The X coordinate of positions described in the Cartesian system are translated to the instrument coordinate system through the use of Equ. 60

$$x = \frac{\frac{y1\sin\alpha}{\cos\theta} + x1}{\cos\alpha - \tan\theta\sin\alpha}$$

Equ. 60

From Fig. 124 in Section 5.2.5.2 it can be deduced that x is the Cartesian X-axis coordinate of a point, while $x1$ is the instrument X axis coordinate of the same point. α is the tilt angle of the Y-axis in the direction of X axis and θ is the angle by which the X axis tilts towards the Y axis. The uncertainty in the X-axis coordinate arising from coordinate system transformation is thus

$$u_x = \sqrt{\left(\frac{\partial x}{\partial \alpha}\right)^2 u_\alpha^2 + \left(\frac{\partial x}{\partial \theta}\right)^2 u_\theta^2}$$

Equ. 200

$$(ux)^2 = \left\{ \frac{y1 + \frac{y1.\sin^2\alpha}{\cos^2\alpha}}{\cos\alpha - \sin\alpha.\tan\theta} + \frac{(\sin\alpha + \cos\alpha\tan\theta)\left(x1 + \frac{y1\sin\alpha}{\cos\alpha}\right)}{(\cos\alpha - \sin\alpha\tan\theta)^2} \right\}^2 u_\alpha^2$$

$$+ \left\{ \frac{\sin\alpha.\left(x1 + \frac{y1\sin\alpha}{\cos\alpha}\right)(\tan^2\theta + 1)}{(\cos\alpha - \sin\alpha\tan\theta)^2} \right\}^2 u_\theta^2 \implies ux = 0.26 \text{ nm}$$

Equ. 201

Similarly, the uncertainty in displacement measurement arising from coordinate system compensations in the X and Y axes, uy and uz, can be calculated to be 0.26 nm.

Location coordinate command uncertainty

The Cartesian command coordinates are translated to instrument coordinates via Equ. 59.

$$x1 = x\cos\alpha - y\sin\alpha$$

Equ. 59

240

Uncertainty in the command signals issued to the X axis piezo arising from coordinate system transformation can be calculated from

$$u_{x1} = \sqrt{\left(\frac{\partial x_1}{\partial \propto}\right)^2 u_{\propto}{}^2} = \sqrt{(-x \sin \propto -y \cos \alpha)^2 \, u_{\propto}{}^2} = 0.26 \text{ nm}$$

Similarly, the uncertainty in displacement commands arising from coordinate system compensations in the X and Y axes, uy_1 and uz_1, can also be calculated to be 0.26 nm.

6.5   Conclusion

This chapter has addressed the uncertainties associated with the instrument measurement system designed specifically for this thesis. Uncertainties such as those concerned with environmental measurement, manufacturing tolerancing, material specification, component location and orientation, etc. have been identified and analysed. By so doing, insight into how they may propagate into measurement uncertainty, and an appreciation of their relative magnitudes, has been achieved. In order to achieve sub-nanometer positioning resolution, it has been found that, in some individual key instances, tight tolerancing is required in terms of temperature measurement (±0.002 K), axial alignment (±0.01 arc sec.) and measurement of set-up offset distances (±1 µm).

A brief description has been given of the standardised method adopted for calculating and expressing these uncertainties. A cause and effects diagram is presented describing the interdependence and propagation of these uncertainties. The individual error sources associated with the capacitance sensors and the reference interferometers were then addressed in turn. The following component uncertainties were included in the analysis.

For the capacitance sensors: measurement linearity, electronic noise, thermal expansion of plates, environmental influence on relative permittivity, and expansion of sensor to sweet-spot offset distances.

For the interferometers: environmental influence on laser wavelength, thermal expansion of dead path, expansion of optical components, periodic variations, expansion of reference mirror offset distances, influence of mirror tilt combined with mirror flatness, Abbe error, cosine error, coordinate transforms.

For each, mathematical functions were derived, relating all significant factors to stage displacement measurement. Type B component uncertainties were calculated for all factors as were their sensitivity functions. Ultimately, combined uncertainty magnitudes were found in accordance with GUM [23] and these values are summarised in the error budget given in Table 26.

The combined uncertainty for each axis is calculated as the root of the sum of the squares of the component uncertainties and is given in Table 26. Expanded uncertainty values corresponding to 95 % confidence are also tabulated in Table 26 and are obtained by multiplying the combined uncertainty values by a coverage factor of two. For example, it is now possible to say that the designed instrument stage can be positioned to within ±3.02 nm of its commanded location (with 95% confidence) along its X axis.

Uncertainty	Description	X Axis	Y axis	Z Axis
u_{NCL}	Non-linearity	0.006 N_P^{-1}m	0.006 N_P^{-1}m	0.006 N_P^{-1}m
u_{SN}	Capacitance sensor noise	0.011 nm	0.011 nm	0.011 nm
u_{IN}	Interferometer sensor noise	0.02 nm	0.02 nm	0.02 nm
u_{MPU}	Mains pick-up noise	0.84 nm	0.84 nm	0.84 nm
u_{qN}	Quantisisation noise	0.0.07 nm	0.07 nm	0.07 nm
u_{noise}	noise	0.843 nm	0.843 nm	0.843 nm
$u_{\Delta T}$	Temperature measurement	0.086 K	0.086 K	0.086 K
$u_{AL\alpha}$	Thermal expansion coefficient of aluminium	2.0785×10^{-6} K^{-1}	2.0785×10^{-6} K^{-1}	2.0785×10^{-6} K^{-1}
u_r	Manufacturing	5.774 μm	5.774 μm	5.774 μm
$u_{C/Rad}$	expansion of plate radii	6.735 nm	6.735 nm	6.735 nm
$u_{MC/Rad}$	measurement uncertainty due to expansion of plate radius	0.09 nm	0.09 nm	0.09 nm

Uncertainty	Description	X Axis	Y axis	Z Axis
$u_{AL\alpha}$	Thermal expansion coefficient of aluminium structures	2.0785×10^{-6} K^{-1}	2.0785×10^{-6} K^{-1}	2.0785×10^{-6} K^{-1}
$u_{AL\alpha}$	Thermal expansion coefficient of aluminium mounts	2.0785×10^{-6} K^{-1}	2.0785×10^{-6} K^{-1}	2.0785×10^{-6} K^{-1}
$u_{AL\alpha}$	Thermal expansion coefficient of aluminium plates	2.0785×10^{-6} K^{-1}	2.0785×10^{-6} K^{-1}	2.0785×10^{-6} K^{-1}
$u_{SS\alpha}$	Thermal expansion coefficient of stainless steel mount screws	0.98×10^{-6} K^{-1}	0.98×10^{-6} K^{-1}	0.98×10^{-6} K^{-1}
$u_{\Delta T}$	Temperature measurement	0.001 K	0.001 K	0.001 K
$U_{L1,L2,L3}$	Offset distance measurement	5.77 μm	5.77 μm	5.77 μm
U_{L4}	Offset distance measurement	3 μm	3 μm	3 μm
$u_{MC/gap}$	Measurement uncertainty due to axial expansion of plates and mounts	0.01 nm	0.01 nm	0.01 nm
u_{RH}	Relative humidity	2.89 %	2.89 %	2.89 %
u_{CO2}	Partial pressure of CO2	0.00004 kPa	0.00004 kPa	0.00004 kPa
$u_{\Delta T}$	Temperature measurement	0.086 K	0.086 K	0.086 K
$u_{(\varepsilon r)}$	Variability in relative permittivity(εr) due to environmental factors	31.93×10^{-6}	31.93×10^{-6}	31.93×10^{-6}
$u_{(M\varepsilon r)}$	Measurement uncertainty due to Variability in relative permittivity(εr) arising from environmental factors	0.47 nm	0.47 nm	0.47 nm
u_{OS}	Offset distance measurement	5.77 μm	5.77 μm	5.77 μm
$u_{\Delta T}$	Temperature measurement	1.155×10^{-3} K	1.155×10^{-3} K	1.155×10^{-3} K
$u_{AL\alpha}$	Thermal expansion coefficient of aluminium	2.0785×10^{-6} K^{-1}	2.0785×10^{-6} K^{-1}	2.0785×10^{-6} K^{-1}
$U_{C/\Delta}$	Sweet-spot offset from capacitor	0.56 nm	0.59 nm	0

Uncertainty	Description	X Axis	Y axis	Z Axis
$U_{M/\Delta}$	Sweet-spot offset from mirror	0.824 nm	0.914 nm	0.72 nm
u_{Calc}	Calculation	N/a	N/a	N/a
$u_{\Delta T}$	Temperature measurement	0.086 K	0.086 K	0.086 K
$u_{\Delta P}$	Pressure measurement	0.309 ppm	0.309 ppm	0.309 ppm
$u_{\Delta H}$	Humidity measurement	0.022 ppm	0.022 ppm	0.022 ppm
$U_{C/WL}$	Measurement uncertainty arising from environmental effect on wavelength	0.005 nm	0.005 nm	0.005 nm
$u_{\Delta T}$	Temperature measurement	0.086 K	0.086 K	0.086 K
$u_{AL\alpha}$	Thermal expansion coefficient of aluminium	2.0785×10^{-6} K^{-1}	2.0785×10^{-6} K^{-1}	2.0785×10^{-6} K^{-1}
$U_{L/DP}$	Dead path distance measurement	5.77 μm	5.77 μm	5.77 μm
u_{DP}	Expansion of interferometer deadpath	0.014 nm	0.014 nm	0.014 nm
$u_{\Delta T}$	Temperature measurement	0.086 K	0.086 K	0.086 K
u_{α}	Thermal expansion coefficient of optics	0.204×10^{-6} K^{-1}	0.204×10^{-6} K^{-1}	0.204×10^{-6} K^{-1}
u_{t}	Manufactures dimensional tolerances	72.168 μm	72.168 μm	72.168 μm
$U_{C/EOC}$	Measurement uncertainty arising from expansion uncertainties of optical components	0.395 nm	0.395 nm	0.395 nm
u_{i}	Mount tilting tolerance (deg)	4.6×10^{-6}	4.6×10^{-6}	4.6×10^{-6}
$U_{Tilt/M}$	Measurement uncertainty arising from mirror tilt and scale factor	0 nm	0 nm	0 nm
u_{i}	Mount tilting tolerance	0.00204^{0}	0.00204^{0}	0.00204^{0}

Uncertainty	Description	X Axis	Y axis	Z Axis
$U_{FL/Retro/BS}$	Flatness tolerance of retro-reflectors and beam splitters	$\dfrac{\lambda}{4\sqrt{3}}$	$\dfrac{\lambda}{4\sqrt{3}}$	$\dfrac{\lambda}{4\sqrt{3}}$
$U_{Fl/M}$	Flatness tolerance of measurement mirrors	$\dfrac{\lambda}{20\sqrt{3}}$	$\dfrac{\lambda}{20\sqrt{3}}$	$\dfrac{\lambda}{20\sqrt{3}}$
U_{mFLt}	uncertainty in measurement due to the optical surface flatness and tilt angle	0.02 nm	0.02 nm	0.02 nm
U_a	Piezo positioning	5.77 μm	5.77 μm	5.77 μm
u_{ia}	Uncertainty in mirror tilt due to Piezo positioning uncertainty (deg)	2.67×10^{-5}	3.353×10^{-6}	4.587×10^{-5}
U_b	Flexure depth (milling process)	0.577 μm	0.577 μm	0.577 μm
u_{ib}	Uncertainty in tilt due to flexure depth uncertainty (deg)	8.092×10^{-9}	2.58×10^{-9}	1.599×10^{-9}
U_d	Flexure depth (EDM process)	0.577 μm	0.577 μm	0.577 μm
u_{id}	Uncertainty in tilt due to flexure thickness uncertainty	4.558×10^{-7} deg	1.453×10^{-7} deg	5.696×10^{-7} deg
U_L	Flexure length (EDM process)	0.577 μm	0.577 μm	0.577 μm
u_{iL}	Uncertainty in tilt due to flexure length uncertainty Equ. 178	2.612×10^{-5} deg	8.325×10^{-6} deg	33.264×10^{-5} deg
u_i	Combined uncertainty in axis yaw	3.735×10^{-5} deg	8.977×10^{-6} deg	5.63×10^{-5} deg
	Combined Uncertainty in mirror tilt angle arising from yaw and piezo positioning	3.735×10^{-5} deg	8.977×10^{-6} deg	5.63×10^{-5} deg
$U_{Tilt/flatness}$	Uncertainty in measurement due to yaw and flatness of optical surfaces	0.205 nm	0.307 nm	0.187 nm

Uncertainty	Description	X Axis	Y axis	Z Axis
u_i	Combined uncertainty in stage yaw due to piezo positioning and flexure non-symmetry (deg)	3.735×10^{-5}	8.977×10^{-6}	5.63×10^{-5}
u_i	Mount tilting uncertainty (deg) (Table 26 and Equ. 126)	0.096^0	0.096^0	0.096^0
u_θ	Combined uncertainty (deg) in the deviation between the measurement and movement axes	3.735×10^{-5}	8.977×10^{-6}	5.63×10^{-5}
$u\varDelta$	Uncertainty in measuring the measurement to movement axis offset	1.155 µm	1.155 µm	1.155 µm
U_{CE}	Uncertainty in Cosine error	0 nm	0 nm	0 nm
U_{AE}	Uncertainty in Abbe error	0.04 nm	0.04 nm	0.04 nm
$U_{XYZ(m)}$	Uncertainty in location coordinate (monitoring)	0.26 nm	0.26 nm	0.26 nm
$U_{XYZ(c)}$	Uncertainty in location coordinate (commanding)	0.26 nm	0.26 nm	0.26 nm
	Combined Uncertainty in yaw (deg)	3.735×10^{-5}	8.977×10^{-6}	5.63×10^{-5}
	Expanded Uncertainty (95 %) in yaw (deg)	7.4×10^{-5}	17.954×10^{-6}	11.26×10^{-5}
	Combined Uncertainty	1.52 nm	1.6 nm	1.35 nm
U	Expanded Uncertainty (95 %) (positioning tolerance)	3.04 nm	3.2 nm	2.7 nm

Table 26 Uncertainty budget for the instrument metrology system.

Fig. 166 Pie charts of axial component uncertainties.
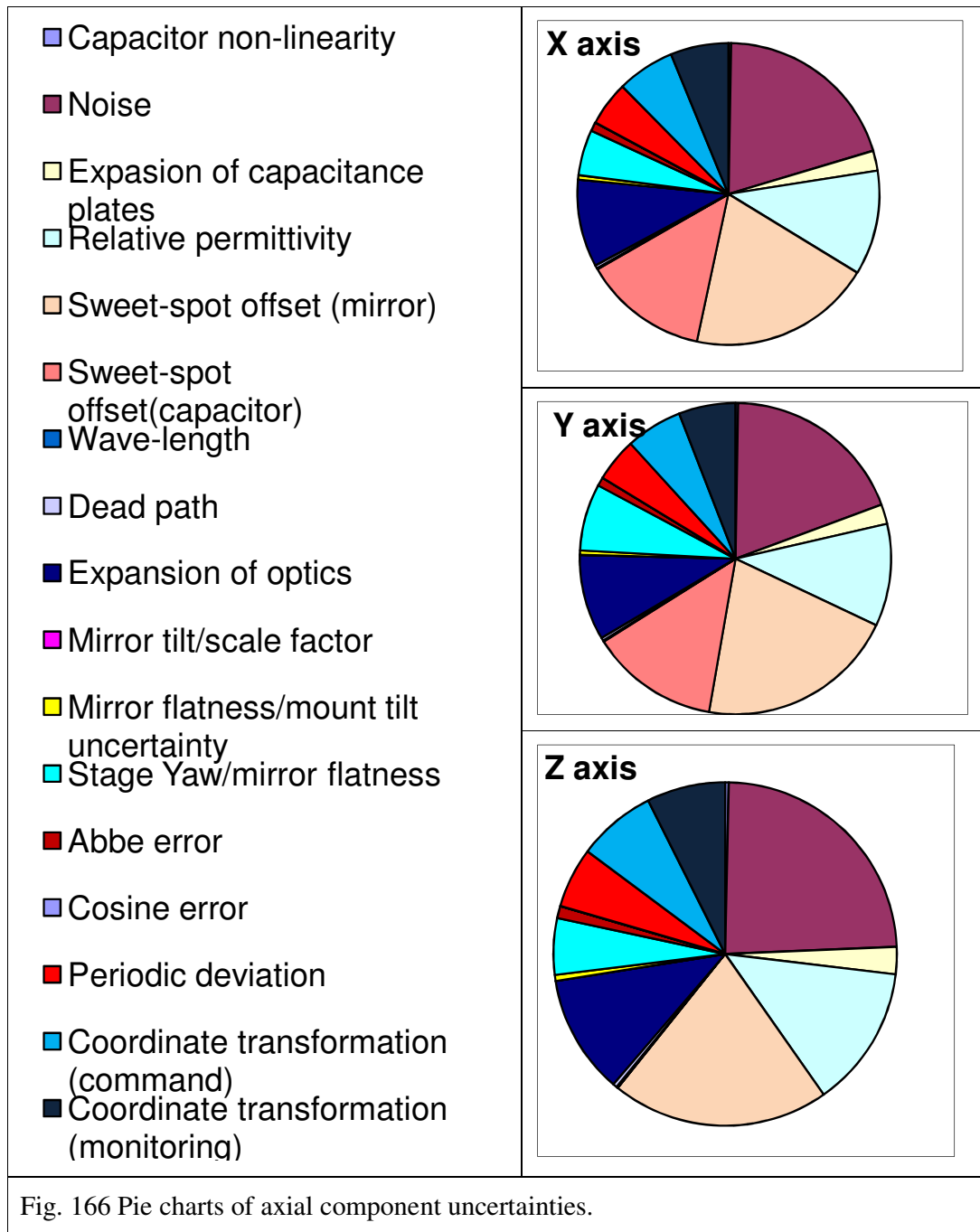
The predicted positioning tolerances indicated in Table 26 are true only if the identified requirements are met in terms of alignment tolerances, environmental monitoring tolerances and maximum environmental parameter ranges. The following chapter describes proposed instrument assembly/alignment and environmental arrangements designed to meet these requirements.

Chapter 7

7 Proposed Set-up Procedures, Environment and Experimentation

7.1 Introduction

This chapter is essentially concerned with the future development of this project. It starts with a discussion of the set-up for rendering the instrument described in this thesis capable of achieving optimum positioning accuracy. The set-up requirements are first established, followed by a step-wise description of procedures, alignments, orientations, and specially designed jacks, jigs and decoupling plates. These steps would lead to a fully assembled, calibrated and error compensated instrument in which the reference axes are orientated near normal to each other and aligned with both the stage movement axes and the measurement axes of the capacitance sensors.

Next the establishment of facilities required to maintain a suitable environment for operating such an accurate instrument is examined. Based on the predicted effects of environmental variation on the instrument performance, the design objectives for the environmental control system are established. These give rise to a proposed environmental arrangement, which, when compared with the present facilities, results in a plan for necessary future development.

Finally, a set of experiments is designed for characterizing the instrument and validating the design work and theory described in previous chapters. From the requirements of the experimentation, the experimental yields are identified and the relevant environmental, compensation, and alignment factors, as well as their main interactions and levels are stated. The treatment combinations and replicates for both full and screening fractional factorial sets of experiments are defined. Randomizing and blocking techniques are also proposed to minimize experimental uncertainty. A subsequent full factorial set of experiments is also designed to specifically examine the effects of contouring factors (radii, speed and resolution) on positioning accuracy.

7.2 Set-up procedure

The system should ultimately enable a single point on the stage to be translated between chosen locations along pre-defined linear and curved paths with a resolution in the nanometre range. As discussed in the previous chapters, to achieve this functional objective the instrument set-up should achieve the following:

- Any deviation of the measurement axes of the calibrating reference interferometers from the ideal mutually normal orientation of the Cartesian coordinate system must be measurable. (Note, as explained in Section 5.2.5.2, instrument location coordinates can be transformed to Gaussian coordinates and vice-versa if the angle between the systems is measured).

- The measurement axes of the interferometers must coincide closely with the measurement axes of the operational location sensors (the capacitors) in order to minimise scalar and non-linearity errors during calibration.

- The measurement axes of the capacitors must in turn be close to coincident with the movement axes of the point of interest on the stage, so as to minimise Abbe and cosine errors.

- The interferometer optics must be accurately aligned so that the paths followed by the optical rays change little as the stage is translated, thus minimising measurement errors related to the flatness of the reflecting optical components.

- The capacitance plates must be near to being mutually parallel so as to minimise non-linearity measurement errors.

- The piezo actuators must be carefully located so as to minimise off-axial displacements of the stage and to prevent damage to the piezo ceramics through bending and shear forces.

The set-up procedures can, therefore, be described as follows.

Step 1: Position the actuators

The piezo actuators are first mounted in position. For this thesis, simple jacks were designed to facilitate the positioning of the actuators. The basic geometries of these jacks mean that they can be easily fabricated in the WIT engineering workshop at minimal cost. They allow the stage to be pulled from its neutral home position, thus increasing the length of the gaps provided for locating the actuators. A drawing of the X axis piezo positioning jack is given in Fig. 167, while a cut-away drawing of this jack, shown in Fig. 168, illustrates how the pulling force is generated. Turning the handle clockwise forces blocks *C* and *D* to move apart. Block *A* and the stage, being connected to block *C* is pulled towards *B*, thus widening the gap for the piezo.

Fig. 167 Jack designed for positioning the X axis piezo actuator, shown with the stage/force frame.	Fig. 168 Cut-away drawing showing the X axis piezo positioning jack.
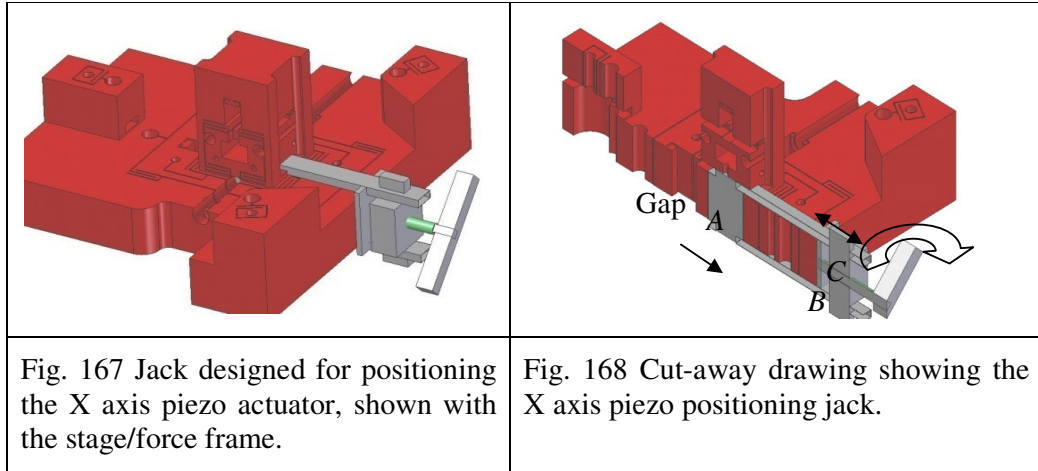
When the handle is then rotated anti-clockwise, the stage returns elastically to its original position, but, because the gap is shorter than the actuator, the piezo is pre-loaded and held in position. Similar jacks, designed for the Y and Z axes, are illustrated in Fig. 169 and Fig. 170. A vernier calliper is be used to ensure that the piezos are centrally placed within the gaps.
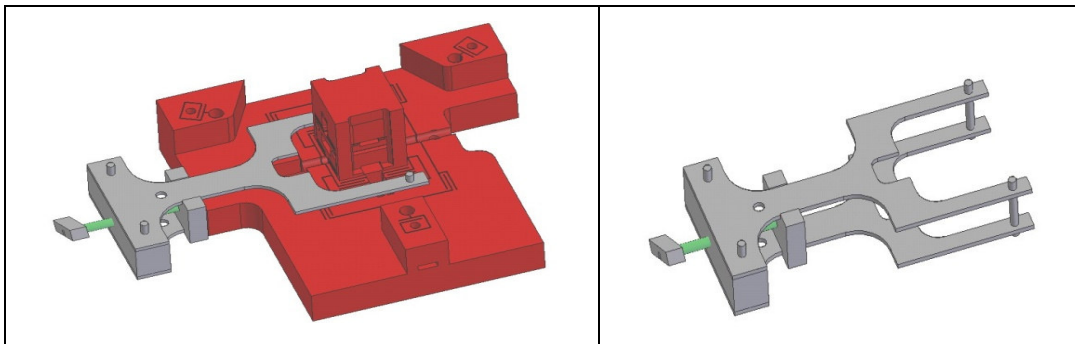
Fig. 169 The Y axis actuator positioning jack.
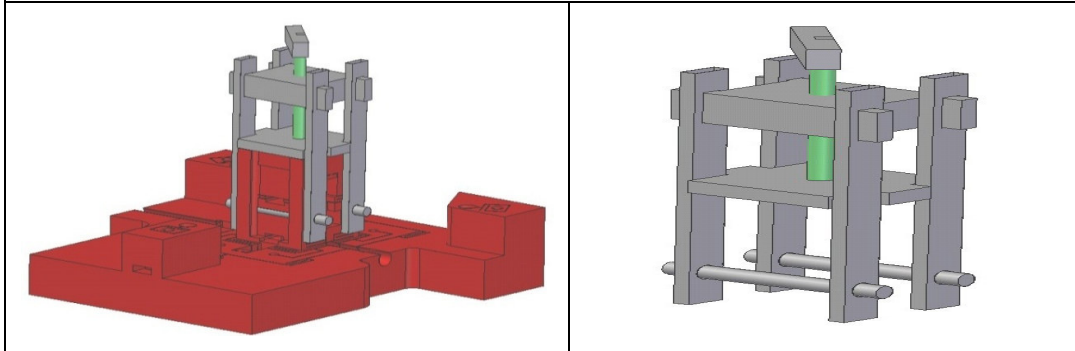
Fig. 170 The Z axis actuator positioning jack.

Use of the jacks ensures that loading of the flexures is even and controllable. Having positioned the piezos, the next step is to set up the interferometers.

Step 2: Assemble and align the X axis interferometer reference mirror with a table-top interferometer

A jig, designed for this thesis, facilitates the stage mounted mirror of each axis interferometer to be orientated at 90° to each other and to be coincident with their respective axes of displacement.
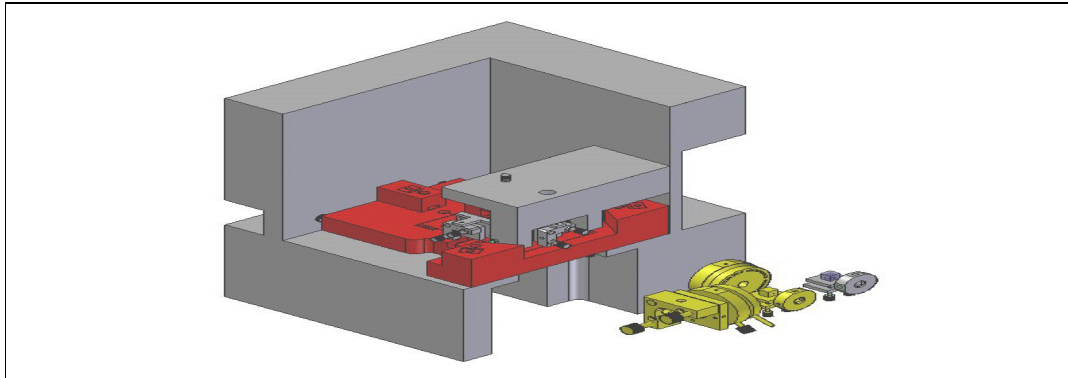
Fig. 171 Interferometer orientation jig. Shown in the position for aligning the X axis.

The measurement mirrors are first mounted on the stage and aligned such that they are visually judged to be mutually normal. The stage is then placed in the purposely designed jig and the X axis mirror should be aligned with a table-top mounted interferometer. For convenience this interferometer may be a single pass Michelson type as described in Section 4.3.1. This arrangement is shown in Fig. 171.

The following widely published, systematic method for interferometer alignment is suggested as experience with the single axis prototype stage indicates it to be effective (names given here to components are those given in Fig. 22, Section2.6.2.1);

- The mirrors are positioned so that the measurement and reference beams (Beam2 and Beam1 respectively as per Fig. 22) travel equal distances and so that the laser beams are at the central height of the moving mirror.

- The reference mirror (*M1*) is blocked from reflecting.

- The tilt of the stage mounted mirror is adjusted until it reflects back along its path to the laser.

252

- A screen is placed so that the beam splitter reflects the light from the moving mirror (Beam2) onto its centre, ignoring the weak internal reflections from the beam splitter.

- The stationary mirror is uncovered and its tilt is adjusted until the reference beam (Beam1) is reflected by the beam splitter to the same spot on the screen as the measurement beam. The beams should now combine to form an interference pattern on the screen.

- A circular fringe pattern, radiating from a single central spot, is formed only when all the mirrors and beam splitter are correctly aligned.

- Further adjustment of the moving mirror (*M2*) may be necessary before a satisfactory fringe pattern is obtained.

On completion of this exercise, the interferometer is correctly aligned with the moving mirror of the X axis.

Step3: Aligning the movement axes with the interferometer measurement axes.

It is still not known whether the interferometer is aligned with the translating axis of the stage point of interest. To check this, the stage should be driven in turn along the Y and Z axes. This causes the measurement beam to scan across the surface of the X axis mirror. If the measurement axis is aligned with its displacement axis and the three displacement axes are themselves normal to each other, then no crosstalk is detected by the interferometer (the fringe pattern remains constant). If crosstalk is detected, it is likely that the measurement and displacement axes do not coincide.

To remedy this, there are two options: reorient the measurement axis or reorient the displacement axis. The first option involves repeatedly and tediously realigning the interferometer, followed by scanning until crosstalk is eliminated. The second is a novel approach developed for this thesis. It involves maintaining the alignment of the interferometer while changing alignment of the stage movement axis.
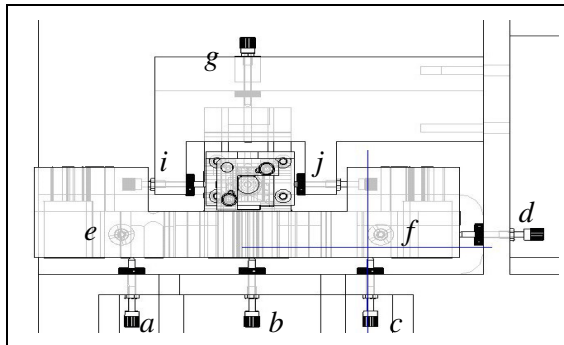
Fig. 172   A wire drawing of the X axis mirror mount clamped after alignment of the interferometer.

To achieve this, the X axis mirror is first clamped in position relative to the interferometer using fine thread locating screws (*i* and *j*) on the orientation jig as illustrated in Fig. 172.

An additional spring loaded adjusting plate is positioned between the mirror mount and the stage/force frame in order to allow the translation axis to be orientated relative to the measurement axis.
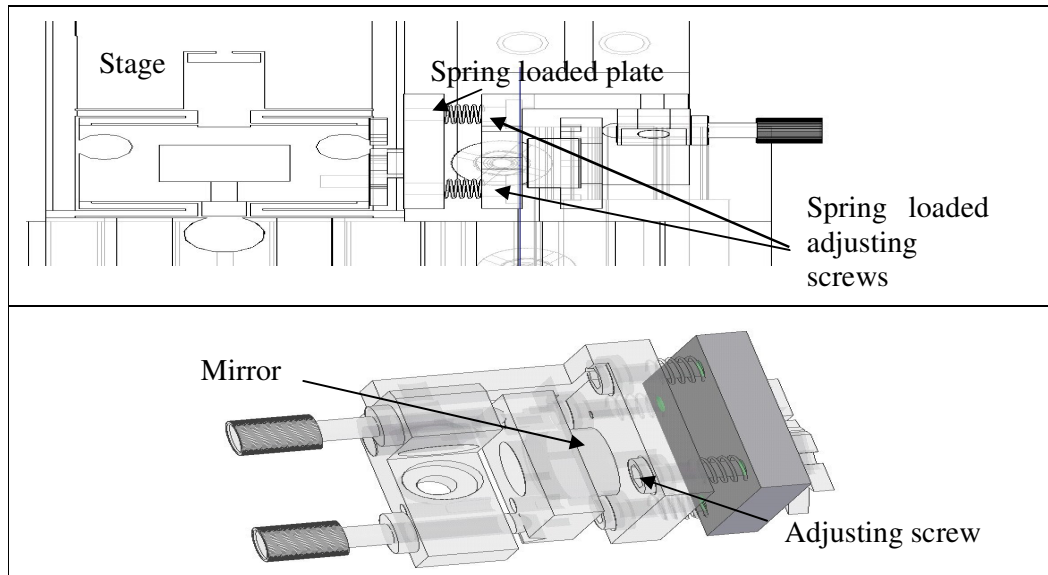
Fig. 173   Spring loaded plate to allow the X translation axis to be orientated while the interferometer mirror is fixed.

The spring mounted plate effectively provides a partial decoupling of the stage from the clamped mirror. When the fine thread positioning screws, (labelled *a, b, c, d, e* and *f* in Fig. 172) that have been up to now supporting the stage/force frame on the jig, are withdrawn, the structure is then held by the orientation plate spring loaded adjusting screws alone. Thus these screws facilitate a means of orientating the stage translation axis relative to the interferometer measurement axis.

The plate remains in place during normal operation of the stage and has several implications for the performance of the design.

254

- The plate springs support the mass of the mirror and its mount, so it introduces additional possible modal resonance frequencies.

- The distance between the measurement mirror and the point of interest is increased.

- Material with a different coefficient of thermal expansion than that of the instrument structures is introduced into the metrology loop.

Spring characteristics were determined on the basis that any additional instrument susceptibility to dynamic effects or environmental factors should be minimized. Within this framework:

- the length of the springs should be short; minimizing the offset distance of the mirror to the point of interest;

- The springs should be made of material with a coefficient of thermal expansion close to that of the instrument structures;

- the spring length to diameter ratios should be low in order to minimize the effects of off axial forces arising from Y and Z axis movements or background vibrations; and

- the resonant frequencies of all modes should be higher than the stage flexure axial natural frequencies.

Displacement of the mirror mount parallel to the movement of the driven stage can be viewed as the dominant mode in the case of a spring with a low length to diameter ratio. For this mode, displacements are due primarily to the expected acceleration/deceleration forces arising from commanded stage displacements along this axis. To determine the spring dimensions a resonant frequency of 2 kHz was chosen (over four times higher than that of the X axis flexures) and the mass of the mount and mirror was estimated to be 20 g. Sandvik 13RM19 stainless steel, with a Young's modulus of 190 GPa, a Poisson's ratio of 0.3 and CTE of 18 μm $(mK)^{-1}$ was chosen as the spring material. Using Equ. 22, the necessary spring stiffness of each of four springs in parallel was calculated to be 1184.34 kN.m^{-1}. Using standard spring formulae, it was found that a suitable spring with five turns and a mean diameter of 5.5 mm, could be made from Ø0.57 mm wire.

Several spring manufacturers could make the springs to specifications, but some also provide a range of suitable standard springs at lower prices. LESJOFORS Springs and Pressings [83], for example, make a large standard range, one being a stainless steel spring (Cat No. 2345) with six turns, wire Ø0.6 mm, outer Ø5.6 mm with a nominal length of 10 mm and stiffness of 1630 kN.m^{-1}. In general, to choose a standard spring involves some trade-off between spring length and stiffness.

<u>Alignment of reference mirrors</u>

The alignment of the measurement and displacement axes in the X direction after the initial alignment of the measurement mirror can be summarized as follows

- Clamp the measurement mirror using screws *i* and *j*. (Note the front plated of the mirror mount is already attached to the jig by a single screw, so the mirror is fully constrained when *i* and *j* are tightened).

- Withdraw the adjustment screws supporting the stage/force frame, leaving it to be held by the spring loaded screws of the orientation plate.

- Adjust the alignment of the displacement axis by means of the plate adjustment screws.

- Support the stage structures again using screws labelled *a, b, c, d, e* and *f* in Fig. 172.

- Unclamp the mirror mount by withdrawing screws *i* and *j*.

- Drive the stage along its Y and Z axis again so that the measurement beam scans across the X axis mirror and again check for crosstalk.

- Repeat the previous steps until crosstalk is eliminated.

Tacit knowledge, gained through practice should increase the speed and accuracy of this procedure, though a more systematic method is also applicable in this instance. By counting the number of fringes when scanning, the distance and direction that the X axis mirror is displaced due to crosstalk can be determined and hence the angle between the displacement and measurement axes can be calculated. Knowing the pitch of the adjusting screw and the distance between the centres of these screws the angle change per screw rotation can also be calculated. This knowledge should be a guide to

256

the magnitude of the adjustments. Due to the manifest sources of uncertainty associated with this technique, such as screw and plate tolerances, etc., only alignments verified by scanning and subsequent examination of the interference pattern can be relied upon.

Upon completion of the alignment procedures so far described, the measurement and movement axes in the X direction are aligned with the table-top interferometer. Also, due to the fixed nature of the stage geometry, the Y and Z displacement axes are as near to being normal to the measurement axis of the interferometer as is achievable. The next step is to align the Y and Z measurement axes, as their orientation is not yet known.

Step4: Make the Y and Z interferometer reference mirrors orthogonal to each other and to that of the X axis.

Fig. 174 Orientation of the alignment jig to align the Y axis measurement mirror. (Drawings show views from above and below for clarity).
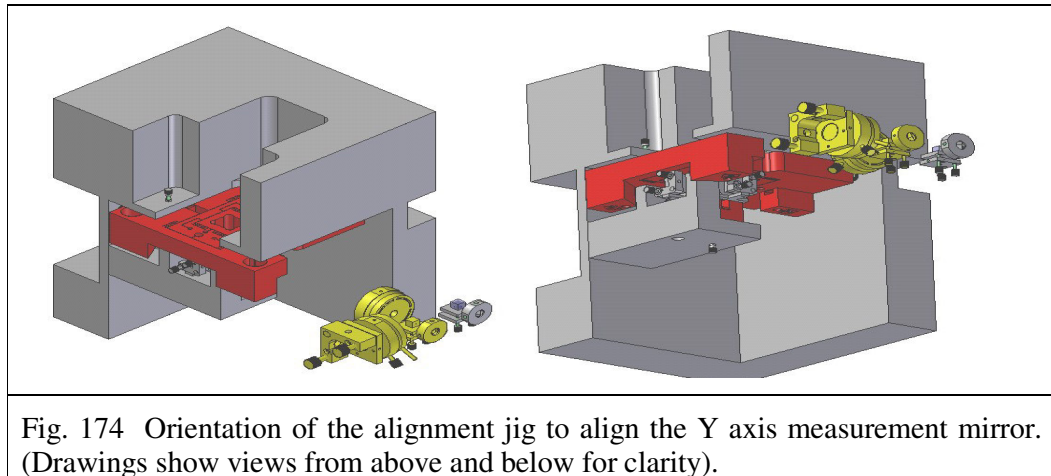
To align the Y axis mirror, the jig must be turned upside down and rotated through 90^0 to the position shown in Fig. 174, while keeping the X axis mirror and the stage/force frame clamped. The jig dimensions are such that, when it is orientated to this position, the measurement beam of the interferometer is reflected from the centre of the Y mirror. The X axis moving mirror is thus effectively replaced by the Y axis moving mirror.
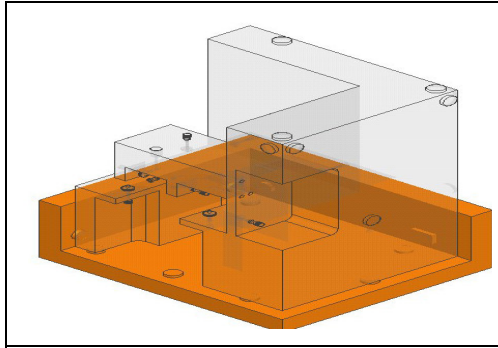
Fig. 175 Positioning right angled plate for the interferometer orientation jig, including the location of positioning pads.

To ensure that the jig is now normal to its original position, a fixed position right angle plate is used as illustrated in Fig. 175. In order that the tolerance requirements of this are such that it can be made in-house and to avoid over-constraint, contact between the jig and this plate is achieved through high surface finished glued pads. Gauge blocks can be used for this purpose.

The tilt of the moving mirror alone is adjusted until the circular fringe pattern is again formed. This indicates that the mirror is correctly aligned to the stationary mirror and beam splitter of the stationary interferometer.

With the aid of the right angled plate, the jig is next reorientation to the position shown in Fig. 176, with the purpose of facilitating the alignment of the Z axis measurement mirror. The only adjustments needed at this stage are to the tilt of this mirror; the re-formation of the circular fringe pattern being an indicator of alignment.
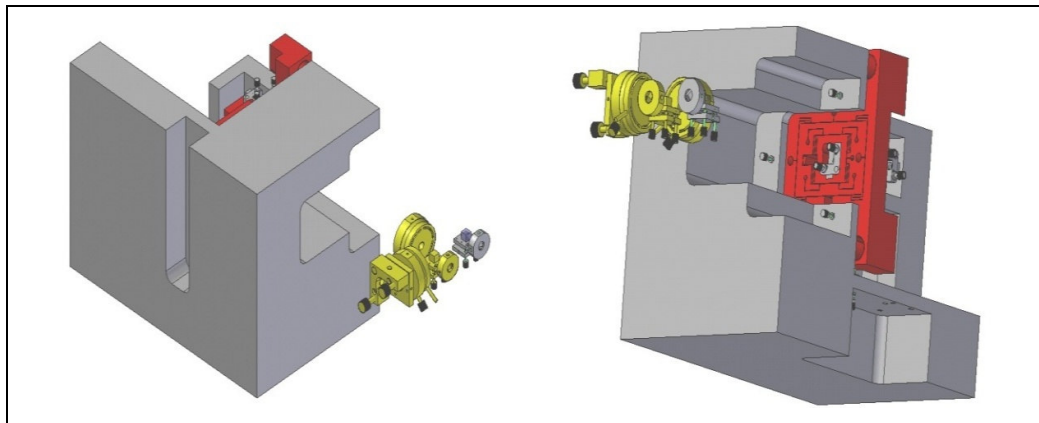
Fig. 176 Orientation of the alignment jig to align the Z axis measurement mirror. (drawings show different views for clarity)

Now that the measurement axes of all three moving mirrors are orientated at 90^0 to each other and coincide with the corresponding displacement axes of the point of interest on the stage, the moving capacitance plates can be mounted on the stage. These are glued in position (glue to be applied at the sides and edges of the

components only), using their accurate construction (the distance of the capacitance plate surface from its mounting surface is specified with a tolerance of ± 0.005 mm) to ensure that the stage displacement axes are near normal to the corresponding plate surfaces. Inaccuracy in the alignment is accommodated through error mapping program during the calibration process as explained in Section 5.2.1. The locations of these plates, relative to each other and to the stage, are illustrated in Fig. 177.
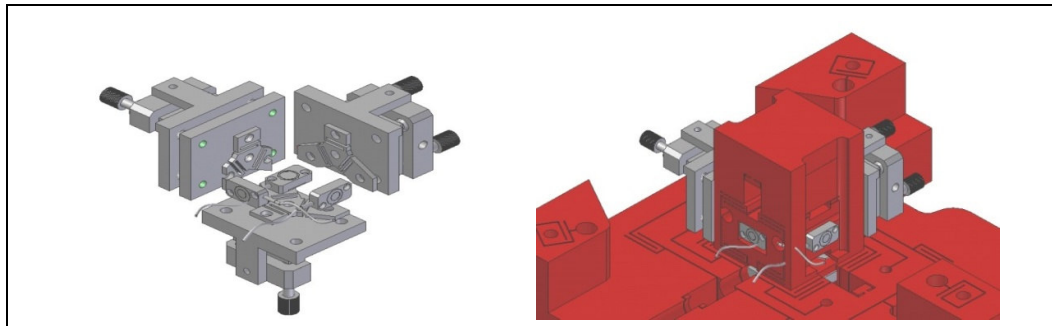
Fig. 177 The moving capacitance plates mounted on the stage with the moving interferometer mirrors.

Step5: Assembling the interferometer inter-axial angular measurement artefact.

The artefact for measuring the angle between the interferometer measurement axes is next mounted. The design, functionality and theory behind the use of this artefact are detailed in Section 4.4. This is screwed to the X and Y moving mirror connection plates, the locations of the threaded holes being indicated in Fig. 178. The orientation of the artefact relative to the moving mirrors and capacitance plates is illustrated in Fig. 179.
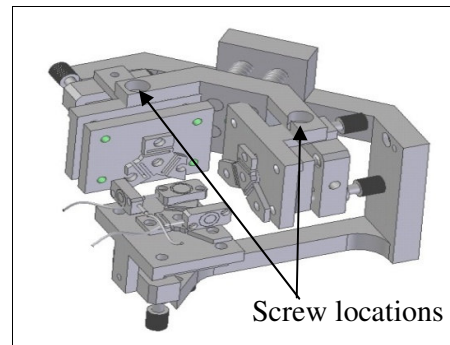
Screw locations

Fig. 178 Location of the artefact mounting screws.
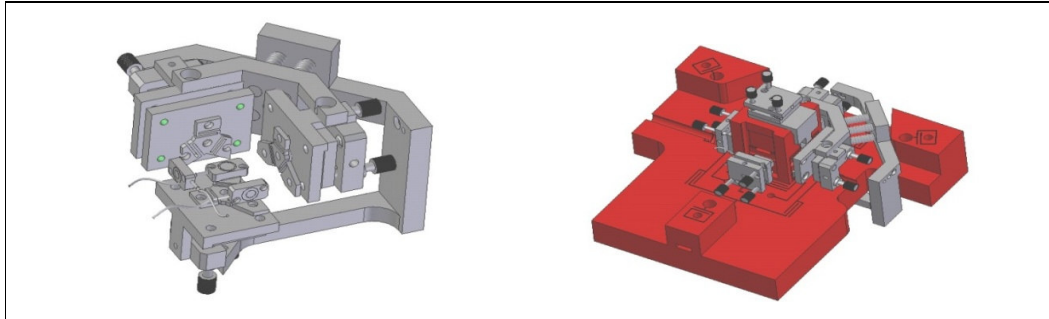
Fig. 179   The artefact designed to ensure orthogonality of the interferometer measurement axes mounted along with the stage mounted reference metrology components.

Step 6: Assembling the mechanical structures and stationary metrology components

The static structures and metrology components are next assembled. Firstly, the support frame is kinematically mounted on the base using ball-bearings in the V grooves. The reasoning for this and a more comprehensive description of arrangement, as applied in this instrument, is provided in Section 3.8.4.

The lower part of the metrology frame is then isostatically mounted on the support frame. The system uses dowel pins inserted in holes located on both the force frame and metrology frame, while most thermally induced stress at the holes is decoupled by use of wire-cut flexures. The pin/hole tolerances have been chosen to give a type IV friction fit, the closest fit which can be assembled by hand. Spacers on the pins help to ensure the correct proximity between frames, necessary if metrology components are to be subsequently properly aligned.

All the stationary components of the X and Y axis interferometers along with the three stationary capacitor plates and their mounts are now located on the metrology frame. This arrangement is illustrated in the drawings given in Fig. 180. The stage/force frame, along with the previously assembled moving metrology components, their mounts and the alignment artefact, is next isostatically mounted on the support frame. This arrangement is shown in Fig. 181.

Again, using dowel pins and the allocated holes, the upper part of the metrology frame can now be fixed in position and the stationary components of the Z axis interferometer are mounted on this member, completing the instrument assembly, as can be seen in Fig. 182.

260
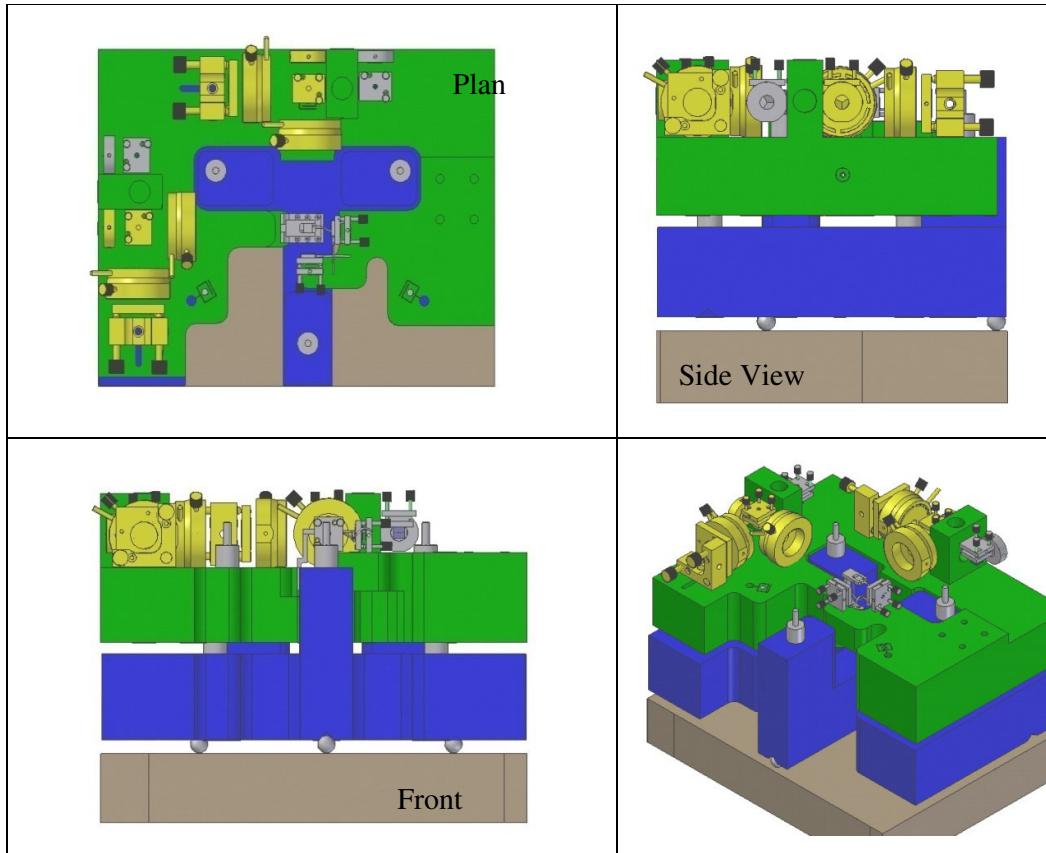
Fig. 180 Drawing of the assembled base (grey), metrology frame (green), support frame (blue) and the stationary metrology components.
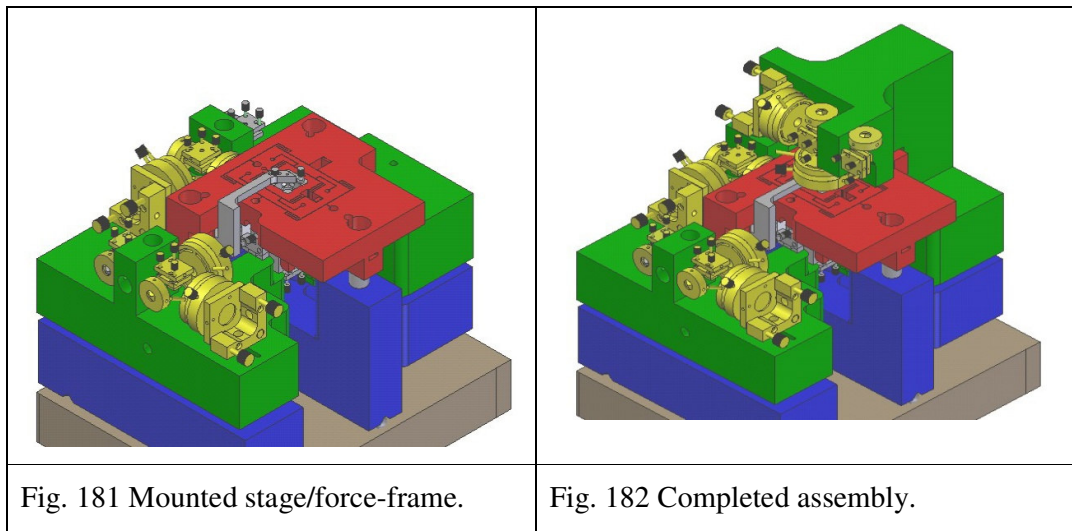
Fig. 181 Mounted stage/force-frame.

Fig. 182 Completed assembly.

Step7: Aligning the instrument interferometers

By now, the three measurement mirrors have been aligned with each other and with the displacement axes of the stage; the instrument structural components, including the

261

support frame, the metrology frame, the force frame and stage, have been assembled; the reference axis angular measurement artefact is in place. But the measurement mirrors have not yet been aligned with the assembled components that make up the individual axis interferometers. These interferometers may be either two pass or four pass arrangements. They are more complex to set up than the desk-top interferometer described in Step 2, involving a greater number of reflections and several polarizations, thus requiring the alignment of a greater number of optical components. The alignment procedure for the three interferometers is as follows.

- The reference mirrors are positioned so that the measurement and reference beams (Beam2 and Beam1 respectively as per Fig. 22) of each interferometer travel equal distances. Slots have been provided in the metrology frame in order to facilitate this adjustment. Vernier calipers may be used to measure the distance involved.
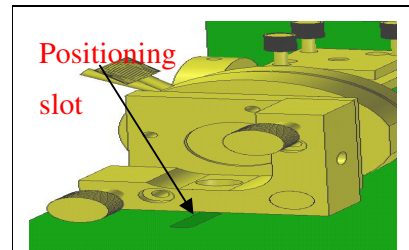
Fig. 183 Reference mirror positioning adjustment slot.

- Care should be taken that the beams are at the central height of and near normal to the moving mirrors.

- The reference mirror, *M1*, is initially blocked and a screen is placed in front of the retro-reflector as illustrated in the interferometer set-up arrangement 1 (Fig. 184). 50 % of the laser beam is reflected by the polarising beam splitter through the quarter wave plate and onto the measurement mirror, *M2*. The beam is then reflected back through the ¼ wave plate to the polarizing beam splitter. For the beam now to pass through the splitter to the screen, its polarization vector must be rotated by a total angle of 90^0 when passing through the ¼ wave plate twice. So, in order to illuminate a single spot on each screen, the orientation of laser and beam splitter must be adjusted and the measurement arm quarter wave plates must be rotated.
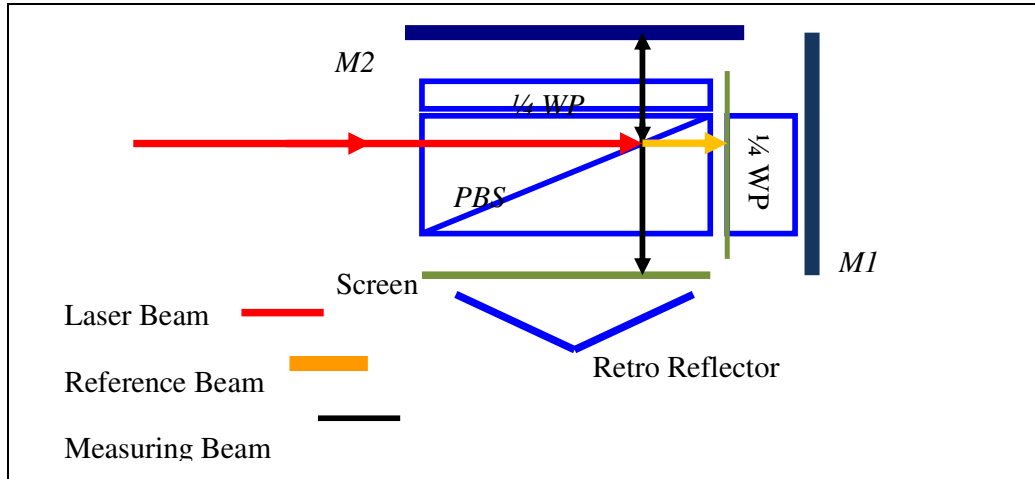
Fig. 184 Interferometer set-up; arrangement 1. (*1/4WP* = quarter Wave Plate; *PBS* = polarising beam-splitter; *M1* = reference mirror; *M2* = measurement mirror).

- The reference mirrors are now uncovered, allowing the portions of the laser beams, transmitted directly through the polarizing beam splitters, to be reflected. Since passing through the quarter wave plates twice causes a 90^0 rotation of the polarization vectors. These reference beams are now reflected by the beam splitters to the screens.

- Further orientation of the reference mirrors and polarisers may be needed before the reference and measurement beams combine to illuminate the same spots on the screens. It is this condition that is illustrated in Fig. 185.
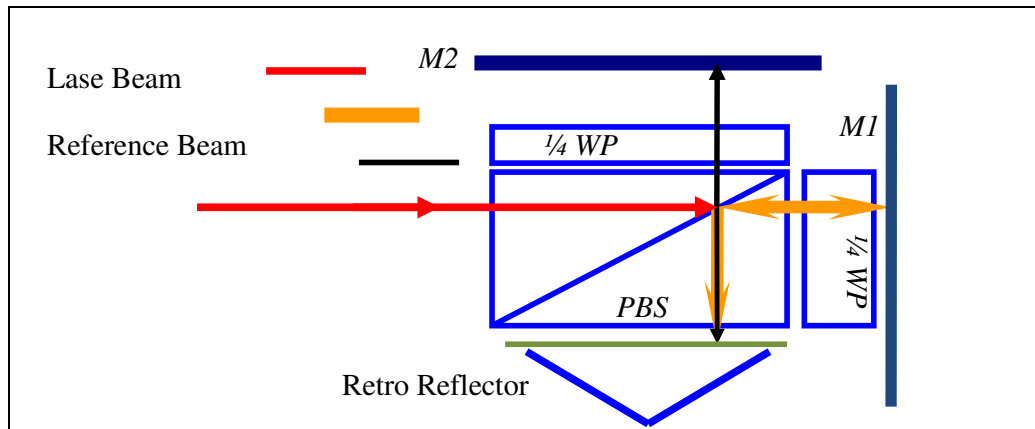
Fig. 185 Interferometer set-up; arrangement 2. (*1/4WP* = quarter wave plate; *PBS* = polarising beam splitter; *M1* = reference mirror; *M2* = measurement mirror).

- The reference mirrors are again covered, preventing reflection of the reference beams to the beam splitter. The screens are moved to the sensor positions, uncovering the retro-reflectors. By orientating the reflectors, the measurement beams are steered through the quarter wave plates to the measurement mirrors for the second time. The beams are now reflected back through the quarter wave plates and, having passed again through the plates twice, the measurement beam vector is rotated through 90^0. As a result, the beams can be reflected by the beam splitter onto the screen as illustrated in Fig. 186.

Fig. 186 Interferometer set-up; arrangement 3.
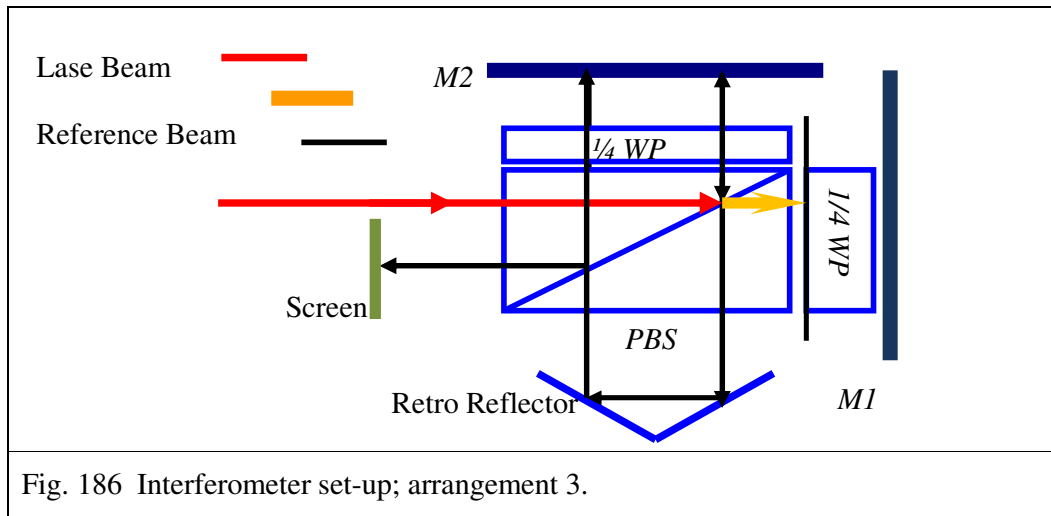
- The reference mirrors are then uncovered, allowing the reference beams to be reflected by the beam splitters towards the retro reflectors. The beams are then reflected back to the beam splitters and onwards, for the second time, to the reference mirrors via the quarter wave plates.

Fig. 187   Final interferometer set-up; arrangement 4.
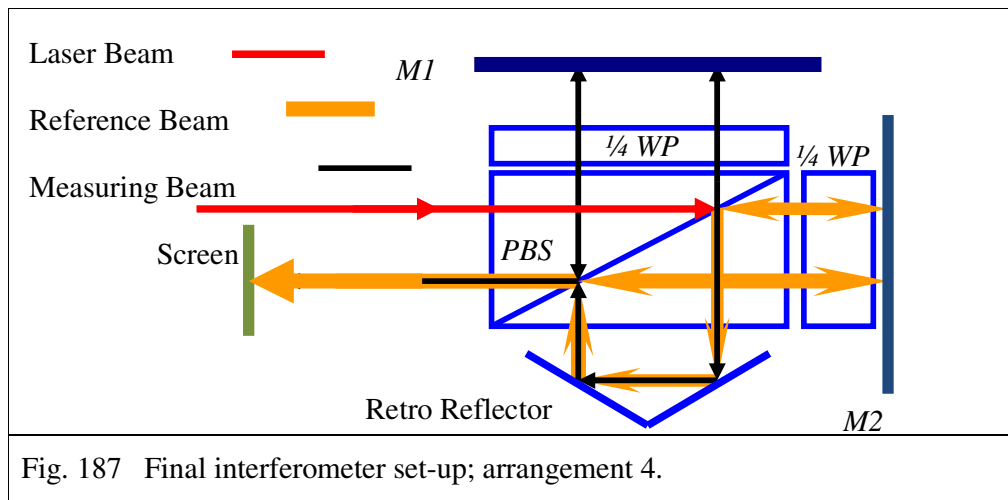
The beams are then reflected back through the quarter wave plates to the beam splitters. Since their polarizing vectors have been rotated 90^0 by the quarter wave plates, they pass un-reflected through the beam splitters to the screens. In order for interference patterns to form at the screens, adjustments may be necessary to the orientations of the retro-reflectors. This arrangement is illustrated in Fig. 187. Circular concentric fringe patterns are indicators of correct alignment.

- By now, the three reference interferometers have been set-up with their measurement axes near normal to each other and coincident with the corresponding stage axes of displacement. It is next necessary to measure the angle between the interferometers.

Step 8: Measuring the angle between the instrument interferometers.

In Section 4.3.2.2, a comprehensive description is given of the artefact (already mentioned in Step 5 of this section) designed for measuring inter-measurement axis orthogonality of the interferometers. The measured deviations from the orthogonal, can then be used in the control LabView programs, as described in Section 5.2.5.2, for driving the actuators and monitoring the stage position

As described in the Section 4.3.2.2, the assembly accuracy of the artefact is not critical, but the angles between the mirror planes must be carefully measured. This could possibly be accomplished prior to assembly by means of a comparator. Subsequently care is required in handling and mounting of the artefact assembly so that the measured angles remain constant.

Step9: Aligning the capacitance sensors.

So far the procedures outlined provide assembled interferometers with their measurement axes orientations measured, near normal to each other and coincident with the correspondent movement axes of the stage. Although the capacitive sensors have also been assembled, only the moving plates are as yet aligned with the interferometers and stage movements. The moving plates are next aligned to each other.

Alignment involves adjustment to the size of the gap between the plates and to their parallelism. By having the stationary plates mounted on a kinematic optical mounts, tilts can be corrected and plate separation altered.

The manufacturer, PI [27], of the D-015 capacitance sensors recommends that the spacing between the plates should equal their nominal measuring distance of 15 µm. A feeler gauge can be used to determine when the spacing is correct.

As explained in Section 4.2.3, plate non parallelism gives rise to measurement non-linearity and scale error. The non-linearity phenomenon may itself be utilised to detect non-parallelism that may then be minimised by adjusting the tilt of the stationary plate.

The procedure for doing this is as follows;

- Drive the stage over its entire range for each axis in turn.

- The Calibration program, described in Section 5.2.2, is used to plot the stage position, as measured using the appropriate interferometer, against the voltage output of the corresponding capacitive sensor and to save the data to a tab-delimited spread sheet file. The movement non-linearity, arising primarily from actuator hysteresis, can be ignored as it equally affects both.

- Open the data file using the MathCad program, Alignment of capacitance sensors. This simple program was written for this thesis specifically to calculate the non-linearity of the capacitance sensors. As defined in Section 4.2.3, linearity is again taken to be half the peak to peak value of the residuals expressed as a percentage of the full range [37].

- Adjust the tilt of the stationary plates using the mount screws and repeat this sequence until non-linearity is minimised for all the axes.

The alignment of the instrument is now optimised.

Step10: Calibration of the instrument

The calibration of the capacitance sensor with respect to the reference interferometers is described in detail in Section 5.2.2. It involves driving the stage over its entire range along each axis, using the purposefully written LabView programs to calibrate the sensors, measure non-linearity, to use this to calculate the mapping function

266

coefficients, and to compensate for effects of environmental changes on the laser light wavelength.

Step11: Operate the instrument.

When the previous ten steps are completed, the instrument is ready to be operated normally. As described in Section 5.2.4 and Section 5.2.5, the command sequences, having first been generated using the Command program, can be used with the Driving and Monitoring programs to facilitate contouring in 3D space. These programs are used to output control signals to the piezos; monitor the displacement of the stage; apply error mapping to both the command and monitoring signals; compensate for environmental induced measurement bias; and convert Gaussian to instrument coordinates and vice-versa.

Step12: Test.

Many sources of error are considered in this thesis, most having been initially identified when reviewing the literature and subsequently examined in the context of a specific imagined instrument. Their effects are predicted and minimized through careful design or are compensated for in the control software. Additionally, B type uncertainties associated with these predictions are calculated in Chapter 6. Although, it is suggested in the GUM [23] and in a technical note on these guidelines, issued by NIST [6] that these Type B uncertainty evaluations (based on manufacturer specifications) could be more accurate than Type A evaluations (based on experimental data), nevertheless the error budget produced may not be completely comprehensive and it is suspected that yet unforeseen interactions between factors may also influence the performance of the stage. For this reason experimentation is proposed. The design of the experimentation is explored in Section 7.4.

Before looking at experimentation, the environment in which the instrument is assembled can also affect its performance and hence is examined in more detail.

7.3 The Environment
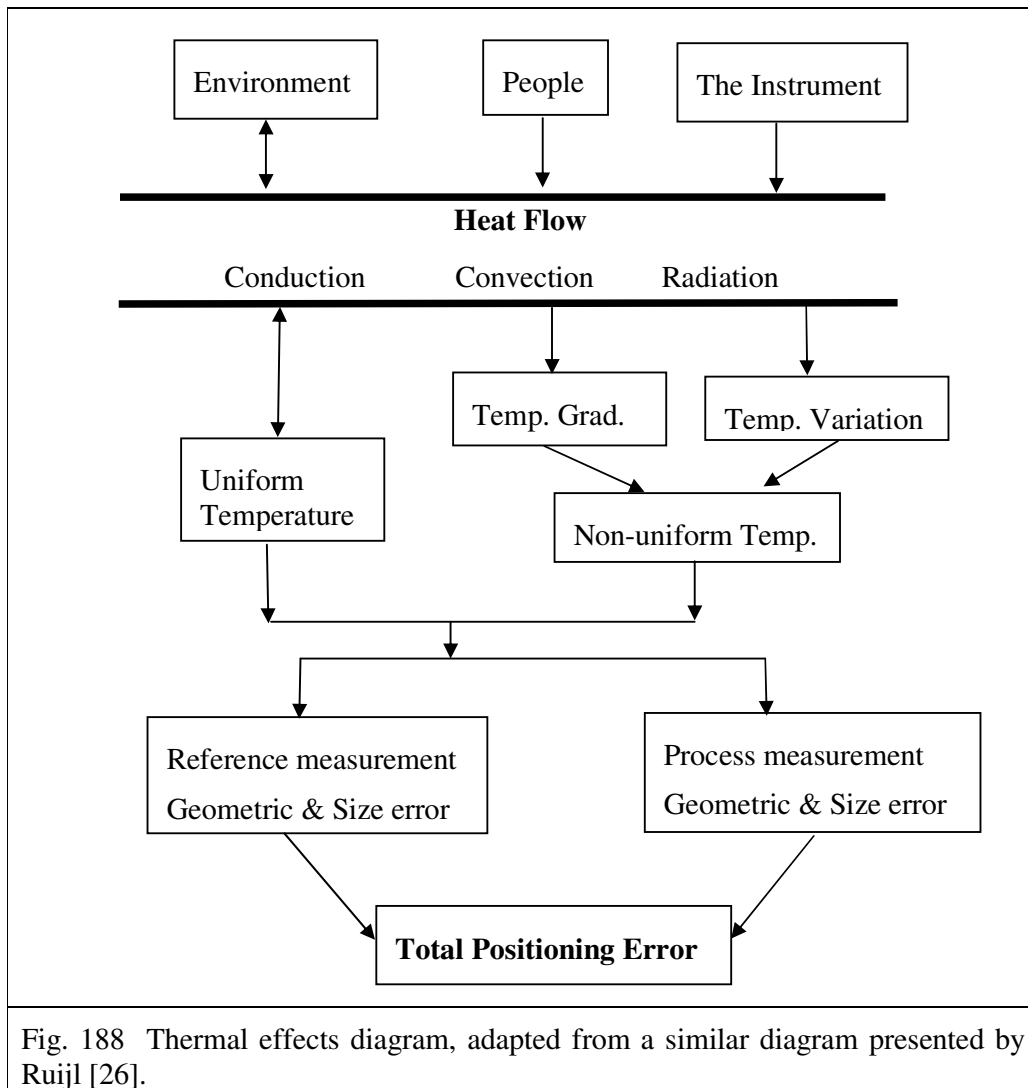
Fig. 188 Thermal effects diagram, adapted from a similar diagram presented by Ruijl [26].

All the instrument systems (mechanical, metrological and control), are effected to some extent by changes and variability of environmental factors. Possible environmentally induced biases in positioning and measurement are either nulled through mechanical design, as described in Chapter 4, or are compensated in the control programs, as described in Chapter 5, while their associated uncertainties are quantified in Chapter 6. It can be deduced from these chapters that thermal variation is the dominant source of bias and a major contributor to uncertainty. The thermal effects diagram given in Fig. 188 is adapted for this thesis from the diagram presented by Ruijl [26].

Fig. 188 shows that the environment (weather variations, lab heating, lighting and air flows), people (operators) and the instrument itself (actuators, power supplies, computers) are the only considered heat sources, as no heat generating processes are involved in this instance. Conduction, convection and radiation are the mechanisms by which the heat is distributed about the instrument. Heat gives rise to transient thermal gradients around and within the instrument components and structures before a stable homogenous state can be reached. Due to thermally induced expansion, the instrument structures (including the support frame, the metrology frame, the stage, the force frame, the optical mounts, the optical components and the capacitance plates) undergo both size and shape changes during the transient thermal phases. Furthermore, since the accuracy of both mechanical nulling and, to a greater extent, software compensation requires that the temperature throughout the instrument is uniform; positioning accuracy can be seriously degraded when thermal fluctuations do not have periods far longer than the stage operation cycle times.

Similarly, the software based compensation uncertainty for pressure and humidity is increased if pressure or humidity varies while the stage is operating. The impact of such variation is not expected to be highly significant, as these factors are compensated in near real time and the homogenisation inertia is expected to be small. The quantification of the effects of these factors, through proposed experimentation, is addressed in Section 7.4.

Electrical and mechanical noise can also degrade the performance of the stage, but neither has been compensated for. Unlike temperature, pressure and humidity, these factors tend to vary normally about a fixed mean. Rather than resulting in a measurement or positioning bias, they cause uncertainty. The capacitance measurement uncertainty associated with electrical noise is quantified in Section 6.2. The mechanical noise is specific to the instrument surroundings and must be characterized through experimentation and its nature studied in the context of the stage geometry so as to understand the mechanism of uncertainty propagation.

Based on the discussion so far in this section, the design objectives for the environmental control system may now be listed as follows.

- To ensure only slow thermal variations about the instrument.

269

- To insulate the instrument from all heat sources, such as operators, power supplies, computers, heaters and weather.

- To ensure only slow pressure and humidity variations about the instrument.

- To minimize the amplitudes of electrical and mechanical noise near the instrument.

- To minimize uncertainty of software based error compensation by maximizing the accuracy of environmental measurement.

To attain these objectives it is proposed:

- To operate the instrument within a highly insulated enclosure located within a highly insulated room. This arrangement ensures that only slow thermal variations occur close to the instrument. The insulation also serves to absorb air borne vibration.

- To locate all computers, controllers and power supplies outside the insulated room.

- To use thermal shielding, as described by Ruijl [26] in order to further ensure that the instrument is subject only to homogenous thermal loading. The reported effectiveness of this method is discussed in Section

Fig. 189 Thermal shield made from crumpled kitchen foil.

2.4.1.1. As described, the method involves using highly thermally conductive sheet metal to envelop the instrument structures at a uniform fixed distance. To shape the shield for the complex geometry of the instrument would be difficult and possibly expensive. A novel variation on the described approach is suggested here; the shield could be made at minimum cost from kitchen foil, shaped by crunching up and pressing against the instrument structures and components.

The shapes could be made more durable by immersing in a resin. Not only does this approach allow shielding of complex shapes, even around individual components, but it also facilitates differential shield thicknesses and spacing. Combining this ability with careful modeling, it may be possible to balance the distribution of heat transfer between thin and thick members. This method is presently the subject of undergraduate projects, where the transient condition of such a system, as applied to several structural profiles under thermal load, is studied.

- To use infra-red shielding on the inside of the enclosure.

- To use a ridged sealed enclosure, capable of maintaining pressure and humidity at fixed levels.

- Encapsulating the enclosure as well as the room within Faraday cages and shielding all sensor/actuator cables should reduce electronic noise.

- To mount the enclosure on a damped heavy granite table.

- To use MC65 precision solid state thermistor sensors (accuracy of ± 0.15 K), made by GE Sensing/Thermoetrics [80], to measure the temperature of the instrument itself and to detect the presence or absence of thermal gradients within its structure. These sensors have maximum diameters of 0.65 mm and a thermal time constant of 8 s. It is proposed that these sensors should be inserted in threaded holes in the support
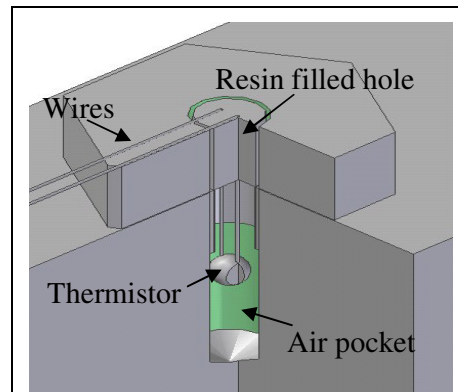
Fig. 190 Fixing method for locating thermistor sensors in the instrument structures.

frame, the metrology frame, the force frame and stage. The sensor can be held in place by passing the wires through resin filled holes, drilled out of fixing nut heads as illustrated in Fig. 190. This arrangement should allow the sensors to be located within air pockets, avoiding contact with the structure materials. Wrapping the protruding wires in foil and gluing them to the surface of the instrument structure for a distance of 25 mm ensures that the measured

271

temperature is not unduly influenced by the surrounding air temperature. Ruijl [26] reports having successfully used this arrangement. Additional AS115 temperature standard sensors (resolution ± 0.002 K) must also be used if uncertainty associated with the expansion of displacement sensor offsets is to be kept to below 1 nm.

- Vibration sensors are required on both the metrology frame and on the stage so that any relative movement between these structures can be detected, as such movement would result unpredictable measurement error.

The current environment

Much of the proposed arrangement is already in place within WIT. Development of an ultra-precision laboratory facility, including an environmentally controlled space has been spearheaded by Mr Joseph Phelan through several under-graduate projects. Progress in the establishment of this facility has already been reported in two papers presented to the Irish Manufacturing Conferences [84] [85].
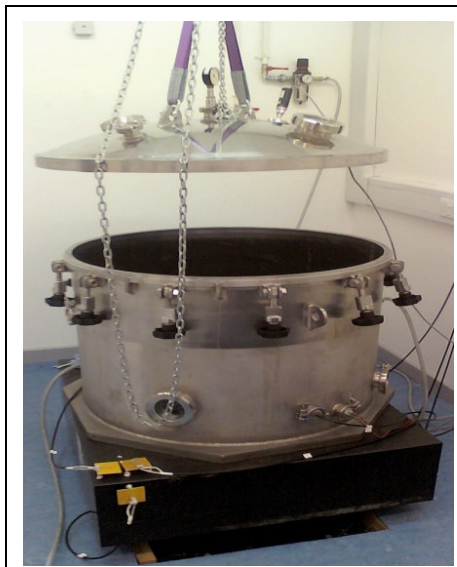
Fig. 191 Pressure vessel and table.

Currently, the vacuum vessel sits on a granite block that is supported on four passive spring dampers (Fig. 191). These dampers have been taken from a redundant coordinate measurement machine.

The vessel and its supports are located within a thermally insulated room that can be isolated from all electrical power (except for wires powering a CO gas sensor, necessary for safety). Wire mesh also provides a degree of electromagnetic field (EMF) insulation. The insulated room is located within a larger laboratory, which is located within a factory building. Heating in the outer building is provided by large roof mounted thermostatically controlled gas powered infra-red heaters.

A hoist is provided for lifting the heavy lid of the vessel (Fig. 191). When this lid is sealed, a vacuum can be pulled, using a BOC Edwards RV12 vacuum pump,

272

positioned outside of the room. The maximum vacuum reported to date [85] is a modest 1 mPa. But possibly more important, in the context of this thesis, is that the vacuum can be maintained over very long periods (days), an indication of excellent sealing.

The temperature within the room is monitored using five LM35DZ IC temperature sensors (manufactured by National Semiconductor), located on the walls and ceiling. These are sealed in hermetic T0-46 transistor packages, have an accuracy of ±0.25 K, are low self heating (< 0.10 K in still air) and give an output that is almost linearly proportional to the temperature. The temperature and relative humidity inside the vessel is monitored using a Precon manufactured HS-2000V sensor. This has a humidity measurement accuracy of ±2 % and a temperature measurement accuracy of ±0.4 K. These sensors were used to simultaneously measure the temperature changes over a forty eight hour period inside the vessel, within the thermally insulated room, in the outer laboratory and in outer building near to the lab. Preliminary results [85], shown in Fig. 192, are indicative of a system capable of maintaining a constant homogenous temperature about a precision instrument.
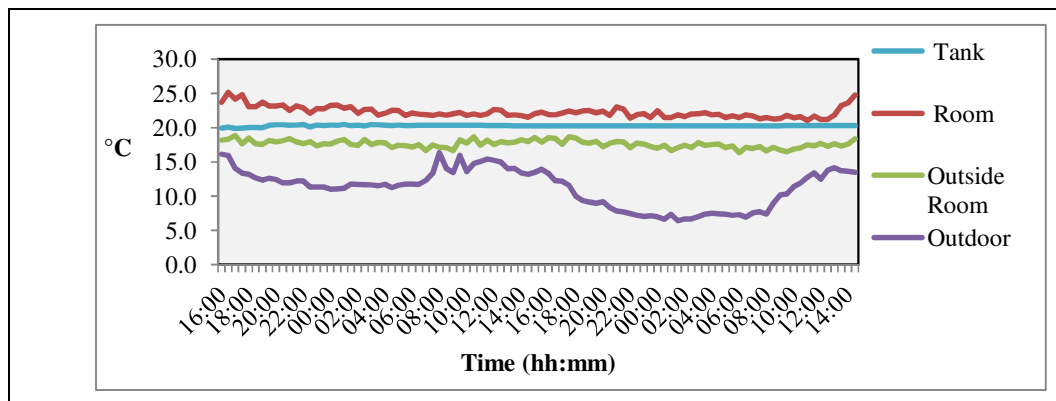
Fig. 192   Temperature variation over a 48 hour period simultaneously measured inside the vessel, in the insulated room, in the laboratory and external to the laboratory. This graph was presented by Phelan et al. [85].

The vessel has been fitted with a Teledyne Hastings active vacuum control gauge (Fig. 193), capable of holding a vacuum of 0.1 Torr. Fig. 194 shows graphically the results, [85], of measuring pressure using this gauge while temperature and humidity are measured with the HS-2000V sensor within the vessel during an evacuation.

Fig. 193 Teledyne Hastings active vacuum control gauge.	Fig. 194 Graph of temperature, pressure and humidity within the vessel while the pressure is lowered by the BOC Edwards RV12 vacuum pump as reported by Phelan et al. [85].
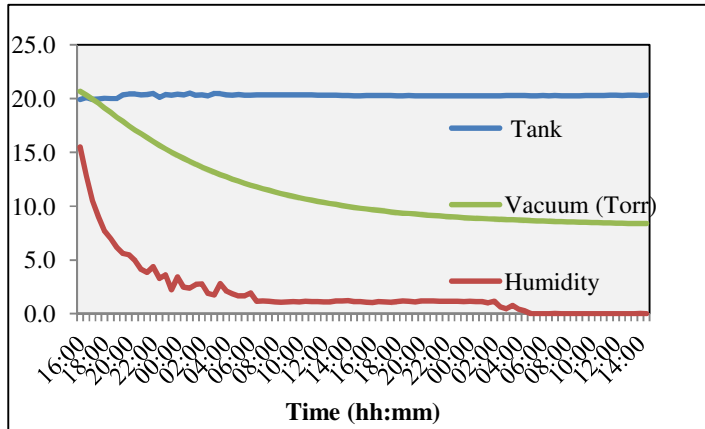
These results indicate that interactions between environmental factors cannot be ignored when experimentally characterizing the instrument.

MSIUSA™ piezo film vibration sensors have been positioned on the floor of the insulated room as well as orientated orthogonal to each other on the granite block.

Simply impacting the floor outside the room, allows useful information to be obtained about the mechanical vibration isolation efficiency of the damped table. Using the manufacturer's recommended 0.4 $V(\mu m)^{-1}$ electrical to mechanical conversion, the displacements resulting from such an impact were calculated and plotted in Fig. 196.

Fig. 195 MSIUSA™ piezo film vibration sensors orientated orthogonal to each other on the granite block.

274
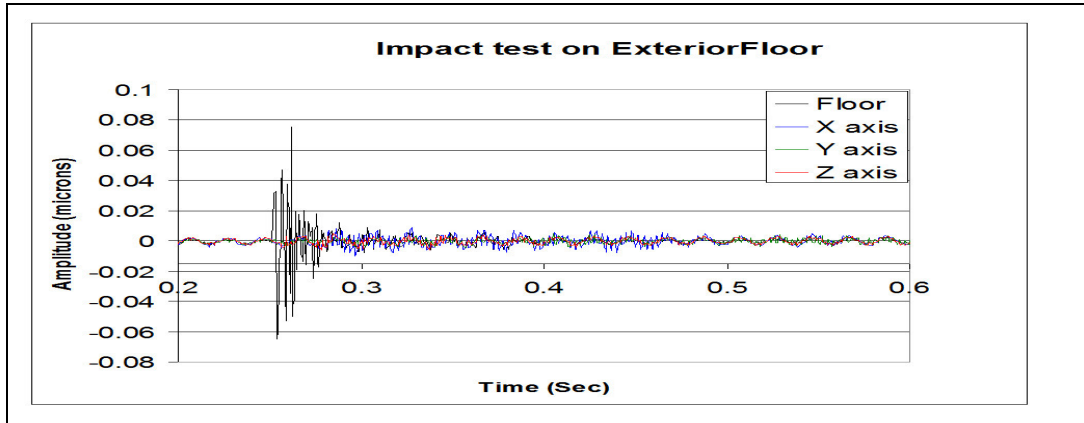
Fig. 196 Directional vibration amplitudes of the block resulting from a single impact to the floor outside of the insulated room.

From this data, the damped natural frequency (f_d), the transmissibility at resonance (T), the damping ratio (ξ) and the isolation efficiency could be calculated using Equ. 202.

$T = \dfrac{1}{2\zeta}$	$T = \dfrac{\text{amplitude of transmitted vibration}}{\text{amplitude of forcing vibration}}$	isolation efficiency $= 100(1 - T)$
Equ. 202	Equ. 203	Equ. 204

These values are tabulated in Table 27.

	X axis	Y axis	Z axis	Floor
Damped Nat Freq (f_d)	306 Hz	306 Hz	326.73 Hz	407 Hz
Transmissibility at resonance (T)	0.118	0.066	.063	N/a
Damping Ratio (ξ)	4.24	7.57	7.93	N/a
Isolation Efficiency	88.2 %	93.4 %	93.7 %	N/a

Table 27 Preliminary results indicating the mechanical vibration isolation properties of the table.

The velocities associated with the displacements were then calculated and expressed in decibels as follows.

When x is the instantaneous displacement, X is the maximum amplitude, f is the frequency of oscillation and ϕ is the phase,

275

$$x = X\cos(2\pi f t + \phi) \qquad\qquad \frac{\mathrm{d}x}{\mathrm{d}t} = v = -2\pi f_n X \sin(2\pi f_n t + \phi)$$

$$v(\mathrm{dB}) = 20\log\left(\frac{v}{0.01}\right) \qquad\qquad v(\mathrm{rms}) = \sqrt{v_{average}^2}$$

<div align="right">Equ. 205</div>
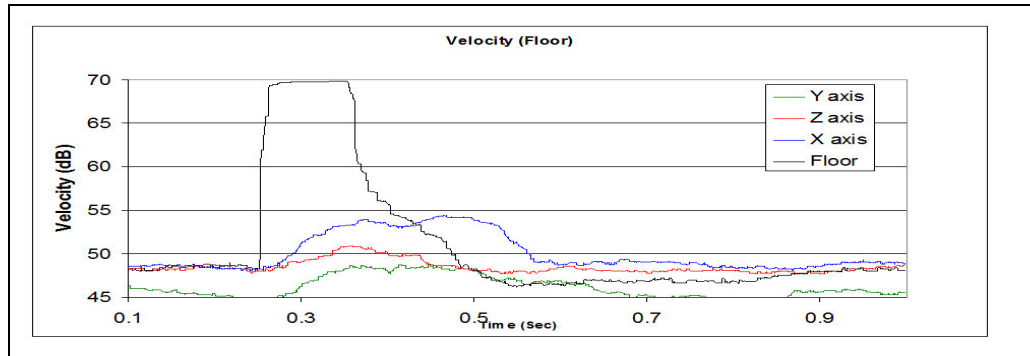
Fig. 197   Calculated table velocities (dB) resulting from a single impact on the floor outside the insulated room.

The velocities (*v*) plotted in Fig. 197 are calculated by averaging the rms values over 0.1 s for the data plotted in Fig. 196 and using the damped natural frequencies as approximations to the undamped natural frequencies (f_n), while referencing the decibel levels to the international standard of 0.01 μm.s^{-1}.
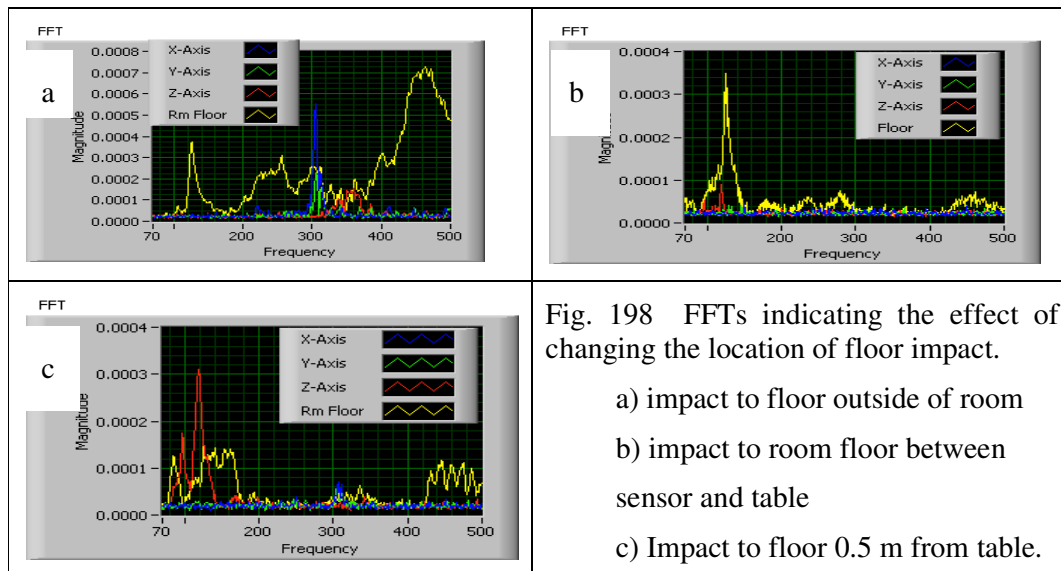
Fig. 198   FFTs indicating the effect of changing the location of floor impact.

a) impact to floor outside of room

b) impact to room floor between sensor and table

c) Impact to floor 0.5 m from table.

The results of this test can only be regarded as preliminary, as they are indicative of only the dynamic response to a laboratory floor impact at one particular location. Fast

Fourier transforms (FFTs) were also used to look at the frequency response from the same sensors, for various impact locations. It can be deduced the FFTs shown in Fig. 198 that the vibrations transmitted to the table are extensively horizontal (X and Y directions) when the site of impact is distant, but the vertical direction becomes principle when the floor is impacted close to the table. It can also be observed by comparing these FFTs that there appears to be a lower resonant frequency in the Z direction in the case of a close impact site than is apparent when the floor is struck distant from the table. This possibly indicates that different resonant modes are being stimulated by different vibration propagation mechanisms.

Completing the environment

Comparing the proposed environment with that currently in existence, suggests that only inexpensive changes, in terms of time and money, are required. These are as follows.

- The vessel must be insulated inside and out using rock wool.

- The vessel should be encased in another Faraday cage.

- The computers and controllers must be relocated outside of the insulated room.

- Additional humidity and thermal sensors are required inside of the vessel.

- The instrument structures must be fitted with the thermistors in the manner described above.

- The thermal shielding must be placed about the instrument after assembly.

- Vibration sensors must be placed on both the metrology frame and on the stage.

Additionally, the experimental work carried out so far on the current arrangement is viewed only as preliminary. The entire environmental system must be thoroughly characterised through experimentation and all environmental factor uncertainties identified and quantified as these determine the accuracy of compensation and ultimately the performance of the instrument itself.

Furthermore, having described how to assemble the instrument and discussed the environment in which it must operate, it is now reasonable to design the experiments necessary to characterise it comprehensively.

7.4   Experimental design

The aim of the experimentation proposed in this thesis is to improve the functional performance of the system, i.e. to improve its positioning accuracy. This can be accomplished through the well established iterative   approach of the Deming cycle (Plan, Do, Check, and Act) [86]. This section constitutes the planning phase of this cycle.

For the particular instrument designed during this thesis, the factors that may influence its positioning accuracy are identified from the analysis undertaken in previous chapters. A combination of experiments is chosen in order to establish the effects of these factors and their interactions on the response of the system. This serves a dual purpose:

- a rational plan is laid down for the future development of this project; and

- designing the experiments directly addresses the research question in that a suitable experimental design may be regarded as an essential component of a specification for a precision positioning instrument.

7.4.1   The aims of experimentation

It is desirable that experimentation would yield the following information.

- Determination of the instrument positioning accuracy susceptibility to environmental variability and set-up uncertainty.

- Validation of the design.

- Validation of the theoretical relationships, proposed in Chapters 5 and 6, relating positional measurement bias to environmental and set-up factors.

- Validation of the software based bias compensation and the physical nullification of error sources.

- Validation of set-up.

- Quantification of the effects of the main factors and interactions between these factors on instrument response.

- Identification of any so far unrecognized interactions between the main factors.

In order for experimentation to adequately address each of these concerns, a suitable methodology must be adopted.

7.4.2 Methodology

Two experimental methods were considered for use in this thesis. Firstly, the commonly used approach to experimentation within engineering of changing-one-thing-at-a-time was considered. This involves changing each variable of interest singularly while leaving all the other variables at constant levels. This has the advantage of simplicity of execution and the system can be tested over a range of values, hence facilitating knowledge of the system sensitivity to variable levels. In this instance, though, it is not considered a suitable experimental approach for instrument validation due to the presence of known and possibly unknown interactions between variables. An example may serve to illustrate this point. If, say, an experimental objective is to find out what is the effect of atmospheric pressure on positioning accuracy, then it may seem reasonable to change the pressure and to compare the experimental position (measured using the capacitance sensors) against a reference position (measured using the interferometers) over several repeats. But lowering the pressure can effect the % Humidity and both the atmospheric pressure and the % Humidity are known to effect the displacement measurements of capacitors (see Section 5.2.5.1), thus making the results from this experiment unreliable. In general interactions between factors render the changing-one-thing-at-a-time approach unsuitable for analysing complex precision instruments. Additionally, although the majority of the interactions may be known, some unforeseen interactions may also exist, so the planned experimentation should also facilitate the detection and quantification of the effects of all such interactions.

The second method considered involved multi-factorial statistically designed experiments as described by Grove et al. [87]. This approach better accommodates the knowledge requirements when in the presence of interactions. According to Grove, the approach can be regarded as trying to answer all possible questions at once. With

multi-factorial statistical design, each factor (the independent variables) has several distinct levels and the strategy involves examining the response (the dependant variable) of the system to all possible combinations of these factor levels. This yields information as to the magnitude of the effect of each factor and the magnitude of the effect of all the interactions between factors. By performing replicate runs for each treatment (combination of levels) it is also possible to establish confidence intervals for each effect based on the t-distribution. Alternatively confidence intervals can be estimated for a single replicate design based on the variance of the effects of insignificant higher order factor combinations.

7.4.3 The experimental design

The developing the experimental design involves the following steps:

- deciding upon the response to be measured;

- identifying the main factors;

- deciding upon the levels of the factors to be considered;

- defining the treatment combinations;

- defining the number of replicates of each treatment;

- deciding to use a full factorial design pattern or a fractional approach; and

- deciding on the order in which the experiments should be carried out.

The experimental response of interest (the dependant variables)

It is first necessary to identify the system response of interest. This must be related to the experimentation aims as listed in Section 7.4.1. Examination of these requirements suggests that positioning accuracy and dynamic characteristics are the experimental yields that should be used. Positioning accuracy consists of positioning repeatability and positioning bias, while the dynamic characteristics are namely the rise time, the settling time and the percentage overshoot. For the instrument designed for this thesis, it is possible and efficient to measure all of these response characteristics simultaneously for each treatment. To do this, a step command should be given to the stage along at least one axis and its position measured by both the capacitance sensors and interferometers. The interferometer measurements are necessary to detect bias

between the true position and the target position, while the capacitance measured positions can be used to calculate repeatability and the dynamic characteristics.

<u>The factors (the independent variables)</u>

It is now necessary to identify the variables that may affect the response of the stage and to define the levels of each. All environmental and set-up factors, that may affect the system response, must be included. Letters are allocated to each factor and they are tabulated in Table 28.

Letter	Factor	Level 1 (at calibration)	Level 2
A	Temperature	Temp at calibration	Temp at calibration $+\varDelta t$ K
B	Pressure	Pressure at calibration	Pressure at calibration $+\varDelta p$ kPa
C	% Humidity	Humidity at calibration	Humidity at calibration $+\varDelta h$ %HR
D	Angle between measurement and reference measurement axes	Angle at calibration	Angle at calibration $+1^0$
E	Reference axis Orthogonality compensation	Present	Not present
G	Tilt of capacitance plates	Angle at calibration	Angle at calibration $+1^0$
H	Temperature compensation	Present	Not present
I	Pressure compensation	Present	Not present
J	% Humidity compensation	Present	Not present

Table 28 The main factors suspected to have a significant effect on the response of the instrument.

The matrix for a full 2^9 factorial design, involving the nine factors identified in Table 28, requires 512 treatment combinations. The time needed to carry out such a series of experiments, would be prohibitive. Even when using only a single replicate, it would be likely that the environmental variables and their interactions would drift. For this reason, a fractional factorial approach was considered for the purpose of identifying

which of the main factors and interactions are actually significant. These factors may subsequently be examined with greater confidence through a lesser order full factorial design.

In the case of the precision positioning instrument designed for this thesis, it is suspected that most of the main factors and some two-factor interactions may be significant, while the 3-factor and higher interactions are not. This assumption is based on the GUM [23] assertion that effects, arising from interdependence of temperature, pressure and humidity relationships, are negligible, but relationships identified in Chapters 5 and 6 indicate that two-factor interactions are possibly significant. This means that designs involving confounding main effects and/or two-factor interactions cannot be used. This is a critical restriction on the choice of experimental design.

So the ideal criteria for choosing the fractional factorial design are:

- the number of treatment combinations should be as small as possible;

- no main factors should be aliased with either main factors or two-factor interactions(note that aliasing is where the influence of an effect is assumed also to include the influence of other, preferably insignificant, effects); and

- no two-factor interactions should be aliased with any other two-factor interactions.

Several designs were considered. NIST [6] provide a table on their web-site from which common fractional designs can be chosen. A 2^{9-5} arrangement involves as few as sixteen experiments, but the main effects are confounded with two-factor interactions or higher. In the case of a 2^{9-3} design, on the other hand, the main effects are not confounded with any two-factor interactions and only four of these two-factor interactions are confounded with other two-factor interactions. By carefully naming the effects in the light of system knowledge, it is possible to arrange it so that that the aliased two-factor interactions are unlikely to be significant. This allows the effects of these confounded interactions to be attributable. Therefore this could be regarded as a valid design for this instrument, but the need for sixty four treatment combinations renders it somewhat less than desirable. A 2^{9-4} design is a resolution IV arrangement, in which the main effects are aliased with 3-factorial interactions and higher and requires a more modest thirty two experiments, but the two-factor interactions are

aliased with each other. This design would give good information about the main effects, but cannot be used to quantify the effects of their two-factor interactions. It can be assumed that if the effect of a main factor is not significant, then any interactions involving that factor are unlikely to be significant. This allows a 2^{9-4} to be used as a screening design, i.e. a design aimed at screening out insignificant factors with a view to performing a subsequent lower order full factorial series of experiments using only factors that are known to be significant. It is this screening design that is described in the following section.

7.4.3.1 The 2^{9-4} screening design

The 2^{9-4} design involves confounding four of the main factors individually with four factor interactions, as indicated in Table 29. The defining relation is derived from this in accordance with the method described by Grove et al. [87].

Main Factors	A	B	C	D	E	F	G	H	I *(the factor)*
Confounding						BCDE	ACDE	ABDE	ABCE
Defining Relation	I = BCDEF = ACDEG = ABDEH = ABCEI = BFAG = CFAH = DFAI = CGBH = DGBI = DHCI = ABCDFGHI								

Table 29   The 2^{9-4} screening design confounding pattern and defining relation.

The defining relation is used to determine the complete aliasing structure for each of the main factors and two-factor interactions. These structures are listed in Table 30.

A = A+ABCDEF + CDEG + BDEH + BCEI + BFG + CFH + DFI + ACGBH + ADGBI + ADHCI + BCDFGHI
B = B+CDEF + ABCDEG + ADEH + ACEI + FAG + BCFAH + BDFAI + CGH + DGI + BDHCI + ACDFGHI
C = C + BDEF + ADEG + ABCDEH + ABEI + BCFAG + FAH + CDFAI + GBH + CDGBI + DHI + ABDFGHI
D = D + BCEF + ACEG + ABEH + ABCDEI + BDFAG + CDFAH + FAI + CDGBH + GBI + HCI + ABCFGHI
E = E + BCDF + ACDG + ABDH + ABCI + BEFAG + CEFAH + DEFAI + CEGBH + DEGBI + DEHCI + ABCDEFGHI

283

$F = F + BCDE + ACDEFG + ABDEFH + ABCEFI + BAG + CAH + DAI + CFGBH + DFGBI + DFHCI + ABCDGHI$
$G = G + BCDEFG + ACDE + ABDEGH + ABCEIG + BFA + CFGAH + DFGAI + CBH + DBI + DGHCI + ABCDFHI$
$H = H + BCDEFH + ACDEGH + ABDE + ABCEIH + BFAGH + CFA + DFHAI + CGB + DGHBI + DCI + ABCDFGI$
$I = I + BCDEFI + ACDEGI + ABDEHI + ABCE + BFAGI + CFAHI + DFA + CGBHI + DGB + DHC + ABCDFGH$
$AB = AB+ACDEF + BCDEG + DEH + CEI + FG + BCFH + BDFI + ACGH + ADGI + ABDHCI + CDFGHI$
$AC = AC+ABDEF + DEG + BCDEH + BEI + BCFG + FH + CDFI + AGBH + ACDGBI + ADHI + BDFGHI$
$AD = AD+ABCEF + CEG + BEH + BCDEI + BDFG + CDFH + FI + ACDGBH + AGBI + AHCI + BCFGHI$
$AE = AE+ABCDF + CDG + BDH + BCI + BFGE + CEFH + DFIE + ACEGBH + ADEGBI + ADEHCI + BCDEFGHI$
$AF = AF+ABCDE + CDEFG + BDEFH + BCEFI + BG + CH + DI + ACFGBH + ADFGBI + ADFHCI + BCDGHI$
$AG = AG+ABCDEFG + CDE + BDEGH + BCEGI + BF + CFGH + DFGI + ACBH + ADBI + ADHCGI + BCDFHI$
$AH = AH+ABCDEFH + CDEGH + BDE + BCEHI + BFGH + CF + DFIH + ACGB + ADGBIH + ADCI + BCDFGI$
$AI = AI+ABCDEFI + CDEGI + BDEHI + BCE + BFGI + CFHI + DF + ACGBHI + ADGB + ADHC + BCDFGH$
$BC = BC + DEF + ABDEG + ACDEH + AEI + FACG + BFAH + BCDFAI + GH + CDGI + BDHI + ADFGHI$
$BD = BD+CEF + ABCEG + AEH + ACDEI + FADG + BCDFAH + BFAI + CDGH + GI + BHCI + ACFGHI$
$BE = BE + CDF + ABCDG + ADH + ACI + FAEG + BCEFAH + BDEFAI + CEGH + DEGI + BDEHCI + ACDEFGHI$
$BF = BF + CDE + ABCDEFG + ADEFH + ACEFI + AG + BCAH + BDAI + CGFH + DFGI + BDFHCI + ACDGHI$
$BG = BG + CDEFG + ABCDE + ADEGH + ACEGI + FA + BCFGAH + BDFGAI + CH + DI + BDGHCI + ACDFHI$
$BH = BH + CDEFH + ABCDEGH + ADE + ACEHI + FAGH + BCFA + BDFHAI + CG + DGHI + BDCI + ACDFGI$
$BI = BI+CDEFI + ABCDEGI + ADEHI + ACE + FAGI + BCFAHI + BDFA + CGHI + DG + BDHC + ACDFGH$
$CD = CD + BEF + AEG + ABCEH + ABDEI + BCDFAG + FADH + CFAI + DGBH + CGBI + HI + ABFGHI$

CE = CE + BDF + ADG + ABCDH + ABI + BCFEAG + FAEH + CDEFAI + GBEH + CDEGBI + DEHI + ABDEFGHI
CF = CF + BDE + ADEFG + ABCDEFH + ABEFI + BCAG + AH + CDAI + GBFH + CDFGBI + DFHI + ABDGHI
CG = CG + BDEFG + ADE + ABCDEGH + ABEGI + BCFA + FAHG + CDFGAI + BH + CDBI + DGHI + ABDFHI
CI = CI + BDEFI + ADEGI + ABCDEHI + ABE + BCFAGI + FAHI + CDFA + GBHI + CDGB + DH + ABDFGH
DE = DE + BCF + ACG + ABH + ABCDI + BDEFAG + CDEFAH + FAEI + CDEGBH + GBEI + HCEI + ABCEFGHI
DF = DF + BCE + ACEFG + ABEFH + ABCDEFI + BDAG + CDAH + AI + CDFGBH + GBFI + HCFI + ABCGHI
DG = DG + BCEFG + ACE + ABEGH + ABCDEGI + BDFA + CDFGAH + FAIG + CDBH + BI + HCGI + ABCFHI
DH = DH + BCEFH + ACEGH + ABE + ABCDEHI + BDFAGH + CDFA + FAHI + CDGB + GBHI + CI + ABCFGI
DI = DI + BCEFI + ACEGI + ABEHI + ABCDE + BDFAGI + CDFAHI + FA + CDGBHI + GB + HC + ABCFGH (note: incorrect on the NIST site)
EF = EF + BCD + ACDFG + ABDFH + ABCFI + BEAG + CEAH + DEAI + CEFGBH + DEFGBI + DEFHCI + ABCDEGHI
EG = EG + BCDFG + ACD + ABDGH + ABCGI + BEFA + CEFAGH + DEFGAI + CEBH + DEBI + DEGHCI + ABCDEFHI
EH = EH + BCDFH + ACDGH + ABD + ABCIH + BEFAGH + CEFA + DEFHAI + CEGB + DEGBHI + DECI + ABCDEFGI
EI = EI + BCDFI + ACDGI + ABDHI + ABC + BEFAGI + CEFAHI + DEFA + CEGBHI + DEGB + DEHC + ABCDEFGH
FG = FG + BCDEG + ACDEF + ABDEFGH + ABCEFGI + BA + CAHG + DAGI + CFBH + DFBI + DFGHCI + ABCDHI
FH = FH + BCDEH + ACDEFGH + ABDEF + ABCEFHI + BAGH + CA + DAHI + CFGB + DFGBHI + DFCI + ABCDGI
FI = FI + BCDEI + ACDEFGI + ABDEFHI + ABCEF + BAGI + CAHI + DA + CFGBHI + DFGB + DFHC + ABCDGH
GH = GH + BCDEFGH + ACDEH + ABDEG+ ABCEIGH + BFAH + CFGA + DFGAHI + CB + DBHI + DGCI + ABCDFI
GI = GI + BCDEFGI + ACDEI + ABDEGHI + ABCEG + BFAI + CFGAHI + DFGA + CBHI + DB + DGHC + ABCDFH
HI = HI + BCDEFHI + ACDEGHI + ABDEI + ABCEH + BFAGHI + CFAI + DFHA + CGBI + DGHB + DC + ABCDFG
Table 30 Aliasing based on the 2^{9-4} design defining relation given in Table 29.

The table of contrasts for the 2^{9-4} screening design is given in Table 31. This table indicates the thirty two combinations of factor levels (+1 indicates a high level, -1 indicates a low level) required. By implementing this in Excel, the linear contrasts can be automatically calculated when the experimental mean yield values are entered for all replicates of each treatment.

Treatments	A	B	C	D	E	F= BCDE	G = ACDE	H = ABDE	I = ABCE	Mean Yield
(1)	-1	-1	-1	-1	-1	1	1	1	1	0
a	1	-1	-1	-1	-1	1	-1	-1	-1	0
b	-1	1	-1	-1	-1	-1	1	-1	-1	0
ab	1	1	-1	-1	-1	-1	-1	1	1	0
c	-1	-1	1	-1	-1	-1	-1	-1	-1	0
ac	1	-1	1	-1	-1	-1	1	1	1	0
bc	-1	1	1	-1	-1	1	-1	1	1	0
abc	1	1	1	-1	-1	1	1	-1	-1	0
d	-1	-1	-1	1	-1	-1	-1	1	1	0
ad	1	-1	-1	1	-1	-1	1	-1	-1	0
bd	-1	1	-1	1	-1	1	-1	-1	-1	0
abd	1	1	-1	1	-1	1	1	1	1	0
cd	-1	-1	1	1	-1	1	1	-1	-1	0
acd	1	-1	1	1	-1	1	-1	1	1	0
bcd	-1	1	1	1	-1	-1	1	1	1	0
abcd	1	1	1	1	-1	-1	-1	-1	-1	0
e	-1	-1	-1	-1	1	-1	-1	-1	-1	0
ae	1	-1	-1	-1	1	-1	1	1	1	0
be	-1	1	-1	-1	1	1	-1	1	1	0
abe	1	1	-1	-1	1	1	1	-1	-1	0
ce	-1	-1	1	-1	1	1	1	1	1	0
ace	1	-1	1	-1	1	1	-1	-1	-1	0
bce	-1	1	1	-1	1	-1	1	-1	-1	0
abce	1	1	1	-1	1	-1	-1	1	1	0
de	-1	-1	-1	1	1	1	1	-1	-1	0
ade	1	-1	-1	1	1	1	-1	1	1	0
bde	-1	1	-1	1	1	-1	1	1	1	0
abde	1	1	-1	1	1	-1	-1	-1	-1	0
cde	-1	-1	1	1	1	-1	-1	1	1	0

Treatments	A	B	C	D	E	F= BCDE	G = ACDE	H = ABDE	I = ABCE	Mean Yield
acde	1	-1	1	1	1	-1	1	-1	-1	0
bcde	-1	1	1	1	1	1	-1	-1	-1	0
abcde	1	1	1	1	1	1	1	1	1	0
Linear Contrast	0.00	0.0	0.0	0.0	0.0	0.00	0.00	0.00	0.00	0.00

Table 31   The $2^{9\text{-}4}$ screening design

The mean yield, referred to in Table 31, is the average of the yields (positioning repeatability, positioning bias, rise time, settling time and the percentage overshoot) from each replica experimental treatment.

The contrast standard deviations are the square root of the variance between these replicate yields. The following common formulae (Equ. 206, Equ. 207 and Equ. 208) can then be used to determine significance for the experimental results.

If k is the number of factors, i, the treatment identifier and σi^2 is the replicate yield variance of the ith treatment, then the pooled variance can be written as

$$\sigma = \sum_{i=1}^{2k} \frac{\sigma_i^2}{2^k}$$

<div align="right">Equ. 206</div>

The standard error of the effect is then taken to be

$$\text{Std. error of the effect} = \sqrt{\frac{4\sigma^2}{N}} \text{ (for } n \text{ replicates } N = n2^k\text{)}$$

<div align="right">Equ. 207</div>

In the case of the screening experiments, if the linear value contrast for a particular factor is three times the standard error, then it can be regarded as being significant. When subsequently carrying out the full factorial set of experiments on the identified significant factors, more accurate confidence limits about the effects can be calculated.

The 95 % confidence limits are given by

$$\text{confidence limits} = t_{0.025}\sqrt{\frac{4\sigma^2}{N}}$$

<div align="right">Equ. 208</div>

The t-distribution is used because the sample size, i.e. the number of replicates, from which σ is calculated must be small and hence the intervals need to be wider than would be the case if the actual population variance is known.

An effect can only be regarded as being significant if its confidence interval does not overlap zero. Otherwise it may be explained by variance arising from experimentation.

7.4.3.2 Replication, repetition and blocking

In the case of both the screening and full factorial designs, the time to set up each treatment may vary substantially, depending on which factors levels require changing e.g. changing environmental factor levels such as humidity could take longer than say adjusting the tilt of an interferometer mirror. This means drift in variables may be dependant upon the order in which the treatments are carried out. To counteract this effect and any other unforseen time dependant variables, several complete replicates should be performed. Each replicate must be completed before the next is begun and all treatments in each replicate are to be carried out in random order.

Because it is suspected that it could take several hours to complete a full set of treatment experiments on the instrument, this may introduce experimental bias between replicates if they are performed one directly after the other. This bias arises from differing background conditions, environmental or otherwise, at different times of the day. The effect of these conditions may also differ, depending on the particular treatment being applied at that time. In order to avoid this problem, it is proposed that each replica set is divided up into quarter sets of treatments, each to be applied at different times of the day and only one full replicate being performed in a single day. It should be noted that this approach does not take into account longer periodic changes such as those arising from seasonal conditions.

Positioning repeatability has been previously identified in Section7.4.3 as being an experimental response of interest. It is the repeatability of the stage that is sought, not the variability created by running the experiments, the later being included in the

intervals calculated using Equ. 206. So to measure the effect of factors on instrument repeatability, each replica of treatment must also include several repetitions, so that a repeatability value can be calculated for each replicate and subsequently averaged to give a mean treatment yield.

7.4.3.3   Testing for contouring ability

Since the instrument described in this thesis is required to contour in three-dimensional space, it is natural that dynamic tracking factors, such as speed, dwell times and the direction change requirements of curved paths, should also be explored through experimentation. The effects of these factors on the instrument performance, in terms of accuracy and repeatability, need to be examined.

To test for contouring ability it is proposed that the stage should be driven over spherical paths. Spherical surface paths are considered a more rigorous and representative test than flat surfaces scanning. This is because each axis can be tested equally over extending and contracting step displacements of varying length while all axial movement combinations are being performed.

The main factors and yields are tabulated in Table 32. Factor B, the resolution, refers to the spacing between the locations on the contour surface to which the stage is commanded. A slider on the front panel of the command program facilitates controlling the resolution. Factor C, the speed, is in effect the dwell time at each commanded location and is set by means of a dial on the front panel of the command program.

Main Factors	A = Sphere Radius	B = Resolution	C = Speed
Table 32 The main factors to be considered when contour testing.			

Since only three main factors are being considered, a full 2^3 factorial experiment design, requiring only eight separate treatments, is a viable option. Table 33 gives the treatment combinations for such a design. Several replicates of each treatment should be performed in order to average out and quantify experimental variability. In order to neutralize the effects of background factors, randomisation of the treatment sequences within the replicate is also necessary. Since positioning repeatability is a desired yield,

as previously explained, repetitions of each treatment within each replicate are needed to be performed. The yields of interest in these experiments are the repeatability and positioning bias.

Treatments	A	B	C	AB	AC	BC	ABC	Mean Yield
-1	-1	-1	-1	1	1	1	-1	
a	1	-1	-1	-1	-1	1	1	
b	-1	1	-1	-1	1	-1	1	
ab	1	1	-1	1	-1	-1	-1	
c	-1	-1	1	1	-1	-1	1	
ac	1	-1	1	-1	1	-1	-1	
bc	-1	1	1	-1	-1	1	-1	
abc	1	1	1	1	1	1	1	
Effects								Table 33

Unlike in the case of the previously described fractional factorial design, control of the factors in this design is almost instantaneously, thus involving no delays between treatments and smaller drift effects.

7.5   Summary

This chapter has addressed: the assembly and alignment of the instrument mechanical and metrology systems; the development of an environment suitable for the operation of a precision positioning instrument; the design of a rational set of experiments for instrument characterization and design validation.

The functional objectives of the set-up were initially stated, followed by the presentation of a proposed ten step set-up procedure.

The effects of environmental factors, thermal, pressure, humidity and noise (electrical and mechanical) are discussed in Section 7.3. It is suggested that variation cycles for temperature, pressure and humidity should be made far longer than the cycle time of the instrument and that noise amplitudes should be minimised. So as to achieve these objectives, an environmental arrangement in which to operate the instrument was proposed. Examination of the current environmental arrangement, developed through under-graduate project work, indicated that little additional improvement is required.

Section 7.4 described the design of experiments aimed at improving the functional performance of the system. The experimentation is targeted at yielding information that validates the entire system design, validates the set-up, validates the theoretical relationships proposed in Chapters 5 and 6, and quantifies the effects of the main environmental and set-up factors, and their interactions, on instrument response. Because of the suspected presence of interactions between the main factors, it is proposed that the methodology that should be adopted to address these issues is the multi-factorial statistical design of experiments, as described by Grove et al. [87]. Section 7.4 described the rationale behind the choice of a 2^{9-4} fractional factorial screening design, followed by a full factorial design to look at significant factors only. The main factors and levels were identified, while issues such as randomization, blocking, replicates of treatments and repetitions of replicates were discussed. A full factorial experimental design was also described that aimed at quantifying specifically the effects that contouring demands have on positioning accuracy and dynamic characteristics.

This chapter has contributed to addressing several aspects related to the research question. Complexity and rigor of set-up procedures were shown to be necessary for ensuring that the designed instrument would attain accurate positioning performance, hence indicating that instructional material (operational, maintenance and commissioning manuals) must be treated as an important consideration when standardising specification documentation.

In conclusion, this chapter provided a template for future development of this project. Procedures and a methodology were provided for assembling the imagined instrument, for establishing a suitable environment and for validating, through experimentation, both the design and the proposed theoretical relationships on which the error budget is based.

Chapter 8

8   Discussion and conclusion

As explained in Chapter 1, there is an ever increasing requirement for instruments capable of positioning tools/probes and work pieces relative to each other with nanometre or near nanometre resolution.   The positioning resolution of such instruments within wafer stepper machines, for example, is a major factor in determining the achievable spacing and consequent density of integrated chip components, thus indicating the economic importance of developing nanopositioning technology.   Furthermore, the contouring resolution of these devices is a limiting factor in the development of the growing range of metrological 2D and 3D surface-characterising scanning instruments and the manufacture of present and future micro and nano-scale products.

The purpose of this thesis was to investigate the documentation requirements of a comprehensive generic specification for instruments capable of positioning and contouring at nanometre scale accuracy.

By carrying out this investigation, identified concerns expressed at a meeting of the 'Nanometre Metrology Network' regarding how highly accurate positioning stages are specified/marketed have been explored. The meeting, held in London in 2003, was attended by the representatives of the UK National Physical Laboratory, academic researchers and manufacturers. Research has shown that Governments and national standards institutes appear to recognise the commercial imperative of standardisation to address these issues. This is evident through their rhetoric and the establishment of various committees; but no standards have so far been written in any country specifically addressing the specification of precision positioning instruments.

As a vehicle for identifying and exploring issues relevant to such specification, a complete system, capable of contouring at nano-scale resolution has been designed.

8.1   The design as a vehicle

The iterative design methodology, adopted for this thesis is summarised in the flowchart presented in Fig. 199. The chart shows the flow of information as the design progressed from research to a viable system. It illustrates how mathematical, FEA and prototype modelling work in tandem to validate and reinforce their respective findings and to subsequently inform the design iteratively and it illustrates that the static and

dynamic predicted behavior were used to repeatedly redesign the instrument until the targeted system positioning requirements were achieved.
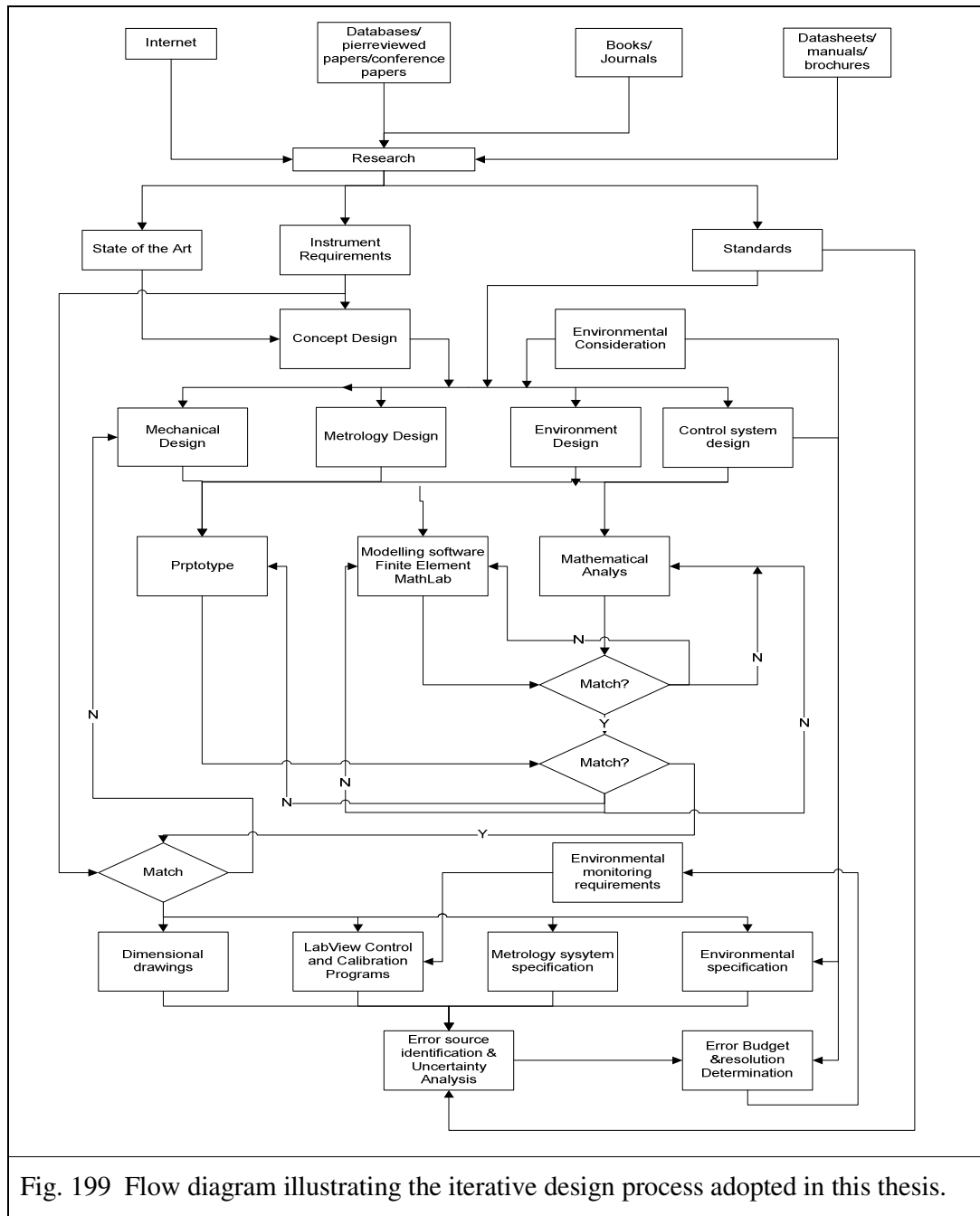
Fig. 199 Flow diagram illustrating the iterative design process adopted in this thesis.

As can be deduced from Fig. 199, the design of the instrument was based on a comprehensive review of the literature. This provided:

- insight into the current state of the art;

294

- requirements of precision positioning instruments;

- an extensive range of possible error sources as well as methods by which these are commonly avoided, reduced or compensated;

- knowledge of commonly used options for the design of the mechanical, metrology, control and environmental systems;

- procedures and standards and guidelines for expressing uncertainties; and

- identification of existing instruments, applications and standards related to precision positing.

The detail of these findings is presented in Chapter 2, while design options, principles and guidelines formed the basis for an effective robust design and subsequently effective investigation into specification requirements.

Chapter 3 described the development from early concept designs through to the final dimensioned functional 3D instrument mechanical components. Materials were chosen based on their mechanical and thermal properties. Guiding systems and structural mounting systems were studied. A parallel three pronged approach of FEA, analytical methods and prototyping was employed to ensure design confidence and optimisation. The final mechanical design has the following characteristics.

- It is entirely made from aluminium alloy 6082 T6. This ensures rapid dissipation of thermal gradients owing to its high thermal conductivity. 6082 T6 has relatively high yield strength (228 MPa), hence facilitating adequate elastic flexure deformations for maximised stroke lengths. Furthermore, the alloy has low density (2810 Kg m^{-3}) enabling higher stage positioning velocities and resonance frequencies.

- Mechanically, the instrument consists of stage/force frame and a metrology frame, both mounted isostatically onto a stiff support frame. This in turn is mounted kinematically onto a base plate. The isostatic mounts allow stiff linkages between structural frames while avoiding stress concentrations and distortions that might arise due to relative thermal expansion. These mounting arrangements have the additional advantage of allowing the designer to

manage the directions of gross thermal expansion, a useful capability when attempting to maintain axial alignment.

- The three axis stage/force frame is of monolithic construction to avoid friction that may occur at component contact surfaces during driven relative motion or thermal expansion. (see photograph in Fig. 200 (c))

- The stage consists of a block made as small and light as possible, yet stiff enough to minimise distortion when displacing forces are applied.

- The flexure based guidance design provides:

  o frictionless motion;

  o resonance frequencies higher than background disturbance frequencies;

  o maximum compliance in the desired directions of motion and high resistance to off axial motion;

  o balance between the opposing requirement for high stiffness and long stroke lengths; and

  o preloads designed to ensure the piezos do not shake loose at resonance, that are practical to implement, while not being so high as to cause plastic deformation or to hinder stroke lengths.

- Piezo actuation allows for highly resolute, repeatable and controllable motion. Piezos provide controlled expansion of the designed gap between the stage and a stiff force frame. The axes of actuation were made to pass through or as close as possible to the stage centre of gravity, avoiding unwanted tilting modes at higher stage accelerations. Preloading was accomplished by making the gaps between the stage and force frames smaller than the length of the piezos. Gap size was based on careful analysis of the flexure geometries and structural stiffness.

- A substantial and stiff metrology frame (see photograph in Fig. 200 (a)) supports the stationary components of the metrology system.

- The support frame is designed with substantial pillars so that short rods can support the force and metrology frames, raising the resonance frequency of relative frame movement modes. (see photograph in Fig. 200 (b))

296
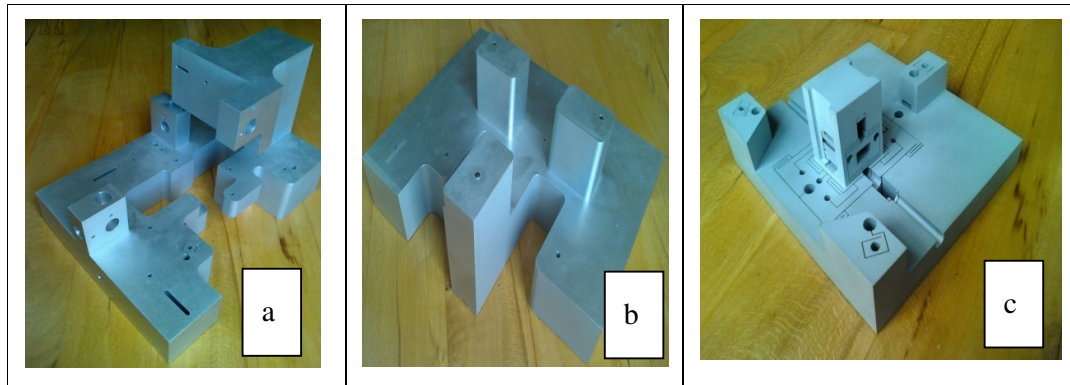
Fig. 200 Photographs of the manufactured structural parts resulting from this study: (a) metrology frame, (b) support frame and (c) stage/force frame.

The metrology system is discussed in detail in Chapter 4. Strain gauges (piezo mounted) and capacitance micrometers were considered for use as in-process displacement measurement sensors. Because the strain gauges are available pre-package, pre-calibrated and attached to the actuators, they are very convenient to use, but they can only be used in series metrology systems. Therefore strain gauges are incapable of measuring axial crosstalk. Nevertheless, they were utilised in the early prototype stage. Capacitance sensors, on the other hand, can be used to provide parallel metrology. These were examined in the context of possible associated error sources. Michelson interferometers were chosen to calibrate the capacitance sensors because of their high resolution, traceability to international standards of length, their non-contact means of measurement and their adaptability to the Abbe principle. Three Michelson configurations were considered; a single pass [37], a double pass [26] and a four pass arrangement [9]. The stage travel distance, represented by a single cycle of the interferogram, is halved when the number of passes of Michelson interferometers is doubled, effectively doubling the measuring resolution if fringes are counted to determine displacement. But so does the interferometer complexity and difficulty of set-up. Uncertain whether the two pass or four pass configurations could be effectively aligned within a reasonable time period, the metrology frame was ultimately made flexible enough to accommodate the use of all three configurations. Consideration was also given to the use of a Haydemann correction to compensate for non-linearity in the component beams of the interference pattern. This would allow accurate interpolation of a simpler single pass interferogram.

Error sources, affecting the interferometer measurement accuracy were identified, extensively examined and their potential magnitudes calculated. These errors were nulled where possible through mechanical design or compensated in the control software programs. Minimising metrology system errors, to a large extent, determined the mechanical design.

Abbe error was identified as the most critical of the metrology errors and much design effort was aimed at ensuring that the measurement and reference measurement axes coincide at a single point of interest (the Abbe principle). The design does not permit complete compliance with the Abbe principle, as the Y and Z stage movement axes are displaced relative to the corresponding measurement axes during normal operation. The resulting Abbe offset is less than 14 µm for each axis. This results in a possible ±0.4 nm Abbe error when a T40 model autocollimator [81] (resolution: ±0.1 arc sec) is used for alignment.

Flexible mounts were seen as necessary for correcting non-parallelism of the interferometry mirrors and capacitance plates during set-up, thus reducing non-linear measurement.   Flexibility in positioning the interferometers was also facilitated through the use of slots on the metrology frame, which would allow relative optical path lengths to be made equal.

A novel artifact was designed specifically for determining the angles between measurement axes of the interferometers so that the instrument coordinate system could be defined, thus allowing displacements to be related, through a set of derived transform equations, to the Cartesian coordinate system.

The command and control system is described in detail in Chapter 5. Fig. 111 presents a schematic diagram illustrating the system control complexity required for accurate positioning. A suite of interdependent LabView and MathCad control programs were written specially for this thesis. These facilitate:

- automated calibration of the in-process capacitance sensors to reference interferometer measurements;

- laser light wavelength to be compensated for environmentally induced changes;

- instrument to Cartesian coordinate axis transformations to be applied and reversed automatically, based on measured individual axis non-orthogonality angles;

- the process measurements to be linearised to the reference measurements through fourth order mapping functions. The coefficients of these functions and the coefficients of their reversing functions are calculated automatically, saved to file and subsequently applied to alter command and monitored data;

- command sequences for user defined 3D scanning scenarios over curved and flat inclined plains to be calculated and interpolation to be applied, ensuring smooth surfaces; and

- possible measurement errors arising from environmental changes to be automatically and appropriately compensated based on real time sensor readings.

Section 5.2 describes in detail the functionality of each of these programs.

The axial dynamic characteristics were studied Section 5.3. Models were created incorporating the stage and flexures (modeled as mass/spring/dampers), piezo actuators (modeled as charging capacitors), the power supply, the proportional integral controller and the notch filter. The open loop transfer functions (Equ. 68) were derived for the single axis prototype stage and each of the 3D instrument axes. Step and frequency responses were predicted for each axis using MathLab software. As in the mechanical design process, the use of the prototype allowed confidence in the predictions. Closed loop functions (Equ. 72) were then derived for the 3D instrument axes. The models indicated that the system would behave in a controlled manner. Overshoot can be avoided, while rise and settling times can be minimized by the correct selection of PI tuning values; essential if the instrument is to be capable of rapid precision contouring. Response step and Bode plots indicated that the axes are well balanced, having very similar response characteristics. The predicted response characteristics are tabulated in Table 17, while the parameter values used to calculate the predictions are given in Table 16. Predictions are regarded merely as indicative, as the tuning values are to be ultimately chosen experimentally using, for example, the Ziegler-Nichols method.

299

The assembly and alignment of the mechanical and metrology systems is described in Chapter 7. A ten step set-up list of procedures, some novel, is presented to ensure the following: the mutual orientation of the reference axes is normal; the capacitor measurement axis, the reference measurement axis and the axis of displacement all coincide with each other; and the interferometer optics and capacitance plate are properly aligned. Furthermore, the tools, specially designed to implement these procedures, are also presented: piezo actuator positioning jacks, an orientation jig, a mirror decoupling plate and an artifact for measuring the angle between reference axes.

The environmental issues are discussed in Section 7.3. Software compensation for non-nulled environmental variation is implemented at calibration and immediately prior to each operational command cycle. Because of this, design of the environment was targeted at elongating the environmental variation cycles, making them far longer than the instrument cycle times, while simultaneously minimising noise amplitudes.

These environmental objectives are to be met through thermally shielding the instrument within a thermally insulation and infra-red shielded vacuum vessel, located on a heavy granite damped table which in turn is located within a thermal and EMF insulated room. All sources of electro-magnetic frequencies are to be operated from outside of this room, while necessary actuator and sensor wiring are to be shielded. A novel method of structurally flexible thermal shielding has been proposed to accommodate the complex instrument geometries. The effectiveness of this is currently the subject of undergraduate projects.

Section 7.4 describes in detail the multi-factorial statistical design of experiments aimed at validating the system itself, the theory behind its design, its set-up, as well as at ultimately improving its functional performance. The section also proposes subsequent full factorial experiments involving only identifiable significant factors along with additional experiments to examine the effects that contouring factors (radii, dwell time, resolution) have on contouring ability.

Associated with all the aforementioned error sources are uncertainties that cannot be compensated or nulled. In Chapter 6 these were investigated in accordance with GUM [23]. For each source of uncertainty, functions have been derived that relate their effects to displacement measurement. Standard Type B uncertainties, u_j, were calculated, based on appropriate component uncertainties and sensitivity coefficients.

Ultimately, a combined uncertainty values was calculated which was then multiplied by a coverage factor (k = 2) to give an expanded uncertainty U, a measure of the instrument positioning resolution. An error budget (Table 26) was constructed, tabulating the following individual standard uncertainties.

Capacitance sensor error sources: linearity, noise, plate expansion, relative permittivity variability, expansion of sweet-spot offset distances.

Interferometer error sources: laser wavelength variability, dead path errors, optical component expansion, periodic deviation, sweet-spot offset expansions, mirror tilt, mirror flatness, Abbe error, cosine error.

For sub-nanometre positioning resolution, it was found necessary that temperature measurement resolution must be better than ±0.002 K when compensating for mirror offset, the movement and reference axes must be aligned to better than ±0.01 arc sec. and the offset distance between them measured to better than ±1 μm so as to ensure adequately small Abbe error. Additionally it was found that in some instances, uncertainty does not only depend on parameter sensor tolerance, but also on the parameter value deviation from that at calibration, e.g. in the case of mirror/point-of - interest offset expansion, the temperature difference cannot be more than ±0.0125 K for the compensating uncertainty to be less than 1 nm.

The purpose of designing the instrument was to identify what is needed to satisfactorily specify a precision positioning instrument. Recommendations for standardising specifications, based on the design process, are presented in Section 8.3, preceded by discussion of the current specification standards.

8.1.1 Current specification standardization

Initially, it is important to realise that positioning devices are not all the same; in general, they can be categorised as guided stages with a) no form of metrology; b) open loop sensing; c) closed loop guidance sensing; and d) closed loop sensing that incorporates automated calibration to reference sensors. For each category, movement characteristics of interest are the same as those identified and examined in the design of the three axis instrument designed for this thesis, i.e. accuracy, positioning resolution, linearity and dynamic behaviour such as rise times, overshoot, settling time etc., although the relevance of individual characteristics vary for each product type,

301

applications and targeted market. Furthermore, as is exemplified by the instrument designed for this thesis, positioning displacements may be on the nano-scale, but the instrument structural sizes and uncertainties are invariably specified on the macro-scale. Nevertheless, common to the specification of all such devices, movements must be measured and these measurements must be traceable to internationally accepted standards of length.

One approach, to achieving this, would be for manufacturers to submit each device for testing and certification to a metrology body such as an NMI or one that is accredited to be in conformance with standards such as ISO/IEC 17025: 2005 (general requirements for the competence of testing and calibration laboratories). These bodies are capable of carrying out tests by expert personnel in accordance with agreed standardised methodology, using standardised and calibrated metrological instrumentation that provides results that are traceable to the SI unit of length. Instead of submitting devices for testing, traceability is commonly achieved by using instrument interferometer lasers that are wavelength calibrated against a primary length standard, such as an iodine-stabilised He-Ne reference laser in accordance with International Committee of Weights and Measures recommendations (CIPM).

Submission of individual devices for testing to accredited metrology bodies means that results are internationally recognised, facilitating customer confidence and enhancing marketability. On the other hand, committing product to accredited bodies may be expensive, may complicate scheduling and lengthen throughput times; consequently purchase prices may be higher, while simultaneously, innovation may be inhibited and product evolution, product flexibility and design of variants may be discouraged. Devices need to be designed to facilitate standard testing methods, or the testing body would have to tool-up so as to accommodate the individual device geometries.

If the laser wavelength is used as the path to traceability, the relationship between the wavelength and the movement of the instrument working point must be well defined. Additionally, for the position of the working point of the stage to be traceable, all possible sources of uncertainty and mechanisms for propagating this uncertainty must be identified and combined into an uncertainty budget in accordance with GUM. Ultimately stage positioning accuracy can be expressed as measured locations accompanied by calculated expanded uncertainty values (U value). Creation of such a

table and the determination of U values for each axis are exemplified in Chapter 6 of this thesis. The approach of achieving traceability through the calibration of instrument interferometers lasers has several advantages. Lasers can be bought pre-calibrated and certified, thus reducing throughput times. Minimisation of in-service recalibration downtime is also made feasible if spare standby calibrated lasers are available, notwithstanding the need for realignment. Design of devices can be changed and device variants made available without resubmission, so long as the all changes are factored into the uncertainty budget and U values are recalculated. Furthermore, cost of calibration may be significantly lower, as testing bodies are tooled-up for the regular calibration of lasers.

As has been shown through the instrument design carried out for this thesis, performance of precise positioning instrumentation is particularly sensitive to set-up/alignment issues, environmental factors and loading, whilst these sensitivities are respectively device specific. Therefore, for test results to be truly reproducible and representative of in-service performance, test environments must accurately mimic service environments, or vice-verse, in terms of parameter levels and variability. Alternatively, calibrated devices can be used in accurately monitored service environments, while appropriate environmental compensations are applied to displacement measurements. In both scenarios significant sources of uncertainty in terms of environmental sensing and compensation are introduced. In addition to certifying the positioners, metrology bodies can also provide certification for the monitoring and compensation systems. NPL, for example, provides a calibration for auto-compensated laser interferometer systems that are sometimes used for direct measurement of stages or for calibrating instrument displacement sensors. In this instance, calibrating is not only applied to the interferometer measurements and the wavelength of the laser light, but also to the environmental sensors that are so important for correct compensation.

Since positioning devices are commonly used in industrial situations and often act as components or sub-systems within measuring instruments for the purpose of quality control, a practical approach would be to characterise and calibrate their movement against parameters related to product functionality. Devices that constitute the movement axes of metrology instruments, such as microtopography instruments, including stylus, optical scanning, SPMs and CMMs can be traceably calibrated and

characterised by using transfer standards in-situ, under the pervading environmental and alignment conditions. For positioning devices used for applications, other than those forming the axes of measurement instruments, the in-situ use of artefacts may not be so convenient. However, Hansen et al. [4] asserts that it is calibration artefacts that are currently integral to dimensional metrology and quality assurance in manufacturing environments.

Ideally, the method involves the use of artefact surfaces, the features of which have been measured in a standardised traceable manor by an accredited body. This is not always the case, as many uncertified reference materials are supplied by instrument manufacturers (see Table 34). Devices differ in terms of dimensionality, measurement technique and accuracy. This diversity is reflected in the wide range of artefacts and calibration services being marketed. NPL, for example, calibrates, supplies and certifies two-dimensional artefacts, used for characterising stylus profile measurement instruments in accordance with ISO 5436-1: 2000 (GPS -- Surface texture: Profile method; Measurement standards -- Part 1: Material measures). The characterised artefact features may be any or all of those described in ISO 4287: 1997 (GPS – Surface texture: Profile method – Terms, definitions and surface texture parameters), with heights ranging from microns to millimetres. NPL is also certifies AFM artefacts with a maximum measurement range in the X and Y direction of 100 µm, with a pitch uncertainty ranging from ± 0.2 nm for a 0.3 µm pitch to ± 2 nm for a 10 µm pitch, along with a step height uncertainty ranging from ± 0.4 nm for a step height of 10 nm to ± 15 nm for a step height of 0.5 µm. Three-dimensional artefacts are also certified for use in areal topography methods as described in ISO 25178-6: 2010 (GPS Surface texture: Areal Part 6: Classification of methods for measuring surface texture).

As illustrated in Fig. 201, SPM measurements are made traceable to the SI unit of length when the reference artefacts are characterised by means of metrological AFMs that use interferometer based axial displacement measurement e.g. the Metrological Atomic Force Microscope (MAFM) that has been developed at NPL.
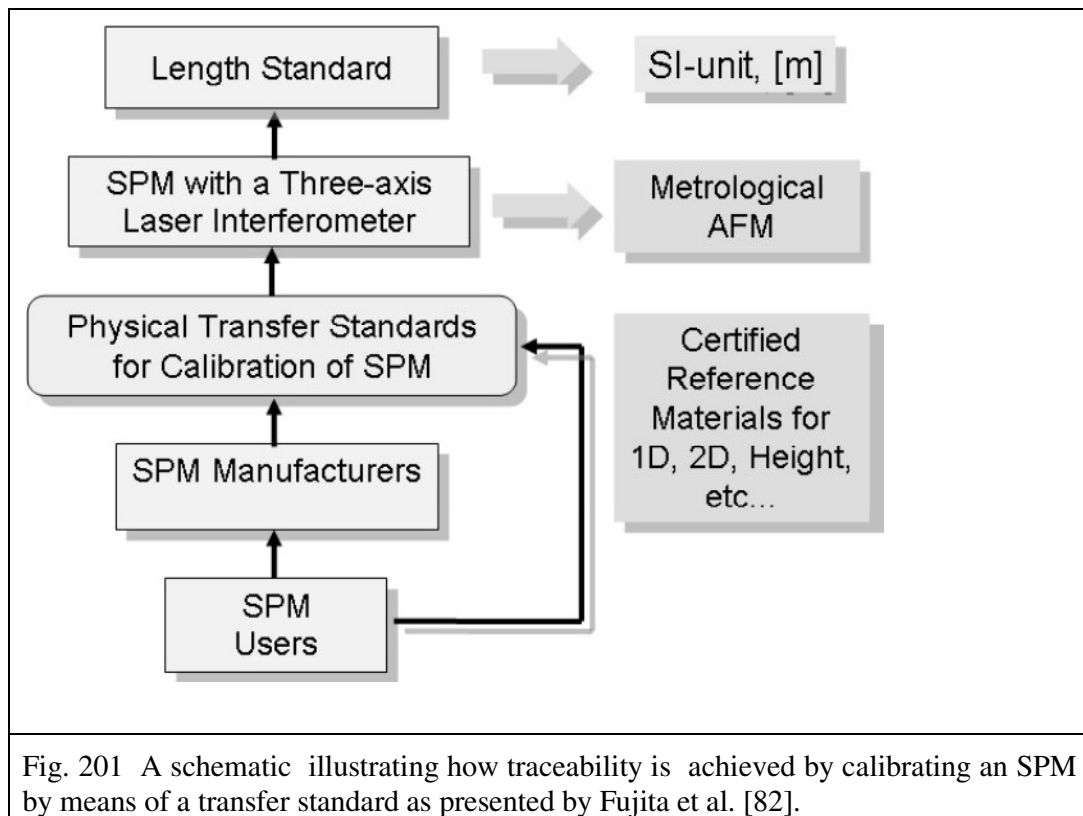
Fig. 201 A schematic illustrating how traceability is achieved by calibrating an SPM by means of a transfer standard as presented by Fujita et al. [82].

In accordance with ISO 5436-1: 2000, each reference artefact that is supplied by NMIs or other accredited bodies is accompanied by the information about the test, such as the probe detail, reference conditions, details of instrument calibration, the number of observations etc., along with mean values of the measured parameters, accompanied by expanded uncertainty values, that are calculated in accordance with GUM. The standard even goes so far as to stipulate that this information should be uniquely related to the individual standard via serial number markings.

As SPMs are the primary tools used to examine surfaces at the nanometer scale, discussion will be limited here to artefacts used to calibrate such instruments. Initially a very brief discussion aims to illuminate the concept of an artefact, describing their uses, their structures, appearance and related standards. For open-loop actuated arrangements, the reference artefact is used to calibrate the signal given to the actuators; in closed loop systems, where axial positioning sensors are used, the artefacts calibrate the sensors.   Not only can the axial displacements of SPMs be calibrated by using artefacts, but also axis orthogonality and crosstalk measured [71]. The scope of individual artefact application is limited by its characteristics and those of

the instrument to be calibrated. It is not necessary to present detailed descriptions of artefacts here. Five main types of artefact, together with variants of these types, are described in ISO 5436-1: 2000 and are subsequently explained in the NPL Good Practice Guide No. 37 [88]. Commonly, artefacts exhibit features such as random samples, one- and two-dimensional gratings with well defined pitches between features and/or step height samples. Fig. 202 illustrates the format of a typical artefact, along with images of three common calibration patterns as presented by PTB [89].

An extensive, though not comprehensive, directory of such standard artefacts for use with micro- and nano-systems is presented by PTB [89]. Included are manufacturers' details, measurement ranges, images of the artefacts, descriptions and suggested applications. The German Federal Institute for Materials Research and Testing (BAM), in cooperation with ISO TC 229 also provide an on-line directory of nano-scaled reference materials [91].
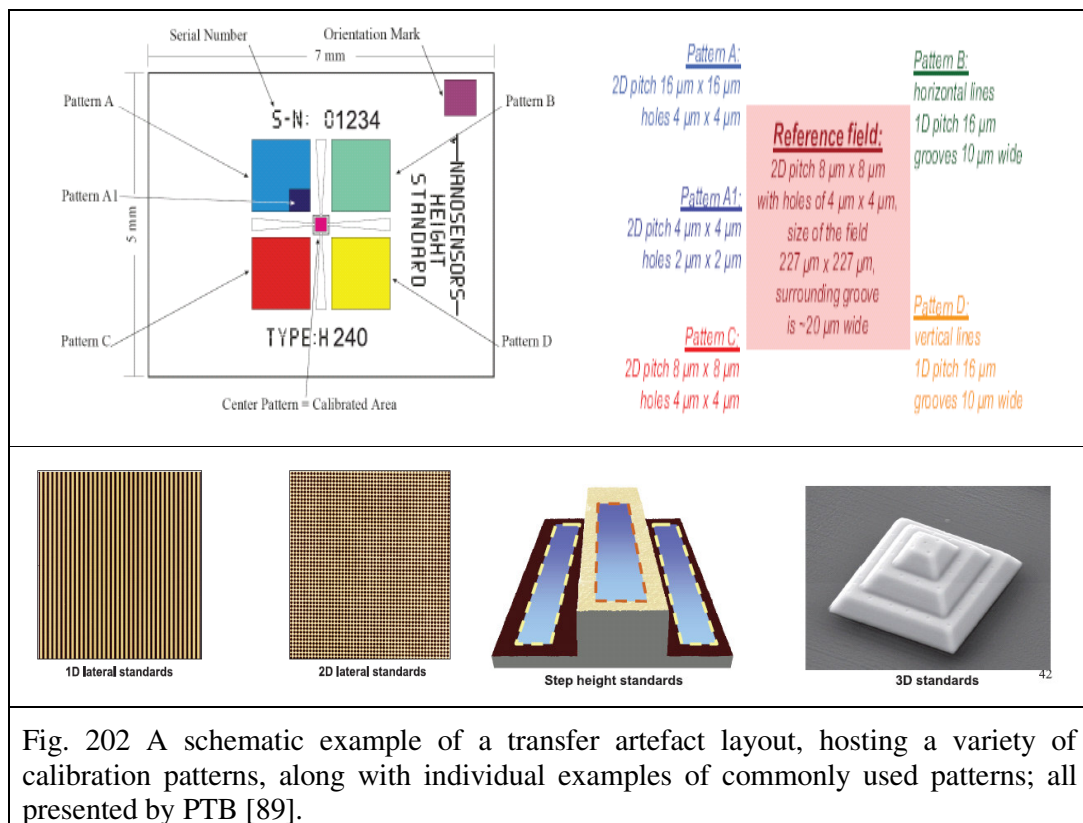
Fig. 202 A schematic example of a transfer artefact layout, hosting a variety of calibration patterns, along with individual examples of commonly used patterns; all presented by PTB [89].

To maintain traceability, the calibration methodology and set-up of the individual process measurement instruments must be carried out in accordance with a suitable

standard, such as ISO 12179: 2000 (GPS – Surface texture: Profile method – Calibration of contact (stylus) instruments), while proper use requires compliance with standards such as ISO 4288 (GPS – Surface texture: Profile method – Rules and procedures for the assessment of surface texture).

Whether calibration artefacts are used in-situ or devices or components thereof are submitted to an accredited testing body, the physical scale of devices is of significant relevance when considering the specification of positioning devices. As is exemplified by the instrument designed for this thesis, although the movement accuracy of positioning devices may be on the nano-scale, the physical structures are usually dimensioned and tolerance in the macro-scale, allowing manufacture via traditional machining processes. Consequently, key aspects of device design methodology, technical documentation, manufacture, expression of uncertainty and verification are described in the set of ISO standards that constitute the Technical Product Specification (TPS). Guidance on the application of TPS is provided in PD ISO/TR 23605:2009 (TPS –Application guidance – International model for national implementation). The guide is designed to effectively act as an index to the relevant ISO standards. Furthermore, a declarations of conformity which complies with ISO/IEC 17050-1:2010, along with the appropriate substantiating documentation, as stipulated in ISO/IEC 17050-1:2004, allows purchasers of SPMs to be assured that a device will perform as expected. Under these conformity standards, the declaration must include a complete list of standards with which the product complies, reference to any accreditation certification, supporting documentation as well as any limitations on the validity of the declaration. The supporting documentation must be made available, on request, to the appropriate regulatory authority and may also be made available to other interested parties. To comply with the standards, the documentation must include design documentation, conformity assessment results and any other relevant information.

It would appear that the specification of positioning devices is effectively accommodated under current provisions and that no additional standards are required. But several issues limit the effectiveness of the current standards regime at the nano-scale.

- Very few calibrated artefacts, especially three-dimensional artefacts, exist at the nano-scale, [4], as can be deduced the quantities of reference materials (RM) and certified reference materials (CRM) included in the BAM list [91] (see Table 34).

Category	Range (nm)	Number of artefacts	CRM values (nm)
Single step	0.31 to 180	12 RM / 0 RCM	
Lateral (1 D)	3.5 to 180	4 RM / 2 CRM	3.5 and 80
Lateral (2 D)	25 to 200	4 RM / 1 CRM	100
3 D	40 to 600	2 RM / 0 CRM	
Table 34 The quantities of reference materials (RM) and certified reference materials (CRM) included in the BAM list [91] (compiled August, 2009)			

- Accurate nano measuring, using SPMs is limited to small ranges [92], as is exemplified by the NPL range of artefacts and artefact calibration services described previously in this section.

- Standardisation of instrumentation, calibration artefacts, methods, documentation and definitions have not yet been fully developed, thus making dissemination of SI-traceability difficult [11]. Currently, to facilitate nano-scale metrology, much effort is targeted at standardising in this area [11], e.g. the ISO technical committee, ISO/TC 201/SC9, is working to provide guidance in measurement and characterisation of nano structures by SPMs, while working groups, under ISO/TC 201/SC9, are examining issues such as the effects of measurement conditions, basic dimensional calibration of SPMs and application-oriented dimensional SPM calibrations. Among several standards under development by this committee is ISO/AWI 13095 - procedures for in situ characterization of AFM probes used for nano structure measurement.

- The GPS standards are based on micro- to macro-scale dimensions, micro- to macro-metrology, traditional manufacturing methods, and continuum mechanics. In the case of SPMs, the underlying traditional concepts, and terminology can no longer be relied upon at the nano-scale, where hitherto little understood interactions, at the atomic level, between surfaces and instrument

probes become significant [11] [4]. Consequently, application of, as of yet unmodified, GPS standards becomes problematic at nano-scale dimensions.

- Parameters related to surface characterisation at the atomic level, such as straightness and roughness measurement, have still to be defined [93]. In the mesoscopic world, there are no straight edges [4], while SPM measurements of roughness cannot be compared with measurements taken by stylus profilers [93] due to inadequate SPM scan ranges preventing conformity with GPS standard definitions. Furthermore localised pitch discontinuities on artefacts are commonly not documented and may result in poor calibration [89].

- Because of the lack of proper standards and guidelines for reproducible measurement results, the commonly supplied uncertified artefacts do not facilitate comparison of instruments or measurements [20].

- Adherence to the model for implementing TPS (PD ISO/TR 23605: 2009) is voluntary, but becomes a legal obligation if referred to within specification documentation. The implementation of the conformity assessment standards (parts one and two of ISO/IEC 17050) is mandatory for European NMIs.

- Since it is desirable for manufacturers to be able to market devices for use in several applications and under differing environments, provisions of test standards must be flexible enough to reflect multiple situations.

In the context of strengths and shortcomings associated with current documentation provisions, observations based on the design of the complex positioning instrument will lead to recommendations for improved specification standardisation.

8.2   Observations based on the instrument design

In the context of the design development carried out for this thesis, some observations stand out as being particularly relevant to standardisation.

- Approaches involving both compensation and nulling of error biases have been adopted for the design, but this may not be the case for many commercially available devices. Information regarding error handling would clearly be of considerable benefit to customers.

309

- The uncertainty analysis, as applied to the imagined instrument here, also highlighted issues that, not only describe the capabilities of a device, but also how it must be used if said claimed capabilities are to be realised. For the designed instrument, the resolution of several categories of sensors must reach certain levels if positioning accuracy targets are to be met. The sensors in question are used for measuring the stage locations, for reference/calibration measurements, for measuring the environmental variability and for measuring set-up alignments and axis offset distances. Use of less adequate sensors for any of these applications would render the device less accurate. This analysis also indicated that, in some instances, uncertainty in instrument positioning may be affected by the absolute environmental parameter values. Although it is understood that the relative relevance of such observations is device specific, it is reasonable to say that having knowledge of permissible operating conditions and minimum sensor tolerance would be critical to proper use of devices. Furthermore there may also be major cost implications associated with need of better sensors and signal conditioning electronics.

- The work, as described in Section 7.2, involving the development of a means by which the thesis instrument could be properly aligned, highlighted the critical role that procedures have in influencing positioning performance. During the development of the procedures and methods needed for correct instrument set-up, the necessity for costly set-up and orientation tooling also became apparent. These needs may differ significantly between devices, but clearly knowledge of such requirements would be of significant relevance to any purchasing decision.

- It would be reasonable to expect that instrument axial step response parameters, such as those given in Table 17 (Section 5.3.2), are included as part of an instruments dynamic specification. The values used to predict the response of the three axes, given in Table 16 (Section 5.3.2), are not absolutely necessary, but may facilitate the end user of such an instrument in predicting the effects of modifications or loading. If values are given for these parameters, the inclusion of a transfer function, describing the control system, is also desirable. Establishing the transfer function for any particular instrument may be difficult

in the absence of supplier information e.g. in the case of the instrument designed for this thesis, the relevance of the capacitive behavior of the piezo and the significance of the notch filter action were not initially readily apparent.

The comprehensive design process undertaken has proven to be an invaluable vehicle by which to address the standardisation requirements of precision positioning instruments. It has provided the knowledge base necessary to facilitate the informed conception of a rational set of proposals that could form the foundation of an important specification standard that could meet the needs of customers and by so doing would strengthen the market position of quality device suppliers. The following section outlines suggestions for standardisation based on experience of the design process.

8.3   Recommendations

As can be deduced from Chapter 6, the analysis requirement for the compilation of a table of uncertainties is a complex task, where both the endeavour and final outcome are instrument specific. Even though the purchasers of precision positioning devices are engineers, it is not reasonable to expect customers to fully understand or appreciate the implications of the complex information presented in its totally. It may be surmised that such a format may even cloud issues and cause confusion around the suitability of devices for user specific applications. For this reason, the author does not see the provision of complete error budgets to customers as being either essential, as suggested by McCarthy [9], or desirable. Instead, based on the work carried out in this thesis, along with consideration of current standard provisions, it is suggested that international standards should be introduced for which vendor accredited compliance would require:

- an uncertainty budget along with its rationale to be compiled and subsequently made available *on request* or, preferably, to be made available for viewing on suppliers' web-sites;

- a statement of all identified possible error sources to be available as well as a description of how the resultant biases are quantified, neutralised or compensated;

- a statement of how traceability to the SI unit of length is achieved. This should include details of metrology loops, testing laboratory accreditation, testing methodology and standards, transfer standards, along with supporting documentation;

- a statement of whichever individual or group of international standards the device conforms e.g. the GPS set of standards;

- experimental data used to characterize the dynamic behavior of the device should to be made available on request, along with transfer functions and the parameter values used in any predictive calculations;

- a comprehensive concise set-up manual to be made available if the device or instrument is not to be commissioned by the supplier, along with detailed specifications of all alignment and component locating tools such as autocollimators and micrometers, necessary jigs, fixtures, clamping, etc. ;

- product and environmental details to be made available, including dimensioned mechanical drawing, electronic/control circuitry and detail of any necessary environmental provisions. In this regard, all information should be included that could effect the performance of devices, such as the types of environmental sensors, the location and mounting method of sensors, levels of insulation, shielding etc. ;

- the sales literature provided to customers should include only 'relevant information' in the interest of clarity, all accompanied by expanded uncertainty values that are traceable to the uncertainty budget.

Manufacturers' desire to protect their intellectual property (IP) can be addressed by allowing information about IP components to be replaced in specification documentation by certification of function and performance from an accredited body.

This approach is close to the Chetwynd et al. [10] view that there is a need to compel manufacturers to justify specifications through a statement of uncertainty. Customers' desire for simple criteria for comparing vendors' products is also satisfied, but now there would be the additional assurance that specified values are underpinned by statistical and scientific methodology. Furthermore, the approach

is complementary to existing standards, not being so unlike, but somewhat more prescriptive than, the ISO conformance standards, ISO 17050 (parts one and two). Compliance can effectively be policed by supplier competitors and adjudicated by accredited bodies such as NMIs. This should not be feared by manufacturers of quality products, whereas possibly hitherto exaggerated specified tolerances afforded to some devices on the market may have to be broadened.

The standardization of the aforementioned 'relevant information' to be included in vendor marketing literature is now considered. Crucial to standardising such information is the realization that there is a vast variety of positioning devices on the market, each satisfying different application needs. Their levels of complexity range from relatively simple open loop single axis translators like as the P250, manufactured by PI [27] (for use in conjunction with micrometers), through to the ultra advanced 3D CMM machine designed by Ruijl [26] and sold under the name ISARA 400 by IBS Precision Engineering. It is reasonable to expect that information required for inclusion in any particular specification should be tailored for the specific device in question and that clarity should not be hindered though unnecessary inclusions enforced by overly restrictive standards.

The 3D positioning instrument designed for this thesis is on the higher end of the complexity scale, but many of the lessons learned through its development are just as applicable to more simple systems. In addition to the obvious inclusions of manufacturer's details, product unique model number, product description and toleranced product performance, the following suggestions for standardising guidelines come as a direct result of issues arising during the design process.

- It became apparent in Chapter 6 that uncertainties on which tolerances are based, may, in some situations, change with change of environmental parameters (see Fig. 163). In such situations the parameter range, over which a stated tolerance is true, should be provided.

- It was found that the magnitude of many uncertainties was determined predominantly or solely by the resolution of the sensors used to measure error contributing factors, e.g. the temperature, pressure and humidity sensors used to measure the environmental conditions about the instrument. All sensor information that may affect the instrument performance should

313

be provided. This must include resolution, but may also include size (may affect time response), location requirements and mounting requirements.

- It is apparent that the characteristics given in Table 17 (rise time, settling time, % overshoot, gain margins and bandwidths) should be included as part of an instruments dynamic specification, though these can only be quoted as indicative of future dynamic performance values, subject to confirmation/change arising from experimental tuning methods and testing during commissioning. The inclusion of the parameters given in Table 16, on which these characteristics have been calculated (the process gain, the controller gain, the resistance of the power electronics, the capacitance of the piezo stacks, the mechanical damping ratio, the notch damping ratio and the natural frequencies), is not absolutely necessary, but would facilitate the end user of such an instrument in predicting the effects of modifications or loading.

- Dynamic characteristics such as rise times, overshoots, settling times, gain margins, bandwidths resonance frequencies, velocities, accelerations, contouring ability are very important for users of positioning instruments. This information should be provided in the context of parameter levels prevailing at the time of test and/or levels used to mathematically predict responses. Contouring ability should be given in the context of dwell times and interpolation strategies. Any movement aberrations that may adversely affect the device dynamic performance, such as the presence of friction or hysteresis should also be stated.

8.3.1 Specification example (the designed 3D instrument)

For the purpose of illustration, the proposed standardisation approach is applied to the thesis instrument. For this particular instrument the documentation includes several elements:

- The customer document (only document to be provided directly to customers) provides:
  - manufacturer and supplier details;
  - model name/ number;

314

- o instrument information, including a description, features, predicted performance and dynamic characteristics);

- o direction to supporting documentation; and

- o safety warning and instructions.

- Assembly instructions provide a step-wise set of instructions for assembling the instrument, including details of necessary tooling.

- Supporting information provides details of:

    - o traceability;

    - o declaration of conformity;

    - o dynamic response (including the transfer function, parameter values); and

    - o uncertainty budget (including relevant contributing information regarding sensors, set-up instrumentation, the metrology loop and instrument structures).

- Uncertainty budget rationale provides the logic leading to the uncertainty budget; it includes the development of the relationship functions and the calculation of the component uncertainties, the, sensitivity factors and combined uncertainties.

- Structural mechanical drawings of the metrology frame, force frame/stage, support frame and isostatic mirror mounts. considering

- Manuals provided by the component manufacturers, for the interferometer laser, the capacitive sensors and the piezo servo control electronics.

Only the customer document is included within the thesis (see Appendix A 1). Much of the supplementary information has already been included in previous chapters e.g. the set-up instructions are included in Chapter 7, while the uncertainty budget, along with its rationale, can be found in Chapter 6. Being cognisant of the extent of the material involved and the need to avoid creating a repetitious bloated document, the supplementary information is therefore provided on a separate disc. On this disc, the assembly instructions and the supporting information files are located in the

315

'supporting documentary' folder, while the mechanical drawings and the manuals are stored in the 'drawings' and the 'manuals' folders respectively.

It should be noted that a different device may have very different information requirements in order to be conform to the same standard. Failure to make sufficient information available to facilitate neutral judgement of device capabilities and/or flawed assessment of the capabilities should become apparent and would lead to withdrawal of certification subject to adequate reappraisal.

8.3.2 Final comment

A set of rational documentation proposals has been presented, based on the design realisation of a complex 3D precision positioning instrument, whilst taking into consideration existing standards normally related to macro-scale products. If adopted, these proposals would provide a basis for a comprehensive generic specification standard for precision positioning devices that is complimentary to current international standard provisions. Such a standard would be verifiable, rigorous in terms of information provision requirements, yet affording IP protection adaptability to diverse device complexities and flexible product evolution. This standard would be a powerful marketing tool for manufacturers of quality devices, while discouraging customer reliance on exaggerated claims made for lesser offerings. Not only would customers be made aware of the capabilities of competing systems, but would also be informed about prerequisites such as environmental conditions, set-up/calibration procedures, tooling, instrumentation and expertise. Thus customers would be afforded the opportunity to consider these peripherals that may pose a significant financial cost and to deem whether they, themselves, have the capability, time or inclination to perform set-ups or calibrations. Furthermore, such a standard can accommodate change when shortcomings associated with current provisions, particularly in terms of metrology and traceability, are overcome through improving technologies and methodologies. Particularly novel to this set of recommendations is the requirement for sufficient information disclosure to facilitate subsequent detailed scrutiny of uncertainty budgets and adjudication on claims related to device performance. Ultimately, right-first-time purchasing and subsequent correct operation of products would be facilitated by such a standard.

References

9 References

1. Taniguchi N., 1996, Nanotechnology: Integrated processing systems for ultra-precision and ultra-fine products), ISBN 0-19-8562837 (Oxford Science Publications).

2. Vorndran S., 2004, Nanopositioning: fighting the myths, Optics and Laser Europe, November.

3. Kramar J. A., Jun J. S., Penzes W. B., Scheuerman V. P., Scire, F., Teague, E. C., (NIST), 2001, Molecular measuring machine design and performance, Proceedings of the American Society for Precision Engineering, Arlington.

4. Engineering Metrology Toolbox, http://emtoolbox.nist.gov/Wavelength/Edlen.asp (referenced last: 4/8/2012).

5. Hansen H.N., Carneiro K., Haitjema H., De Chiffre L., 2006 Dimensional Micro and Nano Metrology, Annals of the CIRP, Vol. 55 721-743.

6. Silver R.M., Overlay Instrument and Wafer Target Designs, NIST Physical Measurement Laboratory website, http://www.nist.gov/pml/div683/grp02/oiwtd.cfm (referenced last: 4/8/2012).

7. Mamalis A.G., 2007, Recent advances in nanotechnology, Journal of Materials Processing Technology, Vol. 181 52–5.

8. Leach R. K. et al., 2010, Consultation on a European Strategy for Nanometrology, report of the Co-ordination of nanometrology in Europe (Co-Nanomet) project, in association with; NPL, European Society for Precision Engineering and Nanotechnology, PTB, Danish Fundamental Metrology, Laboratoire National de Métrologie et d'Essais, QinetiQ, Federal Institute for Materials Research and Testing.

9. McCarthy K, 1991, Accuracy in positioning systems, The Motion Control Technology Conference Proceedings, New England.

10. Chetwynd D.G., Liu X., 2003, Trends in nanometre metrology: report on a meeting of the Nanometre Metrology Network, London.

11. Murashov V., Howard J., 2011, Nanotechnology Standards, ISBN 978-1-4419-7852-3, e-ISBN 978-1-4419-7853-0 (Pub. Springer).

12. Drayson P., Norris D., Merron G., McKenzie B., 2010, The UK Nanotechnologies Strategy: Small technologies, great opportunities, The British ministerial group on nanotechnologies, (HM Government).

13. Johnstone J.E., 2009, Overview of standards for nanotechnology, Co-Nanomet project, EuroNano Forum, Prague.

14. International Standards Organization (ISO), Technical Committee 229 (TC229) (http://www.iso.org/iso/iso_catalogue/catalogue_tc/catalogue_tc_browse.htm?commid=381983) (accessed April 2012).

15. Berger M., 2008, Nanotechnology Standards, nanowerk spotlight, www.nanowerk.com/spotlight/spotid=5736.php (accessed August 2012).

16. Kulinowski K., 2010, Nanotechnology standards, The GoodNanoguide, http://goodnanoguide.org/Nanotechnology+Standards&highlight=standards (last accessed August 2012).

17. Peng D., 2009, Nanotechnology commercialization in China, Workshop on Nanotechnology, Society and Policy, held at the University of Manchester.

18. Organization for Economic Cooperation and Development (OECD), http://www.oecd.org/dataoecd/23/52/39149145.pdf, (accessed August 2012).

19. Mantovani E., Morrison M., Geertsma, 2011, Developments in nanotechnologies regulation and standards, (ObservatoryNANO project deliverable D6.2.3 (WP6)).

20. Osanna P.H., Durakbasa M.N., Krauter L., 2008, Industrial metrology and interchangeable manufacturing under the viewpoint of nanotechnology and nanometrology, Problems of Engineering Cybernetics and Robotics, Vol. 59 60 – 73.

21. International Standards Organization (ISO), Technical Committee 213 (TC213) http://isotc213.ds.dk/ (accessed May 2012).

22. Pendrill L., Flys O., Dirscherl K., Roebben G., 2010, European consultation on metrological traceability, standards and dissemination of metrology in industrial nanotechnology, ISBN 978-0-9566809-8-3 ,(Co-Nanomet).

23. ISO/IEC Guide 98-3:2008, Guide to the expression of Uncertainty in Measurement (GUM).

24. Gao W., Hocken R.J., Patten J.A., Lovingood J., Lucca D.A., 2000, Construction and building of a nanomachining instrument, Precision Engineering, Vol.24 320-328.

25. Xu Y., Atherton P.D., Smith S.T., 1996, A metrological scanning force microscope, Precision Engineering Vol.19 46-55.

26. Ruijl T., 2001, Ultra precision coordinate measuring machine design: Design, calibration and compensation, ISBN 90-6464-287-7 (Ponsen & Looijen).

27. Physik Instrumente (PI) GmbH & Co., http://www.pi.ws, info@pi.ws, (accessed August 2012).

28. Xu Y., .Atherton P.D., .Hicks T.R., McConnell M., 1996, Design and Characterisation of Nanometer Precision Mechanisms (Paper1). Proceedings of American Society for Precision Engineering (ASPE) Annual Meeting, Monteray.

29. Chu C.L., Fan S.H., 2006, A novel long-travel piezoelectric-driven linear nanopositioning stage, Precision Eng. Vol. 30 85-95.

30. Yeh H.C., Ni W.T., Pan S.S., 2005, Digital closed-loop nanopositioning using rectilinear flexure stage and laser interferometry, Control Engineering Practice, Vol. 13 559–566.

31. ISO 5725-1 Accuracy (trueness and precision) of measurement methods and results- Part 1: General principles and definitions Ref No. 5725-1:1994(E).

32. International Vocabulary of Metrology basic and general concepts and associated terms (VIM), Third edition, Joint Committee for Guides in Metrology JCGM, , 2008 version.

33. Taylor B.N., Kuyatt C.E., 1994, Guidelines for evaluating and expressing the uncertainty of NIST measurement results, NIST Technical Note 1297, (U.S. Government Printing Office).

34. Holman A.E., Heerens W.C., Tuinstra F., 1993, Using capacitive sensors for in situ calibration of displacement in the piezo driven translation stage of an STM, Sensors and Actuators A, Vol. 36 37- 42.

35. Selby N., Suehrcke H., 2006, Variation in Heat gain through the roof of a building due to changes in Solar reflectance, Coolshield, http://www.coolshield.com.au (accessed August 2012).

36. Smith S.T. & Chetwynd D.G., 1992, Foundations of ultraprecision mechanism design, ISBN 2-88124-840-3 (Gordon and Breach Science Publishers).

37. Hicks T.R., Atherton P.D., 1997, The Nano Positioning Book: Moving and measuring to better than a nanomtre (Queensgate Instruments), ISBN 0-9530658-0-4 (Penton Press).

38. CVI Melles Griot Inc, Products, https://www.cvimellesgriot.com/Products/Products.aspx, (accessed August 2012).

39. LINOS Photonics Gmbh & Co. KG, Products, www.linos-katalog.de (accessed August 2012).

40. Ciddor P. E., 1996, Refractive index of air: new equations for the visible and near infrared, Applied. Optics, Vol. **35**, 1566–1573.

41. Castro H.F.F., 2008, Uncertainty analysis of a laser calibration system for evaluating the positioning accuracy of a numerically controlled axis of coordinate measuring machines and machine tools, Precision Engineering, Vol. 32 106–113.

42. Baxter L.K., 2000, Capacitive Sensors, IEEE Press, Vol 6 26.

43. Janocha H. Klaus K., 2000, Real-time compensation of hysteresis and creep in piezoelectric actuators, Sensors and Actuators, Vol. 79 83–89.

44. Bertotti G., Mayergoyz I., 2005, The Science of Hysteresis, Volume 3 : Hysteresis in Piezoelectric and Ferroelectric Materials, ISBN 978-0-12-480874-4, (Elsevier Academic Press).

45. Doiron T, Stoup J., 1997, Uncertainty and dimensional calibrations, Journal of Research of NIST, Vol. 102, 647 – 676.

46. Kramar j., Jun J., Penzes W., Scire F., Teague j., Villarrubia J., Amatucci E., Gilsinn D., 1998, The Molecular measuring machine, Precision Engineering Division, NIST, Proceedings of international conference on mechatronic technology 477-487.

47. Bryan J.B., 1979, The Abbe principle revisited: an updated interpretation, Precision Engineering, Vol. 1 129-132.

48. Koevoets A.H., Eggink H.J., van der Sanden J., Dekkers J.,Ruijl T.A.M., 2007Optimal Sensor Configuring Techniques for the Compensation of Thermo-Elastic Deformations in High-Precision Systems, Philips Applied Technologies, ISBN 978-2-35500-002-7 (EDA publishing).

49. Lee C.-W., Kim S.W., 1997, An Ultra Precision Stage for Alignment of Wafers in advanced microlithography, Precision Engineering, Vol. 21 113-122.

50. Woronko A., Huang J., Altintas Y., 2003, Piezoelectric tool actuator for precision machining on conventional CNC turning centres, Precision Eng, Vol. 27 335 - 345.

51. Elmustafa A.A., Lagalla M.G., 2001, Flexural-hinge guided motion nanopositioning stage for precision machining: finite element simulations, Precision Engineering, Vol. 25 77-81.

52. Rankers A.M., 1997, Machine Dynamics in Mechatronic Systems: an engineering approach, ISBN 90 365 0957 2, (Phillips Electronics N.V.).

53. Slocum H.A., 1992, Precision machine design, ISBN 0-13-690918-3, (Prentice Hall).

54. Chen K.S., Trumper D.L., Smith S.T., 2003, Design and control for an electromagnetically driven X-Y-θ stage, Precision Engineering. Vol. 26 355-369.

55. Cuttino J.F., Bart H.C.A, van Dijck A.M., Brown A.M., 2005, Design and development of a toroidal flexure for extended motion applications, Precision Eng., Vol. 29 135-145.

56. Moon Y.M., Trease B.P., Kota S., 2002, Design of large displacement compliant joints, Proceedings of Biennial Mechanical and Robotics Conference, Montreal.

57. Culpepper M.L., Anderson G., 2004, Design of a low cost nano-manipulator which uses a monolithic spatial compliant mechanism, Precision Engineerimg Vol. 28 469-482.

58. Hughes E., 1979, Electrical Technology 5th edition, ISBN 0-582-41145-9, (Longman Group).

59. Fan K.C., Fei Y., Yu X., Wang W., Chen Y., 2007, Study of a non-contact type micro-CMM with arch-bridge and nanopositioning stages, Robotics and Computer-Integrated Manufacturing Vol. 23 276–284.

60. Schmitz T.L., Kim H.S., 2007, Monte Carlo evaluation of periodic error uncertainty, Precision Engineering Vol. 31 251-259.

61. Hansen H. N., 2006, Carneiro K., Haitjema H., DE Chiffre L., Dimensional Micro and Nano Metrology, Annals of CIRP, Vol. 55/2 721-743.

62. Cosijns S.J.A.G., 2004, Displacement laser interferometry with sub-nanometre uncertainty, ISBN 90-386-2656-8, (Grafisch bedrijf Ponsen & Looijen).

63. Peggs G.N., Yacoot A., 2002, A review of recent work in sub-nanometre displacement measurement using optical and X-ray interferometry, NPL, Royal Society Mathematical

and Physical & Engineering Sciences, rsta.royalsocietypublishing.org Vol. 360 953-968.

64. Kiong T.K., Heng L.T., Sunan H., 2008, Precision motion control: design and implementation, ISBN 978-1-84800-020-9 (Springer-Verlag).

65. Choi B.J., Sreenivasan S.V., Johnson S., Colburn M., Wilson C.G., 2001, Design of orientation stages for step and flash imprint lithography, Precision Engineering Vol. 25 192-199.

66. Harris J.O., Spence A.D., 2004, Geometric and quasi-static thermal error compensation for a laser digitiser equipped coordinate measurement machine, International Journal of Machine Tools & Manufacture, Vol.44 65-77.

67. Queensgate Instruments Ltd., http://www.nanopositioning.com, (last opened August 2012).

68. Thiel J., Spanner E., 1999, Interferential Linear Encoder with 270mm measurement length for nanometrology, Proceedings of 1st international comferace of Euspen, 522 – 525.

69. E-funda materials information web-site,
http://www.efunda.com/materials/materials_home/materials.cfm, (accessed August 2012)

70. MatWeb materials information web-site,
http://www.matweb.com/search/DataSheetAppendix, (accessed August 2012)

71. Leach R. K., 2010, Fundamental principles of engineering nanometrology, ISBN 978-0-08-096454-6 (Elsevier).

72. National Instruments Corporation, Products and services, www.ni.com/labview/, (accessed August 2012).

73. Jywe W.Y., Teng Y.F., 2006, New nano-contouring measurement techniques for a nano stage, International Journal of Tools and Manufacture, Vol. 46 869-876.

74. Glöβ R. (2006), Nanometer Precise Hybrid Actuator in Positioning Mechanism with Long Travel Range, Proceedings of Actuator, Bremen, 668 - 671.

75. Figliola R.S., Beasley D.E., 2010, Theory and Design for Mechanical Measurements fifth edition, ISBN 0-470-54741-3 (John Wiley & Sons Inc.).

76. Kirkup L., Frenkel R.E., 2010, An introduction to uncertainty in measurement: using the GUM, ISBN 0-521-84428-4 (Cambridge University Press).

77. Bosch, J.A., 1995, Coordinate Measuring Machines and Systems, ISBN:0-8247-9581-4, (CRC Press).

78. Robert Bosch GmbH, industry and trade, http://www.bosch.com/worldsite_startpage/en/default.aspx (accessed August 2012).

79. Hecht E., 2003, Optics, ISBN 0-321-18878-0, 4th edition (Pearson).

80. GE Sensing/Thermometrics, Temperature, http://www.ge-mcs.com/en/temperature.html (accessed August 2012).

81. Micro-radian instruments, http://www.micro-radian.com (accessed August 2012).

82. Fujita D., Itoh H., Ichimura S., Kurosawa T., 2007, Global standardisation of scanning probe microscopy, Nanotechnology 18 7pp doi: 10.1088/0957-4484/18/8/084002.

83. LESJOFORS-European Springs & Pressings, http://www.lesjoforsab.com/spring-company/lesjofors-elland.asp, (accessed August 2012).

84. Phelan J., Walsh D., 2008, Implementation of a Novel Continuous Improvement Model for Development of Ultra-Precision Equipment, Proceedings of the 25th International Manufacturing Conference (IMC), Dublin.

85. Phelan J., Walsh D., Wemyss T., 2010, On-going evolution of a dedicated environment facility for development of ultra-precision equipment, Proceedings of IMC-27, Galway.

86. Schmenner R.W., 1990, Production/Operation Management Concepts and Situations fourth edition, ISB 0-02-946203-7 (Maxwell Macmillan).

87. Grove D.M., Davis T.P., 1992, Engineering Quality & Experimental Design, , ISBN 0582066875, (Addison Wesley Longman Ltd.).

88. Leach R. K., 2001, The measurement of surface texture using stylus instruments: Measurement good practice guide No. 37, ISSN 1368-6550, NPL Doc. Ref.PDB: 2768, (NPL).

89. Dziomba T., Dai G., Danzebrink H.U., Koenders L., 2009, Standards for scanning probe microscopy, PTB, Euro NanoForum workshop: Application of standards within nanitechnology, Prague.

90. PTB, 2010, Standards and reference samples for nano- and micro-measurement systems, http://www.ptb.de/nanoscale/standards/Standards_preliminary.pdf (accessed August 2012).

91. BAM, Nanoscaled reference materials, http://www.nano-refmat.bam.de/en/index.htm (accessed August 2012).

92. Danzebrink H.U., Dziomba T., Koenders L., Burk T., 2010, Critical Dimensions and scanning probe techniques and thin film metrology: workshop report, ISBN 9/8-0-9566809, (Co-Nanomet Consortium).

93. Weckenmann A., Wiedenhoefer T., 2005, The use of GPS standards in nanometrology, Proceedings of 5th euspen International Conference, Montpellier, Vol 1 169-172.

94. Teague E.C., 1989, The NIST molecular measuring machine project: Metrology and precision engineering design, Journal of vacuum science & technology: microelectronics and nanometre structures, Vol.7 1898 - 1902.

95. Vehar C., 2004, Flexure Design for Precision and Control, http://www.engin.umich.edu/labs/csdl/ppslides/FlexureDesignForPrecisionAndControl_files/frame.html, (accessed August 2012).

96. Xue C., Feng J., Saal A. L., Salsbury J. G., Ness A. R., Lin G.C.S., 2007, Design and analysis of experiments in CMM measurement uncertainty study, Precision Engineering Vol. 31 94–101.

97. Woody S.C., Smith S.T., 2003, Resonance-based vector touch sensors, Precision Engineering, Vol. 27 221-233.

98. Millman J., Halkias C.C., 1973, Integrated Electronics: Analogue and Digital Circuits and Systems, ISBN 10-0074622455, (Tata McGraw-Hill).

99. Spieler H., 2007, Semiconductor Detector Systems, ISBN 978-1-60119-285-1, (Oxford University Press).

100. ANSYS, Inc., www.ansys.com, (accessed August 2012).

101. Moaveni S., 2003, Finite Element Analysis: Theory and Applications with ANSYS 2nd edition, ISBN 978-0-13-111202-5 (Prentice Hall).

102. von Martens H.J., 2002, Evaluation of uncertainty in measurements: problems and tools, Optics and Lasers in Engineering, Vol.38 185-206.

103. Liu C.-H., Jywe W.-Y., Jeng Y.-R, Hsu T.-H, Li Y-T, 2010, Design and control of a long travelling nanopositioning stage, Precision Engineering, Vol 34 497 – 506.

104. Cactus 2000 web-based Air humidity converter: http://www.cactus2000.de/uk/unit/masshum.shtml (last referenced 4/8/2012).

105. Nair V., Strecher V., Fagerlin A., Ubel P., Resnicow K., Murphy S., Little R., Chakraborty B., Zhang A., 2008, Screening Experiments and Fractional Factorial Designs in Behavioural Interventional Research, American Journal of Public Health. Vol. 98 1354-1359.

106. Wemyss T., Phelan J., 2007, The Mechanical Design of a 3- Axis Nano-contouring Stage, proceedings of IMC 24, Waterford.

107. Kim W.-j., Verma S., Shakir H., 2007, Design and precision construction of novel magnetic-levitation-based multi-axis nanoscale positioning systems, Precision Engineering Vol. 31 337–350.

108. Universite de Nante , Science techniques, http://www.sciences.univ-nantes.fr/physique/enseignement/english/s1s2.html, (accessed August 2012).

109. Shehan, M., McCarthy, M., Mulhall, M., Phelan, J., 2004, Low Cost Opposed Pad Hydrostatic Linear Slide Development, proceedings of IMC-21, Limerick.

110. Ryu J.W., Gweon D.G., Moon K.S., 1997, Optional Design of a flexure hinge based XYθ wafer stage, Precision Eng., Vol. 21 18-28.

111. Culpepper M.L., Design of quasi-kinematic couplings, Precision Eng 28(2004)338-357.

112. Hart A.J., Slocum A, Willoughby P., 2004, Kinematic coupling interchangeability, Precision Eng 28 1-15.

113. Culpepper M.L., Kartik M.V., DiBiasio C., 2005, Design of integrated eccentric mechanisms and exact constraint fixtures for micron level repeatability and accuracy, Precision Eng 29 65-80.

114. Picotto G.B., Pisani M., 2001, A sample scanning system with nanometric accuracy for quantitive SPM measurements, Ultra-microscopy Vol. 86 247-254.

115. Lambert B., Valentini A., Lagrange B., De Lit P., Delchambre A., 2003, Design and performances of a one-degree-of-freedom guided nano actuator, Robotics and Computer Integrated Manufacturing 19 89-98.

116. Zhang S., Kiyono S., 2001, An absolute calibration for displacement sensors, Measurement 29 11-20.

117. Chenggang Z., Yingnan W., Yuhang C., Wenhao H., 2006, Alignment measurement of two-dimensional zero-reference marks, Precision Engineering, Vol. 30 238 – 241.

118. Smith P.T., Ryan Vallance R.R., Marsh E.R., 2005, Corrective capacitive displacements in metrology applications with cylindrical artefacts, Precision Eng. Vol. 29 324-335.

119. Fahlbusch S., Fatikow S., 2001, Implementation of self-sensing SPM cantilevers for nano-force measurement in microrobotics, Ultramicroscopy Vol. 86 181-190.

120. Schmitz T.L., Beckwith J.F., 2003, An investigation of two unexplored periodic error sources in differential- path interferometry, Precision Eng. Vol.27 311-322.

121. Rivin E.I., 1995, Vibration isolation of precision equipment, Precision Eng.17 41-56.

122. Jouaneh M., Yang R., 2003, Modelling of flexure-hinge type lever mechanisms, Precision Engineering Vol. 27 407-418.

123. Stone J.A., Howard L.P., 1998, A simple technique for observing periodic nonlinearities in Michelson interferometers, Precision Engineering, Vol. 22 220-232.

124. Awtar S., Slocum A.H., 2007Target block alignment error in XY stage metrology, Precision Engineering Vol. 31 185-187.

125. Pedrotti F.L., Pedrotti L.S. , 1987, Introduction to Optics, ISBN: 0-13-491481-3 (Pearson education).

126. Welford W.T., 1988, Optics, ISBN 0-19-851875-7, (Oxford University Press).

127. Jenkins F.A., White H.E., 1976, Fundamentals of Optics (4th edition), ISBN 0-07-032330-5 (McGraw-Hill college).

Sample specification

A 1. Information to be provided to customer

Specification example (the 3D designed instrument)

1.   Manufacturer details

Manufacturer name:	
Contact details:	Address
	Tel. e-mail Web-site

Regional supplier details

Supplier name:	
Contact details:	Address
	Tel. Web-site e-mail

2.   Instrument details

Instrument type	nanopositioner
Model number	TW1

3.   Instrument description

The TW1 is a three axis positioning instrument, capable of nanometre accuracy while contouring along user defined curved paths or scanning over plane and spherical surfaces.

4.   Instrument features:

- Positioning measurements are traceable to the SI unit of length.
- Smooth frictionless motion is afforded by bracketed cantilever flexure guidance.
- Accurate linear and hysteresis free motion achieved through the use of closed loop proportional integral control.
- Short axially balanced rise and settling times with minimum overshoot.
- A user friendly computer user interface:
o Plane scanning paths can be defined by entering the coordinate locations of three points of the plane, along with the desired scanning resolution.
o Spherical scanning paths can be defined by entering the sphere radius and the desired scanning resolution.
- Automated pre-programmed calibration software allows operators to regularly:
o calibrate, in-situ displacement measurement capacitance sensors to the traceable measurements of Michelson interferometers; and
o transform stage locations that are expressed in the Cartesian coordinate system into coordinates expressed in instrument coordinate system and vice versa.
- Automated software compensation for:
o thermal expansion of mechanical structures; effects of environmental variation (temperature, pressure and humidity) on capacitor relative dielectric; the effects of environmental variation on the wavelength of interferometer laser light; and thermal expansion of capacitor plates; and
o non-linearity between in-process measurement and reference measurements through software based fourth order mapping.

5.   System Performance Characteristics

		X axis	Y axis	Zaxis
Perfomance	Type B Expanded uncertainty in linear positioning (nm) (coverage factor = 2)	3.04	3.2	2.7
	Type B Expanded Uncertainty in yaw (deg)(coverage factor = 2)	7.4×10^{-5}	18.0×10^{-6}	11.3×10^{-5}
	Stroke length (µm)	12.29	12.37	12.92
Dynamic Characteristics (no load)	Rise Time (ms)	3.35	3.65	3.83
	% Overshoot	0.129	0	0
	Settling Time (ms)	6.51	6.97	7.19
	Gain Margin (dB)	14.5 at 346 Hz	18.2 at 461 Hz	20 at 594 Hz
	Phase Margin (deg)	180 at 0 Hz	180 at 0 Hz	180 at 0 Hz
	Bandwidth (Hz)	120	94.5	89.9

Note: the given dynamic characteristics are merely indicative of future dynamic performance values, subject to confirmation/change arising from experimental tuning methods and testing during commissioning.

6.   Physical characteristics

	X axis	Y axis	Z axis
Mass (kg)	0.812	0.457	0.238
Stiffness (N.μm^2)	5.98	5.98	5.166
Natural frequency (Hz)	431.9	475.72	741.5
Stage size (mm)	34	42	21
Instrument footprint (mm)	291	370	231.5

7.   Minimum operational requirements

Maximum change in temperature from temperature at calibration (K)	±0.0125
Maximum Temperature sensor tolerance (K)	±0.002
Pressure sensor tolerance (kPa)	±0.2
Humidity sensor tolerance (%RH)	±5

8.   Supplementary information

- **Assembly instructions** (Located in the supporting documentary file): provide a step-wise set of instructions for assembling and aligning the instrument, including details of necessary tooling.

- **Supporting information** (Located in the supporting documentary file): provides details of:
  - traceability;
  - declaration of conformity;
  - dynamic response (including the transfer function, parameter values); and
  - uncertainty budget (including relevant contributing information regarding sensors, set-up instrumentation, the metrology loop and instrument structures).

- **Uncertainty budget rationale** (Located in the supporting documentary file) provides the rationale leading to the uncertainty budget; it includes the development of the relationship functions and the calculation of the component uncertainties, the, sensitivity factors and combined uncertainties.

- **Structural Mechanical drawings** (Located in the mechanical drawing file), including dimensioned drawing of the metrology frame, force frame/stage, support frame and isostatic mirror mounts.

331

- **Manuals** (Located in the component manuals file): provided is a set of user manuals   for the interferometer laser, the piezo servo control electronics, and the capacitive sensors.

9.   Safety information

Laser safety:

Class IIIa/3R lasers are used in the instrument. Avoid eye exposure to laser beams under direct or specular reflection conditions. Lasers are compliant with CDRH/IEC 60825-1. The following laser safety information is taken from Thorlabs laser manual:

WARNING

Laser Radiation – Avoid Exposure to Beam – Class IIIa/Class 3R Laser Product

As defined by the Federal Register 21 CFR 1040.10 Laser Safety Standard, Thorlabs' Helium Neon laser heads are classified according to output power and wavelength. In compliance with this standard, certain performance features and laser safety labels are provided on the product.

The American National Standards Institute publishes a laser safety standard for users, entitled American National Standard for the Safe Use of Lasers (ANSI Z136.1). Thorlabs strongly recommends that laser users obtain and follow the procedures described in this ANSI standard.

LASER RADIATION IS EMITTED FROM THIS APERTURE

AVOID EXPOSURE

DANGER
LASER RADIATION
AVOID EXPOSURE TO BEAM
CLASS IIIa LASER PRODUCT (CDRH)
CLASS 3R LASER PRODUCT
WAVELENGTH 633 nm
MAXIMUM POWER <4 mW
IEC60825-1:2007 ed2.0

WARNING

Use of controls or adjustments or performance of procedures other than those specified herein may result in hazardous radiation exposure. Avoid unnecessary exposure to laser or collateral radiation that exceeds the acceptable emission limits listed in the safety regulation guidelines 21 CFR Subchapter J 1040.10 and 1040.11. This federal regulation is administered by the National Center for Devices and Radiological Health under the Food and Drug Administration.

It is recommended that all persons who use or are near lasers be aware of the potential hazards.

⚠ **Warning** ⚠

The starting and operating voltages of the laser head are lethal and are specified herein. Ensure that the power supply is turned off and unplugged before attempting to connect or disconnect the lasers.

Do not access the interior of the power supply.
The lasers and the power supplies are not serviceable units.

For more detailed information about laser use and laser safety, see the Thor laser 22154-D02 .pdf included in the manuals folder, located in the supplementary appendix folder.

Piezo control electrical Safety:

(As per component instruction manuals that are provided in the manuals folder, located in the supplementary appendix folder)

CAUTION

E-802 submodule boards are ESD-sensitive (electrostatic discharge sensitive) devices. Observe all precautions against static charge buildup before handling these devices.

Avoid touching circuit components, pins and PCB traces. Discharge any static charge you may have on your body by briefly touching a conductive, grounded object before you touch any electronic assembly. Pose PCBs only on conductive surfaces, such as ESD-safe transport containers (envelopes, foam). Electronic subassemblies must always be kept and transported/shipped in conductive packaging.

Make sure that no conductive particles of any kind (metallic dust or shavings, broken pencil leads, loose screws) get on the card.

DANGER—HAZARDOUS VOLTAGE

The piezo amplifiers described in this manual are High-Voltage devices capable of generating high output currents. They may cause serious or even lethal injury if used improperly.

We strongly advise you to never touch any part that might be connected to the high-voltage output.

Take special care if connecting products from other manufactures. Follow the General Accident Prevention Rules!

Working with high voltage amplifiers requires adequately trained operating personnel.

WARNING—OVERVOLTAGE OR REVERSE POLARITY

Exposing some PZTs to voltages too far outside their operating range will destroy the active element in the actuator. Remember that the active element has only two terminals and is aware only of the potential difference between them. A PZT with -250 V on the negative lead and 0 V on the positive lead sees +250 V. Make sure that both the polarity and the voltage as seen by the PZT are within the allowable range.

CAUTION—INSTALLATION INSTRUCTIONS

E-500 and E-501 chassis need to be installed horizontally with 3 cm air circulation area. Vertical mounting prevents internal convection. Insufficient air flow will cause overheating and premature failure.

Do not use the modules described in this manual with the E-500.621 chassis. That chassis uses the same main connectors, but has incompatible pinouts.

B 1. Tilting of interferometer mirrors; derivation of trigonometric equation

Fig. 203 Measuring beam path resulting from moving mirror tilt. Diagram is adapted from a diagram presented by Theo Ruijl (2001)[26]

$\therefore \Delta L = 4x + 2x \sin \alpha . \tan \alpha$

$\Rightarrow \Delta L = 2x(2 + \sin \alpha . \tan \alpha)$

Fig. 204   Determining Δ
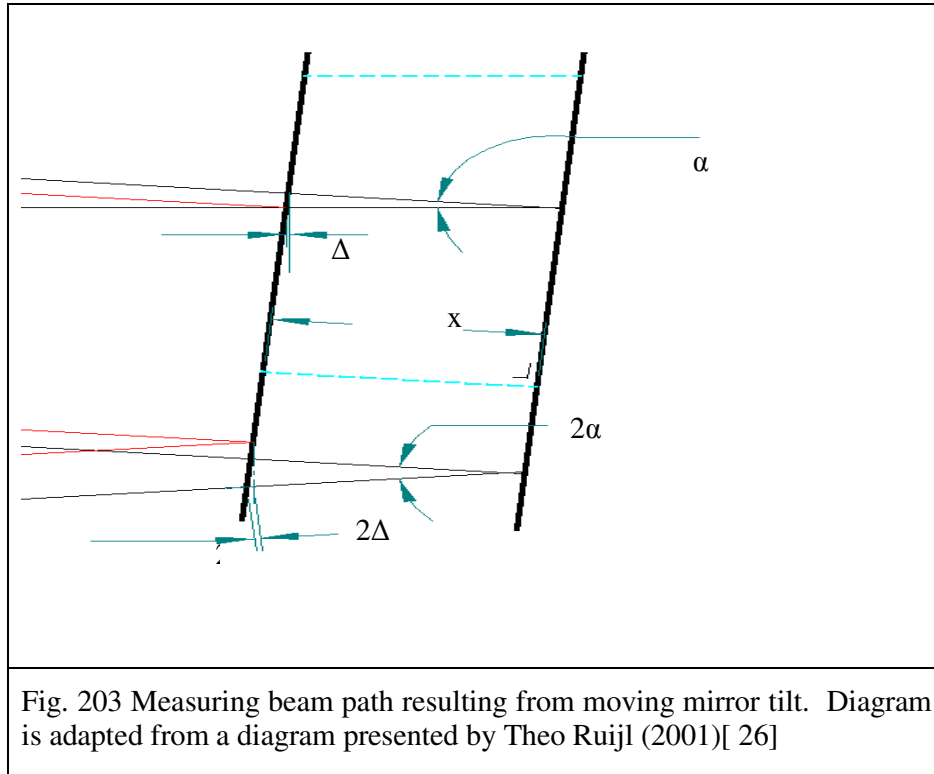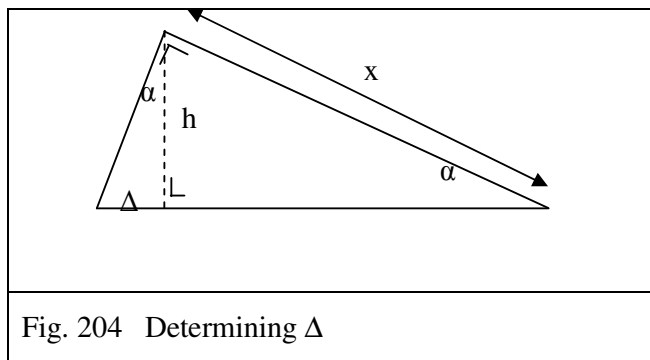
$h = x \sin \alpha$

$\tan \alpha = \dfrac{\Delta}{x \sin \alpha}$

$\therefore \Delta = x \sin \alpha . \tan \alpha$

For a two pass interferometer the measured change in mirror position is given by $\Delta L \big/ 4$.

$Measured \_ translation = \dfrac{x}{2}(2 + \sin \alpha \tan \alpha)$